Acta Pharmacologica Sinica (2011) 32: 279
© 2011 CPS and SIMM All rights reserved 1671-4083/11 $32.00
www.nature.com/aps

Research Highlight

α_2 integrin as regulator of metastatic potential

Miroslav BARANCIK[1], Albert BREIER[2]

Acta Pharmacologica Sinica (2011) 32: 279; doi: 10.1038/aps.2011.12

Regulation of cellular events is a complex process that involves several factors in their specific interactions and interplays. However, within this complexity exist also signs of specificity and changes in single protein could significantly influence the properties and responses of cells.

Recently, Ramirez and colleagues[1] provided innovative results that emphasize the important and selective role of one specific protein, α_2 integrin, in the complex process of tumor metastasis. This protein, as a part of heterodimeric $\alpha2\beta1$ integrin, was identified as a metastasis suppressor in both breast and prostate cancer.

Tumor metastasis is a process by which tumor cells spread from original source tissue to distant sites within the body, and it is not a single event but requires a series of steps. The known key cellular events required for metastasis include invasion of the surrounding stromal tissue, intravasation, evasion of programmed cell death, arrest within the vasculature at a distant site, extravasation, and establishment and growth within a new microenvironment[2]. However, despite intensive research focused on the process of tumor progression and metastasis, the molecular factors involved and mechanisms that determine and drive the dynamic process of cancer metastasis are not fully elucidated. For a better understanding of the biological processes that underline metastasis is essential to identify individual systems that play a key role in these processes.

The study of Ramirez and colleagues[1] represents a valuable contribution to the identification of specific factors that play the key role in tumor invasion. Their data provide important information for identification of potential molecular mechanisms involved in metastatic responses. They highlight the power of a single protein, α_2 integrin, in modulation of tumor invasion and identify also the key mechanistic steps involved in stimulation of metastatic cascade in consequence of loss of $\alpha2\beta1$ integrin expression. The principal model used for the study of processes of breast cancer initiation and progression was a clinically relevant model of tumor-prone genetically engineered animals that spontaneously develop metastasis [mouse mammary tumor virus-Neu (MMTV-Neu) model]. The selective role of α_2 integrin, as a part of heterodimer $\alpha2\beta1$, in breast cancer progression was explored using animals with deleted gene for this protein. Other experimental approaches validated the observed role of the α_2 integrin as a metastasis suppressor also in subtypes of human cancer.

Massive metastatic progression of breast cancer is direct causality of patient death. Therefore, the research focused on regulatory points of metastatic cascade is of great importance. In this respect, recent findings suggest direct links among integrins and tumor metastasis[3]. The integrins are family of extracellular matrix receptors and their actions could be related to altered activation of matrix metalloproteinases[4]. Functions of matrix metalloproteinases were described to be related to intracellular signaling pathways that include some kinase cascades such as ERK[4] and Rho[5]. Detailed description of regulatory sequence determining specific role of α_2 integrin, metalloproteinases and protein kinases in formation of metastasis needs to be studied in future.

Results of Ramirez and colleagues' study further expand our knowledge about the importance of α_2 integrin in cancer progression, and could be explored in improvement of specific diagnosis of breast cancer metastatic potential. Finally, α_2 integrin has to be considered as a potential therapeutic target in the treatment of this disease.

---

[1]*Institute for Heart Research SAS, Dubravska cesta 9, 84005 Bratislava, Slovakia;* [2]*Institute of Molecular Physiology and Genetics SAS, Vlarska 5, 83334 Bratislava, Slovakia*
Correspondence: Dr Miroslav BARANCIK
(miroslav.barancik@savba.sk)

1 Ramirez NE, Zhang Z, Madamanchi A, Boyd KL, O'Rear LD, Nashabi A, *et al*. The $\alpha2\beta1$ integrin is a metastasis suppressor in mouse models and human cancer. J Clin Invest 2011; 121: 226–37.
2 Vernon AE, Bakewell SJ, Chodosh LA. Deciphering the molecular basis of breast cancer metastasis with mouse models. Rev Endocr Metab Disord 2007; 8: 199–213.
3 Rathinam R, Alahari SK. Important role of integrins in the cancer biology. Cancer Metastasis Rev 2010; 29: 223–37.
4 Peng L, Xing X, Li W, Qu L, Meng L, Lian S, *et al*. PRL-3 promotes the motility, invasion, and metastasis of LoVo colon cancer cells through PRL-3-integrin beta1-ERK1/2 and-MMP2 signaling. Mol Cancer 2009; 8: 110.
5 Kidera Y, Tsubaki M, Yamazoe Y, Shoji K, Nakamura H, Ogaki M, *et al*. Reduction of lung metastasis, cell invasion, and adhesion in mouse melanoma by statin-induced blockade of the Rho/Rho-associated coiled-coil-containing protein kinase pathway. J Exp Clin Cancer Res 2010; 29: 127.

npg Acta Pharmacologica Sinica (2011) 32: 280–287
© 2011 CPS and SIMM All rights reserved 1671-4083/11 $32.00
www.nature.com/aps

Review

Synaptic vesicle recycling at the calyx of Held

Lei XUE[1, 2], Yan-ai MEI[1, *]

[1]Institutes of Brain Science, School of Life Sciences and State Key Laboratory of Medical Neurobiology, Fudan University, Shanghai 200433, China; [2]National Institute of Neurological Disorders and Stroke, National Institutes of Health, Bethesda, MD 20892, USA

Efficient endocytosis is crucial for maintaining synaptic transmission because of its role in retrieving constituent membrane and associated proteins. In the past three decades three modes of endocytosis have been proposed involving the central nervous system: clathrin-mediated endocytosis, kiss-and-run endocytosis and bulk endocytosis. These forms of endocytosis can be induced under different conditions, but their detailed molecular mechanisms and functions are largely unknown. Here, we review the existence and initiation of all three modes of endocytosis at a giant glutamatergic synapse, the calyx of Held. The possibility of direct electrophysiology recording in this synapse allows for accurate tracking of exocytosis and endocytosis via capacitance measurements. Future aims will be focused on identifying the molecules that undergo the different mechanisms of endocytosis and the conditions under which different forms of endocytosis predominate.

Keywords: endocytosis; calyx of Held; kiss-and-run; bulk endocytosis; compound fusion; PTP

Acta Pharmacologica Sinica (2011) 32: 280–287; doi: 10.1038/aps.2010.212; published online 24 Jan 2011

Introduction

Neuronal communication relies on synaptic transmission. In the central nervous system (CNS), neurons can fire in the range of 10–100 Hz. However, typical presynaptic terminals in the CNS only have several hundred synaptic vesicles per active zone (AZ). Therefore, efficient endocytosis is crucial to prevent complete exhaustion of secretion-competent vesicles and also to help maintain normal terminal morphology by retrieving excess membrane. A good example of the importance of endocytosis is shibire, a temperature-sensitive phenotype in Drosophila. In this model, neurons cannot retrieve synaptic vesicles at high temperatures, eventually leading to paralysis and falling.

Although the exact mechanisms by which the presynaptic terminal retrieves membrane upon exocytosis are still unclear, there are three hypothetical forms of endocytosis (Figure 1): clathrin-mediated endocytosis (CME), a fast recapture of vesicles called kiss-and-run endocytosis, and bulk endocytosis[1–4]. In 1973, Heuser and Reese published their pioneer electron microscopy (EM) findings describing the CME model in the frog neuromuscular junction (NMJ)[2] . In this model, the vesicles fully collapse with the plasma membrane and are retrieved by CME. The coated pit and cisternae are frequently observed under 10 Hz stimulation for 1 min. In the same year, Ceccarelli demonstrated a second model of endocytosis. Following 2 h of low-frequency stimulation at 2 Hz, the synaptic vesicle was released and retrieved at the same site instead of forming clathrin-coated vesicles[3]. This mode was later named "kiss-and-run" endocytosis[5]. Bulk endocytosis, which is a phenomenon in which a large piece of membrane is retrieved from the presynaptic plasma membrane, has also been frequently observed in several model cells, including the frog NMJ[4], rat hippocampal neurons[6] and goldfish bipolar cells[7]. Here, we review the evidence, the mechanisms, and the physiological importance of all three modes of endocytosis at the calyx of Held, a giant synapse mediating auditory processing in the brain stem[8].

Capacitance measurement at the calyx of Held

Although clathrin-dependent endocytosis is well accepted, the existence of kiss-and-run and bulk endocytosis and their physiological importance are still debated owing to a lack of direct evidence more than three decades after their initial description (See Table 1 for the debate on kiss-and-run). One major difficulty is resolving the rapid fusion and fission processes.

Capacitance measurement, a powerful technique with a time resolution of approximately 1 ms, has been applied to address these problems. The principle on which this technique is based is quite simple: the capacitance of the membrane is proportional to its surface area[9]. When synaptic vesicles fuse with the plasma membrane, the surface area of the presynaptic membrane increases, thereby increasing membrane capaci-

---

* To whom correspondence should be addressed.
E-mail yamei@fudan.edu.cn
Received 2010-10-08 Accepted 2010-11-29

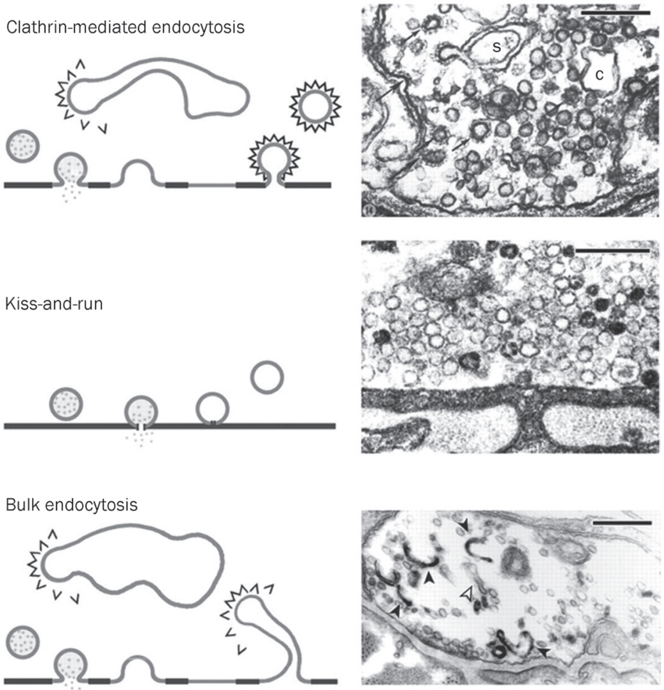

Figure 1. Multiple modes of endocytosis at the frog NMJ. Three modes of synaptic vesicle retrieval from the frog NMJ. Top: Left, clathrin-mediated endocytosis demonstrated by Heuser and Reese. Right, EM figure shows coated pits and vesicles (arrowed) and cisternae (c). Middle: Left, synaptic vesicles are retrieved at the same site, later named "kiss-and-run". Right, EM figure shows no clathrin-coated vesicles and cisternae at low stimulation frequency. Bottom: Left, bulk endocytosis, in which a large piece of membrane internalises after full fusion. New coated vesicles may bud from it or from large, internalised cisternae. Right, EM figure shows internalised cisternae (open arrows: empty; filled arrows: filled with FM1-43). Scale bar: 250 nm in all EM figures. Reprinted by permission from John Wiley and Sons Ltd: Journal of Physiology[1], copyright 2003.

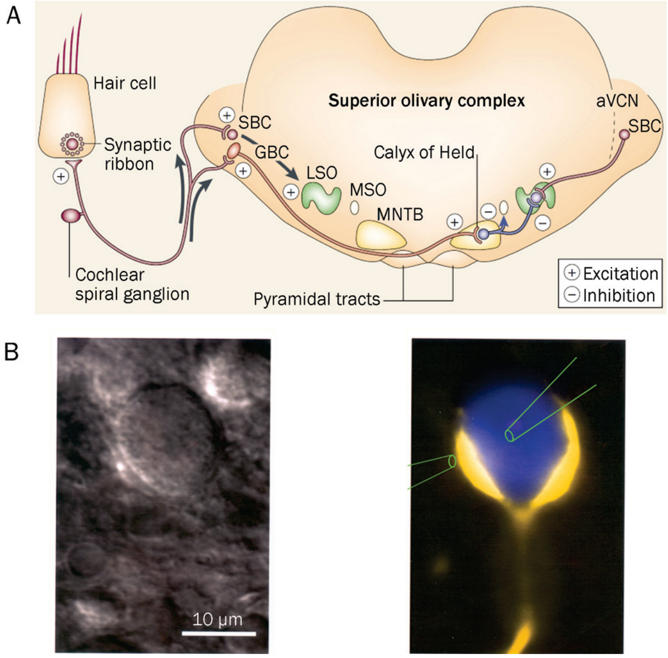

Figure 2. Diagram of the calyx of Held in the mammalian auditory pathway. (A) The calyx of Held functions in sound localization and is located between globular bushy cells (GBCs) and the principal cells of the contralateral medial nucleus of the trapezoid body (MNTB). The calyx of Held is axosomatic and glutamatergic, whereas the principal cell of the MNTB is glycinergic. Reprinted by permission from Macmillan Publishers Ltd: Nature Neuroscience[8], copyright 2002. (B) Left: an infrared differential interference contrast (IR-DIC) image of a calyx of Held and principal cell in a brain slice. Right: pseudo-color image of a calyx and principal cell. The presynaptic terminal was filled with Lucifer Yellow and the postsynaptic cell with Cascade Blue. The two pipettes demonstrate the possibility of simultaneous recordings from both pre- and postsynaptic cells. Reproduced by permission from John Wiley and Sons Ltd: Journal of Physiology[12], copyright 1995.

tance. Therefore, an increase in capacitance indicates exocytosis, whereas a decrease indicates endocytosis. The major drawback of this technique is that it requires patch clamp recordings at large nerve terminals. Certain invertebrate giant synapses have been used to study presynaptic functions[10, 11]. However, similar studies in vertebrate synapses are more difficult due to the technical complexities involved in patch clamp recording from small nerve terminals.

The calyx of Held is a very large glutamatergic synapse of the auditory pathway in the brain stem and is suitable for studying fast transmitter release in the vertebrate CNS (Figure 2A)[12]. The calyx of Held originates from globular bushy cells (GBC) in the anterior ventral cochlear nucleus (aVCN)

Table 1. Debate positions regarding the existence and function of "kiss-and-run" endocytosis.

Model	Supporting	Against
Hippocampus	Tsien RW (Nature, 1998; Neuron, 2000; Nature, 2003; Neuron, 2006) Stevens CF (Nature, 2003) Chapman E (JCB, 2005)	Ryan TA (Neuron, 2004; J Neurosci, 2005) Klingauf J (Nature Neurosci, 2006) Lagnado L (Neuron, 2006)
Calyx of Held	Wu LG (Nature, 2002; Nature, 2006)	Takahashi T (Science, 2005)
Drosophila	Bellen H (Cell, 2002)	Swartz T (Cell, 2005)
Frog	Ceccarelli (1970s–1980s)	Heuser and Reese (1970s–1980s)

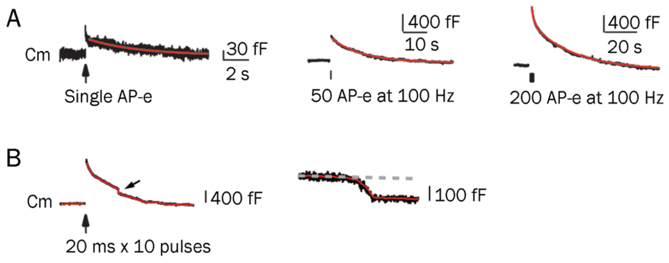

Figure 3. The rate of endocytosis depends on stimulation intensity. (A) Sampled capacitance traces induced by single AP-e (1 ms depolarization from -80 to +7 mV, left), 50 AP-e (middle) and 200 AP-e (right). A fast endocytosis followed by slow endocytosis was observed using 200 AP-e. Scale bars are different in each of the stimulation conditions. Reproduced from Wu *et al* (2005)[18], copyright by the Journal of Neuroscience. (B) Left: sampled membrance capacitance (Cm) traces induced by ten depolarizing pulses of 20 ms from -80 to +10 mV at 10 Hz. Arrow indicates a DCS (downward capacitance shift). Right: plot of the DCS using a larger scale. Note that the DCS is about 100 fF, equivalent to more than 1000 regular vesicles. Reproduced from Wu *et al* (2007)[20], copyright by the Proceedings of the National Academy of Sciences.

and synapses onto a principal cell in the medial nucleus of the trapezoid body (MNTB). Direct electrophysiological recordings can be made simultaneously from both the nerve terminal and the principal cell (Figure 2B). These properties confer unique advantages in the study of the presynaptic mechanisms of transmitter release and short-term plasticity. This model also allows us to characterize the different kinetics involved in endocytosis[13–16].

Rate of endocytosis depends on stimulation intensity

Several studies have determined that the rate of endocytosis depends on stimulation intensity[13, 17, 18]. A mild stimulation (action potential equivalent, AP-e) results in only brief endocytosis. A 50 AP-e stimulation at 100 Hz causes an abrupt increase of capacitance, indicating exocytosis. This is followed by a slow decrease in capacitance, indicating endocytosis with a time constant of 10–20 s. If the stimulation intensity is further increased to 200 AP-e at 100 Hz, the increase in capacitance is higher, and a rapid endocytosis with a time constant of 1–2 s occurs, followed by slow endocytosis (Figure 3A). Rapid endocytosis may be physiologically important during high frequency stimulation because of increased intracellular calcium[18].

Under certain strong stimulation protocols (for example, 10 pulses of 20 ms stimulation at 10 Hz), bulk endocytosis is observed, which is characterized by a large downward shift in capacitance of approximately 50–300 ms (Figure 3B). For a single vesicle, the average membrane capacitance is 23–220 attofarads (aF) with a mean of 73 aF[19]. This decrease in capacitance under strong stimulation therefore reflects the endocytosis of a very large piece of membrane. The decrease in capacitance in these cases may be on the order of 100 femtofarads (fF), equivalent to a simultaneous retrieval of 1000–2000 synaptic vesicles[19, 20].

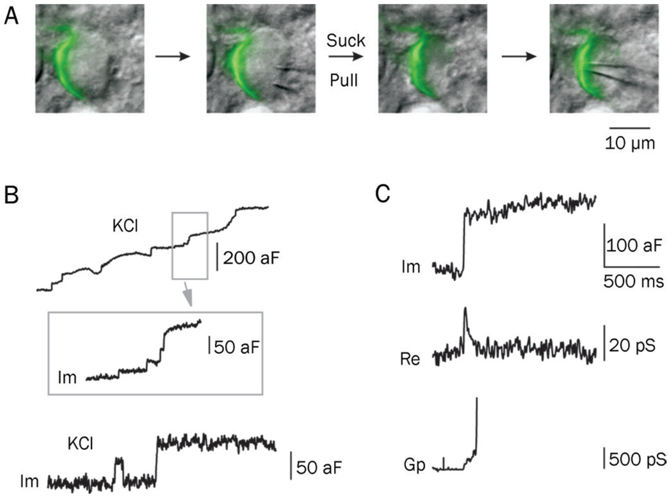

Figure 4. Multiple modes of endocytosis using cell-attached recording at the calyx of Held. (A) The procedure of cell-attached recording at the release site of the calyx. A large pipette was used to remove the postsynaptic principal cell, and a second, smaller pipette was used to make recordings at the release site. The green pseudo-color shows the presynaptic terminal filled with Lucifer Yellow. (B) Top: sampled capacitance trace induced by high KCl stimulation (50–100 mmol/L). Inset shows trace using a larger scale. Im (imaginary part of admittance) reflects capacitance. Up-steps indicate exocytosis upon stimulation. Bottom: a second sample trace shows capacitance flicker and full collapse fusion. Note that the up- and down-step of the flicker has a similar size (about 50 aF), suggestive of a single-vesicle event. (C) Sample Im, Re (real part of admittance) and Gp (conductance of fusion pore) traces of a full collapse event. Note that only a small fraction of the Gp can be detected because of the rapid expansion of fusion pore. A–C are reprinted by permission from Macmillan Publishers Ltd: Nature[19], copyright 2006.

Cell-attached recordings characterize all three modes of endocytosis

The rapid and slow types of endocytosis observed in the calyx of Held may reflect the action of kiss-and-run endocytosis and CME, respectively. Studies from bipolar cells, however, have shown that full collapse fusion could also be followed by rapid endocytosis[21].

In addition to the rate of endocytosis, changes in fusion pore conductance are also used as criteria when distinguishing between kiss-and-run and the full collapse model. A rapid opening and closing of the fusion pore indicates kiss-and-run, whereas fusion pore opening followed by expansion indicates full collapse fusion. Addressing this question requires a similar but different category technique, called cell-attached recording. The signal-to-noise ratio is improved with this technique, and only responses from the small piece of membrane clamped to the electrode are recorded.

Ling-gang WU's group successfully made the first cell-attached recordings at the release sites of the calyx of Held by removing the principal neuron with a large pipette[19] (Figure 4A). When the nerve terminal was depolarized through the addition of a high concentration of KCl in order to trigger vesicle fusion, the magnitude of the small up-steps in the capacitance, indicating exocytosis, agreed with the single-vesicle capacitance estimated from EM studies[22] (Figure 4B). Approximately 20% of the time, capacitance flicker was observed. The term "flicker" is used because the capacitance trace displayed up- and down-steps of similar size with durations of 10 ms to 2 s, suggesting that each step was due to the movement of the same vesicle (Figure 4B). In some cases, fusion pore conductance could be detected with a mean conductance of about 66 picosiemens (ps), equivalent to a fusion pore diameter of about 1 nm (Figure 4C). Within 200 ms, the fusion pore opens, pauses and closes, indicating kiss-and-run endocytosis. This capacitance flicker provides a best piece of evidence for the existence of kiss-and-run endocytosis at CNS synapses. The rapid opening and closing of the fusion pore involved in kiss-and-run endocytosis can control quantal release and thus influence post-synaptic response[19, 23].

In the majority of the fusion events, the up-steps of exocytosis are not followed until much later by the down-steps of endocytosis, presumably reflecting slow endocytosis. In cases where the fusion pore conductance can be measured, the fusion pore opens and expands to an undetectable level within 10–300 ms, demonstrating the full collapse of vesicle fusion[19].

Furthermore, about 20% of the capacitance down-step events induced by stimulation (high KCl or current injection) were large down-steps, with a mean of about 600 aF (ranging from 220–3000 aF). This is a much larger shift than could be explained by a conventional single vesicle's capacitance (22–220 aF, with a mean of about 73 aF). These large down-steps probably reflect bulk endocytosis, which we discuss in a later section[24].

In summary, during the course of cell-attached recordings under high KCl stimulation, the majority of fusion events suggest full collapse with slow endocytosis. Only a small percentage indicate either kiss-and-run endocytosis with different fusion pore sizes or rapid bulk endocytosis.

Calcium/calmodulin triggers all forms of endocytosis

How the different forms of endocytosis are initiated has remained an incompletely resolved question since the discovery of endocytosis three decades ago. Our lack of understanding is likely due to the difficulty in distinguishing between exocytosis and endocytosis. In a recent study[25], when 10 mmol/L of BAPTA (a fast calcium buffer) was added to the presynaptic pipette solution, only a small amount of exocytosis was observed, indicating that the buffer blocked a large amount of calcium-dependent exocytosis. Endocytosis, however, was completely blocked (Figure 5A). This simple experiment indicates that endocytosis is calcium-dependent[25]. Given that calcium is the first signal to trigger exocytosis, it may also be an initiator of endocytosis. If this hypothesis is correct, endocytosis will be slowed or completely inhibited in a low-calcium environment. Conversely, a calcium-initiated model of endocytosis would predict accelerated endocytosis in a high-calcium environment. The inhibition of endocytosis was tested using double-patch recordings at the calyx of Held nerve terminals and principal neurons using a presynaptic pipette solution containing 750 nmol/L calcium. Presynaptic membrane capacitance was measured and analysed in conjunction with postsynaptic miniature excitatory postsynaptic current (mEPSC) events. mEPSC responses reflect only the exocytosis of the presynaptic membrane, whereas presynaptic membrane capacitance demonstrates the net effect between

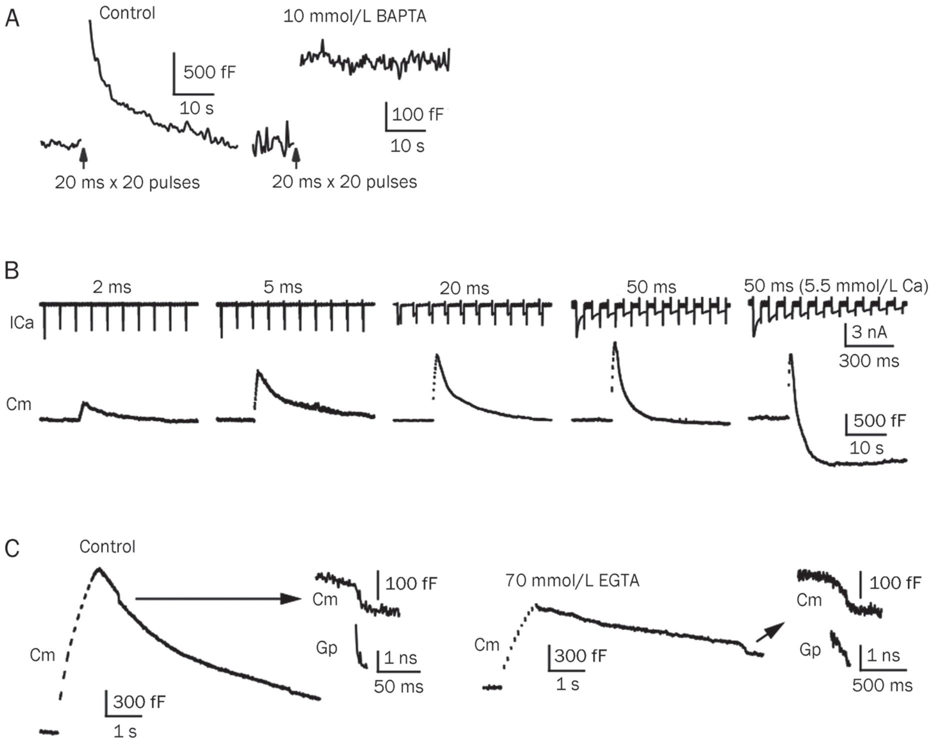

Figure 5. Calcium influx triggers all forms of endocytosis. (A) Endocytosis is initiated by calcium. Left: Cm increase is induced by ten pulses of 20 ms stimulation, depolarized from -80 to +10 mV at 10 Hz. Right: trace from the same stimulation protocol with 10 mmol/L BAPTA in the pipette solution. Most of the exocytosis events were blocked, whereas a small fraction remained. Endocytosis, however, was fully blocked. The scale bars differ between the two conditions. (B) Increasing calcium influx accelerates endocytosis. A bath solution containing 5.5 mmol/L calcium and a stimulation protocol of ten pulses of 50 ms at 10 Hz induced an obvious overshoot. (C) Calcium influx triggers bulk endocytosis and accelerates fission pore closure. Left: ten pulses of 50 ms at 10 Hz induced rapid bulk endocytosis. Right: with 70 mmol/L EGTA, the same stimulation protocol induced fewer and slower bulk endocytosis events. A larger scale of the DCS and a calculation of the Gp are plotted to the right. A–C are reproduced from Wu *et al* (2009)[25].

exocytosis and endocytosis. When capacitance increase data were converted to vesicle releases (about 65–73 aF/vesicle), these data closely matched the mEPSC events (a single mEPSC event reflects a single vesicle fusion event). This nearly perfect match indicates the extreme reduction of endocytosis in this condition[25].

The speeding up of endocytosis was also tested by increasing the stimulation intensity. Ten stimulating pulses at 10 Hz were applied to the nerve terminal with different pulse durations (ranging from 2 to 50 ms) to increase calcium influx. Endocytosis was seen to accelerate following this protocol. If the calcium concentration of the bath solution was increased from 2 mmol/L to 5.5 mmol/L and a 50-ms pulse train was used, both fast endocytosis and an overshoot of endocytosis were observed (Figure 5B). Endocytosis overshoot indicates that the amount of endocytosis is more than the immediately preceding exocytosis[25].

Calcium has also been shown to initiate bulk endocytosis. The addition of 70 mmol/L of EGTA (a slow calcium buffer) to the presynaptic pipette solution dramatically decreased the probability of detecting bulk endocytosis. Furthermore, fusion pore closure was seen to be much slower in the presence of EGTA[25], demonstrating that calcium also controls the fission rate of bulk endocytosis (Figure 5C).

Calmodulin (CaM) is a calcium sensor that mediates all forms of calcium-dependent endocytosis. Using different kinds of calmodulin blockers differentially inhibits either slow or fast endocytosis. Bulk endocytosis can also be blocked by

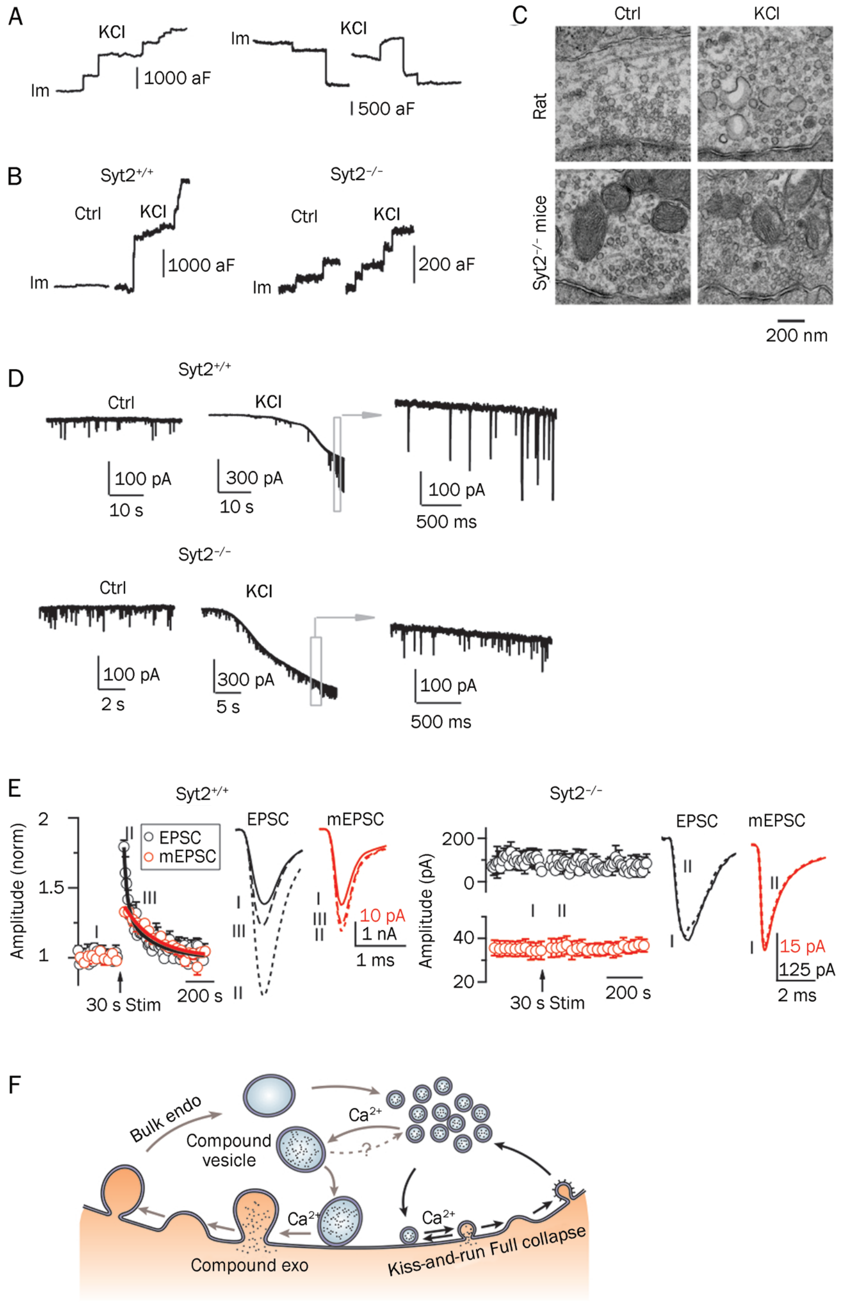

Figure 6. Calcium/synaptotagmin-II-mediated compound vesicle fusion followed by bulk endocytosis. (A) Large up- and down-steps in capacitance can be detected under high KCl stimulation. Left: a sample Im trace shows large up-steps, which reflect compound exocytosis. Right: two sample Im traces show large down-steps, which may reflect bulk endocytosis. (B) Synaptotagmin-II mediates compound vesicle fusion. Left: in wild-type mice, similar large up-steps were observed as were seen in rats. Right: in syt2$^{-/-}$ knockout mice, only small up-steps (<220 aF) were observed. (C) EM images of the calyx in rats and syt2$^{-/-}$ knockout mice. In rats, large vesicle-like structures were observed after about 2 min of high KCl stimulation. In syt2$^{-/-}$ knockout mice, only small vesicles were observed after the same stimulation. (D) Compound vesicle fusion triggers large mEPSCs at the postsynaptic neuron. Top: in wild-type mice, large mEPSCs (100–300 pA) could be induced after high KCl stimulation. Bottom: in syt2$^{-/-}$ knockout mice, compound fusion was blocked; therefore, no large mEPSC was detected. (E) PTP and quantal size increase are calcium/synaptotagmin-II dependent. Left: in wild-type mice, fiber stimulation of 30 s at 100 Hz induced a fast component of PTP followed by a slow component. The fast component is at least partially PKC-dependent. The slow component is dominated by the quantal size increase and is PKC-independent. (F) The new model for vesicle exocytosis and endocytosis at synapses. Endo: endocytosis; kiss-and-run: kiss-and-run fusion and retrieval; exo: exocytosis. A–F are reproduced with modifications from He *et al* (2009)[24].

the calmodulin blocker calmidazolium[25].

Compound vesicle fusion and bulk endocytosis

It is known that there are three forms of endocytosis: clathrin-mediated slow endocytosis, kiss-and-run endocytosis, and bulk endocytosis. It has also been established that there are two forms of vesicle fusion: kiss-and-run fusion and full collapse fusion. Bulk endocytosis does not appear to correlate with any known form of exocytosis. In 2009, a new mode of exocytosis, called compound exocytosis, was proposed in the calyx of Held[24]. Compound fusion describes a kind of fusion among small vesicles forming large vesicles. These large vesicles have an increased quantal size and undergo compound exocytosis followed by bulk endocytosis.

Up-steps and down-steps in capacitance detected by cell-attached recordings at release sites of the calyx of Held reflect exocytosis and endocytosis, respectively. In control conditions, most of the up- and down-steps are smaller than about 220 aF, which is a regular vesicle's maximal capacitance, based on findings from EM studies[22]. This suggests that most of the observed releases are from single vesicles. However, when high KCl (about 75 mmol/L) was applied to stimulate the cell, about 20% of the up-steps were larger than 220 aF with an average of about 600 aF (Figure 6A, 6B). This suggests the possibility of compound fusion among regular vesicles. EM studies have also confirmed this phenomenon. Large vesicle-like structures were observed after 50–100 mmol/L KCl stimulation for about 2 min, which could be interpreted as compound fusion[26](Figure 6C). Recordings of mEPSCs from postsynaptic cells in the presence of high KCl also revealed extraordinarily large mEPSC responses (100–300 pA), further implying that compound fusion could increase quantal size[27–30] (Figure 6D, top). Together, these three pieces of evidence suggest the existence of compound exocytosis.

Compound fusion is observed in both rats and mice. However, in synaptotagmin-II knockout (syt2$^{-/-}$) mice, high KCl failed to induce large up- or down-steps in capacitance; only regular up- and down-steps were observed (Figure 6B, right). Moreover, large vesicle-like structures were not visible by EM following stimulation with high KCl (Figure 6C). Furthermore, the mEPSC measured from the postsynaptic cells showed no large events, indicating a small quantal size (Figure 6D, bottom). Synaptotagmin is an immediate calcium sensor that mediates calcium-dependent exocytosis, and in the calyx of Held, synaptotagmin-II mediates this rapid fusion event[31]. These results together suggest that, similarly to regular fusion events, compound fusion requires synaptotagmin. Experiments have also shown that compound fusion requires calcium. Neither regular nor large up- or down-steps in capacitance are observed when neurons are stimulated with high KCl in a calcium-free extracellular solution.

Calcium and synaptotagmin-II mediate compound fusion[24]. However, all results showing this effect were obtained under high KCl, which is non-physiological condition, raising the question of whether compound fusion also occurs under physiological conditions. Since calyx of Held synapses can fire at rates of up to several hundred Hz of stimulation for relatively long periods of time, Ling-gang WU's group applied 100 Hz stimulation for 20 s to mimic physiological stimulation that may occur *in vivo* during auditory processing. Capacitance recordings from release sites showed that during, and even after, stimulation, large up-steps larger than 220 aF were observed, further confirming the existence of compound fusion[24].

One prediction regarding compound fusion is that it would increase quantal size and synaptic strength. Large mEPSC (100–300 pA) have been demonstrated under high KCl stimulation (Figure 6D, top), suggesting an increase in quantal size. To test the effect of compound fusion on synaptic strength, the same research group applied axonal stimulation to generate action potentials in the nerve terminals and measured mEPSCs along with evoked-EPSCs from the post-synaptic cells[24]. When a 100-Hz train of stimulation was applied, the evoked-EPSC increased immediately, a well-known phenomenon known as PTP (post-tetanic potentiation). PTP was followed by a decay lasting a few minutes[32, 33]. Interestingly, PTP was accompanied by an increase in mEPSC size. The mEPSC size increase did not match the fast EPSC size increase (PTP$_{\text{fast}}$) immediately following stimulation but overlapped with the EPSC increase after about 1–2 min. A most recent work from this group showed that PTP is composed of two components: a PKC (protein kinase C)-dependent increase of quantal content and a PKC-independent increase of quantal size[34]. The slow component of PTP (PTP$_{\text{slow}}$) is dominated by the quantal size increase as a result of compound fusion. Because PTP is widely observed at many synapses following intensive stimulation[32, 35], in addition to the contributions from postsynaptic effects[36–38], it is proposed that compound fusion, may also play an important presynaptic role in synaptic plasticity[35, 39].

Because compound fusion requires calcium and synaptotagmin-II, an intuitive speculation is that the same requirement applies to PTP. PTP in wild-type mice is similar to that observed in rats (Figure 6E, left). In synaptotagmin-II knockout mice, however, EPSC and mEPSC potentiation disappeared following stimulation, which strongly suggests that synaptotagmin-II is required for PTP[24, 31] (Figure 6E, right). When EGTA was added to the extracellular solution to buffer calcium, PTP and mEPSC potentiation disappeared, further confirming the requirement of calcium[24].

In addition to large up-steps in capacitance, large down-steps were also observed in the same conditions used to observe compound fusion. These down-steps occurred later than the up-steps, were of similar size, and were not observed in synaptotagmin-II knockout mice. These results further suggest the existence of bulk endocytosis followed by compound exocytosis.

Taken into account recently published data, a new recycling model has been proposed[24]. In this model, compound fusion occurs among small regular vesicles to form large vesicles. These large vesicles have an increased quantal size and undergo compound exocytosis, thereby increasing synaptic strength through PTP. These vesicles are then retrieved by bulk endocytosis (Figure 6F).

Conclusion and outlook

In summary, influxes of calcium into the nerve terminal trigger different forms of exo- and endocytosis. There are three forms of vesicle cycling: 1) kiss-and-run exo-endocytosis, which involves rapid opening and closure of the fusion pore; 2) full collapse of the vesicle membrane with the plasma membrane, followed by a slow clathrin-mediated endocytosis; and 3) compound vesicle fusion followed by bulk endocytosis (Figure 6F). All three forms cooperate to ensure the efficiency of vesicle recycling at the presynaptic nerve terminal. In addition to recycling, these forms of exo- and endocytosis may also regulate quantal size. Kiss-and-run endocytosis utilizes a small fusion pore that can decrease quantal size and may have effects on synaptic strength. Compound fusion can increase quantal size and subsequently induce synaptic potentiation. Each of these mechanisms provides various ways for the terminal to adjust synaptic transmission and plasticity under different physiological conditions. A recent study from Tsien's group elegantly demonstrated the efficiency of vesicle cycling. Using Qdots (quantum dots) to distinguish between the multiple modes of fusion events, they found that different vesicle cycling modes predominated under different conditions. During a train of stimulation, kiss-and-run endocytosis gradually gave way to full collapse endocytosis[40].

Although our knowledge of vesicle exocytosis and endocytosis has been greatly expanded in the past decades, many questions remain unanswered. We know that many proteins participate in clathrin dependent endocytosis, although their detailed function and mechanisms are still unclear. Other than the existence of kiss-and-run endocytosis, its physiological function and molecular mechanisms are largely unknown. With respect to bulk endocytosis, the final fission process has not been resolved and its molecular regulation has received little attention. Ongoing studies combining capacitance measurements, scanning ion conductance microscopy (SICM), quantum dots, fluorescent dye imaging and series EM reconstructions may give answers to these questions in the near future.

References

1 Royle SJ, Lagnado L. Endocytosis at the synaptic terminal. J Physiol 2003; 553: 345–55.
2 Heuser JE, Reese TS. Evidence for recycling of synaptic vesicle membrane during transmitter release at the frog neuromuscular junction. J Cell Biol 1973; 57: 315–44.
3 Ceccarelli B, Hurlbut WP, Mauro A. Turnover of transmitter and synaptic vesicles at the frog neuromuscular junction. J Cell Biol 1973; 57: 499–524.
4 Richards DA, Guatimosim C, Betz WJ. Two endocytic recycling routes selectively fill two vesicle pools in frog motor nerve terminals. Neuron 2000; 27: 551–9.
5 Fesce R, Grohovaz F, Valtorta F, Meldolesi J. Neurotransmitter release: fusion or 'kiss-and-run'? Trends Cell Biol 1994; 4: 1–4.
6 Takei K, Mundigl O, Daniell L, De Camilli P. The synaptic vesicle cycle: a single vesicle budding step involving clathrin and dynamin. J Cell Biol 1996; 133: 1237–50.
7 Paillart C, Li J, Matthews G, Sterling P. Endocytosis and vesicle recycling at a ribbon synapse. J Neurosci 2003; 23: 4092–9.
8 von Gersdorff H, Borst JG. Short-term plasticity at the calyx of Held. Nat Rev Neurosci 2002; 3: 53–64.
9 Neher E, Marty A. Discrete changes of cell membrane capacitance observed under conditions of enhanced secretion in bovine adrenal chromaffin cells. Proc Natl Acad Sci USA 1982; 79: 6712–6.
10 Augustine GJ, Charlton MP, Smith SJ. Calcium entry and transmitter release at voltage-clamped nerve terminals of squid. J Physiol 1985; 367: 163–81.
11 Young JZ, Keynes R. The Functioning of the Giant Nerve Fibres of the Squid. 1938 - J.Z. and the discovery of squid giant nerve fibres. J Exp Biol 2005; 208: 179–80.
12 Borst JG, Helmchen F, Sakmann B. Pre- and postsynaptic whole-cell recordings in the medial nucleus of the trapezoid body of the rat. J Physiol 1995; 489: 825–40.
13 Sun JY, Wu LG. Fast kinetics of exocytosis revealed by simultaneous measurements of presynaptic capacitance and postsynaptic currents at a central synapse. Neuron 2001; 30: 171–82.
14 Sun JY, Wu XS, Wu W, Jin SX, Dondzillo A, Wu LG. Capacitance measurements at the calyx of Held in the medial nucleus of the trapezoid body. J Neurosci Methods 2004; 134: 121–31.
15 Taschenberger H, Leao RM, Rowland KC, Spirou GA, von Gersdorff H. Optimizing synaptic architecture and efficiency for high-frequency transmission. Neuron 2002; 36: 1127–43.
16 Wolfel M, Schneggenburger R. Presynaptic capacitance measurements and Ca^{2+} uncaging reveal submillisecond exocytosis kinetics and characterize the Ca^{2+} sensitivity of vesicle pool depletion at a fast CNS synapse. J Neurosci 2003; 23: 7059–68.
17 Sun JY, Wu XS, Wu LG. Single and multiple vesicle fusion induce different rates of endocytosis at a central synapse. Nature 2002; 417: 555–9.
18 Wu W, Xu J, Wu XS, Wu LG. Activity-dependent acceleration of endocytosis at a central synapse. J Neurosci 2005; 25: 11676–83.
19 He L, Wu XS, Mohan R, Wu LG. Two modes of fusion pore opening revealed by cell-attached recordings at a synapse. Nature 2006; 444: 102–5.
20 Wu W, Wu LG. Rapid bulk endocytosis and its kinetics of fission pore closure at a central synapse. Proc Natl Acad Sci USA 2007; 104: 10234–9.
21 von Gersdorff H, Matthews G. Dynamics of synaptic vesicle fusion and membrane retrieval in synaptic terminals. Nature 1994; 367: 735–9.
22 Satzler K, Sohl LF, Bollmann JH, Borst JG, Frotscher M, Sakmann B, *et al*. Three-dimensional reconstruction of a calyx of Held and its postsynaptic principal neuron in the medial nucleus of the trapezoid body. J Neurosci 2002; 22: 10567–79.
23 Klyachko VA, Jackson MB. Capacitance steps and fusion pores of small and large-dense-core vesicles in nerve terminals. Nature 2002; 418: 89–92.
24 He L, Xue L, Xu J, McNeil BD, Bai L, Melicoff E, *et al*. Compound vesicle fusion increases quantal size and potentiates synaptic transmission. Nature 2009; 459: 93–7.
25 Wu XS, McNeil BD, Xu J, Fan J, Xue L, Melicoff E, *et al*. Ca^{2+} and calmodulin initiate all forms of endocytosis during depolarization at a nerve terminal. Nat Neurosci 2009; 12: 1003–10.
26 Matthews G, Sterling P. Evidence that vesicles undergo compound fusion on the synaptic ribbon. J Neurosci 2008; 28: 5403–11.
27 Heuser JE. Proceedings: A possible origin of the 'giant' spontaneous potentials that occur after prolonged transmitter release at frog

neuromuscular junctions. J Physiol 1974; 239: 106P–108P.

28 Henze DA, McMahon DB, Harris KM, Barrionuevo G. Giant miniature EPSCs at the hippocampal mossy fiber to CA3 pyramidal cell synapse are monoquantal. J Neurophysiol 2002; 87: 15–29.

29 Llano I, Gonzalez J, Caputo C, Lai FA, Blayney LM, Tan YP, *et al*. Presynaptic calcium stores underlie large-amplitude miniature IPSCs and spontaneous calcium transients. Nat Neurosci 2000; 3: 1256–65.

30 Wall MJ, Usowicz MM. Development of the quantal properties of evoked and spontaneous synaptic currents at a brain synapse. Nat Neurosci 1998; 1: 675–82.

31 Sun J, Pang ZP, Qin D, Fahim AT, Adachi R, Sudhof TC. A dual-Ca^{2+}-sensor model for neurotransmitter release in a central synapse. Nature 2007; 450: 676-82.

32 Korogod N, Lou X, Schneggenburger R. Presynaptic Ca^{2+} requirements and developmental regulation of posttetanic potentiation at the calyx of Held. J Neurosci 2005; 25: 5127–37.

33 Habets RL, Borst JG. Post-tetanic potentiation in the rat calyx of Held synapse. J Physiol 2005; 564: 173–87.

34 Xue L, Wu LG. Post-tetanic potentiation is caused by two signalling mechanisms affecting quantal size and quantal content. J Physiol 2010; 588: 4987-94.

35 Zucker RS, Regehr WG. Short-term synaptic plasticity. Annu Rev Physiol 2002; 64: 355–405.

36 Joshi I, Yang YM, Wang LY. Coincident activation of metabotropic glutamate receptors and NMDA receptors (NMDARs) downregulates perisynaptic/extrasynaptic NMDARs and enhances high-fidelity neurotransmission at the developing calyx of Held synapse. J Neurosci 2007; 27: 9989–99.

37 Joshi I, Wang LY. Developmental profiles of glutamate receptors and synaptic transmission at a single synapse in the mouse auditory brainstem. J Physiol 2002; 540: 861–73.

38 Malenka RC, Bear MF. LTP and LTD: an embarrassment of riches. Neuron 2004; 44: 5–21.

39 Oertel D. The role of timing in the brain stem auditory nuclei of vertebrates. Annu Rev Physiol 1999; 61: 497–519.

40 Zhang Q, Li Y, Tsien RW. The dynamic control of kiss-and-run and vesicular reuse probed with single nanoparticles. Science 2009; 323: 1448–53.

npg
Acta Pharmacologica Sinica (2011) 32: 288–294
© 2011 CPS and SIMM All rights reserved 1671-4083/11 $32.00
www.nature.com/aps

Original Article

Knock-down of protein *L*-isoaspartyl *O*-methyltransferase increases β-amyloid production by decreasing ADAM10 and ADAM17 levels

Narkhyun BAE[1], Se Eun BYEON[1], Jihyuk SONG[1], Sang-Jin LEE[1], Moosik KWON[1], Inhee MOOK-JUNG[2], Jae Youl CHO[1], Sungyoul HONG[1, *]

[1]Department of Genetic Engineering, Sungkyunkwan University, Suwon 440–746, Republic of Korea; [2]Department of Biochemistry and Cancer Research Institute, Seoul National University College of Medicine, Seoul 110–799, Republic of Korea

Aim: To examine the role of protein *L*-isoaspartyl *O*-methyltransferase (PIMT; EC 2.1.1.77) on the secretion of Aβ peptides.
Methods: HEK293 APPsw cells were treated with PIMT siRNA or adenosine dialdehyde (AdOX), a broad-spectrum methyltransferase inhibitor. Under the conditions, the level of Aβ secretion and regulatory mechanism by PIMT were examined.
Results: Knock-down of PIMT and treatment with AdOX significantly increased $A\beta_{40}$ secretion. Reductions in levels of PIMT decreased the secretion of soluble amyloid precursor protein alpha (sAPPα) without altering the total expression of APP or its membrane-bound C83 fragment. However, the levels of the C99 fragment generated by β-secretase were enhanced. Moreover, the decreased secretion of sAPPα resulting from PIMT knock-down seemed to be linked with the suppression of the expression of α-secretase gene products, α-disintegrin and metalloprotease 10 (ADAM10) and ADAM17, as indicated by Western blot analysis. In contrast, ADAM10 was not down-regulated in response to treatment with the protein arginine methyltransferase (PRMT) inhibitor, AMI-1.
Conclusion: This study demonstrates a novel role for PIMT, but not PRMT, as a negative regulator of Aβ peptide formation and a potential protective factor in the pathogenesis of AD.

Keywords: Alzheimer's disease; β-amyloid protein; *L*-isoaspartyl *O*-methyltransferase; soluble amyloid precursor protein alpha; ADAM10; ADAM17

Acta Pharmacologica Sinica (2011) 32: 288–294; doi: 10.1038/aps.2010.228

Introduction

Alzheimer's disease (AD), the most common neurodegenerative disease, is characterized by progressive memory loss and other cognitive impairments[1, 2]. Neuropathological hallmarks of AD include the deposition of amyloid beta (Aβ) peptides, which are organized in senile plaques. In addition, AD is characterized by the accumulation of phosphorylated tau proteins, which are arranged in neurofibrillary tangles (NFTs)[2]. Aβ peptides are generated through the proteolysis of the amyloid precursor protein (APP). In the amyloidogenic pathway, β-secretase cleaves APP to produce soluble amyloid precursor protein beta sAPPβ and a C99 fragment. Membrane-bound C99 can be further processed by γ-secretase to produce Aβ peptides[3, 4]. As an alternative, non-amyloidogenic pathway, α-secretase can cleave within the Aβ region to produce a sAPPα fragment and a C83 fragment[4].

High levels of homocysteine (HCY) can lead to increased concentrations of *S*-adenosylhomocysteine (SAH), a strong methyltransferase inhibitor[5]. This up-regulation of SAH results in an overall decrease in the activity of *S*-adenosylmethionine (SAM)-dependent methyltransferases. Increased SAH levels in the brain tissue of patients with AD has been associated with the inhibition of catechol-*O*-methyltransferase (COMT) and phenylethanolamine-*N*-methyltransferase (PNMT), two enzymes that are widely distributed throughout the human brain[6]. Treatment of Neuro-2a neuroblastoma cells with SAH has been shown to inhibit protein phosphatase 2A methyltransferase (PPMT), resulting in decreased methylation of protein phosphatase 2A[7]. SAH treatment has also been associated with the increased accumulation of APP and phosphorylated tau and with increased Aβ secretion[8]. Protein *L*-isoaspartyl methylation is also essential for the maintenance of neural activity in the central nervous system (CNS). Deficiency of protein *L*-isoaspartyl *O*-methyltransferase (PIMT,

---

* To whom correspondence should be addressed.
E-mail syhong@skku.edu
Received 2010-09-26 Accepted 2010-12-17

EC2.1.1.77), an enzyme that catalyzes the transfer of an active methyl group from SAM to *L*-isoaspartate and *D*-isoaspartate, leads to fatal progressive epileptic disease[9]. Alterations in the SAM/SAH ratio, which is relevant to the overall excitatory state of neurons, have been reported in PIMT-deficient mice[10]. Previous studies have identified deposits of Aβ peptides with isoaspartates in brain tissue isolated from AD patients and PIMT knock-out mice, suggesting a potential pathophysiological role in progressive neurodegeneration[10, 11]. In patients with AD, PIMT is up-regulated in degenerating neurons and is localized in NFTs[10]. Despite the increasing evidence supporting a role for PIMT in neurodegeneration, the mechanism by which PIMT modulates Aβ peptide generation in AD pathogenesis remains unclear. To uncover the mechanism whereby PIMT exerts its effects, we examined the ability of PIMT to regulate Aβ secretion *in vitro*.

Materials and methods

Antibodies and reagents

Adenosine dialdehyde (AdOX), SAM, and mouse anti-β-actin antibodies were purchased from Sigma-Aldrich Chemicals (St Louis, MO, USA). AMI-1 was obtained from Calbiochem (La Jolla, CA, USA). Dulbecco's modified Eagle's medium (DMEM), Opti-MEM, Dulbecco's phosphate buffered saline (DPBS), penicillin, streptomycin, and fetal bovine serum (FBS) were purchased from Gibco (Carlsbad, CA, USA). 3-(4,5-Dimethylthiazol-2-yl)-2,5-diphenyltetrazolium bromide (MTT) was obtained from Calbiochem (La Jolla, CA, USA). Moloney Murine Leukemia virus (M-MLV) reverse transcriptase and polymerase chain reaction (PCR) premix was purchased from Rexgene Biotech Co, Ltd (Ochang, Korea). All of the primers used for PCR were purchased from Bioneer (Daejeon, Korea). A mixture of Stealth™/siRNA duplex oligoribonucleotides against PIMT and Lipofectamine™ RNAiMAX were purchased from Invitrogen (Carlsbad, CA, USA). Monoclonal mouse anti-APP (6E10) antibody was obtained from Signet Laboratories (Dedham, MA, USA). Polyclonal rabbit antibodies to ADAM9, ADAM10, and ADAM17 were obtained from Chemicon International (Temecula, CA, USA). Monoclonal mouse BACE1, monoclonal anti-mouse horseradish peroxidase (HRP)-conjugated secondary antibodies, and anti-rabbit HRP-conjugated secondary antibodies were purchased from Santa Cruz Biotechnology (Santa Cruz, CA, USA). Rabbit anti-PIMT antisera was produced against recombinant porcine PIMT proteins as described[12]. The Genbank nucleotide sequence database accession number of the nucleotide sequence of the clone is AF239700.

Cell culture, drug treatment, and protein preparation

HEK293 APPsw and SH-SY5Y cells were plated on 100-mm culture dishes (Corning Incorporated, Corning, NY, USA). The dishes were filled with DMEM containing 10% FBS, 100 units/mL penicillin, and 100 μg/mL streptomycin. The cultures were maintained at 37 °C with 5% CO_2 under humidified conditions. Cells were treated with drugs (SAM, AdOX, and AMI-1) for indicated times. Vivaspin20 centrifugal filter devices (Satorius, Goettingen, Germany) were used to concentrate conditioned media (CM) from HEK293 APPsw and SH-SY5Y cells collected after drug or siRNA treatments. Cells were washed with DPBS and lysed in Pro-Prep™ protein extraction buffer for 20 min on ice. The protein concentration of each sample was quantified using a Bradford assay (Bio-Rad, Hercules, CA, USA).

Cell viability assay

To determine cell viability, cells were plated on 96-well plates at a density of 2×10^4 cells per well. The original media was then replaced with media containing MTT at a final concentration of 0.5 mg/mL[13]. Four hours later, the medium was discarded, and DMSO was added for the colorimetric assay. Absorption values were determined using an $E_{\max}$ microplate reader from Molecular Devices (Union City, CA, USA) with a 540-nm filter.

Reverse transcriptase-polymerase chain reaction

RNA was isolated from HEK293 APPsw cells treated with or without PIMT siRNA using TRIzol reagent (Gibco BRL) according to the manufacturer's instructions. For each RT-PCR reaction, 1 μg of RNA was used. Each sample was preheated to 60 °C with oligo $(dT)_{18}$ primers for 10 min. One unit per milliliter of M-MLV reverse transcriptase was added. The reaction was then performed at 37 °C for 60 min with the following primers: PIMT, forward 5′-TCAGGAAGGACGATCCAACA-3′, reverse 5′-TCCTCCGGGCTTTAACTGAT-3′; and GAPDH, forward 5′-AAGGGTCATCATCTCTGCCC-3′, reverse 5′-GTGATGGCATGGACTGTGGT-3′. Amplification was carried out for 20 to 30 cycles with the following parameters: 94 °C for 30 s, 55–57 °C for 40 s, and 72 °C for 30 s. These steps were followed by a final 5 min extension step at 72 °C.

siRNA transfection

To conduct the PIMT siRNA transfection, 500 000 cells were seeded onto 100-mm culture plates. Cells were cultured for 48 h at 37 °C in culture medium containing serum, which allowed the cells to be approximately 80% confluent. Immediately prior to transfection, lipofectamine RNAiMAX was incubated with the siRNA of interest in OPTI-MEM (Gibco) at room temperature for 10 min. The cells were then incubated in this mixture for 48 h at 37 °C in fresh medium containing serum.

Immunoblotting

Twenty micrograms of protein mixed with 5×loading buffer [0.313 mol/L Tris-HCl (pH 6.8), 10% SDS, 0.05% bromophenol blue, 50% glycerol], and 20×reducing agent (2 mol/L DTT: Fermentas, Hanover, MD, USA) were boiled for 5 min and loaded onto a 10% SDS-polyacrylamide gel. After electrophoresis, proteins were transferred to a polyvinylidene fluoride (PVDF) membrane (Millipore, Billerica, MA, USA). The membranes were blocked with 5% non-fat milk in 20 mmol/L Tris-HCl (pH 7.4) containing 150 mmol/L NaCl and 0.1% Tween 20 (TBS-T). They were then incubated overnight at 4 °C with primary antibodies (1:2000 for 6E10, 1:1000 for 22C11, 1:3000 for β-actin, 1:2000 for ADAM10, 1:1000 for BACE1, 1:3000 for PIMT) in non-fat milk. The membranes were washed for 10 min in TBS-T and then incubated for 2 h in non-fat milk at room temperature with horseradish peroxidase-conjugated anti-mouse/rabbit secondary antibodies. Bound antibodies were visualized with an enhanced chemiluminescence detection kit (Amersham Bioscience, Pittsburgh, PA, USA).

Cell surface biotinylation

HEK 293 APPsw cells were surface biotinylated by incubation with 2 mg/mL Sulfo-NHS-SS-Biotin (Pierce, Rockford, IL, USA) in ice-cold PBS. After 30 min, the cells were washed and quenched with PBS containing 100 mmol/L glycine. Cells were lysed in 1% NP-40 buffer and incubated with Neutravidin^{TM} immobilized onto 6% cross-linked beaded agarose (Pierce). The beads were washed in NP-40 buffer, boiled in sample buffer, separated using SDS-PAGE, and immunoblotted with the indicated antibodies.

Aβ$_{40}$ ELISA assay

A variety of Aβ peptides, ranging from 38 to 43 amino acids in length, have been shown to be secreted in response to γ-secretase activation[14, 15]. Aβ$_{42}$ is the peptide most widely implicated in AD pathogenesis[16]; however, the antibody for Aβ$_{40}$ was selected based on its reproducibility and accuracy in the Aβ$_{40}$ ELISA kit. The CM was cleared of debris, and the secreted Aβ$_{40}$ was measured using a sandwich ELISA kit (Signet Laboratory, Dedham, MA, USA) according to the manufacturer's instructions.

Statistical analysis

Quantitative analysis of Western blotting was performed by calculating the relative density of immunoreactive bands. The data are expressed as a percentage of the control values. Data are presented as the mean±SD. Each procedure was performed in three to five independent experiments. A Student's *t*-test analysis was used to evaluate statistical significance.

Results

PIMT siRNA and AdOX induce Aβ secretion in HEK293 APPsw cells

As shown in Figure 1A and 1B, PIMT siRNA transfection and AdOX treatment increased the secretion of Aβ$_{40}$ in HEK293 APPsw cells approximately two fold. Compared to controls, PIMT siRNA induced a 35.6%±8.0% reduction in mRNA and protein levels in HEK293 APPsw cells 48 h after transfection (Figure 1C). Importantly, the concentration of AdOX used was not cytotoxic (Figure 1D).

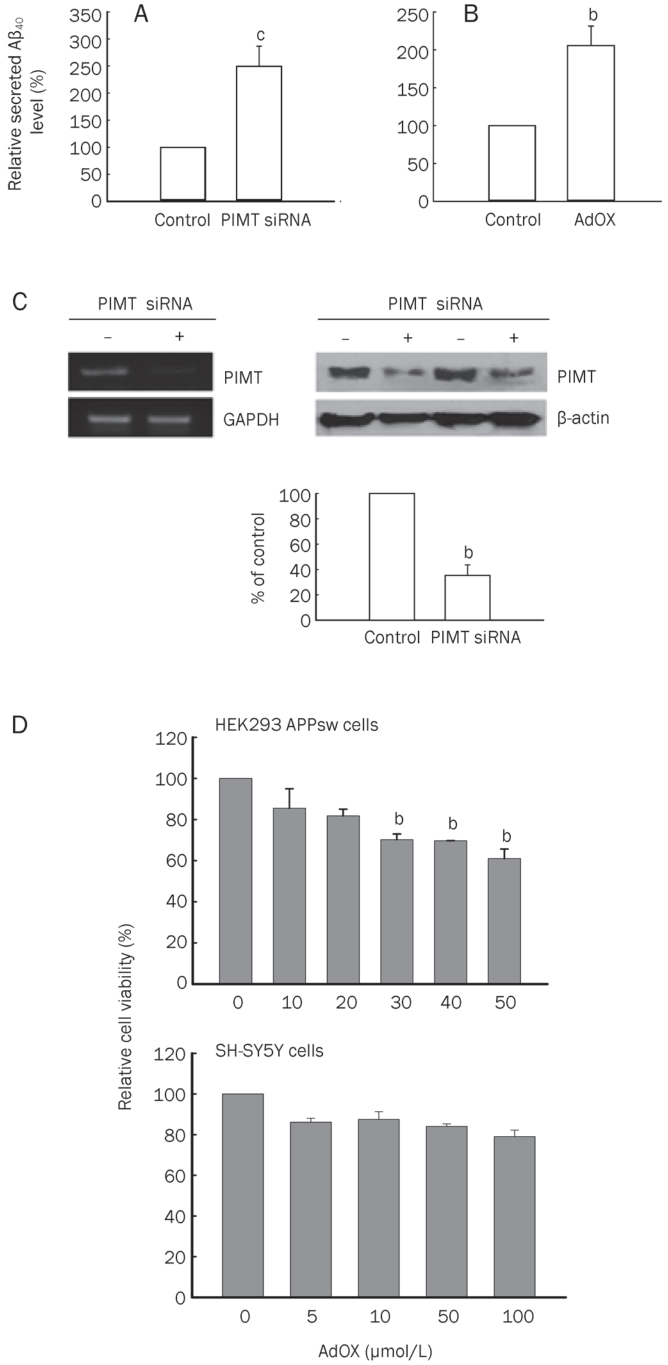

Figure 1. The effects of PIMT siRNA and AdOX treatments on Aβ production. (A and B) HEK293 APPsw cells were treated with or without PIMT siRNA and AdOX. The levels of Aβ$_{40}$ peptide were analyzed using ELISA. (C) HEK293 APPsw cells were transiently transfected with PIMT siRNA at a concentration of 30 nmol/L. RT-PCR of RNA isolated at 48 h shows PIMT mRNA levels were reduced by PIMT siRNA. As a loading control, GAPDH mRNA levels were examined in HEK293 APPsw cells. Expression levels of PIMT protein were analyzed using a Western blot with rabbit anti-PIMT antiserum. As a loading control, levels of β-actin were also determined. (D) HEK293 APPsw cells and SH-SY5Y cells were treated with AdOX. Cell viability was determined using an MTT assay. Results are expressed as the mean±SD for three independent experiments. Mean±SD. $^{b}P<0.05$, $^{c}P<0.01$ compared to untreated or control group.

PIMT siRNA transfection and AdOX decreases sAPPα secretion and increases C99 in HEK293 APPsw cells

To understand the molecular mechanism of PIMT siRNA-mediated Aβ$_{40}$ secretion, we evaluated whether PIMT played a role in the processing of APP. To do this, we measured the levels of the APP cleavage products: sAPPα, C99, and C83.

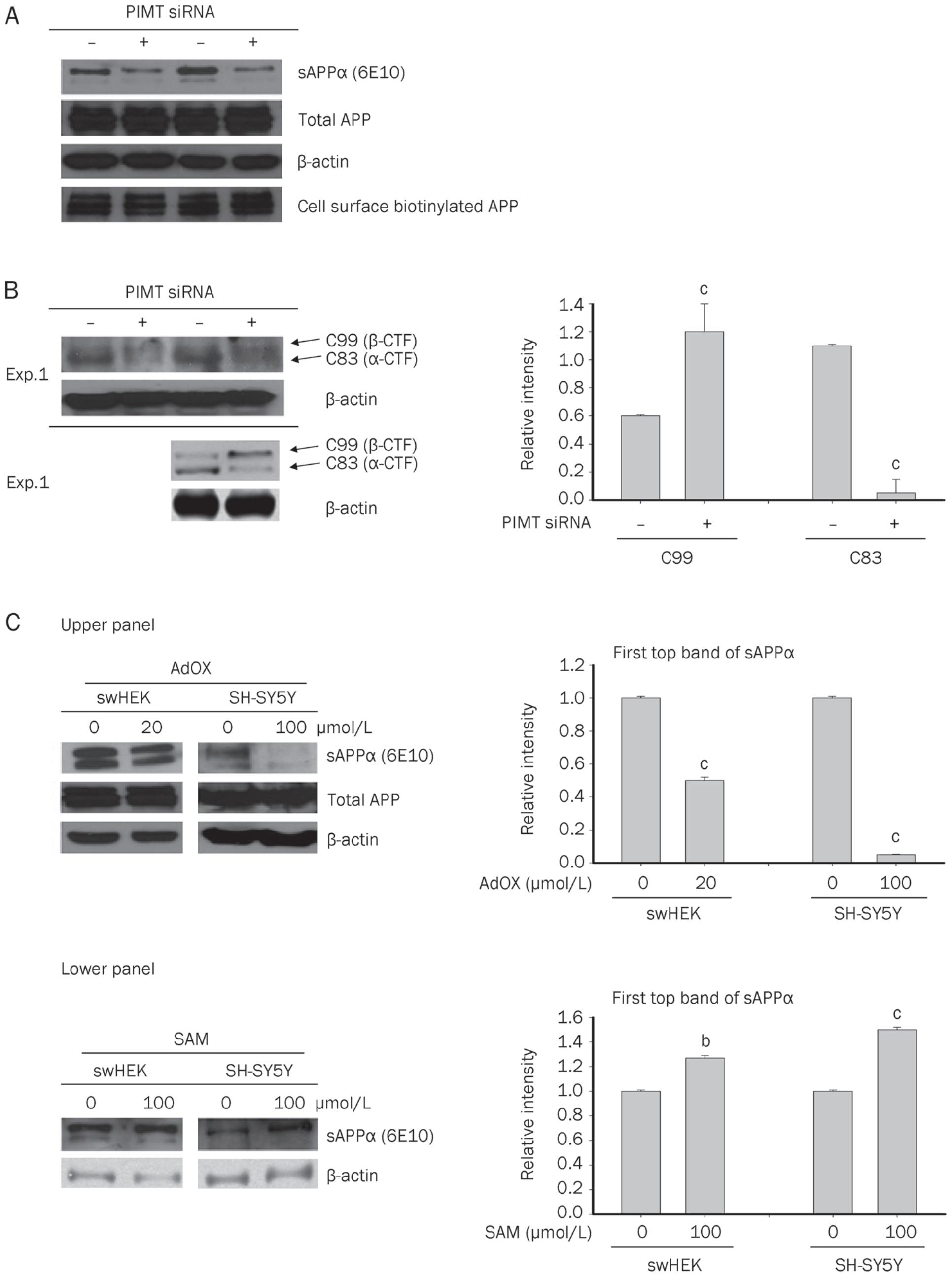

Figure 2. The effects of PIMT siRNA, AdOX, and SAM treatments on levels of membrane bound APP, total APP, and sAPPα. (A) The accumulation of sAPPα in the concentrated media, total cellular and membrane-bound levels of APP, C83, and C99 were analyzed by Western blot analysis. (B) HEK293 APPsw cells were transiently transfected with PIMT siRNA at a concentration of 30 nmol/L. The levels of C99 and C83 proteins were analyzed using Western blotting. As a loading control, levels of β-actin were also determined. (C) HEK293 APPsw (swHEK) and SH-SY5Y cells were incubated without or with AdOX (20 μmol/L) and SAM (100 μmol/L) for 24 h. The levels of sAPPα in the concentrated media, total cellular APP, and membrane-bound APP were analyzed by Western blot analysis. Mean±SD. $^{b}P<0.05$, $^{c}P<0.01$ compared to normal group.

Western blotting for sAPPα in the CM revealed that PIMT siRNA decreased the secretion of sAPPα by 67.4%±3.4%. However, the overall expression of total APP and biotin-labeled membrane APP remained unchanged (Figure 2A), suggesting that the amount of sAPPβ, a critical component for secretion of Aβ_{40}, might be increased. Indeed, the C99 fragment, the cleavage product of β-secretase[17], was increased in PIMT siRNA-treated cells. At the same time, C83 was decreased in PIMT transfected cells (Figure 2B). Similar patterns of sAPPα and total APP were also observed in the AdOX treatment group (Figure 2C, upper panel). In contrast, the induction of transmethylation with 100 μmol/L SAM, a methyl donor[5], increased sAPPα in both cell types (Figure 2C lower panel), demonstrating a critical role of transmethylation in APP processing.

PIMT siRNA transfection decreases ADAM10 and ADAM17 expression

A decrease in sAPPα without a corresponding reduction in total APP expression suggests a potential alteration in the expression or activity of APP processing enzymes. To investigate whether PIMT siRNA altered the expression of APP processing enzymes, we measured the expression levels of several α-secretase candidates: ADAM9, ADAM10, and ADAM17; and the β-secretase candidate, BACE1. As shown in Figure 3A, PIMT siRNA reduced the expression of both the mature and the immature forms of ADAM10 by 45% to 55% compared to controls. In contrast, PIMT siRNA did not significantly

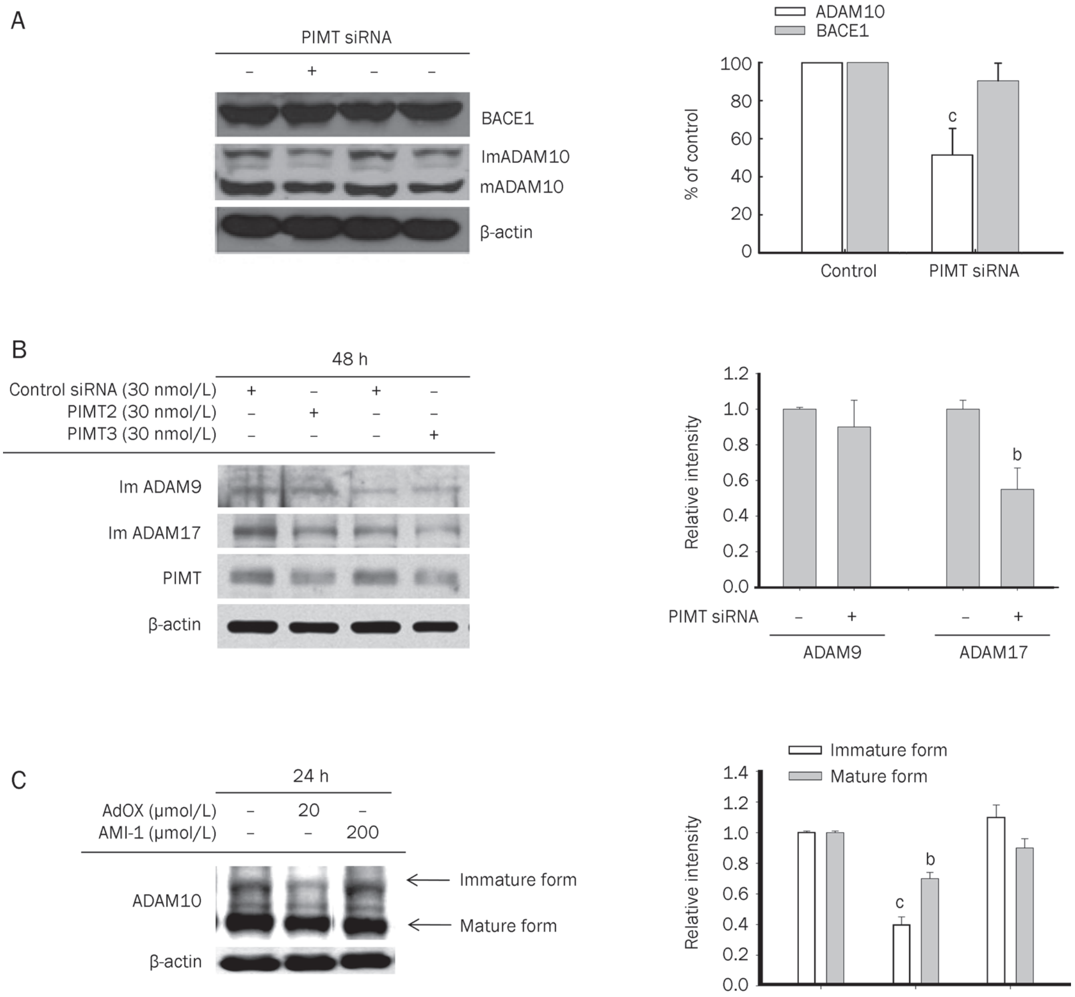

Figure 3. The effects of PIMT siRNA on ADAM10 and BACE1 expression levels. (A) HEK293 APPsw cells were treated with PIMT siRNA for 48 h. Cells were then harvested, and the protein levels of BACE1 and immature (ImADAM10) and mature (mADAM10) forms of ADAM10 were analyzed by Western blot analysis. Densitometric analysis was performed to determine the relative protein level of immature ADAM10 and BACE1. Results are expressed as the mean±SD for three independent experiments. (B) HEK293 APPsw cells were treated with PIMT siRNA for 48 h. Cells were then harvested, and the protein levels of immature ADAM9 and ADAM17, as well as PIMT were analyzed by Western blot analysis. Densitometric analysis was performed to determine the relative protein level of immature ADAM9 and ADAM17. (C) HEK293 APPsw cells were treated with AdOX or AMI-1 for 24 h. Cells were then harvested and the protein levels of immature and mature ADAM10 were analyzed by Western blotting analysis compared to control. Densitometric analysis was performed to determine the relative level of immature and mature ADAM10. Mean±SD. $^{b}P<0.05$, $^{c}P<0.01$ compared to normal group.

alter the levels of BACE1 (90.4%±14% compared to control). PIMT siRNA treatment down-regulated the total protein levels of ADAM17, but not ADAM9 (Figure 3B). In agreement with these data, AdOX, but not AMI-1, a PRMT inhibitor, also strongly reduced ADAM10 levels (Figure 3C). These results suggest that PIMT, but not PRMT, selectively modulates the protein levels of ADAM10 and ADAM17.

Discussion

In this study, we used HEK293 APPsw cells and SH-SY5Y cells to investigate the effects of protein *L*-isoaspartyl methylation on APP processing. HEK293 APPsw cells express high levels of Aβ[18], and SH-SY5Y human neuroblastoma cells express considerable levels of APP and secrete non-toxic, non-amyloidogenic sAPP[17]. Because of this, these cell lines have been widely used to study the regulation of APP processing related to the pathogenesis of AD[19]. Therefore, we used these cells in our study to examine the regulatory role of transmethylation on APP processing. Interestingly, treatment of either cell type with PIMT siRNA and AdOX, a well-known inhibitor of transmethylation[20], remarkably induced the release of $A\beta_{40}$ peptides (Figure 1), indicating the involvement of PIMT-mediated methylation in APP cleavage. Because numerous papers have shown that the secretion of $A\beta_{40}$ is accompanied by the release of additional γ-secretase-generated Aβ peptides, such as $A\beta_{38}$, $A\beta_{42}$, and $A\beta_{43}$, it is likely that the production of these peptides would also be regulated by PIMT siRNA treatment.

To investigate the molecular mechanism underlying this phenomenon, the levels of the enzyme that generate $A\beta_{40}$ peptides were first determined. Figures 2 and 3 reveal that PIMT knock-down modulates both the secretion and cleavage of sAPPα. In response to PIMT siRNA treatment, sAPPα secretion was dramatically diminished, but the levels of total APP and membrane-bound biotinylated APP remained unchanged (Figure 2A). These results suggest that sAPPβ might be relatively enhanced by PIMT siRNA. The C99 fragment, a β-secretase cleavage product of APP, was increased by PIMT knock-down, whereas C83 was dramatically diminished (Figure 2B). Overall, our results suggest that the PIMT-mediated $A\beta_{40}$ production pathway might be primarily associated with the sAPPα cleavage pathway. It has been reported that green tea polyphenol (–)-epigallocatechin-3-gallate (EGCG) exerts a beneficial role in reducing brain Aβ levels by promoting the cleavage of the C99 fragment of APP. The corresponding elevation of sAPPα[21] and G-protein coupled signaling, a major excitatory signal transduction pathway in neuronal cells, is known to activate a sAPPα generation pathway[22]. Therefore, PIMT knock-down could contribute to the down-regulation of sAPPα during $A\beta_{40}$ production.

The improper production of APP isoforms or aberrant APP trafficking during AD pathogenesis is believed to favor the amyloidogenic pathway[23]. In addition, recent reports have shown that Aβ production is influenced more by the location of APP cleavage than the total amount of secretase present within the cell[24]. However, in our study, neither the total amount of APP nor the amount of membrane-associated APP (Figure 2A) was altered in response to PIMT siRNA treatment. These results imply that PIMT does not regulate the trafficking of APP to the cell membrane or its synthesis. Instead, the protein levels of $A\beta_{40}$ generating enzymes (Figure 3) clearly reveal an involvement of proteolytic processing in the observed decrease in sAPPα and increase in $A\beta_{40}$ peptides in response to PIMT siRNA. Indeed, the expression of the α-secretase gene products, α-disintegrin and metalloprotease 10 (ADAM10) and ADAM17[21], was reduced after PIMT siRNA transfection in HEK293 APPsw cells according to Western blot analysis (Figure 3). The facts that BACE1 expression was not altered (Figure 3A) and that the PRMT inhibitor, AMI-1, did not affect ADAM10 levels (Figure 3C) seem to highlight the specificity of this pathway leading to $A\beta_{40}$ generation. However, we cannot exclude the possibility that PIMT knock-down leads to the direct activation of BACE1 despite not affecting its expression level. Indeed, previous work has shown that BACE1-inducible cells exhibit increased production of $A\beta_{40}$ peptides[25]. To date, there is no experimental evidence suggesting that PIMT can regulate the enzyme activity of BACE1. However, several studies have reported that BACE1 can be modified by S-palmitoylation[26] and ubiquitination[27], indicating the importance of post-translational modifications of BACE1. Future studies will determine whether PIMT-induced methylation of BACE1 at aspartyl residues increases its enzyme activity.

In conclusion, we have demonstrated that knock-down of PIMT increased Aβ production via the inhibition of the non-amyloidogenic α-secretase pathway, an effect that is linked to a decrease in sAPPα and ADAM10/17 levels as summarized in Figure 4. Therefore, our study suggests a novel protective role for PIMT in the pathogenesis of AD as a negative regulator of $A\beta_{40}$ peptide formation.

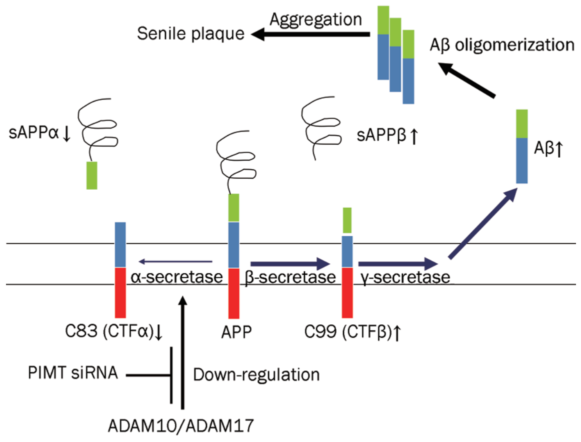

Figure 4. Proposed mechanism of action for PIMT in the regulation of $A\beta_{40}$ peptide generation. Aβ peptides are generated from APP by β- and γ-secretase activity. PIMT seems to modulate the levels of α- and β-secretases synthesized from ADAM10- and -17.

Acknowledgements

This research was supported by Technology Development Program for Agriculture and Forestry, Ministry for Food, Agriculture, Forestry and Fisheries, Republic of Korea.

Author contribution

Narkhyun BAE, Jae Youl CHO, and Sungyoul HONG designed research; Narkhyun BAE, Se Eun BYEON, Jihyuk SONG, and Sang-Jin LEE performed research; Moosik KWON and Inhee MOOK-JUNG analyzed data.

References

1 Dodart JC, May P. Overview on rodent models of Alzheimer's disease. Curr Protoc Neurosci 2005; Chapter 9: Unit 9.22.
2 Hardy J, Selkoe DJ. The amyloid hypothesis of Alzheimer's disease: progress and problems on the road to therapeutics. Science 2002; 297: 353–6.
3 De Strooper B, Saftig P, Craessaerts K, Vanderstichele H, Guhde G, Annaert W, *et al*. Deficiency of presenilin-1 inhibits the normal cleavage of amyloid precursor protein. Nature 1998; 391: 387–90.
4 Buxbaum JD, Liu KN, Luo Y, Slack JL, Stocking KL, Peschon JJ, *et al*. Evidence that tumor necrosis factor alpha converting enzyme is involved in regulated alpha-secretase cleavage of the Alzheimer amyloid protein precursor. J Biol Chem 1998; 273: 27765–7.
5 Grillo MA, Colombatto S. S-adenosylmethionine and its products. Amino Acids 2008; 34: 187–93.
6 Kennedy BP, Bottiglieri T, Arning E, Ziegler MG, Hansen LA, Masliah E. Elevated S-adenosylhomocysteine in Alzheimer brain: influence on methyltransferases and cognitive function. J Neural Transm 2004; 111: 547–67.
7 Sontag E, Nunbhakdi-Craig V, Sontag JM, Diaz-Arrastia R, Ogris E, Dayal S, *et al*. Protein phosphatase 2A methyltransferase links homocysteine metabolism with tau and amyloid precursor protein regulation. J Neurosci 2007; 27: 2751–9.
8 Bottiglieri T. *S*-Adenosyl-*L*-methionine (SAMe): from the bench to the

bedside — molecular basis of a pleiotrophic molecule. Am J Clin Nutr 2002; 76: 1151S–7S.

9 Yamamoto A, Takagi H, Kitamura D, Tatsuoka H, Nakano H, Kawano H, *et al*. Deficiency in protein *L*-isoaspartyl methyltransferase results in a fatal progressive epilepsy. J Neurosci 1998; 18: 2063–74.

10 Shimizu T, Watanabe A, Ogawara M, Mori H, Shirasawa T. Isoaspartate formation and neurodegeneration in Alzheimer's disease. Arch Biochem Biophys 2000; 381: 225–34.

11 Shimizu T, Matsuoka Y, Shirasawa T. Biological significance of isoaspartate and its repair system. Biol Pharm Bull 2005; 28: 1590–6.

12 Kim CM, Hong WS, Lee JO, Kang TW, Kim YH, Cho CG, *et al*. A retrospective study on radiotherapy and radiochemotherapy in esophageal cancer. Korean J Intern Med 1988; 3: 58–63.

13 Kim JY, Lee YG, Kim MY, Byeon SE, Rhee MH, Park J, *et al*. Src-mediated regulation of inflammatory responses by actin polymerization. Biochem Pharmacol 2010; 79: 431–43.

14 Paris D, Ganey NJ, Laporte V, Patel NS, Beaulieu-Abdelahad D, Bachmeier C, *et al*. Reduction of beta-amyloid pathology by celastrol in a transgenic mouse model of Alzheimer's disease. J Neuroinflammation 2010; 7: 17.

15 Iwatsubo T. Pathogenesis of Alzheimer's disease: implications from amyloid research front. Rinsho Shinkeigaku 2004; 44: 768–70.

16 Okamura N, Arai H, Higuchi M, Tashiro M, Matsui T, Itoh M, *et al*. Cerebrospinal fluid levels of amyloid beta-peptide1–42, but not tau have positive correlation with brain glucose metabolism in humans. Neurosci Lett 1999; 273: 203–7.

17 Mills J, Reiner PB. Regulation of amyloid precursor protein cleavage. J Neurochem 1999; 72: 443–60.

18 Citron M, Oltersdorf T, Haass C, McConlogue L, Hung AY, Seubert P, *et al*. Mutation of the beta-amyloid precursor protein in familial Alzheimer's disease increases beta-protein production. Nature 1992; 360: 672–4.

19 Liu F, Su Y, Li B, Ni B. Regulation of amyloid precursor protein expression and secretion via activation of ERK1/2 by hepatocyte growth factor in HEK293 cells transfected with APP751. Exp Cell Res 2003; 287: 387–96.

20 Hong S, Heo J, Lee S, Heo S, Kim SS, Lee YD, *et al*. Methyltransferase-inhibition interferes with neuronal differentiation of P19 embryonal carcinoma cells. Biochem Biophys Res Commun 2008; 377: 935–40.

21 Obregon DF, Rezai-Zadeh K, Bai Y, Sun N, Hou H, Ehrhart J, *et al*. ADAM10 activation is required for green tea (–)-epigallocatechin-3-gallate-induced alpha-secretase cleavage of amyloid precursor protein. J Biol Chem 2006; 281: 16419–27.

22 Camden JM, Schrader AM, Camden RE, Gonzalez FA, Erb L, Seye CI, *et al*. P2Y2 nucleotide receptors enhance alpha-secretase-dependent amyloid precursor protein processing. J Biol Chem 2005; 280: 18696–702.

23 Kins S, Lauther N, Szodorai A, Beyreuther K. Subcellular trafficking of the amyloid precursor protein gene family and its pathogenic role in Alzheimer's disease. Neurodegener Dis 2006; 3: 218–26.

24 Massone S, Argellati F, Passalacqua M, Armirotti A, Melone L, d'Abramo C, *et al*. Downregulation of myosin II-B by siRNA alters the subcellular localization of the amyloid precursor protein and increases amyloid-beta deposition in N2a cells. Biochem Biophys Res Commun 2007; 362: 633–8.

25 Li Y, Zhou W, Tong Y, He G, Song W. Control of APP processing and Abeta generation level by BACE1 enzymatic activity and transcription. FASEB J 2006; 20: 285–92.

26 Cheng H, Vetrivel KS, Drisdel RC, Meckler X, Gong P, Leem JY, *et al*. *S*-palmitoylation of gamma-secretase subunits nicastrin and APH-1. J Biol Chem 2009; 284: 1373–84.

27 Kang EL, Cameron AN, Piazza F, Walker KR, Tesco G. Ubiquitin regulates GGA3-mediated degradation of BACE1. J Biol Chem 2010; 285: 24108–19.

Acta Pharmacologica Sinica (2011) 32: 295–302

www.nature.com/aps

Original Article

Evodiamine improves congnitive abilities in SAMP8 and APP^{swe}/PS1$^{\Delta E9}$ transgenic mouse models of Alzheimer's disease

Shu-min YUAN[1], Kai GAO[1], Dong-mei WANG[1], Xiong-zhi QUAN[1], Jiang-ning LIU[1], Chun-mei MA[2], Chuan QIN[2, *], Lian-feng ZHANG[1, *]

[1]Key Laboratory of Human Disease Comparative Medicine, Ministry of Health and [2]Department of Pathology, Institute of Laboratory Animal Science, Chinese Academy of Medical Sciences & Comparative Medical Center, Peking Union Medical College, Beijing 100021, China

---

Aim: To investigate the effect of evodiamine (a quinolone alkaloid from the fruit of *Evodia rutaecarpa*) on the progression of Alzheimer's disease in SAMP8 and APP^{swe}/PS1$^{\Delta E9}$ transgenic mouse models.
Methods: The mice at age of 5 months were randomized into the model group, two evodiamine (50 mg·kg^{-1}·d^{-1} and 100 mg·kg^{-1}·d^{-1}) groups and an Aricept (2 mg·kg^{-1}·d^{-1}) group. The littermates of no-transgenic mice and senescence accelerated mouse/resistance 1 mice (SAMR1) were used as controls. After 4 weeks of treatment, learning abilities and memory were assessed using Morris water-maze test, and glucose uptake by the brain was detected using positron emission tomography/computed tomography (PET/CT). Expression levels of IL-1β, IL-6, and TNF-α in brain tissues were detected using ELISA. Expression of COX-2 protein was determined using Western blot.
Results: In Morris water-maze test, evodiamine (100 mg·kg^{-1}·d^{-1}) significantly alleviated the impairments of learning ability and memory. Evodiamine (100 mg·kg^{-1}·d^{-1}) also reversed the inhibition of glucose uptake due to development of Alzheimer's disease traits in mice. Furthermore, the dose of evodiamine significantly decreased the expression of IL-1β, IL-6, TNF-α, and COX-2 that were involved in the inflammation due to Alzheimer's disease.
Conclusion: The results indicate that evodiamine (100 mg·kg^{-1}·d^{-1}) improves cognitive abilities in the transgenic models of Alzheimer's disease.

Keywords: evodiamine; Alzheimer's disease; imaging; Morris water-maze test; SAMP8; APP^{swe}/PS1$^{\Delta E9}$; inflammation

---

Acta Pharmacologica Sinica (2011) 32: 295–302; doi: 10.1038/aps.2010.230;

Introduction

Alzheimer's disease (AD) is a progressive and irreversible neuro-degenerative disorder that leads to cognitive, memory and behavioral impairments. Brain regions involved in learning and memory processes, including the temporal and frontal lobes, are reduced in size in AD patients as the result of degeneration of synapses and death of neurons. The pathogenesis of AD is complex, and involves many molecular, cellular and physiological pathologies[1]. The 'amyloid cascade hypothesis' emphasizes a central role for amyloid beta-peptide (Aβ) in the pathogenesis of AD, and suggests that formation and aggregation of Aβ represent key features and possibly involve a triggering mechanism of AD. Based on the amyloid cascade hypothesis, Aβ has become a major therapeutic target[2]. However, amyloid plaques also accumulate during aging, and the stage of AD does not always correlate with the level of neuritic plaques[3]. Recently, it was reported that immunisation with Aβ42 resulted in clearance of amyloid plaques in AD patients, but this clearance did not prevent progressive neurodegeneration[4]. Accumulating evidence increasingly indicates that the inflammatory process is encountered in the pathology of AD. Examination of postmortem brains of AD patients has revealed an abundant presence of inflammatory mediators, such as pro-inflammatory cytokines and chemokines[5–7]. Epidemiological studies indicate that anti-inflammatory drug consumption can significantly reduce the risk of AD[8].

Transgenic mice produced by crossing animals expressing

---

* To whom correspondence should be addressed.
E-mail Zhanglf@cnilas.org (Lian-feng ZHANG);
qinchuan@pumc.edu.cn (Chuan QIN)
Received 2010-06-20 Accepted 2010-12-22

mutant amyloid precursor protein and presenilin 1 (APP^{swe}/PS1$^{\Delta E9}$) and senescence-accelerated mouse/prone 8 (SAMP8) transgenic mice mimic the AD phenotype via different mechanisms. The APP^{swe} transgene encodes a mouse–human hybrid with the mouse sequence in the extracellular and intracellular regions and a human sequence within the Aβ domain with Swedish mutations K594N/M595L. The PS1$^{\Delta E9}$ transgene encodes the exon 9-deleted human presenilin-1. The APP^{swe}/PS1$^{\Delta E9}$ double transgenic mice develop behavioral phenotypic and pathological features which make them useful as an AD model[9]. The senescence-accelerated mouse (SAM) is an accelerated aging model that was established through phenotypic selection from a common genetic pool of the AKR/J strain of mice. The SAMP8 mice show significant impairments in a variety of learning tasks, when compared with senescence accelerated mouse/resistance 1 (SAMR1) mice. Moreover, the abnormal APP and Aβ metabolism in the SAMP8 mice brain suggests that SAMP8 is not only a good model for studying age-related learning and memory deficits, but may also prove to be a useful model for studying Aβ-mediated effects in cognitive decline[10–12].

Chinese herbs have been and still are widely used as important remedies in Oriental medicine. Over recent years, a variety of biologically active constituents have been isolated from these sources. It is reported that tea polyphenol can reverse scopolamine- or *D*-galactose-induced deficits in cognitive abilities[13, 14]. Resveratrol acts to reduce pathological plaques in mice[15, 16] and has anti-oxidant activity *in vitro* and *in vivo*[16, 17]. Evodiamine, a quinolone alkaloid, is a component isolated from the fruit of *Evodia rutaecarpa*, a traditional Chinese herb that has been used for treatment of headaches, abdominal pain, postpartum hemorrhage, dysentery and amenorrhea[18, 19]. However, the treatment of AD with evodiamine has not been reported. In the present study, we investigated the effect and the possible mechanisms of action of evodiamine in mouse models of AD.

Materials and methods

Animal models

The APP^{swe}/PS1$^{\Delta E9}$ double-transgenic mouse in a C57BL/6J genetic background was bred in our laboratory. This mouse shows spatial memory deficits at 3 months of age and senile plaques in brain tissue at 4.5 months of age[9]. SAMP8 and SAMR1 mouse were obtained from the Department of Laboratory Animal Science, Peking University Health Science Center (Beijing, China). SAMR1 is one species of SAM, which shows normal aging characteristics. SAMP8 is a model of age-related dementia of the Alzheimer type and shows significant impairment in a variety of learning tasks[10–12]. All mice were maintained in an AAALAC-accredited facility and the use of animals was approved by the Animal Care and Use Committee of the Institute of Laboratory Animal Science of Peking Union Medical College (SCXK-2005-0013).

Groups and treatment

For screening of 12 herbal monomers, 5 month old transgenic mice were randomly divided into 13 groups (*n*=16 to 20 per group). One group was used as a vehicle control group and the remaining 12 groups were used for treatment with herbal monomers. The herbal monomers were purchased from Qingdao University Natural Product Institute (Qingdao, China). The littermates of non-transgenic mice were used as wild type (WT) controls. The WT and vehicle groups received a standard diet and the treated groups received a standard diet plus the respective monomers at the doses described in Table 1. The doses of 12 individual herbal monomers were selected based on human-equivalent dosages and data in previous reports[13, 14, 16, 20]. Morris water-maze tests were performed after 4 weeks of treatment, since this time period was believed sufficient for APP^{swe}/PS1$^{\Delta E9}$ transgenic mice to show significant impairments in function when compared with WT mice.

For evodiamine analysis, APP^{swe}/PS1$^{\Delta E9}$ and SAMP8 transgenic mice at 5 months of age were randomized into vehicle, evodiamine-Evo 50 (50 mg·kg^{-1}·d^{-1}), evodiamine-Evo 100 (100 mg·kg^{-1}·d^{-1}) and Aricept (2 mg·kg^{-1}·d^{-1}) groups. Aricept is an inhibitor of acetyl-cholinesterase and is presently used in long-term symptomatic treatments for patients with AD, since it enhances CNS levels of synaptic acetyl-choline. The administered does of Aricept was the human-equivalent dosage, calculated according to the weights of the mice. The littermates of no-negative mice and SAMR1 mice were used as WT controls. The mice were treated with standard diet or standard diet plus monomer for 4 weeks and their capacities for learning and memory were assessed by the Morris water-maze test.

Morris water-maze test

The protocol of the Morris water-maze test was modified from the reported methods[21–23]. Briefly, the apparatus included a pool with a diameter of 100 cm, filled with opaque water at 22–24 °C. An escape platform (15 cm in diameter) was placed 0.5 cm below the water surface. Two tests, constituting two blocks of trials, 60 s each, were performed daily for 5 consecutive days. The platform location and the animal starting point were held constant within each pair of daily tests, but they were changed from day to day. The mice were allowed to stay on the platform for 15 s before and after each trial. The time taken for an animal to reach the platform (latency period) was recorded. On the fifth day, a probe test was performed after the second daily trial; briefly, the platform was removed from the maze, and the number of crossings by the mice when the area from which the platform had been removed was recorded (for a maximal period of 60 s). Monitoring was performed with a video tracking system (Noldus Ltd, Ethovision XT, Holland). Results are represented as mean±SEM.

Histochemical analysis

The brain tissues from 6 month old animals were fixed in neutral buffered formalin. The tissues were dehydrated in an alcohol gradient then embedded in paraffin and sliced at 4 μm thickness. Thioflavin-S staining was performed on these slices[24]. After de-paraffinization and hydration, sections were washed in PBS and incubated in 2% potassium metabisulfite and 1% oxalic acid until they appeared white. The sections were then washed in water and stained for 10 min with a solution of 0.015% Thioflavin-S in 50% ethanol. Finally, the sections were washed in 50% ethanol and in water, then dried, and dipped in Histo-Clear before being cover-slipped with Permount. All chemicals were obtained from Sigma.

PET/CT images analysis

The PET/CT scan was modified from the reported method[25]. Briefly, mice from treated and positive and negative control groups were randomly chosen. They were anesthetized using 1.5% isoflurane, along with 31% O_2 inhalation (flow rate: 2.5 L/min) through a nose cone prior to injection of the tracer. During operation, the body temperature of each mouse was maintained by a thermostat-controlled thermal heater; the mouse was imaged on a small-animal scanner (microPET/CT, Inveon, Siemens). Prior to the dynamic small-animal procedure, ^{18}F-FDG tracer (FDG) (at ~14.8–18.5 MBq) was injected as a bolus (~200 μL) through a tail vein catheter and the animal was kept at room temperature for 45 min. FDG is a glucose analog that is actively transported into cells. Then the mouse was exposed to a 10-min PET scan, and a 10-min CT scan was obtained for attenuation correction of small-animal PET images. Images were reconstructed using the filtered back-projection algorithm with CT-based photon-attenuation correction[26]. The voxel size was $0.2 \times 0.2 \times 0.8$ mm^3. The field of view was 11.28×12.66 cm^2.

ELISA

Mouse brain tissue was sampled and 100 mg of tissue per animal was homogenized in 1.0 mL of 0.9% NaCl solution containing 0.1% PMSF (Sigma, MO, USA). After centrifugation at 14 000 rpm for 15 min at 4 °C, the resulting supernatants were sampled in triplicate to detect the levels of IL-1β, IL-6, and TNF-α by an ELISA kit (R&D Systems and Invitrogen) according to the provided instructions.

Western blot

Mouse brain tissue was sampled and 100 mg of tissue per animal was homogenized in 1.0 mL of RIPA buffer containing 0.1% PMSF and 0.1% protease inhibitor cocktail (Sigma, MO, USA). After centrifugation at 14 000 round per minute for 15 min at 4 °C, the protein concentration in the resulting supernatants was detected by the BCA method. Aliquots of 60 μg per sample were subjected to 10% SDS-PAGE, followed by transfer onto a nitrocellulose membrane (Immobilon NC; Millipore, Molsheim, France). Immunoblotting was then carried out with antibodies specific for COX-2 at 1:100 dilution (Cayman Chemical, USA). Primary antibodies were visualized with anti-rabbit HRP-conjugated secondary antibodies (Santa Cruz) using a chemiluminescence detection system (Western Blotting Luminal Reagent, Santa Cruz). Sample loading was normalized with GAPDH. Bands were quantified by the densitometry function of the Quantity One software.

Statistical analyses

Statistical analyses were performed by one-way ANOVA followed by Tukey's Honestly Significantly Different (HSD) test. Data with a $P<0.05$ were deemed statistically significant. Results are expressed as mean±SEM.

Results

Comparative analysis of the effects of 12 different herbal monomers in $APP^{swe}/PS1^{\Delta E9}$ transgenic mice

Twelve herbal monomers, that have varied effects on the CNS, microcirculation, anti-oxidative or anti-inflammatory responses, were selected to analyze their respective effects on cognitive abilities of $APP^{swe}/PS1^{\Delta E9}$ transgenic mice. These herbal monomers and their usages are illustrated by Table 1, which shows their individual effects as evaluated by the Morris water-maze test. Only evodiamine showed the capacity to significantly improve cognitive abilities of $APP^{swe}/PS1^{\Delta E9}$ transgenic mice, specifically referring to their spatial memory deficits at 3 months of age and the AD phenotype which progressively develops as the animals age.

Table 1. Screening of herbal monomers with the Morris water-maze test. Twelve herbal monomers were selected for preliminary treatment of $APP^{swe}/PS1^{\Delta E9}$ transgenic mice with the indicated doses and their effects were evaluated by the Morris water-maze test. Latency on the third day of the tests and platform crossings on the day after the five-day training period were recorded. ($^aP>0.05$, $^bP<0.05$, $^cP<0.01$ *vs* vehicle group).

Group	Dose (mg·kg^{-1}·d^{-1})	Latency (s)	Platform crossings (count)	Number of animals
WT	–	10.62 ± 2.01^c	5.20 ± 0.81^b	*n*=20
Vehicle	–	21.23 ± 3.48	3.75 ± 0.53	*n*=16
Curinine	80	18.58 ± 4.17^a	4.75 ± 1.11^a	*n*=16
Evodiamine	100	12.18 ± 3.03^b	6.63 ± 1.15^b	*n*=16
Tea polyphenols	100	15.05 ± 3.50^a	4.89 ± 0.54^a	*n*=16
Chuanxiongzine	50	14.17 ± 3.50^a	4.75 ± 0.92^a	*n*=18
Polydatin	100	20.94 ± 3.34^a	3.89 ± 0.75^a	*n*=18
Tanshinone IIA	100	14.65 ± 2.51^a	3.67 ± 0.53^a	*n*=18
Astragaloside	100	14.67 ± 2.17^a	2.89 ± 0.54^a	*n*=16
Puerarin	100	18.59 ± 3.36^a	2.88 ± 0.35^a	*n*=20
Salvianic acid A	100	14.62 ± 2.43^a	3.78 ± 0.57^a	*n*=20
Quercetin	100	24.17 ± 3.03^a	5.00 ± 0.54^a	*n*=20
Resveratrol	150	15.64 ± 2.94^a	3.60 ± 0.76^a	*n*=20
Tetrahydropalmatine	100	20.22 ± 3.80^a	3.80 ± 0.44^a	*n*=16

Evodiamine treatment increased spatial learning and memory in SAMP8 and $APP^{swe}/PS1^{\Delta E9}$ transgenic mice

To investigate the effect of evodiamine on AD models, it was used to treat both $APP^{swe}/PS1^{\Delta E9}$ and SAMP8 transgenic mice at age of 5 months. In consideration of the welfare of the animals, administration of evodiamine was effected through oral administration via their diet. After 4 weeks of treatment, learning capacity and memory were assessed by the Morris water-maze test (Figure 1A–1D). During training d 1 the

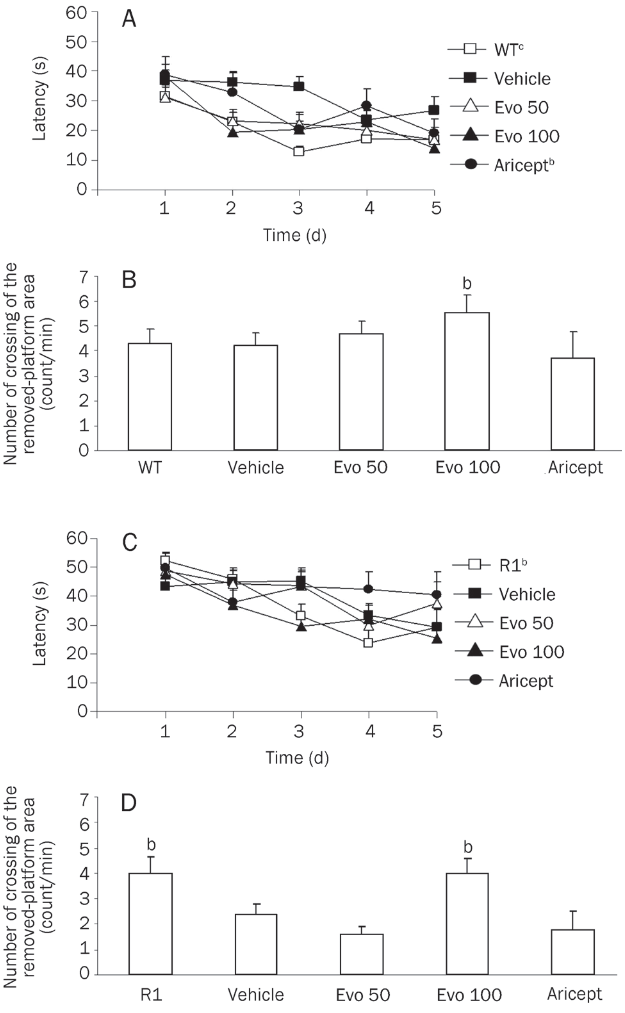

Figure 1. Determination of the effect of evodiamine on mouse models of AD by the Morris water-maze test. The non-transgenic littermates (WT) and SAMR1 mice (R1) were given a standard diet and used as normal controls for $APP^{swe}/PS1^{\Delta E9}$ and for SAMP8 mice, respectively. The $APP^{swe}/PS1^{\Delta E9}$ and SAMP8 groups were given standard diet and used as normal vehicle controls (Vehicle). The $APP^{swe}/PS1^{\Delta E9}$ and SAMP8 transgenic mice were treated with evodiamine at a dose of 50 mg·kg^{-1}·d^{-1} (Evo 50) or 100 mg·kg^{-1}·d^{-1} (Evo 100) for 4 weeks. $APP^{swe}/PS1^{\Delta E9}$ and SAMP8 transgenic mice were treated with Aricept at a dose of 2 mg·kg^{-1}·d^{-1} in the same manner as for treatment with evodiamine and used as positive controls (Aricept). Latency during 5 d of the Morris water-maze tests and platform crossings on the day after the 5-d training period were tabulated for $APP^{swe}/PS1^{\Delta E9}$ (A and B) and SAMP8 (C and D) transgenic mice. ($^bP<0.05$, $^cP<0.01$ *vs* vehicle group).

latency period in each group was approximately 40 s, and no significant differences were observed among the groups, over the five days of testing, during which performance of all five groups improved significantly in diminishing latency. On the third day of evodiamine treatment there was improvement in the behavior of the $APP^{swe}/PS1^{\Delta E9}$ transgenic mice, evinced by decrease of latency by 35% ($P<0.05$, $n=13$) in the Evo 50 group and by 41% ($P<0.05$, $n=17$) in the Evo 100 group comparing the data with those of the vehicle group (Figure 1A). The probe trial in the Morris water-maze test on the day after the 5-day training showed that the number of crossings of the area from which the platform had been removed increased by 33% ($P<0.05$, $n=17$) in the Evo 100 group compared with the vehicle group (Figure 1B), and no significant differences were observed between Evo 50 group and vehicle groups. Evodiamine treatment also resulted in improvement in the behavior of the SAMP8 mice, evinced by a decrease in the latency period of 43% ($P<0.05$, $n=12$) (Figure 1C) and by a significantly increased number of crossings of the original platform area equivalent to 42% ($P<0.05$, $n=12$) in the Evo 100 group (Figure 1D), compared with observations for the vehicle group. Treatment with evodiamine at a dose of 50 mg·kg^{-1}·d^{-1} showed no improvement in the behavior of the SAMP8 mice. Thus, the administration of the dose of 100 mg·kg^{-1}·d^{-1} was significantly effective in improvement of behavior in both the SAMP8 and $APP^{swe}/PS1^{\Delta E9}$ transgenic mouse models, which develop AD characteristics via different pathological mechanism[9, 12].

Evodiamine had no effect on Aβ deposition in the $APP^{swe}/PS1^{\Delta E9}$ transgenic mouse

Since the dose of 100 mg·kg^{-1}·d^{-1} was effective in both SAMP8 mice and $APP^{swe}/PS1^{\Delta E9}$ mice, we used this dose to investigate whether evodiamine treatment would inhibit Aβ deposition in the $APP^{swe}/PS1^{\Delta E9}$ transgenic mouse, which forms senile plaque in brain tissue after 6 months of age[9]. After 4 weeks of administration, hippocampus tissues were sampled from the WT, vehicle, Evo 100, and Aricept groups. Paraffin sections were prepared and stained with thioflavin-S medium. Observation using the fluorescence microscope showed that Aβ deposition clearly occurred in the $APP^{swe}/PS1^{\Delta E9}$ transgenic mice compared with those in the WT control group. Neither evodiamine nor Aricept treatment showed observable inhibition of Aβ deposition in $APP^{swe}/PS1^{\Delta E9}$ transgenic mice (Figure 2), suggesting that the effect of evodiamine on improvement of behavior in AD mouse models involves other mechanisms.

Evodiamine treatment increased glucose uptake in brain tissue in the $APP^{swe}/PS1^{\Delta E9}$ transgenic mouse

The AD patient exhibits large decreases in glucose uptake and energy metabolism in the frontal cortex and temporal lobes[1]. Brain glucose uptake was detected by PET scan in living mice of the WT, vehicle, Evo 100, and Aricept groups after 4 weeks of treatment (Figure 3A, 3B). The results showed that glucose uptake by $APP^{swe}/PS1^{\Delta E9}$ transgenic mice was significantly decreased by 16% ($P<0.05$, $n=3$), compared with that of WT controls. Treatment with evodiamine ameliorated the glucose uptake decrease caused by $APP^{swe}/PS1^{\Delta E9}$ expression by 16% ($P<0.05$, $n=4$). Aricept administration also improved glucose uptake in $APP^{swe}/PS1^{\Delta E9}$ transgenic mice by 23% ($P<0.05$, $n=3$).

Evodiamine treatment inhibited the expression of inflammatory cytokines in the $APP^{swe}/PS1^{\Delta E9}$ transgenic mouse

Inflammatory factors IL-1β, IL-6, and TNF-α were detected with the ELISA in lysates of brain tissues from WT, vehicle, Evo 100 and Aricept groups after 4 weeks of treatment (Figure 4). The results indicated that evodiamine decreased the levels of IL-1β by 23% ($P<0.05$), IL-6 by 27% ($P<0.05$), and TNF-α by 26% ($P<0.05$), compared with their levels in the vehicle group. Aricept administration also significantly decreased the levels of IL-1β and IL-6, but not that of TNF-α.

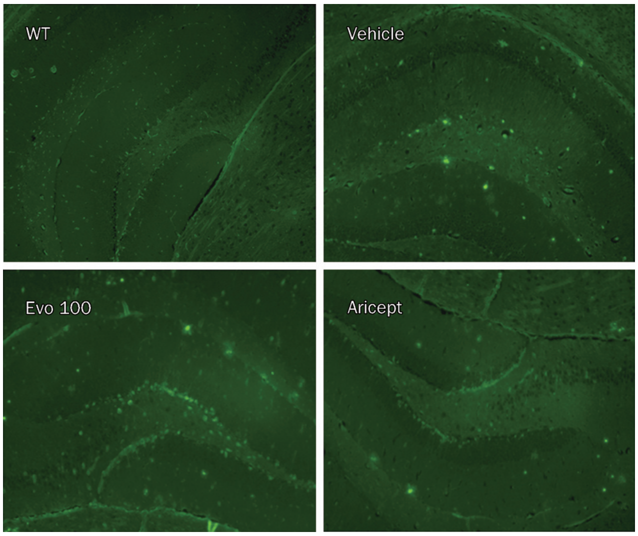

Figure 2. Evodiamine treatment has no effect on Aβ deposition in the brain of the APP^{swe}/PS1^{ΔE9} transgenic mouse. After 4 weeks of administration, brain tissues from WT and vehicle mice, and mice treated with evodiamine at a dose of 100 mg·kg^{-1}·d^{-1} (Evo 100) or with Aricept at a dose of 2 mg·kg^{-1}·d^{-1} (Aricept) were utilized in standard pathological procedures and sections were stained with Thioflavin-S to visualize the deposition of Aβ. (Magnification×100).

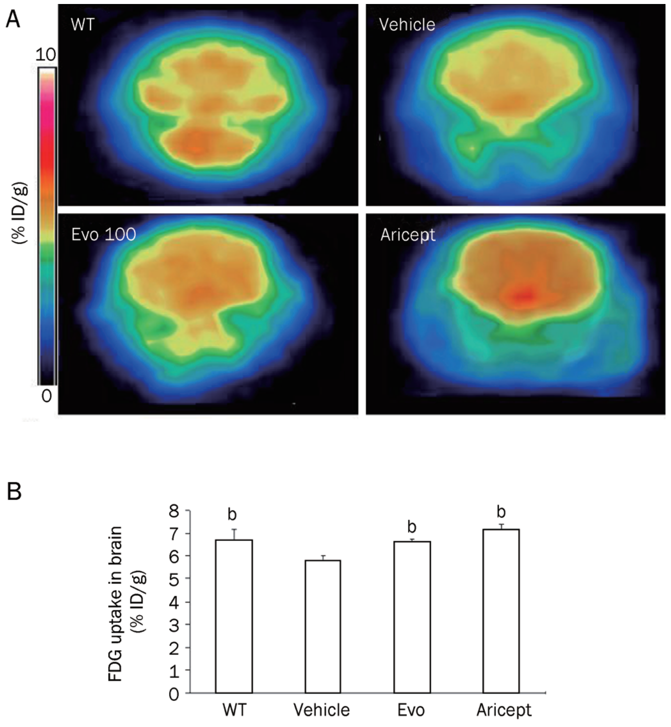

Figure 3. Evodiamine treatment increases glucose uptake in the brain of the APP^{swe}/PS1^{ΔE9} transgenic mouse. After 4 weeks administration, the WT and Vehicle mice, and those treated with evodiamine at a dose of 100 mg·kg^{-1}·d^{-1} (Evo 100) or Aricept at a dose of 2 mg·kg^{-1}·d^{-1} (Aricept) were subjected to the PET/CT scan to obtain typical images as shown in panel A. Glucose (as FDG) uptake per gram of brain tissue is depicted in panel B (n=3–4). ($^bP<0.05$ *vs* vehicle group).

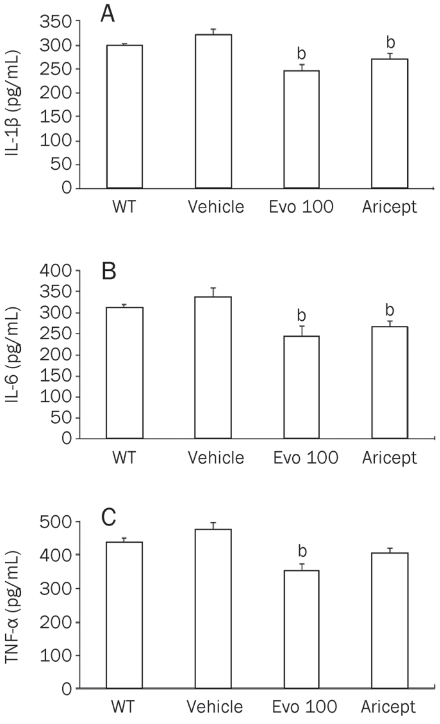

Figure 4. Evodiamine treatment inhibits the expression of inflammatory cytokines in the APP^{swe}/PS1^{ΔE9} transgenic mouse. After 4 weeks of administration, brain tissue from WT and Vehicle mice and those treated with evodiamine at a dose of 100 mg·kg^{-1}·d^{-1} (Evo 100) or Aricept at a dose of 2 mg·kg^{-1}·d^{-1} (Aricept) were sampled and total lysates were isolated. The levels of IL-1β (A, n=6), IL-6 (B, n=6), and TNF-α (C, n=6) were detected by ELISA kits. ($^bP<0.05$ *vs* vehicle group).

Evodiamine treatment decreased the expression of COX-2 in the APP^{swe}/PS1^{ΔE9} transgenic mouse

COX-2 is one of the important determinants in inflammatory response-mediated cytotoxicity. Accumulation of COX-2 protein was observed in the vehicle group, compared with WT mice, and the accumulation of COX-2 protein caused by expression of APP^{swe}/PS1^{ΔE9} transgenic genes was significantly reduced by evodiamine, by up to 73% ($P<0.01$, n=4) and reduced by Aricept by up to 67% ($P<0.01$, n=4) after 4 weeks of treatment (Figure 5A, 5B).

Discussion

In the present study we evaluated 12 herbal monomers in APP^{swe}/PS1^{ΔE9} transgenic mice by the Morris water-maze test (Table 1). Evodiamine alone, from among the 12 herbal

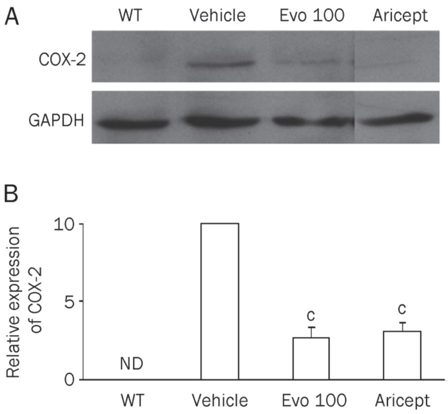

Figure 5. Western blot analysis for COX-2 protein. Brain tissues from WT and Vehicle mice and those treated with evodiamine at a dose of 100 mg·kg^{-1}·d^{-1} (Evo 100) or Aricept at a dose of 2 mg·kg^{-1}·d^{-1} (Aricept) were sampled and total lysates were isolated. COX-2 levels were detected by Western blot, using GAPDH for normalization (A). The density of bands (B, n=4) was quantified by densitometry using the Bio-Rad Quantity One software. (^cP<0.01 *vs* vehicle group). ND: not detected.

monomers, showed some effect on reversal of the AD phenotype through capacity to improve the cognitive abilities of the APP^{swe}/PS1$^{\Delta E9}$ transgenic mice.

We first showed that 4 weeks of administration of evodiamine to the APP^{swe}/PS1$^{\Delta E9}$ and SAMP8 transgenic mice improved spatial learning and memory of mice with symptoms of AD at 5 months of age (Figure 1). Our results indicate that evodiamine can improve spatial learning and memory in APP^{swe}/PS1$^{\Delta E9}$ and SAMP8 transgenic mice, but that the improvement is not due to reduction in the pathological development of senile plaque in brain tissues (Figure 2). The perturbations in energy metabolism in the AD patient evinced by large decreases in glucose uptake and energy metabolism in the frontal cortex and temporal lobes[27] are also present in the transgenic mouse model of AD (Figure 3). Evodiamine also significantly ameliorates the decrease in glucose uptake caused by APP^{swe}/PS1$^{\Delta E9}$ expression (Figure 3), suggesting on this basis that treatment with evodiamine could contribute to improvement of brain function in the AD model.

Evodiamine has been shown to have various effects on biological processes, such as testosterone[28] and catecholamine secretion[29], as well as vasodilative[30], anti-nociceptive[31], obesity[20], and thermoregulatory and uterotonic effects[32]. Evodiamine has anti-tumor potential through its ability to inhibit proliferation, induce apoptosis and reduce invasion and metastasis of a wide variety of tumor cells, including breast cancer, prostate cancer, leukemic T-lymphocyte, melanoma, cervical cancer, colon cancer and lung cancer cells[33]. Previous studies indicated that evodiamine represses COX-2 and inducible nitric oxide synthase (iNOS) expression and PGE2 release in RAW264.7 cells[34] and inhibits LPS-induced NO production and iNOS up-regulation in microglial cells[35], suggesting that evodiamine has anti-inflammatory activity. Our results demonstrated that evodiamine decreased the levels of IL-1β, IL-6, TNF-α and COX-2 protein, compared with levels in the vehicle group (Figures 4 and 5).

Examination of postmortem brains of AD patients reveals the abundant presence of inflammatory mediators, such as pro-inflammatory cytokines and chemokines, *eg*, IL-1, IL-6, TNF-α, MIP-1b, complement activation products, and oxygen radicals[5–7]. Inflammatory processes are present also in transgenic AD mouse models[5–7]. Our results indicated that evodiamine decreased the levels of IL-1β (Figure 4). IL-1 is reported to induce expression of AChE protein and mRNA and to increase AChE enzyme activity, and that such an effect exacebates cholinergic decline and dysfunction in AD[36]. Our results also indicated that evodiamine decreased the levels of IL-6 (Figure 4). IL-6 occurs normally at barely detectable levels in the adult CNS, and is strongly induced under pathological conditions[37, 38] . We found that evodiamine decreased the levels of TNF-α (Figure 4). TNF-α is a proinflammatory cytokine, the biological effects of which include stimulation of the acute-phase response, and cytotoxicity; furthermore, TNF-α stimulates IL-1 and IL-6 production, expression of adhesion molecules, and procoagulant activity[39]. In our studies evodiamine was shown to decrease the levels of COX-2 protein (Figure 5). COX-2 is an enzyme that plays a pivotal role in the arachidonate cascade leading to prostaglandin synthesis. Because the latter is so deeply intertwined with other inflammatory mechanisms, the inhibition of COX-2, with the attendant inhibition of prostaglandins, is a central target for anti-inflammatory therapy[40]. COX-2 mRNA and protein are considerably up-regulated in affected areas of the brain in AD. COX-2 helps mediate production of prostaglandins and other inflammatory factors, and it is itself up-regulated by pro-inflammatory mediators. For example, IL-1 and TNF-α are known to regulate COX-2 expression. Thus, this enzyme occupies a pivotal amplifying position for inflammatory reactions[41, 42]. Since evodiamine inhibits the expression of IL-1β, IL-6, TNF-α, and COX-2 protein, it may effect attenuation of CNS dysfunction in AD. However, the role of inflammation in the pathogenic process is still a matter of debate. One proposal is that the deposition of fibrillated Aβs in the human cortex could induce a local inflammatory reaction. Thus, neuro-inflammation is still considered to be a downstream consequence in the amyloid hypothesis, and inflammation has been considered as a secondary bystander response to neuronal degeneration and death[3]. Salminen *et al*[43] indicate that increased production of amyloid-β oligomers can activate the innate immunity system via pattern-recognition receptors and evoke the pathology of AD. In addition, the pathology of AD seems be the outcome of the activation of innate immunologic defenses in the brain. Therefore, inflammation is not merely a bystander in neurodegeneration but a powerful pathogenic force in the disease process.

The preponderance of our present findings suggests that evodiamine could alleviate impairment of learning abilities and memory and significantly improve the glucose uptake in the APP^{swe}/PS1$^{\Delta E9}$ transgenic mice, and that the therapeutic effect of evodiamine was likely mediated through the inhibition of the inflammatory process, but not of senile plaque reduction. Our results suggest that evodiamine could have potential usage in treatment of AD.

Acknowledgements

The present work was supported in part by the Ministry of Health Foundation (No̲ 200802036) and the National Science and Technology Major Projects (No̲ 2009ZX09501-026).

The authors appreciate that Dr JAMES improved the expression of English and the figures.

Author contribution

Lian-feng ZHANG designed research; Shu-min YUAN perfermed research; Kai GAO contributed PET/CT images analysis; Xiong-zhi QUAN helped with Western blot analysis; Jiang-ning LIU helped with modifying figures; Chuan QIN, Dong-mei WANG, Chun-mei MA contributed pathological analysis; and Lian-feng ZHANG and Shu-min YUAN wrote the paper.

References

1 Mattson MP. Pathways towards and away from Alzheimer's disease. Nature 2004; 430: 631−9.
2 Hardy J, Selkoe DJ. The amyloid hypothesis of Alzheimer's disease: progress and problems on the road to therapeutics. Science 2002; 297: 353−6.
3 Eikelenboom P, Veerhuis R, Scheper W, Rozemuller AJ, van Gool WA, Hoozemans JJ. The significance of neuroinflammation in understanding Alzheimer's disease. J Neural Transm 2006; 113: 1685-95.
4 Holmes C, Boche D, Wilkinson D, Yadegarfar G, Hopkins V, Bayer A, *et al*. Long-term effects of Abeta42 immunisation in Alzheimer's disease: follow-up of a randomised, placebo-controlled phase I trial. Lancet 2008; 372: 216–23.
5 McGeer EG, McGeer PL. Inflammatory processes in Alzheimer's disease. Prog Neuropsychopharmacol Biol Psychiatry 2003; 27: 741–9.
6 Heneka MT, O'Banion MK. Inflammatory processes in Alzheimer's disease. J Neuroimmunol 2007; 184: 69–91.
7 Rojo LE, Fernandez JA, Maccioni AA, Jimenez JM, Maccioni RB. Neuroinflammation: implications for the pathogenesis and molecular diagnosis of Alzheimer's disease. Arch Med Res 2008; 39: 1–16.
8 Hayden KM, Zandi PP, Khachaturian AS, Szekely CA, Fotuhi M, Norton MC, *et al*. Does NSAID use modify cognitive trajectories in the elderly? The Cache County study. Neurology 2007; 69: 275–82.
9 Wang X, Liu P, Zhu H, Xu Y, Ma C, Dai X, *et al*. miR-34a, a microRNA up-regulated in a double transgenic mouse model of Alzheimer's disease, inhibits bcl2 translation. Brain Res Bull 2009; 80: 268–73.
10 Butterfield DA, Poon HF. The senescence-accelerated prone mouse (SAMP8): a model of age-related cognitive decline with relevance to alterations of the gene expression and protein abnormalities in Alzheimer's disease. Exp Gerontol 2005; 40: 774–83.
11 Miyamoto M. Characteristics of age-related behavioral changes in senescence-accelerated mouse SAMP8 and SAMP10. Exp Gerontol 1997; 32: 139–48.
12 Flood JF, Morley JE. Learning and memory in the SAMP8 mouse. Neurosci Biobehav Rev 1998; 22: 1–20.
13 Kim HK, Kim M, Kim S, Kim M, Chung JH. Effects of green tea polyphenol on cognitive and acetylcholinesterase activities. Biosci Biotechnol Biochem 2004; 68: 1977–9.
14 Lu JH, Guo J, Yang WH. Effects of green tea polyphenol on the behaviour of Alzheimer' s disease like mice induced by *D*-galactose and Abeta$_{25\text{-}35}$. Zhong Yao Cai 2006; 29: 352–4.
15 Marambaud P, Zhao H, Davies P. Resveratrol promotes clearance of Alzheimer's disease amyloid-beta peptides. J Biol Chem 2005; 280: 37377–82.
16 Karuppagounder SS, Pinto JT, Xu H, Chen HL, Beal MF, Gibson GE. Dietary supplementation with resveratrol reduces plaque pathology in a transgenic model of Alzheimer's disease. Neurochem Int 2009; 54: 111–8.
17 Sehirli O, Tozan A, Omurtag GZ, Cetinel S, Contuk G, Gedik N, *et al*. Protective effect of resveratrol against naphthalene-induced oxidative stress in mice. Ecotoxicol Environ Saf 2008; 71: 301−8.
18 Lee SH, Son JK, Jeong BS, Jeong TC, Chang HW, Lee ES, *et al*. Progress in the studies on rutaecarpine. Molecules 2008; 13: 272–300.
19 Wang L, Hu CP, Deng PY, Shen SS, Zhu HQ, Ding JS, *et al*. The protective effects of rutaecarpine on gastric mucosa injury in rats. Planta Med 2005; 71: 416–9.
20 Kobayashi Y, Nakano Y, Kizaki M, Hoshikuma K, Yokoo Y, Kamiya T. Capsaicin-like anti-obese activities of evodiamine from fruits of Evodia rutaecarpa, a vanilloid receptor agonist. Planta Med 2001; 67: 628–33.
21 Cox MM, Tucker AM, Tang J, Talbot K, Richer DC, Yeh L, *et al*. Neurobehavioral abnormalities in the dysbindin-1 mutant, sandy, on a C57BL/6J genetic background. Genes Brain Behav 2009; 8: 390–7.
22 Imbimbo BP, Hutter-Paier B, Villetti G, Facchinetti F, Cenacchi V, Volta R, *et al*. CHF5074, a novel gamma-secretase modulator, attenuates brain beta-amyloid pathology and learning deficit in a mouse model of Alzheimer's disease. Br J Pharmacol 2009; 156: 982–93.
23 Shiryaev N, Jouroukhin Y, Giladi E, Polyzoidou E, Grigoriadis NC, Rosenmann H, *et al*. NAP protects memory, increases soluble tau and reduces tau hyperphosphorylation in a tauopathy model. Neurobiol Dis 2009; 34: 381–8.
24 Bussiere T, Bard F, Barbour R, Grajeda H, Guido T, Khan K, *et al*. Morphological characterization of thioflavin-S-positive amyloid plaques in transgenic Alzheimer mice and effect of passive Abeta immunotherapy on their clearance. Am J Pathol 2004; 165: 987–95.
25 Yu AS, Lin HD, Huang SC, Phelps ME, Wu HM. Quantification of cerebral glucose metabolic rate in mice using ^{18}F-FDG and small-animal PET. J Nucl Med 2009; 50: 966–73.
26 Chow PL, Rannou FR, Chatziioannou AF. Attenuation correction for small animal PET tomographs. Phys Med Biol 2005; 50: 1837–50.
27 Blass JP. Brain metabolism and brain disease: is metabolic deficiency the proximate cause of Alzheimer dementia? J Neurosci Res 2001; 66: 851–6.
28 Lin H, Tsai SC, Chen JJ, Chiao YC, Wang SW, Wang GJ, *et al*. Effects of evodiamine on the secretion of testosterone in rat testicular interstitial cells. Metabolism 1999; 48: 1532–5.
29 Yoshizumi M, Houchi H, Ishimura Y, Hirose M, Kitagawa T, Tsuchiya K, *et al*. Effect of evodiamine on catecholamine secretion from bovine adrenal medulla. J Med Invest 1997; 44: 79–82.
30 Chiou WF, Chou CJ, Shum AY, Chen CF. The vasorelaxant effect of evodiamine in rat isolated mesenteric arteries: mode of action. Eur J Pharmacol 1992; 215: 277–83.
31 Kobayashi Y. The nociceptive and anti-nociceptive effects of evodiamine from fruits of Evodia rutaecarpa in mice. Planta Med 2003; 69: 425–8.
32 King CL, Kong YC, Wong NS, Yeung HW, Fong HH, Sankawa U. Uterotonic effect of Evodia rutaecarpa alkaloids. J Nat Prod 1980; 43: 577–82.
33 Jiang J, Hu C. Evodiamine: a novel anti-cancer alkaloid from Evodia

rutaecarpa. Molecules 2009; 14: 1852–9.

34 Liu YN, Pan SL, Liao CH, Huang DY, Guh JH, Peng CY, *et al*. Evodiamine represses hypoxia-induced inflammatory proteins expression and hypoxia-inducible factor 1alpha accumulation in RAW264.7. Shock 2009; 32: 263–9.

35 Ko HC, Wang YH, Liou KT, Chen CM, Chen CH, Wang WY, *et al*. Anti-inflammatory effects and mechanisms of the ethanol extract of Evodia rutaecarpa and its bioactive components on neutrophils and microglial cells. Eur J Pharmacol 2007; 555: 211–7.

36 Li Y, Liu L, Kang J, Sheng JG, Barger SW, Mrak RE, *et al*. Neuronal-glial interactions mediated by interleukin-1 enhance neuronal acetylcholinesterase activity and mRNA expression. J Neurosci 2000; 20: 149–55.

37 Vallieres L, Rivest S. Regulation of the genes encoding interleukin-6, its receptor, and gp130 in the rat brain in response to the immune activator lipopolysaccharide and the proinflammatory cytokine interleukin-1beta. J Neurochem 1997; 69: 1668–83.

38 Gruol DL, Nelson TE. Physiological and pathological roles of interleukin-6 in the central nervous system. Mol Neurobiol 1997; 15: 307–39.

39 Baert FJ, D'Haens GR, Peeters M, Hiele MI, Schaible TF, Shealy D, *et al*. Tumor necrosis factor alpha antibody (infliximab) therapy profoundly down-regulates the inflammation in Crohn's ileocolitis. Gastroenterology 1999; 116: 22–8.

40 Akiyama H, Barger S, Barnum S, Bradt B, Bauer J, Cole GM, *et al*. Inflammation and Alzheimer's disease. Neurobiol Aging 2000; 21: 383–421.

41 O'Banion MK, Miller JC, Chang JW, Kaplan MD, Coleman PD. Interleukin-1 beta induces prostaglandin G/H synthase-2 (cyclooxygenase-2) in primary murine astrocyte cultures. J Neurochem 1996; 66: 2532–40.

42 Yamamoto K, Arakawa T, Ueda N, Yamamoto S. Transcriptional roles of nuclear factor kappa B and nuclear factor-interleukin-6 in the tumor necrosis factor alpha-dependent induction of cyclooxygenase-2 in MC3T3-E1 cells. J Biol Chem 1995; 270: 31315–20.

43 Salminen A, Ojala J, Kauppinen A, Kaarniranta K, Suuronen T. Inflammation in Alzheimer's disease: amyloid-beta oligomers trigger innate immunity defence via pattern recognition receptors. Prog Neurobiol 2009; 87: 181–94.

Acta Pharmacologica Sinica (2011) 32: 303–310
© 2011 CPS and SIMM All rights reserved 1671-4083/11 $32.00
www.nature.com/aps

Original Article

Combined prostaglandin E1 and lithium exert potent neuroprotection in a rat model of cerebral ischemia

Rui SHENG#, Li-sha ZHANG#, Rong HAN, Bo GAO, Xiao-qian LIU, Zheng-hong QIN*

Department of Pharmacology and Laboratory of Aging and Nervous Diseases, Soochow University School of Medicine, Suzhou 215123, China

Aim: To examine the effects of a mixed formulation composed of prostaglandin E1 and lithium (PGE1+Li mixture) on brain damage after cerebral ischemia. The effects of the mixture on protein expression of heat shock proteins (HSPs), p53, and Bcl-2 were also determined.
Methods: Brain ischemia was induced with a permanent middle cerebral artery occlusion (pMCAO) in rats. Rats were treated with a single intravenous administration of PGE1, lithium or a PGE1+Li mixture immediately after the ischemic insult. The infarct volume and motor behavior deficits were analyzed 24 h after the ischemic insult. The protein levels of HSP70, glucose-regulated protein 78 (GRP78), HSP60, Bcl-2, and p53 in the striatum of the ipsilateral hemisphere were examined using immunoblotting.
Results: The mixture (PGE1 22.6 nmol/kg+Li 0.5 mmol/kg) reduced infarct volume and neurological deficits induced by focal cerebral ischemia. Moreover, the mixture had a greater neuroprotective effect against cerebral ischemia compared with PGE1 or lithium alone. The mixture was effective even if it was administered 3 h after ischemia. PGE1+Li also significantly upregulated cytoprotective HSP70, GRP78, HSP60, and Bcl-2 protein levels, while decreasing p53 expression.
Conclusion: These results demonstrated a PGE1+Li mixture with a therapeutic window of up to 3 h for clinical treatment of cerebral ischemia. The PGE1+Li mixture potentially exerts a protective effect after stroke through the induction of HSPs and Bcl-2 proteins.

Keywords: prostaglandin E1; lithium; PGE1+Li mixture; heat shock proteins; cerebral ischemia; Bcl-2; p53

Acta Pharmacologica Sinica (2011) 32: 303–310; doi: 10.1038/aps.2010.211; published online 24 Jan 2011

Introduction

Development of neuroprotective agents against ischemia-induced brain damage is needed to reduce the mortality and morbidity associated with stroke[1]. Heat shock proteins (HSPs) are molecular chaperones that regulate folding of nascent and denatured proteins, act as transport proteins between subcellular compartments and modify the activities of proteins by altering their conformational states[2]. HSPs may exert neuroprotective effects by antagonizing apoptotic and necrotic cell death during cerebral ischemia[3]. Induction of HSPs also plays a role in the preconditioning-induced resistance of neurons to ischemic insults[4, 5]. HSPs such as HSP70, glucose-regulated protein 78 (GRP78) and HSP60 are important regulators of cellular survival and may be used as potential therapeutic targets for treating ischemic neuronal injury[6–8].

Prostaglandin E1 (PGE1) has several pharmacological effects, including cytoprotection, vasodilation, inhibition of platelet aggregation, membrane stabilization and anti-inflammation[9]. The clinical uses of PGE1 include the treatment of ischemic diseases such as cerebral, myocardial and hepatic ischemia. In recent studies, Matsuo reported that PGE1 induces HSP70, GRP78, and HSP86 immediately after hepatic ischemia reperfusion. Therefore, HSPs might play an important role in mediating the protective actions of PGE1 against ischemia/reperfusion injury in the liver[10].

Lithium has been extensively used in the treatment of bipolar mood disorders[11]. Growing evidence suggests that lithium is a neuroprotective drug that is effective against a variety of insults, including glutamate-induced excitotoxicity, ischemia-induced neuronal damage and other neurodegenerative conditions[12]. Recently, Ren *et al*[13] reported that treatment of rats with lithium decreased the infarct volume in a permanent focal cerebral ischemia model, and the neuroprotective effects of lithium were associated with the upregulation of cytoprotective HSP70 in the ischemic brain hemispheres.

In a previous study, research from our laboratory[14] found that lithium could potentiate the neuroprotective effects of PGE1 through synergistic induction of HSPs, but the differ-

---

# These authors contributed equally to this work.
* To whom correspondence should be addressed.
E-mail Zhqin5@hotmail.com
Received 2010-08-16 Accepted 2010-11-23

ent administration routes of PGE1 (intravenous injection, iv) and lithium (subcutaneous injection, sc) make the clinical administration of drug combination inconvenient. Therefore, in the present study, we formulated a PGE1+Li mixture for intravenous administration. We verified that the mixture had neuroprotective actions with a therapeutic window up to 3 h. The mixture also induced the expression of HSPs and Bcl-2 in animals with ischemic injuries.

Materials and methods

Preparation of the PGE1+Li mixture and experimental protocol

PGE1 (NanYang Pukang Pharmaceutical Co ltd, Henan, China) and lithium (Sigma, St Louis, MO, USA) were dissolved successively in sterile normal saline (pH 7.2–7.4) to prepare the PGE1+Li mixture. Male Sprague–Dawley rats weighing 280–300 g were purchased from the Center for Experimental Animals at Soochow University. The NIH guidelines for the Care and Use of Laboratory Animals were followed during all animal procedures. In this study, three batches of rats were used. The first batch of 70 rats was randomly divided into 7 groups: the sham-operated group, the permanent middle cerebral artery occlusion (pMCAO) group, the lithium group (Li 0.5 mmol/kg), the PGE1(S) group (PGE1 22.6 nmol/kg), the PGE1(L) group (PGE1 45.2 nmol/kg), the PGE1(S)+Li mixture group (PGE1 22.6 nmol/kg+Li 0.5 mmol/kg), and the PGE1(L)+Li mixture group (PGE1 45.2 nmol/kg+Li 0.5 mmol/kg). The regional cerebrocortical blood flow (rCBF) in the rats was monitored, and the infarct volume, brain water content and neurological deficits were also evaluated in the animals. A second batch of 50 rats was randomly divided into 5 groups: the sham-operated group, the pMCAO group, the lithium group, the PGE1(S) group, and the PGE1(S)+Li mixture group. These rats were used for the immunoblotting procedures. In these two experiments, PGE1, lithium, and the PGE1+Li mixture were injected intravenously immediately after the onset of pMCAO. The last batch of 40 rats was randomly divided into 4 groups: the pMCAO group, the PGE1(S)+Li mixture 1.5 h group, the PGE1(S)+Li mixture 3 h group, and the PGE1(S)+Li mixture 6 h group. These rats were used to evaluate the therapeutic window of the PGE1+Li mixture for the treatment of ischemia. The PGE1(S)+Li mixture was administered 1.5 h, 3 h, or 6 h after the onset of pMCAO. In all of the experiments, sham-operated and model animals received injections of normal saline using the same volume as the various treatments.

Rat pMCAO model

The rat pMCAO model was produced using the intraluminal suture technique described by Longa with minor modifications[15, 16]. The rats were anesthetized with 4% chloral hydrate (350 mg/kg). A 30 mm length of monofilament nylon suture (Φ0.22–Φ0.24 mm) with a rounded tip was inserted into the internal carotid artery through a small incision in the right common carotid artery and then advanced to the Circle of Willis. The suture remained in place until the rats were killed. Laser-Doppler flowmetry (LDF, ML191 Laser Doppler Blood FlowMeter) was used to monitor the blockade of cerebral blood flow. The rCBF was detected prior to onset of ischemia to acquire the preischemia blood flow level. After the pMCAO operation, the rCBF sharply dropped to approximately 5%–10% of the preischemia value. Then the rCBF was measured again 5, 10, 15, 30, 60, and 120 min after drug administration[14]. Body temperature was closely monitored with a rectal probe and maintained in the range of 37.0±0.5 °C with a heating pad (Institute of Biomedical Engineering, CAMS, BME-412A ANIMAL REGULATOR) during and after surgery until the animals recovered from the anesthesia. Sham-operated rats underwent the same procedures except for the pMCAO. About 20%–30% of the rats died 24 h after ischemia onset and were excluded from further analysis. Rats that showed tremors and seizures were also excluded from further analysis.

Evaluation of infarct volume, brain water content and neurological deficit

Twenty-four hours after ischemia, the neurological deficits in rats subjected to pMCAO were evaluated with a protocol that was previously described by an observer who was blinded to the treatment[15]. A total score of a possible 10 was determined as follows: (1) when the rats were suspended by the tail, the left forelimb was flexed and the flex was scored 1–4 according to severity; (2) when rats were placed on a smooth plane, the lateral push resistance toward the left side decreased, which was scored from 1–3; (3) the rats were pulled gently backward by the tail and the left forelimb showed decreased strength, which was scored from 1–3. After the animals were scored, they were euthanized. The brains were dissected out and sliced in a plastic module (3-mm thickness, Harvard Apparatus, MA, USA). Then 5 slices of coronal sections were stained with 4% 2, 3, 5-triphenyltetrazolium chloride (TTC) for 30 min and fixed with 4% paraformaldehyde. Image analyzing software called SigmaScan Pro5 was used to measure brain infarcts. Considering the fact that infarct volume expands due to edematous change, the infarct volume was calculated with the following formula: infarct volume=(red area of the contralateral side – red area of the ipsilateral side)/total area×100%[17].

Immunoblotting

Immunoblotting was carried out as previously described[18]. Brain tissues from the ischemic striatum of the right middle cerebral artery territory and the corresponding area of the sham-operated rats were homogenized. Then the proteins were extracted with a lysis buffer (10 mmol/L Tris-HCl, pH 7.4, 150 mmol/L NaCl, 1% Triton-100, 0.1% SDS, 5 mmol/L ethylenediaminetetraacetic acid [EDTA], 1 mmol/L phenylmethylsulfonyl fluoride [PMSF], 0.28 U/mL aprotinin, 50 μg/mL leupeptin, 1 mmol/L benzamidine, 7 μg/mL pepstatin A). The protein concentrations were determined (SmartSpec3000 Spectrophotometer, Bio-Rad, Hercules, CA, USA) using a BCA kit (Pierce, Rockford, IL, USA). A 50 μg aliquot of protein from each sample was separated with a 10% SDS-PAGE gel and subsequently transferred to a nitrocellulose membrane.

Afterward, the membranes were incubated with antibodies against HSP70 (1:200; Mouse derived anti-HSP70 monoclonal antibody; Santa Cruz Biotechnology, Santa Cruz, CA, USA), GRP78 (1:400; Rabbit derived anti-GRP78 polyclonal antibody; Stressgen Bioreagents, Canada), HSP60 (1:100; Mouse derived anti-HSP60 monoclonal antibody; Sigma, St Louis, MO, USA), p53 (1:1000; Mouse derived anti-p53 monoclonal antibody; Cell Signaling, Woburn, MA, USA), or Bcl-2 (1:200; Rabbit derived anti-Bcl-2 polyclonal antibody; Santa Cruz Biotechnology, Santa Cruz, CA, USA) at 4 °C for 3 h. Next, the membranes were incubated with a horseradish peroxidase-conjugated secondary antibody (1:5000; Sigma, St Louis, MO, USA) at room temperature for 1 h. Immunoreactivity was detected with enhanced chemiluminescent autoradiography (ECL kit; Amersham, Piscataway, NJ, USA) according to the manufacturer's instructions. The membranes were reprobed with β-actin (1:5000; Sigma) after the membrane was stripped with Tris-buffered saline containing 0.1% Tween-20 (TBST) and 2% β-mercaptoethanol at 65 °C for 1 h.

Statistical analysis

Statistical analysis was carried out with one-way ANOVA. The intergroup comparisons (*post-hoc* analysis) among data with equal variances were carried out with the least significant difference (LSD) method, whereas Tamhane's T2 method was used for data with unequal variances. $P<0.05$ was considered significant.

Results

PGE1+Li mixture had no significant improvement on rCBF

After the pMCAO operation, the rCBF decreased to approximately 5%–10% of the preischemic values and remained low in all of the rats that were subjected to pMCAO. PGE1, lithium and the PGE1+Li mixture produced no statistically significant improvements in the reduction of rCBF within 5 min, 10 min, 15 min, 30 min, 60 min, and 120 min after the surgical operation (Table 1).

PGE1+Li mixture reduced pMCAO-induced brain damage

In the rats subjected to pMCAO for 24 h, extensive infarction was detected in the cerebral cortical and subcortical areas over a series of brain sections. Treatment with a single intravenous injection of lithium (0.5 mmol/kg), PGE1 (S), PGE1(L), the PGE1(S)+Li mixture or the PGE1(L)+Li mixture immediately after the onset of pMCAO resulted in a significant reduction in infarct volume that was detected by TTC staining ($P<0.05$ or $P<0.01$ *vs* model group). Moreover, administration of the PGE1(S)+Li mixture (PGE1 22.6 nmol/kg+Li 0.5 mmol/kg) produced a greater reduction in infarct volume ($P<0.01$ *vs* PGE1(S) group) (Figure 1A and 1B).

Rats subjected to pMCAO were examined and scored for motor deficits using a 10-point scale as described in the Methods. The pMCAO rats displayed marked motor behavioral deficits. Treatment with lithium, PGE1(S), PGE1(L), the PGE1(S)+Li mixture or the PGE1(L)+Li mixture resulted in a significant reduction in behavioral deficits ($P<0.05$ or $P<0.01$ *vs* model group). In addition, administration of the PGE1(S)+Li mixture produced a greater improvement in motor deficits ($P<0.05$ *vs* PGE1(S) group) (Figure 1C).

The therapeutic window of the PGE1+Li mixture's neuroprotecion on pMCAO

We sought to determine the time interval after ischemia in which the PGE1+Li mixture would be able to protect the brain (therapeutic window). The PGE1(S)+Li mixture was administered 1.5, 3, or 6 h after the onset of pMCAO. Significant infarct volume reductions were observed when the PGE1+Li mixture was administered 1.5 h (-36.6%) or 3 h (-31.3%) after ischemia ($P<0.01$ *vs* model group), but not when the administration of the mixture was delayed by 6 h ($P>0.05$; Figure 2).

Enhanced induction of HSP70, HSP60, and GRP78 by the PGE1+Li mixture

The expression of HSP70, GRP78 and HSP60 was significantly upregulated in the ischemic striatum after pMCAO ($P<0.05$ *vs* sham group). Although PGE1(S) (22.6 nmol/kg) or lithium (0.5 mmol/kg) alone had no significant effects on the these proteins, the PGE1(S)+Li mixture (PGE1 22.6 nmol/kg+Li 0.5 mmol/kg) significantly increased HSP70, GRP78, and HSP60 protein levels compared with both the model group and the PGE1(S) group ($P<0.05$ or $P<0.01$ *vs* model group and PGE1(S) group, Figure 3–4).

Table 1. The effects of the PGE1+Li mixture on rCBF (% of preischemia value) in rats subjected to pMCAO. The rCBF was measured in the ipsilateral ischemic hemisphere with LDF before the onset of ischemia, immediately after ischemia and 5, 10, 15, 30, 60, and 120 min after drug administration. Postischemic rCBF values are expressed as a percentage of the preischemic values (100%). PGE1(S)=PGE1 22.6 nmol/kg, PGE1(L)=PGE1 45.2 nmol/kg. *n*=6 rats. The data are expressed as means±SD. $^c P<0.01$ compared with preischemia.

	Time after drug administration						
	0 min	5 min	10 min	15 min	30 min	1 h	2 h
Model	9.6±6.5^c	9.5±5.9	9.4±6.4	10.0±5.3	10.1±5.2	10.5±7.1	9.8±6.4
PGE1(S)	8.1±6.0^c	14.2±8.3	14.8±7.6	14.6±8.5	13.3±6.9	9.6±7.7	9.4±6.7
PGE1(L)	10.2±6.2^c	14.0±8.6	15.2±6.5	12.8±6.4	12.3±8.5	12.0±6.6	11.0±7.4
Lithium	10.9±5.8^c	11.3±8.1	12.0±8.4	11.1±8.6	11.2±9.5	11.1±5.8	11.2±6.4
PGE1(S)+Li	7.2±5.2^c	10.4±4.6	10.6±4.9	9.9±5.6	9.1±5.5	9.3±3.1	8.2±5.0
PGE1(L)+Li	10.1±8.6^c	12.4±9.7	15.5±6.2	11.5±7.1	10.2±7.4	10.6±7.9	10.6±7.6

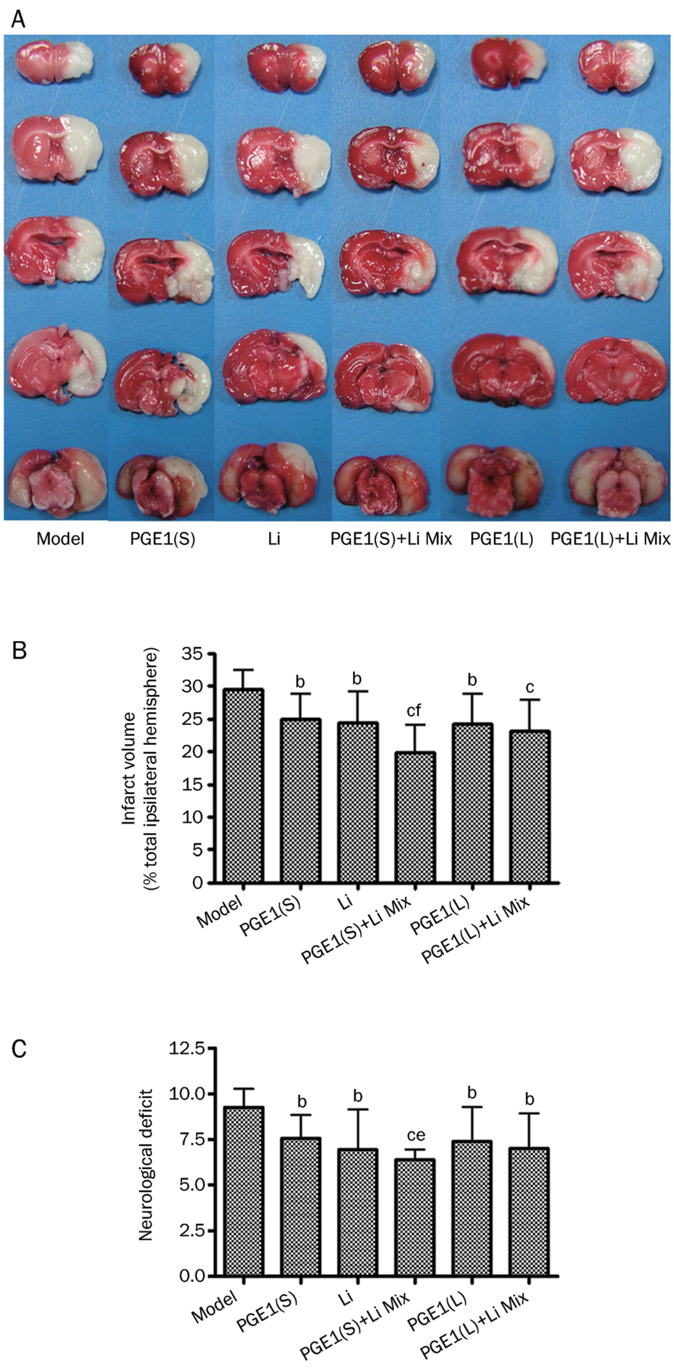

Figure 1. The PGE1+Li mixture reduced pMCAO-induced cerebral ischemia. Rats were injected intravenously with PGE1, Li and a PGE1+Li mixture immediately after pMCAO. The rats were euthanized 24 h after ischemia. (A) TTC staining of brain sections. The infarct brain regions are white. The results indicated that animals treated with PGE1, lithium or the PGE1(S)+Li mixture had smaller infarct volumes. (B) Quantitative analysis of brain infarct volume. (C) PGE1 and lithium treatment reduced pMCAO-induced neurological deficits. PGE1(S)=PGE1 22.6 nmol/kg, PGE1(L)=PGE1 45.2 nmol/kg. *n*=6 rats. The bar represents the mean±SD. ^{b}*P*<0.05, ^{c}*P*<0.01 compared with the model group; ^{e}*P*<0.05, ^{f}*P*<0.01 compared with the PGE1(S) group.

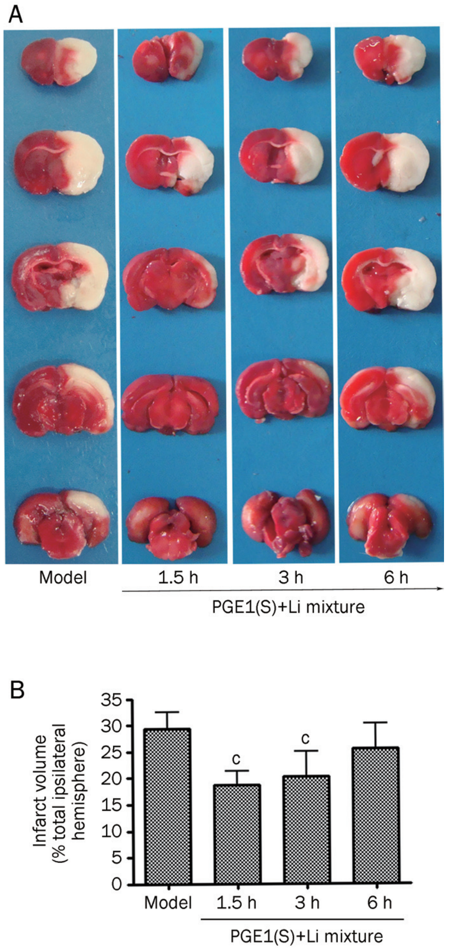

Figure 2. The therapeutic window of the neuroprotective effect of the PGE1+Li mixture in the pMCAO model. Rats were injected intravenously with the PGE1(S)+Li mixture (PGE1 22.6 nmol/kg+Li 0.5mmol/kg) 1.5, 3, or 6 h after the pMCAO. (A) TTC staining of brain sections. The infarct brain regions are white. (B) Quantitative analysis of brain infarct volume. PGE1(S)=PGE1 22.6 nmol/kg. *n*=6 rats. The bar represents the mean±SD. ^{c}*P*<0.01 compared with the model group.

PGE1+Li mixture increased Bcl-2, but decreased p53 protein levels

Expression of Bcl-2 was significantly downregulated in the ischemic striatum after pMCAO. Lithium significantly upregulated Bcl-2 protein levels compared with the model group (*P*<0.01 *vs* model group). Furthermore, the PGE1(S)+Li mixture (PGE1 22.6 nmol/kg+Li 0.5 mmol/kg) further increased Bcl-2 protein levels (*P*<0.01 *vs* model group and PGE1(S) group, Figure 5A).

Expression of p53 was significantly upregulated in the ischemic striatum after pMCAO. However, PGE1(S) (22.6 nmol/kg) or lithium (0.5 mmol/kg) significantly decreased p53 protein levels compared with the model group (*P*<0.05 or *P*<0.01 *vs* model group). In addition, the PGE1(S)+Li mixture (PGE1 22.6 nmol/kg+Li 0.5 mmol/kg) further decreased p53

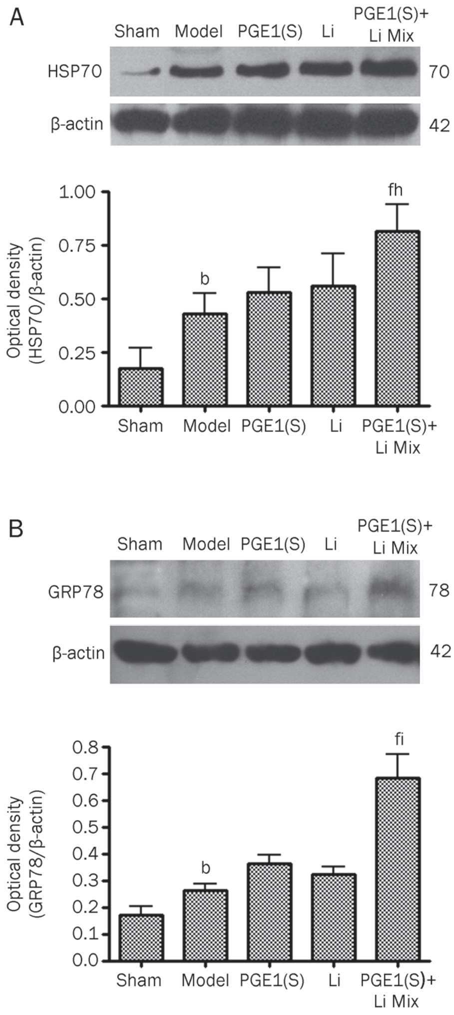

Figure 3. The PGE1+Li mixture enhanced pMCAO-induced HSP70 and GRP78 expression. The rats were injected intravenously with PGE1(S) 22.6 nmol/kg, Li 0.5 mmol/kg or a PGE1(S)+Li mixture (PGE1 22.6 nmol/kg+Li 0.5 mmol/kg) immediately after pMCAO. The rats were euthanized 24 h after ischemia. Protein levels of HSP70 and GRP78 in extracts from the striatum of the ipsilateral hemisphere were detected with immunoblotting. Levels of β-actin protein were used as the loading control. (A) The PGE1+Li mixture enhanced HSP70 protein expression. (B) The PGE1(S)+Li mixture enhanced GRP78 protein expression. The bar represents the mean±SD, *n*=6 rats. $^{b}P<0.05$ compared with the sham-operated group; $^{f}P<0.01$ compared with the model group; $^{h}P<0.05$, $^{i}P<0.01$ compared with the PGE1(S) group.

protein levels ($P<0.01$ *vs* model group and PGE1(S) group, Figure 5B).

Discussion

In a previous study, we found that coadministration of PGE1 (22.6 and 45.2 nmol/kg, iv) and lithium (0.5 mmol/kg, sc) can induce substantial synergistic neuroprotection on focal cerebral ischemia compared with PGE1 or lithium alone. Thus, we formulated a PGE1+Li mixture (PGE1 22.6 nmol/kg+Li 0.5 mmol/kg or PGE1 45.2 nmol/kg+Li 0.5 mmol/kg) for intravenous administration. The results showed that the pMCAO rats had significant motor behavioral deficits and extensive infarction in the ipsilateral cerebral cortical and subcortical areas throughout a series of brain sections. In the groups treated with PGE1 or lithium alone, a reduction in infarct volume and improvement of neurological deficits was observed, but a greater reduction in infarct volume and neurological deficits was seen in rats that were given a PGE1(S)+Li mixture (PGE1 22.6 nmol/kg+Li 0.5 mmol/kg). These results suggest that the PGE1+Li mixture might mimic the synergistic combination therapy of PGE1 and lithium reported in the previous study[14]. The suitable molar ratio of PGE1 to lithium for the PGE1+Li mixture was about 4.5×10^{-5}:1. Moreover, the PGE1+Li mixture was effective even if it was administered 3 h after ischemia. Therefore, the PGE1+Li mixture might be an effective drug combination for the treatment of cerebral ischemia in clinical situations.

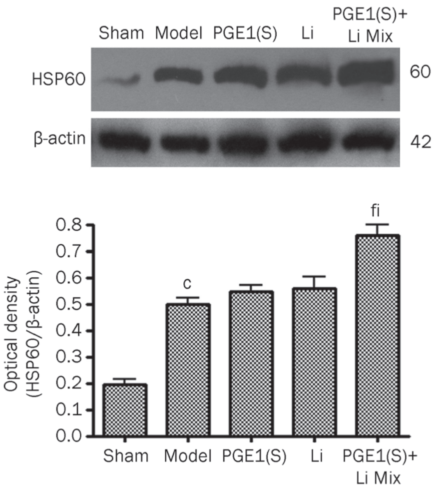

Figure 4. The PGE1+Li mixture enhanced pMCAO-induced HSP60 expression. The rats were injected intravenously with PGE1 22.6 nmol/kg, Li 0.5 mmol/kg or a PGE1(S)+Li mixture (PGE1 22.6 nmol/kg+Li 0.5 mmol/kg) immediately after pMCAO. The rats were euthanized 24 h after ischemia. Protein levels of HSP60 in extracts from the striatum of the ipsilateral hemisphere were detected with immunoblotting. Levels of β-actin protein were used as the loading control. Bar represents mean±SD, *n*=6 rats. $^{c}P<0.01$ compared with the sham-operated group; $^{f}P<0.01$ compared with the model group; $^{i}P<0.01$ compared with the PGE1(S) group.

Previous work showed that neither PGE1 alone nor a combination of PGE1 with lithium influences the cerebrocortical blood flow of the pMCAO animals[14]. The results in this study were similar. When we monitored cerebrocortical blood flow after drug treatment, PGE1, lithium and the mixture of both compounds showed no significant improvements in the reduction of rCBF until 2 h after ischemia. Thus, the neuroprotection exerted by the PGE1+Li mixture in the rat brain ischemia model in this study could not be the result of increased cerebrocortical blood flow.

HSPs are molecular chaperones that bind to unfolded or

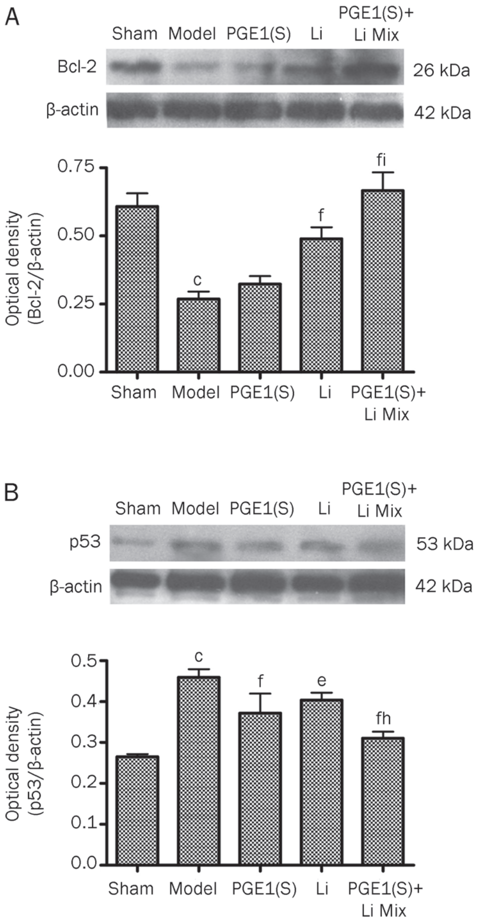

Figure 5. The PGE1+Li mixture increased Bcl-2 protein expression, but decreased p53 protein expression. The rats were injected intravenously with PGE1(S) 22.6 nmol/kg, Li 0.5 mmol/kg or the PGE1(S)+Li mixture (PGE1 22.6 nmol/kg+Li 0.5 mmol/kg) immediately after pMCAO. The rats were euthanized 24 h after ischemia. Protein levels of Bcl-2 and p53 in extracts from the striatum of the ipsilateral hemisphere were detected with immunoblotting. Levels of β-actin protein were used as the loading control. (A) The PGE1(S)+Li mixture increased Bcl-2 expression. (B) The PGE1(S)+Li mixture decreased p53 expression. The bar represents the mean±SD. *n*=6 rats. $^{c}P<0.01$ compared with the sham-operated group; $^{e}P<0.05$, $^{f}P<0.01$ compared with the model group; $^{h}P<0.05$, $^{i}P<0.01$ compared with the PGE1(S) group.

misfolded proteins to ensure proper folding and prevent intracellular protein aggregation[2]. A number of studies have documented that HSP levels increase in the ischemic penumbra of the brain in animal models of focal ischemia, which is an area where many injured neurons survive[19]. It has been reported that gene transfer induced HSP70 overexpression protects neurons from ischemic brain damage in experimental rat stroke models[20]. Additionally, the overexpression of HSP70 inhibits the activation of NF-κB, which is persistently activated during ischemia and appears to promote apoptotic cell death[21]. In contrast, the deletion of the HSP70 gene increases cytochrome *c* release into the cytoplasm and subsequent caspase-3 activation, thereby exacerbating apoptosis and increasing infarction volume after focal cerebral ischemia[22]. GRP78/Bip is one of the molecular chaperones localized to the ER membrane, which is also a highly conserved member of the 70-kDa heat shock protein family[8]. The main function of this protein is to restore folding of misfolded or incompletely assembled proteins. Previous reports showed that induction of GRP78 prevented the neuronal death induced by ER stress[23], and BIX, a selective inducer of GRP78, could be used to prevent neuronal damage both *in vitro* and *in vivo*[24]. HSP60 is a mitochondrial matrix protein induced by stress that forms a chaperonin complex within the mitochondria, which is important for mitochondrial protein folding and function[9]. In prior studies, it was shown that induction of HSP60 protects neurons from ischemic damage[25]. In our ischemic model, HSP70, HSP60, and GRP78 protein levels significantly increased in the ischemic striatum after pMCAO. Although no significant increases in these HSPs were found when the animals were treated with PGE1 22.6 nmol/kg or lithium 0.5 mmol/kg alone, the PGE1(S)+Li mixture robustly enhanced the increase in HSP70, GRP78, and HSP60 protein levels in the ischemic striatum. Therefore, induction of HSPs by the PGE1+Li mixture may play an important role in protecting neurons against ischemia-induced injury.

Overexpression of HSPs protects neurons against apoptotic and necrotic cell death during cerebral ischemia[4, 26]. Thus, the combined treatment enhanced the changes in the expression levels of pro-apoptotic and antiapoptotic proteins. Recently, Bian reported that the neuroprotective effects of lithium were associated with a dramatic suppression in p53 expression as well as the upregulation of Bcl-2[27]. Bcl-2 expression has been proposed as an important marker of the survival probability of neurons[28]. Bcl-2 has multiple neuroprotective actions including its ability to decrease Bax-induced cytochrome *c* release from mitochondria and inhibit subsequent caspase activation[29]. Lithium-induced upregulation of Bcl-2 was reported in cultured neurons and rat brains following protracted or short-term treatment[30]. The tumor suppressor protein p53, a transcriptional modulator of the Bcl-2 genes, can produce cell cycle arrest and facilitate apoptosis[28]. The putative role of p53 in cerebral ischemia was based on observations that p53 is upregulated in the brain of rats subjected to focal ischemia[31]. Pifithrin-α, a p53 inhibitor, decreased the expression of p53-targeted genes as well as the number of apoptotic cells in ischemic brains[32]. In the present study, the expression of p53 was significantly upregulated in the ischemic striatum accompanied by downregulation of Bcl-2. However, the PGE1+Li mixture significantly decreased p53 protein levels and increased Bcl-2 levels compared with the model group and the PGE1 group. These results suggest that the PGE1+Li mixture might protect neurons from cerebral ischemia by upregulating anti-apoptotic proteins and downregulating pro-apoptotic proteins.

Although treatment with PGE1 or lithium alone reduced infarct volume, we did not find a significant increase in HSPs levels when the animals were treated with 22.6 or 45.2 nmol/kg PGE1 or 0.5 mmol/kg lithium alone. The lack of effect on HSPs might be due to, in part, the low doses of lithium and PGE1 used in this study. Also, the effects on HSPs may have been too small to be detected with current methods. The alternative interpretation is that neuroprotection of PGE1 and lithium at these doses was not related to the induction of HSPs. It is possible that other molecular and cellular actions may participate in PGE1 and lithium-induced neuroprotection in the pMCAO model. These actions include the effects of PGE1 on cytoprotection, inhibiting platelet aggregation, membrane stabilization and anti-inflammation[10, 33], as well as the ability of lithium to inhibit *N*-methyl-*D*-aspartate receptors [34], inhibit glycogen synthase kinase-3 (GSK-3)[35], and induce expression of brain-derived neurotrophic factor in discrete brain areas[36]. The roles of other molecules in the neuroprotective effect caused by the PGE1+Li mixture in the ischemic model have yet to be defined. Nevertheless, the PGE1+Li mixture significantly enhanced the expression of HSP70, HSP60, and GRP78 in the ischemic striatum. These results suggest that induction of HSPs might take part in the molecular mechanisms of the neuroprotective effect of the PGE1+Li mixture against cerebral ischemia. However, it should be noted that these results can only provide indirect proof that the PGE1+Li mixture may exert protective effects on stroke through the induction of HSP proteins. Further study using HSP70 or GRP78 RNA silencing technology is needed to verify that the neuroprotective effect of the PGE1+Li mixture is actually mediated by HSPs.

In previous research from our laboratory[14, 37], lithium potentiated the neuroprotective effects of PGA1 and PGE1 through the upregulation of HSPs. However, PGA1 could only be delivered through intracerebral ventricle administration[37], which is not a viable delivery route in clinics. Yet, the different administration routes of PGE1 (intravenous injection) and lithium (subcutaneous injection) made that drug combination inconvenient. In the present study, we prepared a combination of PGE1 and lithium that could be administered intravenously. This mixture produced synergistic neuroprotection against cerebral ischemia that was similar to the findings in our previous study. We believe that this PGE1+Li mixture has more practical application value, which might support a potential clinical therapy for ischemic cerebrovascular diseases.

In conclusion, we provided pharmacological evidence indicating that an intravenous PGE1+Li mixture was neuroprotective against cerebral ischemia. Reduction in injury volume was obtained even if the drug was administered 3 h after the induction of ischemia. The neuroprotective effect of the PGE1+Li mixture was associated with up-regulation of cytoprotective Bcl-2 and HSPs as well as down-regulation of the pro-apoptotic p53 protein in the ischemic brains. Our studies may provide a novel intravenous preparation for the clinical treatment of cerebrovascular diseases.

Acknowledgements

This work was supported by grants from the National Natural Science Foundation of China (N<u>o</u> 30801391 and 30930035), the Natural Science Foundation of Jiangsu Province (N<u>o</u> BK2007548), and the Social Progress and Medicine Foundation of Suzhou (N<u>o</u> SS0729).

Author contribution

Zheng-hong QIN designed research and wrote the paper; Rui SHENG and Li-sa ZHANG performed research; Rui SHENG wrote the paper; Rong HAN corrected data; Bo GAO and Xiao-qian LIU analyzed data.

References

1 Onteniente B, Rasika S, Benchoua A, Guegan C. Molecular pathways in cerebral ischemia: cues to novel therapeutic strategies. Mol Neurobiol 2003; 27: 33–72.

2 Ohtsuka K, Suzuki T. Roles of molecular chaperones in the nervous system. Brain Res Bull 2000; 53: 141–6.

3 Yenari MA, Liu J, Zheng Z, Vexler ZS, Lee JE, Giffard RG. Antiapoptotic and anti-inflammatory mechanisms of heat-shock protein protection. Ann N Y Acad Sci 2005; 1053: 74–83.

4 Liu XQ, Sheng R, Qin ZH. The neuroprotective mechanism of brain ischemic preconditioning. Acta Pharmacol Sin 2009; 30: 1071–80.

5 Sheng R, Zhang LS, Han R, Liu XQ, Gao B, Qin ZH. Autophagy activation is associated with neuroprotection in a rat model of focal cerebral ischemic preconditioning. Autophagy 2010; 6: 482-94.

6 Tsuchiya D, Hong S, Matsumori Y, Shiina H, Kayama T, Swanson RA, *et al*. Overerexpression of rat heat shock protein 70 is associated with reduction of early mitochondrial cytochrome *c* release and subsequent DNA fragmentation after permanent focal ischemia. J Cereb Blood Metab 2003; 23: 718–27.

7 Lee AS. The glucose-regulated proteins: stress induction and clinical applications. Trends Biochem Sci 2001; 26: 504–10.

8 Voos W, Rottgers K. Molecular chaperones as essential mediators of mitochondrial biogenesis. Biochim Biophys Acta 2002; 1592: 51–62.

9 Schror K, Hohlfeld T. Mechanisms of anti-ischemic action of prostaglandin E1 in peripheral arterial occlusive disease. Vasa 2004; 33: 119–24.

10 Matsuo K, Togo S, Sekido H, Morita T, Kamiyama M, Morioka D, *et al*. Pharmacologic preconditioning effects: prostaglandin E1 induces heat-shock proteins immediately after ischemia/reperfusion of the mouse liver. J Gastrointest Surg 2005; 9: 758–68.

11 Bauer M, Alda M, Priller J, Young LT. International group for the study of lithium treated patients (IGSLI). Implications of the neuroprotective effects of lithium for the treatment of bipolar and neurodegerative disorders. Pharmacopsychiatry 2003; 36: S250–4.

12 Chuang DM, Chen RW, Chalecka-Franaszek E, Ren M, Hashimoto R, Senatorov V, *et al*. Neuroprotective effects of lithium in cultured cells and animal models of diseases. Bipolar Disord 2002; 4: 129–36.

13 Ren M, Senatotov VV, Chen RW, Chuang DM. Postinsult treatment with lithium reduces brain damage and facilitates neurological recovery in a rat ischemia/reperfusion model. Proc Natl Acad Sci USA 2003; 100: 6210–5.

14 Han R, Gao B, Sheng R, Zhang LS, Zhang HL, Gu ZL, *et al*. Synergistic effects of prostaglandin E1 and lithium in a rat model of cerebral ischemia. Acta Pharmacol Sin 2008; 29: 1141–9.

15 Longa EZ, Weinstein PR, Carlson S, Cummins R. Reversible middle cerebral artery occlusion without craniectomy in rats. Stroke 1989; 20: 84–91.

16 Li F, Omae T, Fisher M. Spontaneous hyperthermia and its mechanism in the intraluminal suture middle cerebral artery occlusion model of rats. Stroke 1999; 30: 2464–71.

17 Tamura A, Graham DI, McCulloch J, Teasdale GM. Focal cerebral ischemia in the rat: 1. Description of technique and early neuropathological consequences following middle cerebral artery occlusion. J Cereb Blood Flow Metab 1981; 1: 53–60.

18 Qin ZH, Chen RW, Wang Y, Nakai M, Chuang DM, Chase TN. Nuclear factor kappar B nuclear translocation upregulates c-Myc and p53 expression during NMDA receptor-mediated apoptosis in rat stratium. J Neurosci 1999; 19: 4023–33.

19 Wagstaff MJD, Collaco-Moraes Y, Aspey BS, Coffin RS, Harrison MJG, Latchman DS, *et al*. Focal cerebral ischaemia increases the levels of several classes of heat shock proteins and their corresponding mRNAs. Mole Brain Res 1996; 42: 236–44.

20 Li CY, Lee JS, Ko YG, Kim JI, Seo JS. Heat shock protein 70 inhibits apoptosis downstream of cytochrome *c* release and up stream of caspase-3 activation. J Biol Chem 2000; 275: 25665–71.

21 Feinstein DL, Galea E, Aquino DA, Li GC, Xu H, Reis DJ. Heat shock protein 70 suppresses astroglial-inducible nitric-oxide synthase expression by decreasing NFkappaB activation. J Biol Chem 1996; 271: 17724–32.

22 Lee SH, Kwon HM, Kim YJ, Lee KM, Kim M, Yoon BW. Effects of hsp70.1 gene knockout on the mitochondrial apoptotic pathway after focal cerebral ischemia. Stroke 2004; 35: 2195–9.

23 Reddy RK, Mao C, Baumeister P, Austin RC, Kaufman RJ, Lee AS. Endoplasmic reticulum chaperone protein GRP78 protects cells from apoptosis induced by topoisomerase inhibitors: role of ATP binding site in suppression of caspase-7 activation. J Biol Chem 2003; 278: 20915–24.

24 Oidaa Y, Izutaa H, Oyagia A, Shimazawaa M, Kudob T, Imaizumic K, *et al*. Induction of BiP, an ER-resident protein, prevents the neuronal death induced by transient forebrain ischemia in gerbil. Brain Res 2008; 1208: 217–24.

25 Hwang IK , Ahn HC, Yoo KY, Lee JY, Suh HW, Kwon YG, *et al*. Changes in immunoreactivity of HSP60 and its neuroprotective effects in the gerbil hippocampal CA1 region induced by transient ischemia. Exp Neurol 2007; 208: 247–56.

26 Rajdev S, Hara K, Kokubo Y, Mestril R, Dillmann W, Weinstein PR, *et al*. Mice overexpressing rat heat shock protein 70 are protected against cerebral infarction. Ann Neurol 2000; 47: 782–91.

27 Bian Q, Shi T, Chuang DM, Qian Y. Lithium reduces ischemia-induced hippocampal CA1 damage and behavioral deficits in gerbils. Brain Res 2007; 1184: 270–6.

28 Li PF, Dietz R, von Harsdorf R. p53 regulates mitochondrial membrane potential through reactive oxygen species and induces cytochrome *c*-independent apoptosis blocked by bcl-2. EMBO J 1999; 21: 6027–36.

29 Wada A, Yokoo H, Yanagita T, Kobayashi H. Lithium: potential therapeutics against acute brain injuries and chronic neurodegenerative diseases. J Pharmacol Sci 2005; 99: 307–21.

30 Chen RW, Chuang DM. Long-term lithium treatment suppresses p53 and Bax expression but increases Bcl-2 expression. J Biol Chem 1999; 274: 6039–42.

31 Watanabe H, Ohta S, Kumon Y, Sakaki S, Sakanaka M. Increase in p53 protein expression following cortical infarction in the spontaneously hypertensive rat. Brain Res 1999; 837: 38–45.

32 Leker RR, Aharonowiz M, Greig NH, Ovadia H. The role of p53-induced apoptosis in cerebral ischemia: effects of the p53 inhibitor pifithrin α. Exp Neurol 2004; 187: 478–86.

33 Moncada S, Higgs EA. Prostaglandins in the pathogenesis and prevention of vascular disease. Blood Rev 1987; 1: 141–5.

34 Ma J, Zhang GY. Lithium reduced *N*-methyl-*D*-aspartate receptor subunit 2A tyrosine phosphorylation and its interactions with Src and Fyn mediated by PSD-95 in rat hippocampus following cerebral ischemia. Neurosci Lett 2003; 348: 185–9.

35 Rowe MK, Chuang DM. Lithium neuroprotection: molecular mechanisms and clinical implications. Expert Rev Mol Med 2004; 6: 1–18.

36 Fukumoto T, Morinobu S, Okamoto Y, Kagaya A, Yamawaki S. Chronic lithium treatment increases the expression of brain-derived neurotrophic factor in the brain. Psychopharmacology 2001; 158: 100–6.

37 Xu XH, Zhang HL, Han R, Gu ZL, Qin ZH. Enhancement of neuroprotection and heat shock protein induction by combined prostaglandin A1 and lithium in rodent models of focal ischemia. Brain Res 2006; 1102: 154–62.

Acta Pharmacologica Sinica (2011) 32: 311–320

www.nature.com/aps

Original Article

Electrophysiological mechanisms of sophocarpine as a potential antiarrhythmic agent

Zhi-fang YANG[1], Ci-zhen LI[1], Wei WANG[2], Ying-min CHEN[3], Ying ZHANG[1], Yuan-mou LIU[1], Hong-wei WANG[1, *]

[1]Department of Physiology, Shanghai Jiaotong University School of Medicine, Shanghai 200025, China; [2]Department of Geriatrics, Ruijing Hospital, Affiliated to Shanghai Jiaotong University School of Medicine, Shanghai 200025, China; [3]Department of Cardiology, Renji Hospital, Affiliated to Shanghai Jiaotong University School of Medicine, Shanghai 200001, China

---

Aim: To examine the electrophysiological effects of sophocarpine on action potentials (AP) and ionic currents of cardiac myocytes and to compare some of these effects with those of amiodarone.
Methods: Langendorff perfusion set-up was used in isolated guinea pig heart, and responses to sophocarpine were monitored using electrocardiograph. Conventional microelectrode, voltage clamp technique and perforated patch were employed to record fast response AP (fAP), slow response AP (sAP) and ionic currents in guinea pig papillary muscle or rabbit sinus node cells.
Results: Tachyarrhythmia produced by isoprenaline (15 μmol/L) could be reversed by sophocarpine (300 μmol/L). Sophocarpine (10 μmol/L) decreased the amplitude by 4.0%, maximal depolarization velocity (V_{max}) of the fAP by 24.4%, and Na^+ current (I_{Na}) by 18.0%, while it prolonged the effective refractory period (ERP) by 21.1%. The same concentration of sophocarpine could also decrease the amplitude and V_{max} of the sAP, by 26.8% and 25.7%, respectively, and attenuated the Ca^{2+} current (I_{CaL}) and the K^+ tail current substantially. Comparison of sophocarpine with amiodarone demonstrated that both prolonged the duration and the ERP of fAP and sAP, both decreased the amplitude and V_{max} of the fAP and sAP, and both slowed the automatic heart rate.
Conclusion: Sophocarpine could reverse isoprenaline-induced arrhythmia and inhibit I_{Na}, I_{CaL}, and I_{Kr} currents. The electrophysiological effects of sophocarpine are similar to those of amiodarone, which might be regarded as a prospective antiarrhythmic agent.

Keywords: sophocarpine; action potential; anti-arrhythmia; voltage clamp; potassium current; sodium current; calcium current

---

Acta Pharmacologica Sinica (2011) 32: 311–320; doi: 10.1038/aps.2010.207;

Introduction

Sophora flavescens is a traditional Chinese medicine that has been used for nearly 2000 years in China. It contains several types of alkaloids such as aloperin, matrine and sophocarpine. Some reports have found that *Sophora flavescens* has antiarrhythmic effects. Matrine, one extract from *Sophora flavescens*, was able to decrease abnormal spontaneous activities of the rat right atrium at 220 μmol/L[1]. It was also reported that matrine protects against aconitine-induced arrhythmia[2]. In 2008, Chen *et al* reported that sophocarpine could inhibit ouabain-induced arrhythmias in guinea pigs[3].

Zhang *et al*[4] found that sophocarpine, the extract from *Sophora flavescens*, was an effective drug in the treatment of viral myocarditis, not only for its antiviral effects, but also for its antiarrhythmic properties. According to Chen's data[5], 220 patients were enrolled in the sophocarpine therapeutic group, most of whom had shown different types of extra systoles. After treatment with sophocarpine (5–6 mg/kg in 500 mL of 5% glucose, iv for 4 h/d, 2–4 weeks as a course), the case analyses indicated that the antiarrhythmic efficiency of sophocarpine had reached 89.7%. Among these patients, complete data from 24 h Holter records were available for 49; the average number of extra systole cycles was decreased from 6120±3966 to 112±179 by sophocarpine in these patients. This report was very impressive, but the mechanism for its antiarrhythmic action needed to be further resolved. Chen *et al*[6] reported that sophocarpine could prolong the effective refractory period and raise the ventricular fibrillation threshold. However, those results were not enough to explain the drug's efficacy in clinical use.

In spite of those experimental studies and case reports, very little work has been done regarding the electrophysiological effects of sophocarpine on the heart, cardiac myocytes and ion channels. The aim of this paper was to fully study the electrophysiological properties of sophocarpine and explore the mechanism of its antiarrhythmic function. We took 3

---

* To whom correspondence should be addressed.
E-mail jywanghw@shsmu.edu.cn
Received 2010-06-25 Accepted 2010-10-28

steps to fulfill this purpose: first, we tried to confirm whether sophocarpine had antiarrhythmic effects in an arrhythmic model; second, we studied the effects of sophocarpine on action potentials (AP), whole cell and single channel currents to understand its electrophysiological properties; and third, we intended to compare the effects of sophocarpine with those of some known antiarrhythmic drugs.

Materials and methods

In the experiments, all of the procedures were approved by the Animal Care and Use Committee at Shanghai Jiaotong University. The investigation conforms to the Guide for the Care and Use of Laboratory Animals published by the US National Institutes of Health (NIH Publication No 85–23, revised 1996).

Solution preparation and materials

Tyrode's solution for perfusion preparations consisted of the following (in mmol/L): NaCl, 138; KCl, 5.4; CaCl$_2$, 1.8; MgCl$_2$, 1; glucose, 10; and HEPES, 10; pH 7.4±0.05 saturated by 100% O$_2$.

For whole cell Na$^+$ current recordings, the pipette solution contained (in mmol/L): KCl, 120; CaCl$_2$, 0.1; MgCl$_2$, 2; EGTA, 1.1; and HEPES, 10; pH 7.2. The bath solution was Tyrode's solution.

For inside-out Na$^+$ channel current recording, the bath solution was (in mmol/L): KCl, 120; MgCl$_2$, 2; CaCl$_2$, 0.1; HEPES, 10; and EGTA, 1.1; pH 7.4, while the pipette solution contained (in mmol/L): NaCl, 180; KCl, 1.3; MgCl$_2$, 0.5; CaCl$_2$, 1.5; glucose, 5; HEPES, 5; CoCl$_2$, 3; TEA, 10; 4-AP, 10; and CsCl, 10; pH 7.2.

The pipette solution for the perforated patch clamp contained (in mmol/L): K-aspartate, 130; MgCl$_2$, 2; CaCl$_2$, 5; EGTA, 11; Na-HEPES, 10; and Na$_2$-ATP, 2; pH 7.2. The concentration of amphotericin B was 240 µmol/L.

Sophocarpine (13,14-didehydromatridin-15-one, M_w 246.2, purity 99.7%, Figure 1A) was provided by Shanghai Institute of Pharmaceutical Industry (Shanghai, China). The injection solution of sophocarpine (10 g/L), produced by Shanghai Hejia Pharmaceutical Company (No 030827), was diluted to the final concentrations for the experiments. Amiodarone was purchased from the Mingzhu Pharmaceutical Factory of Sanofi-aventis China.

Chromanol 293B was provided by Aventis Pharma (Frankfurt, Germany), dofetilide by EGIS Pharmaceuticals Ltd (Pfizer Global Research & Development, UK, Batch 3644–399). Chromanol 293 B and dofetilide were initially dissolved in 100% DMSO to make a stock solution (10 mmol/L).

Electrocardiogram (ECG) recording in isolated guinea pig hearts

Guinea pigs (weighing approximately 250–300 g) of either sex were anesthetized with an intraperitoneal injection of urethane (20%, 5 mL/kg). The hearts were quickly taken out of the chest and perfused using a Langendorff perfusion setup at the recorded pressure of 80 cm H$_2$O. The temperature of Tyrode's solution was maintained at 37±0.5 °C. Three platinum electrodes, which had been placed on the cardiac apex, right atrium, and aortic root, were used to record the ECG. The signals were documented on a computer with the PowerLab system (PowerLab ML135, ML 785, ADInstruments, Australia)[7].

Primary culture of neonatal rat ventricular myocytes

Neonatal Sprague-Dawley (SD) rats of either sex (postnatal 1 d) were anesthetized by intraperitoneal injection of urethane (20%, 5 mL/kg). After the heart had been taken out, the ventricles were cut into small pieces and processed by collagenase-containing solution for digestion. The myocytes were separated from the cell suspension by centrifuging twice. The isolated ventricular myocytes were planted and grown on glass coverslips in DMEM (Invitrogen, Burlington, OH, USA) with 10% fetal bovine serum for 5-6 d[8, 9].

Preparation of guinea pig papillary muscles and rabbit sinus node

Guinea pigs (250–300 g) or rabbits (1.5–2.5 kg) of either sex were sacrificed by venesection under deep anesthesia with an intravenous injection of sodium pentobarbital (30 mg/kg). The hearts were rapidly removed into the dissection chamber filled with Tyrode's solution. The right ventricular papillary

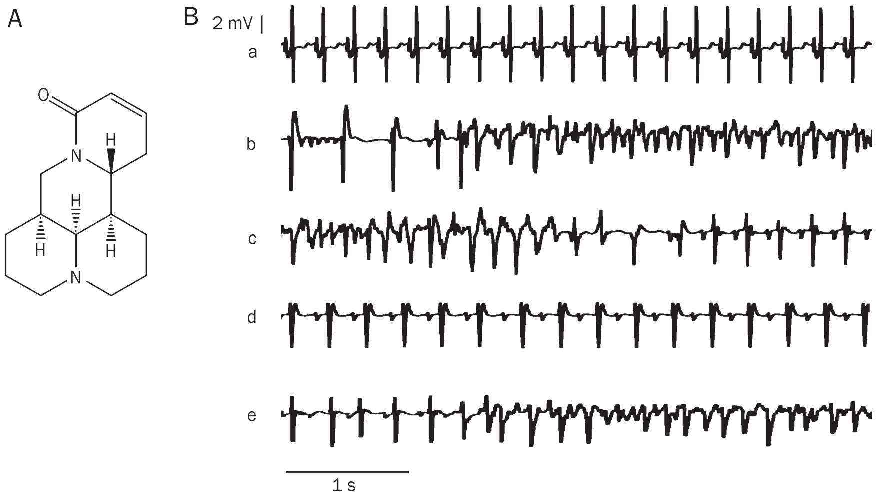

Figure 1. Sophocarpine (Soph) reversed the tachyarrhythmia of guinea pig.
A: Molecular structure of Soph.
B: Soph reversed the isoprenaline-induced tachyarrhythmia of guinea pig. (a) Control ECG. (b) The tachyarrhythmia was initiated after 6 min perfusion of the heart with isoprenaline 15 µmol/L. (c) The tachyarrhythmia began to be reversed after the heart had been exposed to Soph (300 µmol/L) plus isoprenaline solution for 13 min. (d) Two minutes later, the regular beating appeared on the ECG in the Soph-isoprenaline-contained solution. (e) The tachyarrhythmia recurred after Soph had been washed out for 7 min with the same solution as the one used in trace b.

muscles (from guinea pig) or the sinus nodes with partial right atrium (from rabbit) were excised and pinned to the bottom of a recording chamber. The chamber was perfused with Tyrode's solution at a constant rate of 3 mL/min and maintained at a temperature of 37±0.5 °C[7, 10].

Recording of the fast-response and slow-response AP

Bipolar platinum electrodes were used to drive the preparations with rectangular current pulses at a stimulation frequency of 1 Hz for papillary muscle and 2.2 Hz for the sinus node. Each pulse lasted 0.1 ms with a strength of about 1.5 times the threshold value. After 30 min of stimulation, transmembrane AP was recorded by a conventional glass microelectrode that was filled with 3 mol/L KCl and had a tip resistance of 15–20 MΩ. The records were sampled and stored in the computer through the amplifier (MEZ8201, Nihon Kohden, Japan) and PowerLab interface (PowerLab ML785, ADInstruments, Australia)[7, 10]. The calculated parameters for the fast response AP included the resting potential (RP), the action potential amplitude (APA), the maximal depolarization velocity ($V_{\max}$), the action potential duration (APD_{50} and APD_{90}), and the effective refractory period (ERP). To measure the ERP, the preparations of guinea pig were driven by a series of 8 stimuli pulses at a frequency of 1 Hz. Following the last pulse, an additional test pulse was added. By adjusting the time interval between the eighth pulse and the test stimulus, which was able to elicit an extra AP, the minimum interval was calculated as the ERP.

In our study of the sinus node, the parameters of the slow response AP were measured as APA, $V_{\max}$, APD_{90}, the maximum repolarization potential (MRP) and the spontaneous depolarization rate (SDR) in phase 4.

Voltage clamp experiment

The patch clamp technique was used to record the whole-cell and single channel currents. The cells were perfused with the bath solution mentioned above at a rate of 3 mL/min. The protocol for whole cell current recording is shown in the Results section.

Single Na^+ channel current was recorded in an inside-out configuration. Since K^+ and Ca^{2+} channels were blocked by TEA, 4-AP, $CoCl_2$, and CsCl in the pipette solution[11], the only channel that allowed an inward current to pass through would be the Na^+ channel.

Regarding the whole cell calcium current recording, the perforated patch clamp technique described in detail by our previous papers[12, 13] was used to prevent the run-down of calcium current. The perfusion solution contained 4-aminopyridine (4-AP, Sigma, USA), which was used to block the transient outward current (I_{to}) to reveal the Ca^{2+} current. An oscilloscope (DSS6521, Kikusui, Japan) and Axopatch-1D amplifier (Axon Instruments, Foster City, CA, USA) were used to monitor and record the clamped voltage and channel currents. The data were sampled with the Clampex 9.0 software suite (Axon Instruments) and stored in the computer through the interface (Digidata 1320, Axon Instruments). The sample rate was 100 kHz with a filtering frequency of 10 kHz.

Statistical analysis

Chart 5 (ADInstruments, Australia) software, Clampex 9.0, and Origin 6 (Microcal Software, Inc, USA) were used for measurement and statistical analysis. All of the results were expressed as means±SEM. Statistical significance was determined using Student's *t*-test for paired data. $P<0.05$ was considered statistically significant.

Results

Sophocarpine did exert an anti-arrhythmic effect

During tachyarrhythmia modeling, the heart was first perfused with isoprenaline (15 μmol/L)-containing Tyrode's solution. About 6–8 min later, the tachyarrhythmia or ventricular fibrillation was initiated and recorded. After that, sophocarpine was added to the isoprenaline-containing perfusion solution. About 11–17 min later, the tachyarrhythmia or the ventricular fibrillation was stopped, and the regular heartbeats appeared again on the ECG. Six guinea pig hearts were subjected to this protocol. All of them developed the tachyarrhythmia produced by isoprenaline, and all of the tachyarrhythmia was inhibited by sophocarpine (300 μmol/L). Isoprenaline increased the heart rate from 218±26 to 284±37 beats/min, leading to tachyarrhythmia; in contrast, sophocarpine returned the heart rate to 179±24 beats/min and finally stopped the tachyarrhythmia. The washing out of sophocarpine and isoprenaline returned the heart rate to 207±28 beats/min. Figure 1B-e shows that after the sophocarpine had been washed out with the same isoprenaline-containing solution, the tachyarrhythmia recurred.

The cardiac electrophysiological properties of sophocarpine

Four types of experiments were carried out to study the electrophysiological properties of sophocarpine: 1) recording of the fast response AP, 2) recording of the slow response AP, 3) measuring of Na^+ current in whole cell and single channel configurations, and 4) observing the changes in Ca^{2+} and K^+-tail currents.

The effects of sophocarpine on the fast response AP of ventricular cells

After the APs of the guinea pig papillary muscles had stabilized, the preparations were then perfused consecutively with different concentrations of sophocarpine-containing Tyrode's solution. Each perfusion lasted for about 8–10 min; meanwhile the RP, APA, $V_{\max}$, and APD were measured[7].

The effective refractory period was obtained by an extra super-threshold stimulus, which was applied during different repolarizing phases of the AP. Figure 2A shows that the APA was decreased while the APD and the effective refractory periods of the AP were dose-dependently prolonged by sophocarpine. The data from 6 experiments are presented in Table 1.

For measurement of the dose relationship between APD and sophocarpine, the concentrations of sophocarpine used ranged

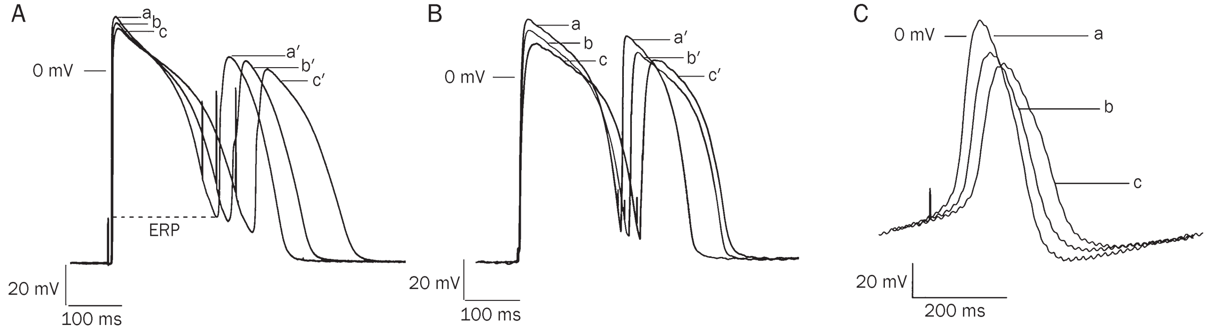

Figure 2. The effects of sophocarpine (Soph) and amiodarone (Amio) on the fast response AP of guinea pig papillary muscle and the slow response AP of rabbit sinus node cells.

A: The superimposed traces of the AP with the extra responses in different concentrations of Soph. The short upward straight lines before the AP and the each extra-response (a′, b′, and c′) were stimulus artifacts. The figure showed that Soph not only decreased the APA (from trace a to c) but also prolonged the action potential durations and the effective refractory period (ERP) in a dose-dependent manner, and at the same time it did not change the resting membrane potential very much. (a) Control; (b) Soph 1 μmol/L. (c) Soph 10 μmol/L.

B: The effect of Amio on the AP. (a) Control; (b) Amio 1 μmol/L; (c) Amio 10 μmol/L.

C: The superimposed action potential traces of sinus node with different concentrations of Soph. The short vertical bars before APs were the stimulus artifacts. Soph dose-dependently decreased the APA and prolonged the APD (from trace a to c). (a) Control; (b) Soph 0.5 μmol/L; (c) Soph 1 μmol/L.

Table 1. The electrophysiological effects of sophocarpine (Soph) and amiodarone (Amio) on the AP of ventricular myocytes of guinea pig (n=6, mean±SEM). [a]P>0.05, [b]P<0.05, [c]P<0.01 *vs* control. [d]P>0.05, [e]P<0.05, [f]P<0.01 *vs* 1 μmol/L group. [g]P>0.05, [h]P<0.05, [i]P<0.01 *vs* 5 μmol/L group.

	μmol/L	RP (mV)	APA (mV)	V_{max} (V/s)	APD_{50} (ms)	APD_{90} (ms)	ERP (ms)
Soph	Control	-90.5±0.5	124.2±1.3	221.7±10.4	207.1±14.9	250.0±15.7	244.0±12.4
	1	-89.4±0.7[a]	123.3±1.7[a]	204.2±10.8[b]	212.5±16.4[a]	261.2±13.8[a]	244.6±14.5[a]
	5	-89.3±1.0[ad]	121.6±1.5[bd]	192.6±10.0[cd]	225.5±9.5[bd]	283.4±13.5[ce]	270.2±17.9[be]
	10	-89.9±1.1[adg]	119.2±1.6[cfh]	167.5±11.5[cfi]	234.8±10.0[ceg]	302.3±14.7[cfg]	295.5±13.6[cfh]
		(-0.7%)	(-4.0%)	(-24.4%)	(13.4%)	(20.9%)	(21.1%)
	Washout	-90.1±0.8	123.5±2.0	202.9±13.1	210.5±15.7	264.3±16.1	247.3±16.4
Amio	Control	-90.8±0.7	123.3±3.2	221.3±11.5	203.5±10.1	240.9±13.6	231.6±12.7
	1	-90.5±0.5[a]	115.4±3.9[b]	204.1±15.7[a]	209.4±12.0[a]	251.6±15.3[a]	246.2±11.5[b]
	10	-90.0±0.3[ad]	109.6±4.5[cd]	161.5±10.2[cf]	226.9±12.3[be]	267.6±16.0[bd]	265.6±13.0[ce]
		(-0.9%)	(-11.1%)	(-27.2%)	(11.5%)	(11.1%)	(14.7%)
	Washout	-89.9±0.6	118.9±4.7	187.8±13.4	205.6±9.8	243.7±14.8	228.9±13.1

The numbers in the brackets are the percentage changes *vs* controls.

from 1 to 100 μmol/L. EC_{50} (median effective concentration) of the prolonged APD_{90} was 5.93 μmol/L; the dose response curve is presented in Figure 3.

The effect of sophocarpine on the slow response AP of rabbit sinus node

In order to observe the effect of sophocarpine on the slow response AP of sinus node, the preparation of rabbit sinus node had to be driven by electric stimulus at the rate of 130 times/min (faster than its own spontaneous beating). In this way, we could eliminate the influence of the varying rhythm of spontaneous activity of the sinus node on the APD; otherwise, it might interfere with the calculation of the AP parameters, for it is known that the faster the heart beats, the shorter the APD will be. In those experiments, the stimulated APs were recorded by glass microelectrode[10]. The changes in AP parameters induced by sophocarpine are listed in Table 2. Figure 2C presents results from 5 experiments on the sinus node. In Figure 2C, the decreases in both the APA and the V_{max} were observed after the application of different concentrations of sophocarpine. Furthermore, the APD_{90} was also prolonged by sophocarpine, which was in accordance with the results from the fast response AP recordings (Figure 2A).

The possible mechanism for the sophocarpine-mediated prolongation of the APD

Chromanol 293 B[14] specifically blocks I_{Ks}, while dofetilide[15] blocks I_{Kr}. In this experiment, chromanol 293 B was first applied to block I_{Ks}, and then sophocarpine with different concentrations was consecutively added to the perfus-

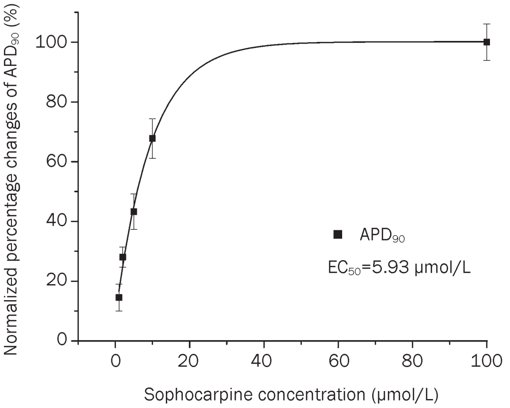

Figure 3. Dose-response of the APD$_{90}$ of the papillary muscle to sophocarpine (Soph). Abscissa, concentration of Soph. Ordinate, normalized percentage changes of APD$_{90}$ by Soph (n=5). Data was fitted with Exponential Decay Function. EC$_{50}$ was 5.93 μmol/L.

ing solution. Figure 4-IA shows that the prolongation of APD induced by chromanol 293 B (trace b) was further increased by sophocarpine (trace c and d), which suggests that sophocarpine might inhibit I_{Kr}, resulting in the increased APD. To confirm this, the following protocol was used (Figure 4-IB): Dofetilide was first used to inhibit the I_{Kr}, leading to the increase in APD (trace b); then sophocarpine at different concentrations was added to the perfusing solution. Figure 4-IB demonstrates that the APD was no longer affected by sophocarpine (traces c and d). The above results indicate that sophocarpine could block I_{Kr} rather than I_{Ks}, leading to prolongation of the APD. Figure 4-II presents the 5 experimental results with the washing-out data.

Table 2. The effects of sophocarpine (Soph) on the slow response AP of rabbit sinus node cells (n=5, mean±SEM). $^{a}P>0.05$, $^{b}P<0.05$, $^{c}P<0.01$ *vs* control. $^{d}P>0.05$, $^{e}P<0.05$, $^{f}P<0.01$ *vs* 0.1 μmol /L group. $^{g}P>0.05$, $^{h}P<0.05$, $^{i}P<0.01$ *vs* 0.5 μmol/L group. MRP, the maximum repolarization potential.

Soph (μmol /L)	APA (mV)	V_{max} (V/s)	APD$_{90}$ (ms)	MRP (mV)
Control	68.0±3.3	9.8±0.5	123.2±8.3	-65.8±3.1
0.1	64.7±2.2^{a}	9.1±0.4^{b}	124.8±7.1^{a}	-65.2±3.3^{a}
0.5	58.1±3.9^{ce}	8.8±0.5^{cd}	127.7±7.1^{ad}	-63.1±2.5^{ad}
1	53.4±3.0^{cfg}	8.3±0.6^{cfg}	140.7±7.0^{cfh}	-61.6±2.7^{beg}
Washout	66.3±4.2	9.4±0.7	128.3±7.2	-65.5±2.9

The effect of sophocarpine on the cardiac Na^{+} current

The action of sophocarpine on the cardiac Na^{+} current was carried out in 2 experimental levels: the whole cell I_{Na} recording and single Na^{+} channel current recording.

Sophocarpine decreased the whole cell I_{Na}

Whole cell current recording was carried out in enzyme-isolated ventricular cells of neonatal rat heart. The cell was depolarized from the holding potential (-110 mV) to the testing potential (-50 mV) for 300 ms before it was returned to the holding potential. The initial large inward current was invoked by depolarization clamping, as shown in Figure 5A.

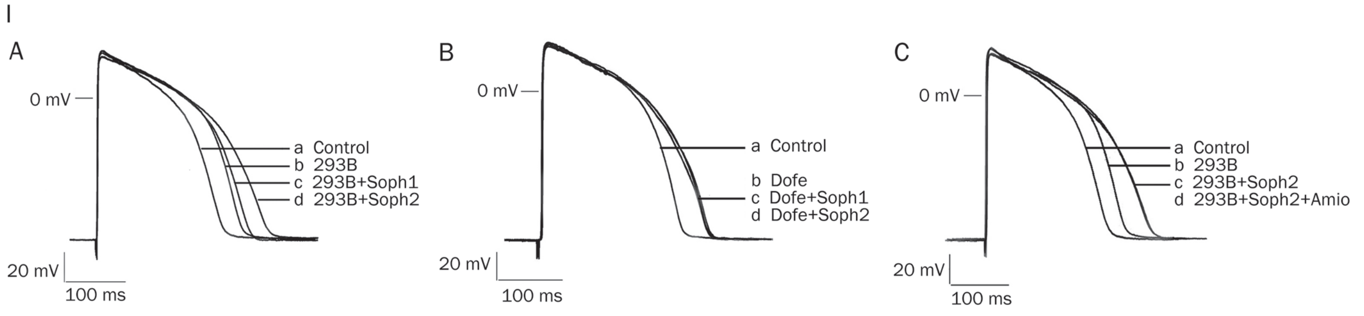

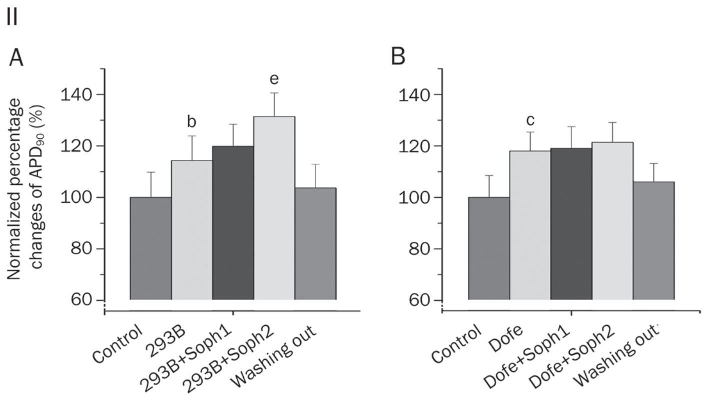

Figure 4. Sophocarpine (Soph) inhibits $I_{Kr.}$ Soph1, sophocarpine 5 μmol/L. Soph2, sophocarpine 10 μmol/L. Dofe: dofetilide 1 μmol/L. 293B, chromanol 293B of 15 μmol/L. Amio: amiodarone 10 μmol/L.
Part I
A: The effect of Soph on APD after the I_{Ks} had been blocked by chromanol 293B.
B: The effect of Soph on APD after I_{Kr} had been blocked by Dofe.
Section C: Amio did not prolong APD after the action of Soph.
Part II
The statistical data (n=5) showing the percentage changes of APD$_{90}$ by different drugs as indicated in part I A and B.
Ordinate: normalized percentage changes of APD$_{90}$. Abscissa: the symbols corresponded to those of the Part I plus the washing out. $^{b}P<0.05$, $^{c}P<0.01$ *vs* control. $^{e}P<0.05$ *vs* 293B+Soph1.

As this inward current had been blocked by the special Na^+ channel blocker TTX 10 μmol/L (not shown), this current could be regarded as I_{Na}[7]. After the cell was perfused with sophocarpine (10 μmol/L), the inward current was decreased substantially. From 3 experiments that involved whole cell recordings, the average decrease of the I_{Na} induced by sophocarpine (10 μmol/L) was about 18.0%.

Sophocarpine inhibited single Na^+ channel activity

Single Na^+ channel current recordings were carried out in an inside-out configuration on isolated ventricular myocytes from neonatal rats. The patch membrane was first held at -110 mV and then depolarized to and clamped at -50 mV for 500 ms before it was returned to the holding potential. As the pipette solution contained Ca^{2+} and K^+ channel blockers (see Material and methods section), the recorded channel current may have represented the Na^+ current.

Single channel openings were observed on the recording traces. Both the open occurrences and the averaged inward current were decreased after the cells had been perfused with a sophocarpine (30 μmol/L)-containing solution in 3 experiments. Figure 5B shows one of the results.

Sophocarpine inhibited the I_{CaL} of cardiac myocytes

The whole cell recording configuration and perforated patch technique were used in this experiment. The ventricular cells of neonatal rat were first held at -40 mV to inactivate the Na^+ channels and then depolarized to the command potential of 20 mV for 500 ms before they were returned to the holding potential (Figure 6). As 4-AP had been used to block the I_{to}, the inward current was clearly discernible at the command potential (Figure 6a). Sophocarpine (10 μmol/L) was then added to the perfusion solution. About 3 min later, not only had the inward current decreased, but also the tail current (outward K^+ current, a′) was diminished. Compared with the controls in 3 experiments, average I_{CaL} decreased by 33.2%±11.7% at the command potential of 20 mV.

Comparison of electrophysiological effects between sophocarpine and amiodarone

From the above results, we can see that sophocarpine induced effects similar to those of class III anti-arrhythmic drug amiodarone, *ie*, it was also able to prolong the APD. The following experiments were designed to compare these two drugs in their effects on both the fast and the slow response AP morphologies.

Effect of amiodarone on the fast response AP

The preparation and the experimental protocol were the same as sophocarpine section. Amiodarone at a concentration of 10 μmol/L not only prolonged the APD and ERP by 11.1% and 14.7%, respectively, but also decreased the APA and V_{max}. The results from 6 experiments are presented in Table 1, and one example is shown in Figure 2B.

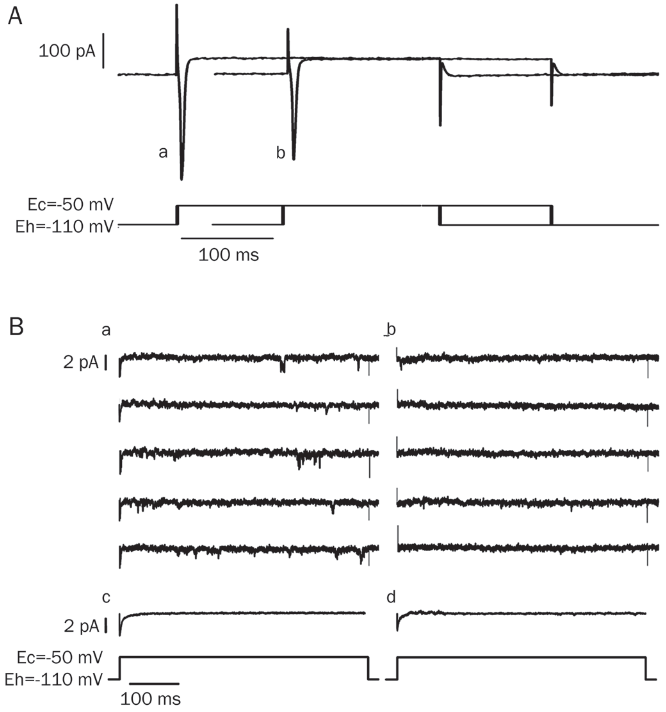

Figure 5. Sophocarpine (Soph) decreased the early Na^+ current.
A: Soph decreased I_{Na} in the whole cell recording configuration. The upper half showed the whole cell sodium current recordings; the lower one was the voltage clamp protocol. (a) Control inward current. (b) The decreased current by Soph 10 μmol/L.
B: Soph decreased the Na^+ current in the single channel recording configuration. The upper parts (a, b, c, d) referred to the channel current recording; the lower was the voltage clamp protocol. (a) A group of control traces. (b) The traces after Soph 30 μmol/L. (c and d) The averaged inward currents which were calculated before and after the Soph from 43 and 35 trails respectively.

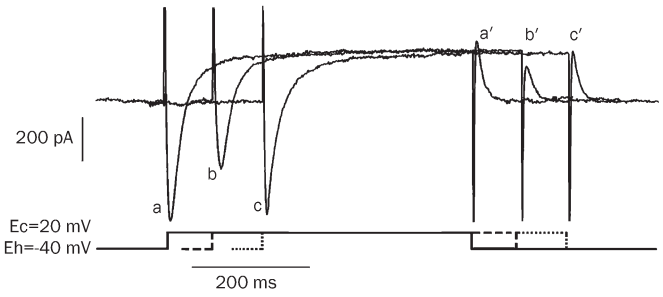

Figure 6. Sophocarpine (Soph) inhibited I_{CaL} and I_k tail current. The a, b, c, and a′, b′, c′ represented I_{CaL} and I_K tail currents respectively. (a) Control. (b) Soph 10 μmol/L. (c) Washing out.

Because our results confirmed that sophocarpine could inhibit I_{Kr} to prolong the APD and that amiodarone could block the I_{Kr}, the following experiment was designed to determine what would happen to amiodarone if sophocarpine were first used to inhibit I_{Kr}.

Figure 4-IC shows that after chromanol 293B had blocked the I_{Ks} (from trace a to trace b) leaving I_{Kr}, sophocarpine increased the APD (from b to c), and then amiodarone (at the

same concentration as sophocarpine) was added to the perfusing solution. The latter had no obvious effect on the APD (traces c and d were superimposed); neither were substantial changes to the APD observed when sophocarpine was administered before amiodarone (data not shown).

The effects of amiodarone and sophocarpine on the spontaneous AP of rabbit sinus node

The preparation of rabbit sinus node did not involve electric stimulus; spontaneous APs were recorded with a glass microelectrode. After the control AP was recorded in Tyrode's solution, amiodarone (10 μmol/L) or sophocarpine (10 μmol/L) was added to the perfusion solution. About 10 min later, the changes in AP produced by the drugs were measured, and then the drugs were washed out with control Tyrode's solution. Sophocarpine-mediated inhibition of $V_{\max}$ and APA started at about 2 min and reached the maximum in another 1 min. The inhibitory effect on APA or $V_{\max}$ lasted stably for a considerable time. In our records, we only pre-treated the preparations for about 30–50 min and then washed them out to observe the recovery process. Full recovery could be obtained after 8 to 10 min of washing out. Figure 7 illustrates the comparison. The results from 5 experiments are shown in Table 3. In short, the data show that both drugs could decrease the APA, the $V_{\max}$ and the spontaneous heart rate and that both could prolong the APD to some extent.

Discussion

The electrophysiological effects of sophocarpine on the heart

Phase 0 of the fast response AP is initiated by the fast inward Na^+ current. The APA and $V_{\max}$ are related to the dynamics of this current. Our whole current experiments demonstrated that sophocarpine could substantially inhibit the I_{Na}, which would explain why sophocarpine decreased APA and $V_{\max}$ in the experiment on the fast response AP. In the inside-out recording experiments, K^+ and Ca^{2+} channels had been blocked by $CoCl_2$, TEA, 4-AP, and CsCl in the pipette solution; hence, the inward current in Figure 5 must have been the Na^+ current. The decreased opening and reduced magnitude of the Na^+ channel current following sophocarpine treatment confirmed the inhibitory effect of sophocarpine on Na^+ channels.

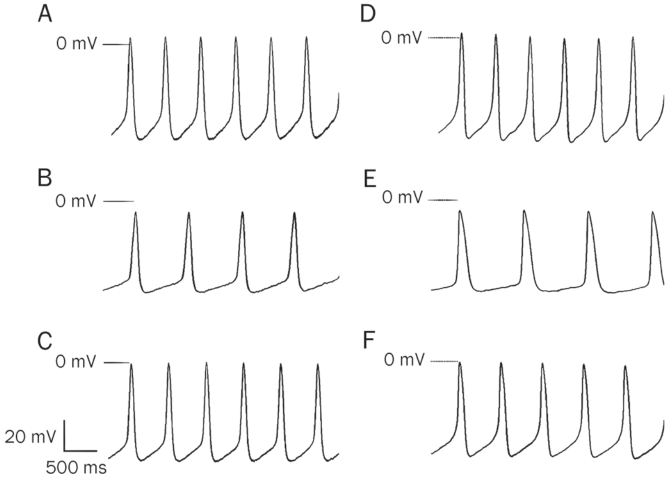

Figure 7. Sophocarpine (Soph) and amiodarone (Amio) had the similar effects on the spontaneous AP of rabbit sinus node. The traces of A, B, C, D, E, and F were spontaneous APs. A, B, C belonged to Soph experiment, and D, E, F to those of Amio's. A and D: Controls. B: Ten minutes after Soph 10 μmol/L. E: Ten minutes after Amio 10 μmol/L. C and F: Washout with the control Tyrode's solution.

During the whole cell recording of the slow inward current (I_{CaL}), sophocarpine substantially decreased the current. The slow response AP, such as the AP in sinus node, is initiated by the slow I_{CaL}. The APA and $V_{\max}$ of the slow AP are dependent on the dynamics or conditions of the Ca^{2+} channel. The decreases in APA and $V_{\max}$ induced by sophocarpine could result from the inhibitory effect of sophocarpine on the Ca^{2+} channel.

APD is mainly related to the balance between the inward I_{CaL} and the outward K^+ current. The observed prolongations of the APD in both the fast response AP (papillary muscle myocytes) and the slow response AP (sinus node cells) mediated by sophocarpine suggest that sophocarpine could also inhibit the outward K^+ current, which would result in retardation of

Table 3. The effects of sophocarpine (Soph) and amiodarone (Amio) on the slow response AP of rabbit sinus node (*n*=5, mean±SEM). [a]$P>0.05$, [b]$P<0.05$, [c]$P<0.01$ *vs* control.

	μmol/L	APA (mV)	$V_{\max}$ (V/s)	APD_{90} (ms)	MRP (mV)	SDR (mV/s)	HR (beat/min)
Soph	Control	70.2±1.2	10.1±0.7	110.5±7.2	-66.3±1.2	55.3±2.4	110.4±5.3
	10	51.4±3.0[c]	7.5±0.6[c]	122.7±8.1[b]	-60.2±1.5[b]	29.2±2.8[c]	80.7±4.4[c]
		(-26.8%)	(-25.7%)	(11.0%)	(-9.2%)	(-47.2%)	(-26.9%)
	Washout	64.5±2.2	9.2±0.7	112.9±7.6	-64.2±1.0	43.6±4.5	102.5±6.8
Amio	Control	69.8±1.5	9.8±1.0	106.8±8.7	-67.2±1.7	56.0±2.6	112.7±6.1
	10	50.9±2.6[c]	4.7±0.8[c]	135.6±10.2[c]	-60.9±2.1[b]	18.8±3.2[c]	71.4±5.7[c]
		(-27.1%)	(52.0%)	(27.0%)	(-9.4%)	(-66.4%)	(-36.6%)
	Washout	62.7±4.3	8.5±1.3	110.2±9.4	-63.1±3.8	40.1±4.7	100.9±7.5

SDR, spontaneous depolarization potential rate in phase 4; HR, heart rate.

the repolarization and prolongation of the APD. The direct evidence for sophocarpine-mediated inhibition of the K$^+$ current is presented in Figure 6, which presents the sophocarpine-mediated reduction of the K$^+$ tail current (Figure 6b′). Notably, after I_{Ks} had been blocked by chromanol 293B, sophocarpine was capable to dose-dependently prolong the APD; however, if I_{Kr} was first inhibited by the I_{Kr}-blocker dofetilide, sophocarpine did not demonstrate this effect. Although this design was unable to rule out whether I_{Kr} was involved in the process, our results coincided with those described by Yang *et al* in their study of the effect of sophocarpine on HERG channel stably expressed in human embryonic kidney-293 cells[13]. The authors demonstrated that sophocarpine inhibited the transfected HERG channels by influencing the inactivation state[16].

Sophocarpine could decrease the *L*-type calcium current, which might shorten the APD$_{90}$ and interfere with its prolongation effect on APD[17] that there are two different repolarizing currents that are activated by a rise in cytosolic calcium concentration[17]. One current, $I_{K.Ca}$, appears to be a member of the K$_v$ family of potassium channels; the other, I_{to2}, is probably a calcium-activated chloride channel. Both respond to a rise in cytosolic calcium by shortening the action potential duration, limiting further calcium entry into the heart. According to this opinion, we suppose that the reduction of the calcium current by sophocarpine would therefore have less effect on $I_{K.Ca}$ and be conducive to the prolongation of APD. Valenzuela *et al*[18], in their experiments on guinea pig ventricular myocytes, found that amiodarone (16 μmol/L) induced dramatic tonic and phasic reductions of the Ca^{2+} current. Nonetheless, amiodarone still prolonged the APD.

The possible mechanism of the anti-arrhythmic function of sophocarpine

β-adrenergic agonists lead to the elevation of cytosolic cyclic AMP levels and the activation of protein kinase A. This kinase phosphorylates *L*-type Ca^{2+} channels and thereby increases the channel's open probability, resulting in large Ca^{2+} current into the cell. Normally, the inward Ca^{2+} current is balanced by the Ca^{2+} pumps located in the sarcoplasmic reticulum and cell membrane and in the Na$^+$/Ca^{2+} exchangers in the cell membrane. The tachyarrhythmia produced in our experiment may be due to the use of high concentrations of isoprenaline (15 μmol/L) in the perfused solution. Isoprenaline could induce the delayed after-depolarization (DAD) by increasing sarcoplasmic reticulum (SR) Ca^{2+} load, leading to spontaneous SR Ca^{2+} release and activation of transient inward current (I_{ti}), which underlies DADs[19]. Ultimately, ECG revealed tachyarrhythmia or fibrillation of the ventricle.

Tosaki *et al*[20] reported that in the isolated rat heart, reperfusion-induced arrhythmias were exacerbated by isoproterenol (0.01–1.0 μmol/L). The proarrhythmic action of isoproterenol was primarily the result of a β$_1$-receptor-mediated tachycardia rather than a free radical mediated process[21], since it was prevented competitively by the β$_1$-receptor antagonist metoprolol, but not by the free radical scavengers. The authors also found[22] that drugs such as lidocaine, which prevent ion movements induced by some pathologic changes, protected against reperfusion-induced arrhythmias.

It has been said that 'Virtually all anti-arrhythmic drugs inhibit the opening or reactivation of voltage-gated ion channels'[23]. Because sophocarpine inhibited Ca^{2+} channel current, it was expected to relieve the Ca^{2+}-overload produced by isoprenaline. Furthermore, sophocarpine, with its inhibitory effects on potassium and sodium currents, was not only able to prolong the effective refractory period but also able to decrease the conduction velocity via its inhibition of APA and V_{max} of the AP. Those two effects might be conducive to its antiarrhythmic effect because propagation of the AP can be interrupted by those two effects if reentry occurs during tachyarrhythmia. However, one reporter showed that the increase or decrease in heart rate was closely correlated with the development of arrhythmias[24]. The investigation showed that increasing the heart rate in increments from 200 to 400 beats/min caused an increased incidence of ventricular fibrillation and ventricular tachycardia during reperfusion. Some researchers[25] explained that a higher heart rate would cause the accumulation of extracellular potassium. Loss of cellular potassium was a critical factor in determining the vulnerability of the heart to arrhythmias. Furthermore, a lower heart rate also directly decreases the possibility of triggered activity[26]. In our experiment with isoprenaline, the perfused heart rate increased from 218±26 to 284±37 beats/min and tachyarrhythmia developed. After sophocarpine, the heart rate decreased to 179±24 beats/min and the tachyarrhythmia disappeared (Figure 1). In terms of Tosaki's point of view, the heart-rate-slowing effect of sophocarpine may explain one of its antiarrhythmic mechanisms. Although we have no direct evidence to support the above hypotheses or experiments to rule out whether sophocarpine could act as a β-receptor antagonist, the fact is that sophocarpine does reverse the tachyarrhythmia and fibrillation produced by isoprenaline. This antiarrhythmic function of sophocarpine has been proven by other experimental reports[1–4] and clinical practice[5, 27].

According to Chen's clinical observations[5, 27], sophocarpine has no obvious harmful effects on the functions of the liver or kidney or on the blood system. A few patients have exhibited nausea or urticaria. After a decrease in the dosage, the symptoms disappeared in a few days. A clinical trial on sophocarpine conducted by researchers at Renji Hospital has progressed from stage II to stage III. The information gathered should be illuminating.

Comparison of sophocarpine with amiodarone with regard to electrophysiological characteristics

In our preliminary experiments, we found that sophocarpine had some inhibitory effect on potassium, sodium and calcium currents, similar to amiodarone[28]. It has been reported that sotalol has no effects on sodium or calcium currents. That was the main reason we chose amiodarone instead of sotalol for comparison with sophocarpine. Furthermore, the clinical review maintains: Despite limited indication, amiodarone is one of the most frequently prescribed specific antiarrhythmic drugs in the United States[29–31]. Amiodarone is a class III antiarrhythmic drug. It inhibits repolarizing K^+ currents and so prolongs the cardiac AP; it weakly inhibits depolarizing currents, such as those mediated by the Na^+ and Ca^{2+} channels[32–34]. Therefore, it was worth comparing the electrophysiological effects of these two drugs. Our results indicated that their effects were very similar: both can inhibit the APA and $V_{\max}$ of the fast and the slow response APs; both can prolong the APD and the ERP of ventricular myocytes; both can decrease the automatic heartbeat and spontaneous depolarization rate in phase 4 of the sinus node AP. However, in some respects, for example in the reduction of spontaneous heart beating, amiodarone seemed more powerful than sophocarpine: 10 μmol/L amiodarone decreased the heartbeat by 36.6%, while 10 μmol/L sophocarpine decreased the heartbeat by only 26.9%. In other respects, sophocarpine could increase the APD and prolong the ERP for a little longer than amiodarone. Actually, we do not know which is more effective in clinical use, for this kind of comparison must include many other factors, such as the side effects or the kinetics of the drugs, *etc*. However, Li *et al,* in their study on the antiarrhythmic properties of long-term treatment with matrine in rats with arrhythmia induced by coronary ligation, found that long term oral administration of Martine reduced arrhythmia and mortality more effectively than did amiodarone[35].

Study limitations

One limitation of the present study is the lack of a comparison between sophocarpine and amiodarone and the short-lived duration of the effects of amiodarone on $I_{\rm Na}$, $I_{\rm CaL}$, and $I_{\rm Kr}$ currents. Thus, further studies are needed.

Another limitation is that sophocarpine has obvious inhibitory effects on the isoprenaline-induced tachyarrhythmia, yet it is still unclear which of its electrophysiological properties plays the crucial role in this action. The mechanism by which isoprenaline induces tachyarrhythmia is complicated. Either the delayed after-depolarization or the re-entry mechanisms or the changes in heart rate may take part in the process. Further study will be necessary.

Conclusion

Sophocarpine could reverse isoprenaline-induced arrhythmia and inhibit $I_{\rm Na}$, $I_{\rm CaL}$, and $I_{\rm Kr}$ currents. The electrophysiological effects of sophocarpine are similar to those induced by amiodarone, which might be regarded as a prospective antiarrhythmic drug in clinical practice.

Acknowledgements

This work was supported by the Science Foundation of the Shanghai Science Committee Foundation (№ 06JC14045) and the Science Foundation of Shanghai Health Bureau (№ 2009045).

Author contribution

Ci-zhen LI and Yuan-mou LIU designed the research plan; Zhi-fang YANG, Ci-zhen LI, Hong-wei WANG, Wei WANG, and Ying ZHANG performed the research: Zhi-fang YANG, Hong-wei WANG, Ci-zhen LI, and Ying-min CHEN analyzed the data; Hong-wei Wang and Yuan-mou LIU wrote the paper.

References

1 Zhang BH, Wang NS, Li XJ, Kong XJ, Cai YL. Anti-arrhythmic effects of matrine. Acta Pharmacol Sin 1990; 11: 253–7.

2 Huang CY, Xie SR, Huang SY, Gao GY. Experimental studies of antiarrhythmic effects of matrine. J Dalian Med Univ 2002; 24: 177–9.

3 Chen YM, Xu J, Li HB, Chen MF, Qian FR, Chen SX, *et al*. Effect of sophocarpine on ouabain-induced arrhythmia in guinea pigs. Chin J New Drugs Clin Rem 2008; 27: 576–8.

4 Zhang XY, Chen SX, Liu JX, Qian FR. Protection of cardiomyocytes from coxsackievirus B_3 by sophocarpine. Chin J New Drugs Clin Rem 2006; 25: 709–12.

5 Chen SX, Chen MF, Qian FR, Xie LS. A clinical research of sophocarpine in treatment of viral myocarditis. Chin J Clin Cardiol 2005; 211: 608–11.

6 Chen YM, Xu J, Ye Q, Chen MF, Shen HF, Chen SX. Effect of sophocarpine in raising ventricular fibrillation threshold and prolonging ventricular effective refractory period of early acute myocardial ischemia in canine. Chin J New Drugs Clin Rem 2006; 25: 252–5.

7 Wang HW, Yang ZF, Zhang Y, Yang JM, Liu YM, Li CZ. Beta-receptor activation increases sodium current in guinea pig heart. Acta Pharmacol Sin 2009; 30: 1115–22.

8 Baetz D, Regula KM, Ens K, Shaw J, Kothari S, Yurkova N, *et al*. Nuclear factor kappaB-mediated cell survival involves transcriptional silencing of the mitochondrial death gene BNIP3 in ventricular myocytes. Circulation 2005; 112: 3777–85.

9 Zhang Y, Zheng YQ, Wang HW, Yang Zf, Liu YM, Li CZ. Method for culturing neonatal rat cardiac myocytes and observation of its electrophysiological properties. J Shanghai Jiaotong Univ (Med Sci) 2007; 27: 398–400.

10 Yang ZF, Wang HW, Zheng YQ, Zhang Y, Liu YM, Li CZ. Possible arrhythmiogenic mechanism produced by ibuprofen1. Acta Pharmacol Sin 2008; 29: 421–9.

11 Liu YM, DeFelice LJ, Mazzanti M. Na channels that remain open throughout the cardiac action potential plateau. Biophys J 1992; 63: 654–62.

12 Liu YM, Yu H, Li CZ, Cohen IS, Vassalle M. Cesium effects on $I_{\rm f}$ and $I_{\rm k}$ in rabbit sinoatrial node myocytes: implications for SA node automaticity. J Cardiovasc Pharmacol 1998; 32: 783–90.

13 Li CZ, Liu YM, Yang ZF, Wang HW, Yang JM. An improved method of isolation of rabbit sinus node cells and the perforated patch recording with amphotericin B. Chin J Appl Physiol 1999; 15: 89–92.

14 Ding WG, Toyoda F, Mastsuura H. Blocking action of chromanol 293B on the slow component of delayed rectifier K^+ current in guinea-pig sino-atrial node cells. Br J Pharmacol 2002; 137: 253–62.

15 Roukoz H, Saliba W. Dofetilide: a new class III anti-arrhythmic agent. Expert Rev Cardiovasc Ther 2007; 5: 9–19.

16 Qi ZP, Shi SS, Zhao XL, Zhao WX, Bai YL, Lu YJ, *et al*. Effect of Sophocarpine on HERG K^+ Channels. Yao Xue Xue Bao 2008; 43: 44–9.

17 Katz AM. The Cardiac Action Potential. In: Kartz AM, editors. Physiology of the heart 3rd ed. Philadelphia: Lippincott Williams & Wilkins 2001: P 478–516.

18 Valenzuela C, Bennett PB. Voltage-and use-dependent modulation of calcium channel current in guinea pig ventricular cells by amiodarone and des-oxo-amiodarone. J Cardiovasc Pharmacol 1991; 17: 894–902.

19 Desantiago J, Ai X, Islam M, Acuna G, Ziolo MT, Bers DM, *et al*. Arrhythmogenic effects of β_2-adrenergic stimulation in the failing heart are due to enhanced SR Ca load. Circ Res 2008; 102: 1389–97.

20 Tosaki A, Woodward B, Yamamoto F, Hearse DJ. Isoproterenol and the genesis of reperfusion-induced arrhythmias in isolated rat heart: adrenoceptor or free radical-mediated mechanisms? J Cardiovasc Pharmacol 1990; 15: 398–407.

21 Tosaki A, Braquet P. DMPO and reperfusion injury: Arrhythmia, heart function, electron spin resonance, and nuclear magnetic resonance studies in isolated working guinea pig hearts. Am Heart J 1990; 120: 819–30.

22 Tosaki A, Balint S, Szekeres L. Protective effect of lidocaine against ischemia and reperfusion-induced arrhythmias and shifts of myocardial sodium, potassium, and calcium content. J Cardiovasc Pharmacol 1988; 12: 621–8.

23 Katz AM. Arrhythmias II: Clinical Manifestations and Principles of Therapy. In: Katz AM, editors. Physiology of the heart 3rd ed. Philadelphia: Lippincott Williams & Wilkins 2001: P 580–629.

24 Tosaki A, Balint S, Szekeres L. Pacing and reperfusion induced arrhythmias: protection by slow heart rate in the rat heart. Cardiovasc Res 1988; 22: 818–25.

25 Weiss J, Shine KI. Effect of heart rate on extracellular K^+ accumulation during myocardial ischemia. AM J Physiol 1986; 250: H982–91.

26 Zuanetti G, DeFerrari GM, Priori SG, Schwartz PJ. Protective effect of vagal stimulation on reperfusion arrhythmias in cats. Circ Res 1987; 61: 429–35.

27 Chen SX, Xu XH, Zhang DQ, Mei SW, Xie LS, Chen MF, *et al*. The study on the expression of IFN-γ and IL-10 in patients with viral myocarditis and their interference with Chinese drugs. Chin J Endocrinol Metab 2001; 21: 14–7.

28 Zhao XJ, Guo DL, Wu Y, Liu TX, Yan GX. Effects of chronic amiodarone therapy on *L*-type calcium current recovery and action potential duration of rabbit ventricular myocytes. Chin J Cardiol 2009; 37: 528–31.

29 Singh BN. Expanding indications for the use of class III agents in patients at high risk for sudden death. J Cardiovasc Electr 1995; 6: 887–900.

30 Anderson JL. Contemporary clinical trials in ventricular tachycardia and fibrillation: implications of ESVEM, CASCADE, and CASH for clinical management. J Cardiovasc Electr 1995; 6: 880–6.

31 Vassallo P, Trohman RG. Prescribing amiodarone an evidence-based review of clinical indications. J Am Med Assoc 2007; 298: 1312–22.

32 Sicouri S, Belardinelli L, Carlsson L, Antzelevitch C. Potent antiarrhythmic effects of chronic amiodarone in canine pulmonary vein sleeve preparations. J Cardiovasc Electr 2009; 20: 803–10.

33 Kodama I, Kamiya K, Toyama J. Amiodarone: Ionic and cellular mechanisms of action of the most promising class III agent. Am J Cardiol 1999; 9: 20–8.

34 Singh BN. Amiodarone: A multifaceted antiarrhythmic drug. Curr Cardiol Rep 2006; 5: 349–55.

35 Li XL, Chu WM, Liu JL, Xue XR, Lu YJ, Shan HL, *et al*. Antiarrhythmic properties of long-term treatment with Matrine in arrhythmic rat induced by coronary ligation. Biol Pharm Bull 2009; 32: 1521–6.

Acta Pharmacologica Sinica (2011) 32: 321–328
© 2011 CPS and SIMM All rights reserved 1671-4083/11 $32.00
www.nature.com/aps

Original Article

Influence of fluvastatin on cardiac function and baroreflex sensitivity in diabetic rats

Fang XIE[1, #], Chao SUN[1, 2, #], Li-hua SUN[1], Jing-yuan LI[1], Xin CHEN[1], Hui CHE[1], Guan-yi LU[1], Bao-feng YANG[1], Jing AI[1, *]

[1]*Department of Pharmacology, and the State-Province Key Laboratory of Biomedicine and Pharmaceutics, Harbin Medical University, Harbin 150081, China;* [2]*Department of Pharmacology, Qiqihaer Medical College, Qiqihaer 161006, China*

Aim: To investigate whether fluvastatin is able to ameliorate the impaired cardiac function or baroreflex sensitivity (BRS) in rats with type 1 diabetes.

Methods: Type 1 diabetic rats were induced by intraperitoneal injection of streptozotocin (STZ) and then administered fluvastatin (1.5, 3.0, and 6.0 $mg \cdot kg^{-1} \cdot d^{-1}$) for 30 d. Food and drink intake was recorded every day. Fasting blood glucose (FBG) level, blood lipid level, cardiac function and BRS were measured in diabetic rats after fluvastatin treatment for 30 d.

Results: The polydipsia, polyphagia and abnormal biochemical indexes of blood were significantly ameliorated by the the 3.0- and 6.0-mg doses of fluvastatin in STZ-induced diabetic rats. FBG was decreased in diabetic rats after fluvastatin treatment for 30 d. The left ventricular systolic pressure (LVSP) and the maximum rate of change of left ventricular pressure in the isovolumic contraction and relaxation period ($\pm dp/dt_{max}$) were elevated, and left ventricular diastolic pressure (LVEDP) was decreased by fluvastatin. The attenuated heart rate responses to arterial blood pressure (ABP) increase induced by phenylephrine (PE) and ABP decrease induced by sodium nitroprusside (SNP) were reversed by the 3.0-mg dose of fluvastatin.

Conclusion: Fluvastatin regulates blood lipid levels and decreases the FBG level in diabetic rats. These responses can protect the diabetic heart from complications by improving cardiac function and BRS.

Keywords: fluvastatin; diabetes; cardiac function; baroreflex sensitivity

Acta Pharmacologica Sinica (2011) 32: 321–328; doi: 10.1038/aps.2010.221

Introduction

Diabetic heart complications influence the prognosis of patients and are the main reason for the high mortality of diabetic patients[1]. A number of studies have reported that diabetes mellitus (DM) leads to autonomic neuropathic dysfunctions, including impairment of the baroreflex control of heart rate (HR) in both diabetic patients and chemically induced diabetic rats[2, 3]. Impairment of the baroreflex sensitivity (BRS) underlying the diabetic state was closely related to life-threatening arrhythmias, heart failure and sudden death[4, 5]. Hypoglycemic agents, such as thiazolidinediones (TDs), which are the most common drugs used for DM, mainly ameliorate insulin resistance and regulate lipid metabolism. Therefore, it is necessary to find drugs that will relieve the impairment of BRS to prevent further cardiac complications in diabetic patients.

It is known that inhibition of 3-hydroxy-3-methylglutaryl coenzyme A (HMG-CoA), the rate-limiting enzyme in cholesterol synthetic pathways, will reduce the release of cholesterol into the blood in the form of very low density lipoprotein[6]. Fluvastatin, an HMG-CoA reductase inhibitor, which is the first wholly synthetic statin on the market, has been widely used as a classic lipid-regulating drug to treat hypercholesterolemia[7]. The advantages of fluvastatin, compared to other statins, are as follows: fluvastatin is well tolerated[8, 9], substantial benefits of fluvastatin have been confirmed in clinical trials[10], and fluvastatin is more cost effective for long-term treatment[11]. Beyond its regulation of blood lipids, the anti-atherogenic, antithrombotic and antioxidative actions of fluvastatin have been used to prevent cardiovascular disease[12]. As shown in previous studies, fluvastatin was found to reduce the increased incidence of long-term adverse complications associated with diabetes[13]. Other roles of fluvastatin in diabetic treatment have also been reported, such as ameliorating cardiac sympathetic neural dysfunction in association with the attenuation of increased myocardial oxidative stress; preventing left ventricular remodeling by reducing myocardial fibro-

---

[#] The first two authors contributed equally to this work.

[*] To whom correspondence should be addressed.

E-mail a.z.hrbmu@gmail.com

Received 2010-08-17 Accepted 2010-12-02

sis; exerting a protective action on vascular endothelial cells; and protecting against oxidative DNA damage[14, 15]. Although various functions of fluvastatin have been studied in the treatment of diabetes, whether it plays a role in ameliorating impaired BRS is unknown.

In this work, the BRS measured with baroreflex control of HR and other parameters, biochemical indexes of blood and cardiac function were examined in streptozotocin (STZ)-induced diabetic rats to evaluate the effects of fluvastatin. We found that fluvastatin could effectively preserve impaired BRS in diabetic rats. Moreover, it shows promise in the development of improved drugs to address the adverse cardiac complications associated with diabetes.

Materials and methods

Chemicals

Fluvastatin was purchased from Novartis Pharma (Beijing, China). STZ was obtained from Sigma-Aldrich (St Louis, MO, USA). Adrenaline was obtained from Shanghai Harvest Pharmaceutical Co, Ltd (Shanghai, China). Sodium nitroprusside was acquired from Shanghai N̲o̲ 1 Biochemical and Pharmaceutical Co, Ltd (Shanghai, China). All other chemicals were of analytical grade from local suppliers.

Animals

Male Wistar rats (n=34, weight 220–260 g, age approximately 3–4 months) were obtained from the Animal Center of the Second Affiliated Hospital of Harbin Medical University (Harbin, China) and housed at 23±1 °C with 55%±5% humidity and a 12-h light–dark cycle. The use of these animals was in accordance with the regulations of the Ethics Committees of Harbin Medical University (N̲o̲ HMUIRB-2008-06).

Establishment of a diabetic model

DM was induced in the 28 randomly chosen rats by intraperitoneal (ip) injection of 40 mg·kg^{-1} of streptozocin (STZ) in a 0.1 mol·L^{-1} citrate buffer solution (pH 4.2) each day for 2 d after fasting for 12 h. The FBG level was measured using a Grace glucometer (Grace Medical, Inc, USA) from the tail vein 72 h after the final injection of STZ. Twenty-four of the STZ-induced rats with a FBG ≥16.7 mm were used as established DM models.

Group treatment

Twenty-four rats with DM were randomly divided into four groups with six rats per group as follows: diabetes mellitus (DM), DM with a high dose of fluvastatin (6.0 $\text{mg·kg}^{-1}\text{·d}^{-1}$) (DM+FH), DM with a middle dose of fluvastatin (3.0 $\text{mg·kg}^{-1}\text{·d}^{-1}$) (DM+FM) and DM with a low dose of fluvastatin (1.5 $\text{mg·kg}^{-1}\text{·d}^{-1}$) (DM+FL). Fluvastatin was intragastrically administered for 30 d after confirmation of DM with the different doses described previously. The other six healthy Wistar rats were used as a control group (Ctr) and were treated with the same quantity of vehicle (citrate buffer) and 0.9% NaCl.

Measurement of food and drink intake

From the beginning of fluvastatin administration, the food and drink intake for all animals was recorded every 24 h for 30 d. The average food and drink intake for each group was determined by dividing the total amount of food and drink consumed by the total number of rats in each group.

Biochemical indexes of blood

After 30 d of fluvastatin treatment, the FBG level was measured from the tail vein using a Grace glucometer after a fasting period of 12 h. Following cardiac function and BRS studies, blood samples were collected from the heart and then separated to analyze for total cholesterol (TC), triglycerides (TG), low-density lipoprotein (LDL), high-density lipoprotein (HDL), free fatty acids (FFA) and malondialdehyde (MDA), using the appropriate kit (Shanghai Rongsheng Biotech Co, Ltd, China) for each test.

In vivo cardiac function studies

After determination of FBG level from the tail vein, all rats from each group were anesthetized with sodium pentobarbital (40 mg·kg^{-1}) via ip injection. Cardiac function was calculated as previously described[16]; briefly, the catheter was inserted into the left ventricle via the right common carotid artery to record cardiac electrophysiologic parameters. Arterial blood pressure (ABP), heart rate (HR), left ventricular systolic pressure (LVSP), left ventricular diastolic pressure (LVEDP) and the maximum rate of change in left ventricular pressure in the isovolumic contraction or relaxation period ($\pm dp/dt_{\max}$) were measured using a BL-420 Data Acquisition & Analysis System (Chengdu Tme Technology Co, Ltd, China).

Surgical procedure

After cardiac function studies were completed, the surgery proceeded on all rats from the Ctr, DM and DM+FM groups. These rats were anesthetized with an ip injection of sodium pentobarbital (40 mg·kg^{-1}). The surgical procedure was in accordance with previous studies[17–19]. Briefly, supplemental doses of anesthetics (0.1 mL of 1% sodium pentobarbital) were administered every 30 min to prevent eye blinking and pedal-withdrawal reflexes. The tips of polyethylene-50 catheters were tapered to a diameter of 0.5 mm. After the exposure of the femoral artery (left) and the femoral vein (right), the tapered tips of two catheters filled with heparinized saline were then inserted into the femoral artery and vein. Vasoactive drugs were injected into the femoral vein, and blood pressure was measured in the femoral artery.

Baroreflex sensitivity

The blood pressure catheter was connected to a blood pressure transducer (MlT0699; AD Instruments, Australia) placed in a horizontal position level with the heart. ABP was measured automatically using the BL-420 Data Acquisition & Analysis System. HR was calculated from pulse pressures using the Ratemeter function. Phenylephrine (PE) or sodium nitropruside (SNP) was injected at various dosage levels (PE: 16, 32, 64, 128, and 256 μg·mL^{-1}; SNP: 10, 20, 40, 80, and 160 μg·mL^{-1}) with an injection speed of 0.04 mL·100 mg^{-1}. A second drug administration was not performed until the HR and ABP responses reached a steady-state response. The maximal HR responses relative to the HR baseline level (ΔHR) and mean ABP (MABP) changes relative to the ABP baseline level (ΔMABP) induced by injection of PE or SNP were recorded and analyzed. The averaged ratio of the HR change over the MABP change (ΔHR/ΔMABP) was used to evaluate the baroreflex sensitivity (BRS) for each dose of each drug given. Dose-dependent curves for ΔMABP and ΔHR/ΔMABP as functions of PE and SNP concentration were plotted for each group. Curves of ΔHR-ΔMABP were also plotted to display the maximal HR responses induced by MABP changes. The Boltzmann equation in Prism 5.0 software (GraphPad Software Inc, San Diego, CA, USA) was used to fit all curves[17, 20].

Statistical analysis

Data were analyzed using one-way ANOVA, and $P<0.05$ was considered statistically significant. Data were expressed as mean±SEM. Different baseline MABP and HR were compared for the divided groups using Student's *t*-tests.

Results

Effects of fluvastatin on food and drink intake

After the initial fluvastatin administration, the average food and drink consumption for rats in each group were recorded each day (Figure 1). The results demonstrate that both food and drink consumptions were greatly increased in the diabetic rats until a steady dose-dependent decrease in consumption occurred after approximately 12 d of fluvastatin treatment in DM rats. Polydipsia and polyphagia were remarkably improved in the DM+FM and DM+FH groups ($P<0.05$).

Effects of fluvastatin on biochemical indexes of blood

Thirty days after the establishment of the STZ-induced DM rats, TC, TG, LDL, FBG, FFA, and MDA were significantly increased, while HDL was decreased (Table 1). This suggests that after 30 d of treatment, fluvastatin effectively improved TC, TG, HDL, LDL, and FBG in a dose-dependent manner. However, only slight changes in FFA and MDA were observed in all of the groups.

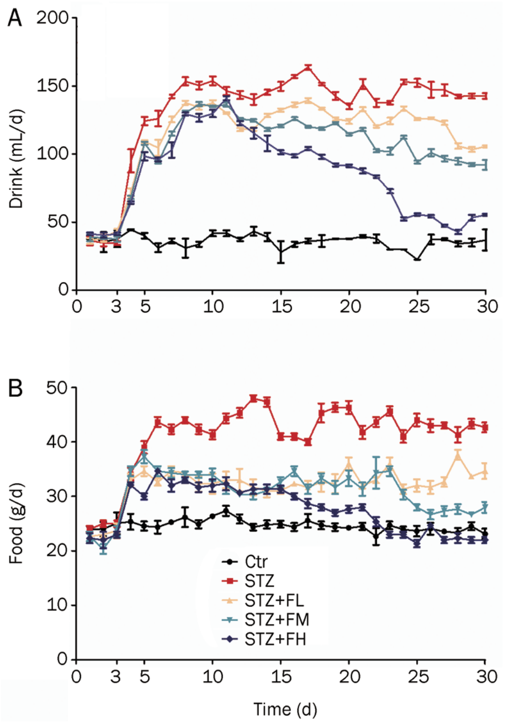

Figure 1. Drink and food intake *versus* time after fluvastatin administration in the four groups: streptozotocin (STZ)-induced diabetes mellitus (DM) rats, DM rats with low-dose fluvastatin (DM+FL), middle-dose fluvastatin (DM+FM) and high-dose fluvastatin (DM+FH) treatment. (A) Changes of drink intake of rats in the four groups. (B) Changes of food intake of rats in the four groups. STZ-induced DM rats significantly increased both drink and food consumptions while DM rats with fluvastatin treatment had a steady dose-dependent downward trend of drink and food intake (n=6).

Effects of fluvastatin on cardiac function

The LVSP was significantly decreased in the DM group compared with the Ctr group (Figure 2A; 14.87±0.25 kPa and 11.63±0.22 kPa for Ctr rats and DM rats, respectively;

Table 1. The effect of fluvastatin on biochemical indexes of blood in diabetic rats (n=6). Ctr: control group; DM: diabetic group; DM+FL: DM with low-dose fluvastatin (1.5 mg·kg^{-1}·d^{-1}); DM+FM: DM with middle-dose fluvastatin (3.0 mg·kg^{-1}·d^{-1}); DM+FH: DM with high-dose fluvastatin (6.0 mg·kg^{-1}·d^{-1}). Mean±SEM. $^{b}P<0.05$, $^{c}P<0.01$ *vs* control group; $^{f}P<0.05$ *vs* diabetic group.

Groups	TC (mmol/L)	TG (mmol/L)	HDL (mmol/L)	LDL (mmol/L)	FBG (mmol/L)	FFA (nmol/L)	MDA (nmol/L)
Ctr	1.19±0.05	0.37±0.03	0.52±0.02	0.44±0.03	5.23±0.12	0.55±0.04	5.25±0.21
DM	1.24±0.02^{b}	0.51±0.02^{b}	0.32±0.02^{b}	0.53±0.02^{b}	21.95±3.92^{c}	1.10±0.06^{b}	8.42±0.41^{b}
DM+FL	1.22±0.06^{b}	0.42±0.01^{bf}	0.35±0.01^{f}	0.45±0.02^{f}	21.01±3.67^{c}	0.82±0.04^{b}	7.06±0.32^{b}
DM+FM	1.21±0.04	0.40±0.02^{f}	0.44±0.02^{f}	0.42±0.01^{f}	14.15±1.34^{bf}	0.76±0.03^{b}	6.32±0.33^{b}
DM+FH	1.21±0.05	0.39±0.03^{f}	0.47±0.01^{f}	0.41±0.02^{f}	9.42±1.28^{bf}	0.64±0.02^{b}	5.86±0.29^{b}

TC, total cholesterol; TG, triglyceride; HDL, high density lipoprotein; LDL, low density lipoprotein; FBG, fasting blood glucose; FFA, free fatty acids; MDA, malondialdehyde.

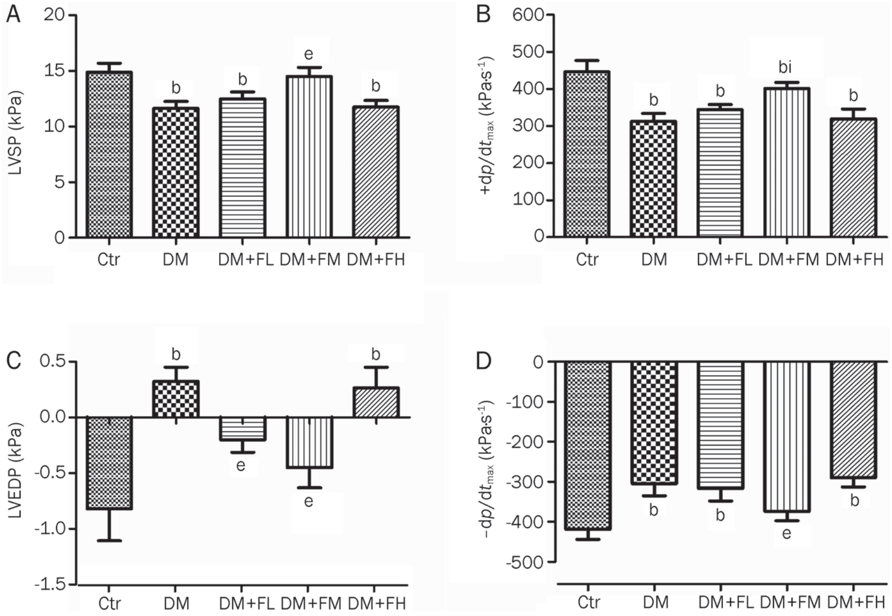

Figure 2. Quantitative analysis of parameters of cardiac function in control rats (Ctr), streptozotocin (STZ)-induced diabetes mellitus (DM) rats, DM rats with low-dose fluvastatin (DM+FL), middle-dose fluvastatin (DM+FM) and high-dose fluvastatin (DM+FH). (A) left ventricular systolic pressure (LVSP); (B) maximum change velocity of left ventricular pressure in the isovolumic contraction period (+dp/dt_{max}); (C) left ventricular diastolic pressure (LVEDP); (D) maximum change velocity of left ventricular pressure in the isovolumic relaxation period (-dp/dt_{max}). $^{b}P<0.05$ *vs* Ctr; $^{e}P<0.05$, $^{i}P<0.01$ *vs* DM (n=6).

$P<0.05$). This effect was offset by the middle dose of fluvastatin (14.49±0.39 kPa; $P<0.05$); however, neither the low dose (12.50±0.29 kPa; $P>0.05$) nor the high dose (11.76±0.27 kPa; $P>0.05$) of fluvastatin improved LVSP.

As shown in Figure 2B, the decreased +dp/dt_{max} in DM rats was increased following treatment with the middle dose of fluvastatin for 30 d (446.00±9.21 kPa·s^{-1} for the Ctr rats, 312.89±8.00 kPa·s^{-1} for the DM rats and 401.11±6.21 kPa·s^{-1} for the DM+FM rats; $P<0.05$), but this effect was not seen in the DM+FL or the DM+FH group (344.22±5.08 kPa·s^{-1} for the DM+FL rats and 319.56±9.98 kPa·s^{-1} for the DM+FH rats; $P>0.05$).

LVEDP sharply increased in the DM rats (0.32±0.05 kPa) compared with the Ctr rats (-0.82±0.08 kPa; $P<0.05$). As shown in Figure 2C, LVEDP in the DM+FL (-0.20±0.04 kPa) and DM+FM (-0.45±0.07 kPa) rats experienced a substantial decrease compared with the DM rats ($P<0.05$). However, the DM+FH rats did not show significant improvement in LVEDP (0.26±0.07 kPa; $P>0.05$).

The -dp/dt_{max}, an indicator of diastolic function, was significantly impaired in the DM rats compared with the Ctr rats (Figure 2D; -418.88±10.13 kPa·s^{-1} for the Ctr rats and -304.38±12.29 kPa·s^{-1} for the DM rats; $P<0.05$). While the middle dose of fluvastatin successfully reversed this parameter to -373.63±9.62 kPa·s^{-1} ($P<0.05$), the low dose (-316.75±12.38 kPa·s^{-1}) and the high dose (-290.13±9.08 kPa·s^{-1}) of fluvastatin did not have the same effect ($P>0.05$).

Baroreflex control of heart rate during phenylephrine administration

MABP was gradually raised by doses of PE in the Ctr, DM, and DM+FM rats (Figure 3A, 3B, and 3C). Meanwhile, the dose-dependent curves used to assess the maximal ΔMABP over various PE doses are shown in Figure 3D. The magnitude of the increase in ΔMABP following PE injection appeared less significant for all doses in the DM rats when compared to the Ctr rats ($P<0.05$); this is consistent with previous studies[20, 21]. This decrease was dramatically alleviated in the DM+FM rats ($P<0.05$). For example, the 256 μg·mL^{-1} dose of PE caused the ΔMABP to collapse to 29.42±3.54 mmHg in the DM rats compared with 48.99±3.79 mmHg in the Ctr rats ($P<0.05$), and it was greatly improved to 43.61±4.46 mmHg in the DM+FM rats ($P<0.05$).

To estimate the BRS, the ΔHR/ΔMABP ratio was depicted as an index. As shown in Figure 3E, with the increase in the PE dose, the ΔHR/ΔMABP displayed an increasing trend for all of the groups, although the margins of the increases varied. Of note, the ΔHR/ΔMABP value was significantly increased in the DM rats as compared to the Ctr rats at every dosage level of PE ($P<0.05$). The middle dose of fluvastatin caused the variation to diminish ($P<0.05$). For instance, at the dose of 256 μg·mL^{-1} of PE, the middle dose of fluvastatin reversed the increased ΔHR/ΔMABP value from 2.22±0.11 beats·min^{-1}·mmHg^{-1} in the DM rats to 1.91±0.13 beats·min^{-1}·mmHg^{-1} in the DM+FM rats; this was a partial recovery when compared with the Ctr rats (1.74±0.11 beats·min^{-1}·mmHg^{-1}).

The maximal HR responses at steady state to the maximal changes of MABP induced by different doses of PE and ΔHR were plotted as functions of ΔMABP (Figure 3F). The curves were fit using the Boltzmann equation after maximal ΔHR and ΔMABP were averaged at the different PE doses within each group[22]. As expected, the maximal ΔHR in response to the maximal ΔMABP was reduced in the DM rats (31.42 mmHg) compared with the Ctr rats (43.98 mmHg), and this reduction could also be seen in the DM+FM rats (40.58 mmHg).

Baroreflex control of heart rate during sodium nitroprusside administration

The decrease of MABP was induced by SNP in a dose-depen-

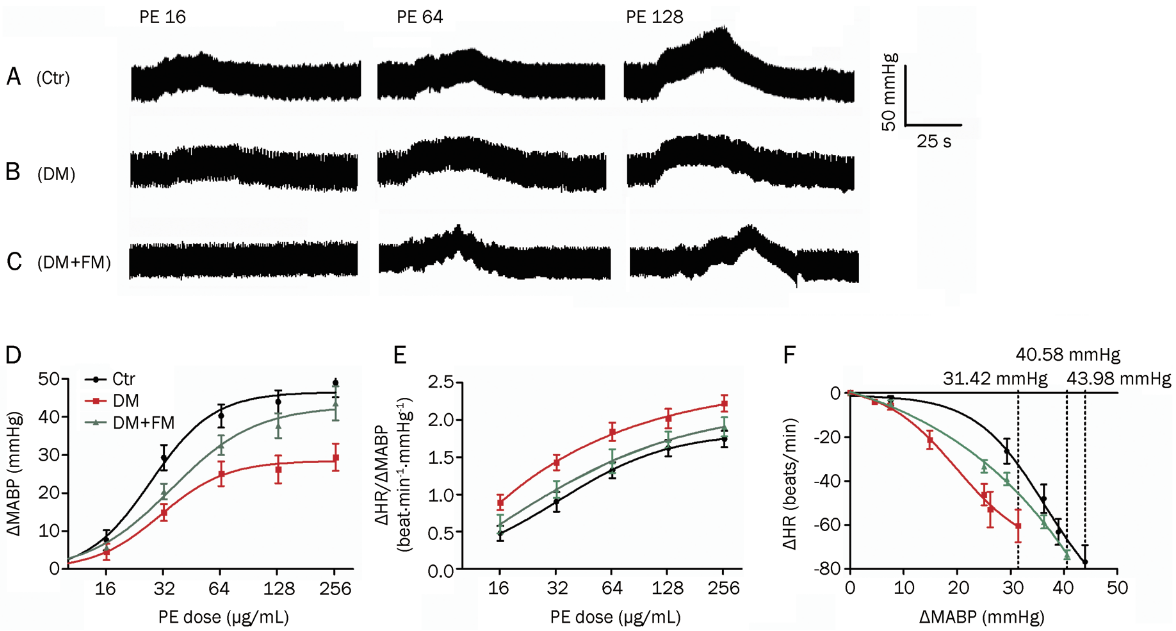

Figure 3. Significant amelioration of impaired baroreflex sensitivity in streptozotocin (STZ)-induced diabetes mellitus (DM) rats after 30-d treatment with middle-dose fluvastatin following phenylephrine (PE) administration. Traces of blood pressure changes induced by PE application at 16, 64, and 128 μg/mL in (A) control rats (Ctr), (B) STZ-induced DM rats (DM) and (C) DM rats with middle-dose fluvastatin (DM+FM). (D) The curve of change in mean arterial blood pressure (ΔMABP) against each dose of PE in the three groups. (E) The curve of ΔHR/ΔMABP against different doses of PE in the three groups. (F) The curve of ΔHR against ΔMABP in the three groups. Values are means (*n*=6) with standard errors represented by vertical bars.

dent manner for the Ctr, the DM and the DM+FM rats, as shown in Figure 4A, 4B, and 4C. Furthermore, the ΔMABP dose-dependent curve in the DM and the DM+FM rats for each dose of SNP appeared similar to that of the PE curves. The ΔMABP was decreased in the DM rats compared with the Ctr rats, and this decrease was partly recovered by adminis-

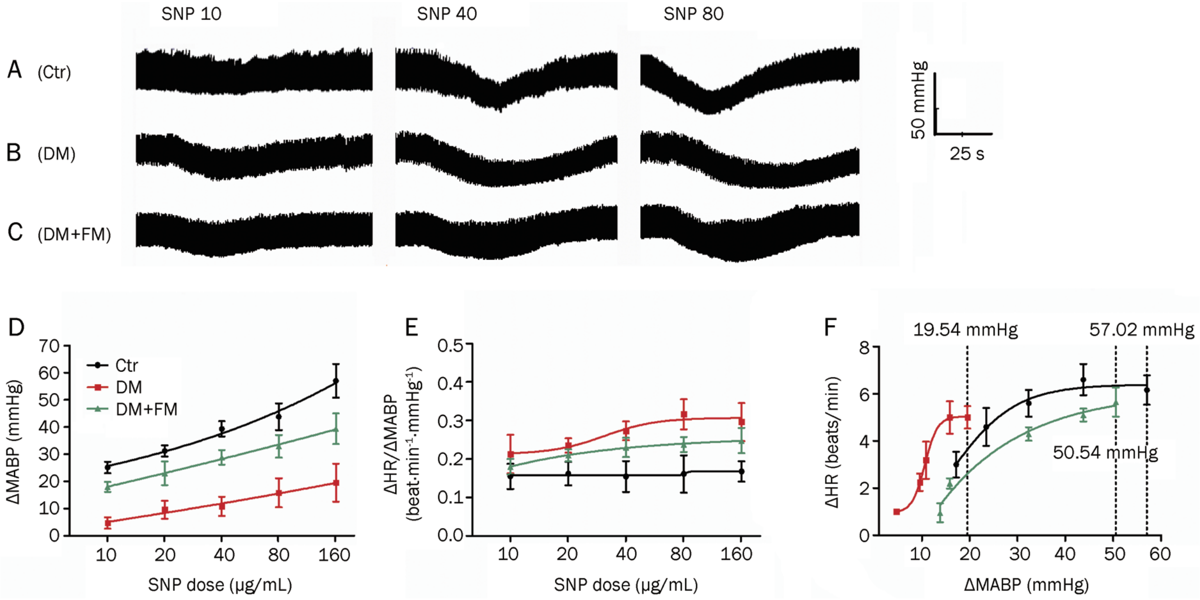

Figure 4. Effects of middle-dose fluvastatin on baroreflex sensitivities of rats with diabetes mellitus (DM) induced by streptozotocin (STZ) during sodium nitroprusside (SNP) application. Traces of blood pressure changes induced by SNP application at 10, 40, and 80 μg/mL in (A) control rats (Ctr), (B) STZ-induced DM rats (DM) and (C) DM rats with middle-dose fluvastatin (DM+FM). (D) The curve of change in mean arterial blood pressure (ΔMABP) against different doses of SNP in the three groups. (E) The curve of ΔHR/ΔMABP against different doses of SNP in the three groups. (F) The curve of ΔHR against ΔMABP in the three groups. Values are means (*n*=6) with standard errors represented by vertical bars.

tration of the middle-dose of fluvastatin (Figure 4D; $P<0.05$). This was fully demonstrated by the values at the SNP dose of 160 μg·mL^{-1} (57.02±6.19 mmHg for the Ctr rats; 19.54±6.97 mmHg for the DM rats and 39.43±5.61 mmHg for the DM+FM rats).

No significant changes in the ΔHR/ΔMABP were noted in the Ctr rats, and only a slight increase in ΔHR/ΔMABP was detected with the increase in SNP administered to the DM and the DM+FM rats (Figure 4E). However, the ΔHR/ΔMABP value was marginally increased with the same dose of SNP administered to the DM rats compared to the Ctr rats. Meanwhile, the ΔHR/ΔMABP value of the DM+FM rats was located between that of the other two groups. When 160 μg·mL^{-1} of SNP was given to rats in all of the groups, the ΔHR/ΔMABP increased from 0.17±0.03 beats·min^{-1}·mmHg^{-1} in the Ctr rats to 0.30±0.05 beats·min^{-1}·mmHg^{-1} in the DM rats and 0.25±0.03 beats·min^{-1}·mmHg^{-1} in the DM+FM rats.

It should be noted that the response of the maximal ΔHR to the maximal ΔMABP displayed a sharp decrease in the DM rats (19.54 mmHg) compared with the Ctr rats (57.02 mmHg). Similarly, the middle dose of fluvastatin reversed this effect, resulting in a value of 50.54 mmHg (Figure 4F).

Discussion

The type 1 diabetic model has been successfully established by the intraperitoneal injection of STZ in Wistar rats. Our studies have shown that food and drink consumption began to decrease in a dose-dependent manner in the DM rats after approximately 12 d of fluvastatin treatments, particularly in the DM+FM and the DM+FH groups. This phenomenon undoubtedly indicates that fluvastatin could ameliorate polydipsia and polyphagia, which are typical symptoms of DM.

As predicted, in the DM rats the levels of TC, TG, and LDL were significantly reduced, but the HDL level was increased by fluvastatin. However, the FFA and the MDA were slightly decreased by any dose of fluvastatin in the DM rats. These results demonstrate that fluvastatin can dramatically regulate blood lipid, and the mechanism has been well documented[6, 7]. These are the main reasons that fluvastatin is used to treat diabetic patients with hyperlipemia. The FBG level in the DM+FM and the DM+FH rats dropped significantly; however, the low dose of fluvastatin did not achieve this effect. It is reasonable to presume that regulating blood lipid and improving insulin sensitivity may contribute to the hypoglycemic effect of fluvastatin. Therefore, if the underlying mechanisms for the effect of fluvastatin identified in clinical trials could be determined, diabetic patients using fluvastatin would not only pay attention to its classic lipid-regulating effect but also benefit from its hypoglycemic action.

In this study, impaired cardiac function was confirmed in the DM rats by the following parameters: LVSP, LVEDP, and $\pm dp/dt_{\max}$. Nevertheless, fluvastatin could partially reverse the impairment of both contractile and diastolic functions in a dose-independent manner; however, the middle dose rather than the high dose of fluvastatin was significantly more effective in improving cardiac function in the DM rats. The DM+FH rats suffered severe rhabdomyolysis—toxicity of the skeletal muscle due to RhoA dysfunction following the loss of lipid modification with geranylgeranyl pyrophosphate[23, 24]. Consequently, it was reasonable to presume that pain caused by severe rhabdomyolysis may contribute to the negative impact on cardiac function seen in the DM+FH rats. It is known that primary myocardial defect and BRS impairment may both underlie the impaired cardiac function of diabetic patients. According to recent studies, fluvastatin can reduce myocardial fibrosis and exert a direct anti-atherosclerotic action on the arterial wall, which may improve cardiac function in an experimental model of diabetic cardiomyopathy[12]. All the facts addressed above may contribute to the amelioration of the primary myocardial defect that accompanies fluvastatin administration in DM rats. Consequently, it is important to determine whether fluvastatin could improve impaired BRS and lead to an improvement in cardiac function.

The optimal dose of fluvastatin is 6.0 mg·kg^{-1}·d^{-1} (the middle dose) and was chosen for the BRS study based on the following observations: the middle dose of fluvastatin exerted the most obvious effect according to cardiac function analysis; the blood lipid and the FBG were significantly regulated in both the DM+FM and the DM+FH rats; the middle dose of fluvastatin was equal to the clinical dosage amount; and the DM+FH rats suffered severe rhabdomyolysis, suggesting that clinical application of high-dose fluvastatin may result in severe side effects.

Our results showed that fluvastatin could reverse the decreased ΔMABP caused by DM when various dosages of PE and SNP were administered. Interestingly, the increase of ΔHR/ΔMABP, an indicator of BRS, was greater in DM rats compared with Ctr rats in response to PE and SNP injections. This result is not consistent with those of some DM models, which may be largely attributed to the different time course of development for diabetes (*ie*, 12, 24, and 48 weeks): metabolic disorders caused by a hyperglycemic state or insulinopenia may be related to time-dependent changes in parasympathetic and sympathetic control[25, 26] and different osmotic diuresis after the DM model was established[27, 28]. In addition, discrepancies in species, experimental design and diabetic inducer may also affect the results to some extent[29, 30]. However, our results are consistent with the findings of Jackson and colleagues[31] that blood pressure responses to vasopressor agonists were depressed in STZ-induced DM rats while the baroreceptor reflexes in these rats were more sensitive to increases in blood pressure. Our experiments were similar to those of Jackson and colleagues in a number of ways, including HR changes to the altered arterial pressure (AP) used to evaluate the BRS of the STZ-induced short-term DM rates used in both studies. As the variable factors above lead to different BRSs, yet were equal in these two studies, the identical changes of BRS testify to the reliability of our study. Of note, the authors examined the BRS in the conscious state rather than in the anesthetized state as we did in our study. Previous studies have used conscious animals because anesthesia inhibits the baroreflex function and causes difficulties in recording changes of the BRS under different stimuli[32, 33]. In our study, despite the possible inhibition of the baroreflex function caused by anesthesia, changes of the BRS were still obvious following various doses of injected PE and SNP. Furthermore, the comparison of our results with those of Jackson revealed that different states did not result in any evident discrepancies in BRS changes. Therefore, using anesthetized rats to evaluate the influence of fluvastatin on cardiac function and BRS is rational and clinically significant. Regardless of the unexpected ΔHR/ΔMABP changes, fluvastatin still decreased the ΔHR/ΔMABP increase back to the level of that in Ctr rats. Furthermore, the maximal HR responses to the maximal changes of MABP induced by various doses of PE or SNP were used as another indicator to estimate BRS. It can be concluded that fluvastatin could improve the significantly decreased maximal HR responses to the maximal changes of MABP in STZ-induced DM rats. According to recent reports, statins, including fluvastatin, exert a positive influence on the cardiovascular system not only by regulating blood lipids but also in a cholesterol-independent manner[34, 35]. Tawfik *et al* demonstrated that simvastatin, a drug similar to fluvastatin, prevented impaired coronary endothelial cell-dependent vasorelaxation in 4-week STZ-induced diabetic rats[36]. Moreover, statins up-regulated neuronal nitric oxide synthase (nNOS) expression in the rostral ventrolateral medulla (RVLM), a vasomotor center in the brainstem, down-regulated sympathetic nerve activity and achieved an improvement in the BRS[37]. The nNOS mechanism responded relatively quickly and led to an improved BRS after 30 d of fluvastatin treatment. As discussed above, the exact mechanism by which fluvastatin was able to improve impaired BRS requires further study.

In our study, fluvastatin significantly ameliorated the impaired cardiac function and BRS in STZ-induced type 1 DM rats. The results were consistent with previously observed positive effects of long-term fluvastatin treatment in patients with coronary heart disease or undergoing coronary intervention[38–40]. Because the parasympathomimetic activity reflected by the baroreflex activity in turn exerts an antiarrythmogenic effect counteracting the proarrhythmic effect of the sympathetic nervous system, the fluvastatin-ameliorated BRS can contribute to a reduction in cardiac mortality[38–41]. Undoubtedly, these findings will result in increased interest in the use of fluvastatin to treat diabetic patients with cardiac complications, and the mechanisms behind these effects deserve further study.

Acknowledgements

This study was financially supported by the National Natural Science Foundation of China (No 30870862), the Key Project of Natural Science Foundation of Heilongjiang Province (No ZJY0703-02), New Century Excellent Talents in University supported by the Ministry of Education of China (No NCET-08) and the Heilongjiang Postdoctoral Science Starting Foundation.

Author contribution

Jing AI, Li-hua SUN, and Bao-feng YANG designed the research and supervised the project; Fang XIE and Chao SUN established the diabetic model; Jing-yuan LI and Guan-yi LU measured food and drink intake; Chao SUN, Xin CHEN, and Hui CHE performed the animal studies, including the biochemical indexes of blood and the recording of blood pressure, HR and BRS; Jing AI, Fang XIE, and Chao SUN analyzed the data; Fang XIE and Jing AI wrote the manuscript; and Jing AI and Li-hua SUN revised the manuscript.

References

1 Rubler S, Dlugash J, Yuceoglu YZ, Kumral T, Branwood AW, Grishman A. New type of cardiomyopathy associated with diabetic glomerulosclerosis. Am J Cardiol 1972; 30: 595–602.
2 Vinik AI, Ziegler D. Diabetic cardiovascular autonomic neuropathy. Circulation 2007; 115: 387–97.
3 De Angelis K, Schaan BD, Maeda CY, Dall'Ago P, Wichi RB, Irigoyen MC. Cardiovascular control in experimental diabetes. Braz J Med Biol Res 2002; 35: 1091–100.
4 El-Menyar AA. Dysrhythmia and electrocardiographic changes in diabetes mellitus: pathophysiology and impact on the incidence of sudden cardiac death. J Cardiovasc Med (Hagerstown) 2006; 7: 580–5.
5 La Rovere MT, Pinna GD, Hohnloser SH, Marcus FI, Mortara A, Nohara R, *et al*. Baroreflex sensitivity and heart rate variability in the identification of patients at risk for life-threatening arrhythmias: implications of clinical trials. Circulation 2001; 103: 2072–7.
6 Endo A, Kuroda M, Tanzawa K. Competitive inhibition of 3-hydroxy-3-methylglutaryl coenzyme A reductase by ML-236A and ML-236B fungal metabolites, having hypocholesterolemic activity. FEBS Lett 1976; 72: 323–6.
7 Lawrence JM, Reckless JP. Fluvastatin. Expert Opin Pharmacother 2002; 3: 1631–41.
8 Christians U, Jacobsen W, Floren LC. Metabolism and drug interactions of 3-hydroxy-3-methylglutaryl coenzyme A reductase inhibitors in transplant patients: are the statins mechanistically similar? Pharmacol Ther 1998; 80: 1–34.
9 Corsini A, Bellosta S, Baetta R, Fumagalli R, Paoletti R, Bernini F. New insights into the pharmacodynamic and pharmacokinetic properties of statins. Pharmacol Ther 1999; 84: 413–28.
10 Corsini A, Jacobson TA, Ballantyne CM. Fluvastatin: clinical and safety profile. Drugs 2004; 64: 1305–23.
11 Perreault S, Hamilton VH, Lavoie F, Grover S. A head-to-head comparison of the cost effectiveness of HMG-CoA reductase inhibitors and fibrates in different types of primary hyperlipidemia. Cardiovasc Drugs Ther 1997; 10: 787–94.
12 Bellosta S, Ferri N, Arnaboldi L, Bernini F, Paoletti R, Corsinin A. Pleiotropic effects of statins in atherosclerosis and diabetes. Diabetes Care 2000; 23: B72–8.
13 Armpatzis CA, Goedhart D, Serruys PW, Saia F, Lemos PA, de Feyter P. Fluvastatin reduces the impact of diabetes on long-term outcome after coronary intervention — a Lescol Intervention Prevention Study (LIPS) substudy. Am Heart J 2005; 149: 329–35.
14 Matsuki A, Nozawa T, Igarashi N, Sobajima M, Ohori T, Suzuki T, *et al*. Fluvastatin attenuates diabetes-induced cardiac sympathetic neuropathy in association with a decrease in oxidative stress. Circ J 2010; 74: 468–75.
15 Imaeda A, Aoki T, Kondo Y, Hori M, Ogata M, Obayashi H, *et al*.

Protective effects of fluvastatin against reactive oxygen species induced DNA damage and mutagenesis. Free Radic Res 2001; 34: 33–44.

16 Ai J, Yan X, Zhao L, Lu Y, Liang F, Cai B, *et al*. The protective effect of Daming capsule on heart function in streptozocin-induced diabetic rats with hyperlipidemia. Biol Pharm Bull 2009; 32: 1354−8.

17 Ai J, Liang F, Zhou H, Zhao J, Wang N, Zhu S, *et al*. Mechanism of impaired baroreflex sensitivity in Wistar rats fed a high-fat and -carbohydrate diet. Br J Nutr 2010; 104: 291–7.

18 Lin M, Liu R, Gozal D, Wead WB, Chapleau MW, Wurster R, *et al*. Chronic intermittent hypoxia impairs baroreflex control of heart rate but enhances heart rate responses to vagal efferent stimulation in anesthetized mice. Am J Physiol Heart Circ Physiol 2007; 293: H997–1006.

19 Patel KP, Zhang PL. Baroreflex function in streptozotocin (STZ) induced diabetic rats. Diabetes Res Clin Pract 1995; 27: 1–9.

20 Lin M, Ai J, Harden SW, Huang C, Li L, Wurster RD, *et al*. Impairment of baroreflex control of heart rate and structural changes of cardiac ganglia in conscious streptozotocin (STZ)-induced diabetic mice. Auton Neurosci 2010; 155: 39–48.

21 Dall'ago P, D'Agord Schaan B, da Silva VO, Werner J, da Silva Soares PP, de Angelis K, *et al*. Parasympathetic dysfunction is associated with baroreflex and chemoreflex impairment in streptozotocin-induced diabetes in rats. Auton Neurosci 2007; 131: 28–35.

22 Meyrelles SS, Mauad H, Mathias SC, Cabral AM, Vasquez EC. Effects of myocardial hypertrophy on neural reflexes controlling cardiovascular function. J Auton Nerv Syst 1998; 73: 135−42.

23 Itagaki M, Takaguri A, Kano S, Kaneta S, Ichihara K, Satoh K. Possible mechanisms underlying statin-induced skeletal muscle toxicity in L6 fibroblasts and in rats. J Pharamacol Sci 2009; 109: 94−101.

24 Basic-Jukic N, Kes P, Bubic-Filipi L, Vranjican Z. Rhabdomyolysis and acute kidney injury secondary to concomitant use of fluvastatin and rapamycin in a renal transplant recipient. Nephrol Dial Transplant 2010; 25: 2036; author reply 2036–7.

25 Chang KS, Lund DD. Alterations in the baroreceptor reflex control of heart rate in streptozotocin diabetic rats. J Mol Cell Cardiol 1986; 18: 617–24.

26 Homma S, Yamazaki Y, Karakida T. Blood pressure and heart rate relationships during cervical sympathetic and vagus nerve stimulation in streptozotocin diabetic rats. Brain Res 1993; 629: 342–4.

27 Cohen AJ, McCarthy DM, Rossetti RR. Renin secretion by the spontaneously diabetic rat. Diabetes 1986; 35: 341–6.

28 Dall'Ago P, Fernandes TG, Machado UF, Belló AA, Irigoyen MC. Baroreflex and chemoreflex dysfunction in streptozotocin-diabetic rats. Braz J Med Biol Res 1997; 30: 119–24.

29 Maeda CY, Fernandes TG, Lulhier F, Irigoyen MC. Streptozotocin diabetes modifies arterial pressure and baroreflex sensitivity in rats. Braz J Med Biol Res 1995; 28: 497–501.

30 Heistad DD, Abboud FM, Mark AL, Schmid PG. Interaction of baroreceptor and chemoreceptor reflexes. Modulation of the chemoreceptor reflex by changes in baroreceptor activity. J Clin Invest 1974; 53: 1226–36.

31 Jackson CV, Carrier GO. Influence of short-term experimental diabetes on blood pressure and heart rate in response to norepinephrine and angiotensin II in the conscious rat. J Cardiovasc Pharmacol 1983; 5: 260–5.

32 Shimokawa A, Kunitake T, Takasaki M, Kannan H. Differential effects of anesthetics on sympathetic nerve activity and arterial baroreceptor reflex in chronically instrumented rats. J Auton Nerv Syst 1998; 72: 46–54.

33 Van Leeuwen AF, Evans RG, Ludbrook J. Effects of halothane, ketamine, propofol and alfentanil anaesthesia on circulatory control in rabbits. Clin Exp Pharmacol Physiol 1990; 17: 781–98.

34 Maron DJ, Fazio S, Linton MF. Current perspectives on statins. Circulation 2000; 101: 207–13.

35 Liao JK. Isoprenoids as mediators of the biological effects of statins. J Clin Invest 2002; 110: 285–8.

36 Tawfik HE, El-Remessy AB, Matragoon S, Ma G, Caldwell RB, Caldwell RW. Simvastatin improves diabetes-induced coronary endothelial dysfunction. J Pharmacol Exp Ther 2006; 319: 386–95.

37 Gao L, Wang W, Zucker IH. Simvastatin inhibits central sympathetic outflow in heart failure by a nitric-oxide synthase mechanism. J Pharmacol Exp Ther 2008; 326: 278–85.

38 Ballantyne CM, Riegger G, Moore N, Saia F, Serruys PW. Fluvastatin reduces cardiac mortality in patients with coronary heart disease. Cardiovasc Drugs Ther 2004; 18: 67–75.

39 Riegger G, Abletshauser C, Ludwig M, Schwandt P, Widimsky J, Weidinger G, *et al*. The effect of fluvastatin on cardiac events in patients with symptomatic coronary artery disease during one year of treatment. Atherosclerosis 1999; 144: 263–70.

40 Serruys PW, de Feyter P, Macaya C, Kokott N, Puel J, Vrolix M, *et al*. Fluvastatin for prevention of cardiac events following successful first percutaneous coronary intervention: a randomized controlled trial. JAMA 2002; 287: 3215–22.

41 Serruys PW, De Feyter PJ, Benghozi R, Hugenholtz PG, Lesaffre E. The Lescol(R) Intervention Prevention Study (LIPS): a double-blind, placebo-controlled, randomized trial of the long-term effects of fluvastatin after successful transcatheter therapy in patients with coronary heart disease. Int J Cardiovasc Intervent 2001; 4: 165–72.

Acta Pharmacologica Sinica (2011) 32: 329–337
© 2011 CPS and SIMM All rights reserved 1671-4083/11 $32.00
www.nature.com/aps

Original Article

Generation and characterization of the human neutralizing antibody fragment Fab091 against rabies virus

Chen LI[1, 3, 4], Feng ZHANG[1, 3], Hong LIN[1], Zhong-can WANG[2], Xin-jian LIU[1], Zhen-qing FENG[1, 3], Jin ZHU[1, 2, *], Xiao-hong GUAN[1, *]

[1]Key Laboratory of Antibody Technique of Ministry of Health, Nanjing Medical University, Nanjing 210029, China; *[2]Huadong Medical Institute of Biotechniques, Nanjing 210002, China*; *[3]Department of Pathology, Nanjing Medical University, Nanjing 210029, China*; *[4]Department of Pathology, the Affiliated Hospital of Xuzhou Medical College, Xuzhou 221002, China*

Aim: To transform the human anti-rabies virus glycoprotein (anti-RABVG) single-chain variable fragment (scFv) into a Fab fragment and to analyze its immunological activity.
Methods: The Fab gene was amplified using overlap PCR and inserted into the vector pComb3XSS. The recombinant vector was then transformed into *E coli* Top10F′ for expression and purification. The purified Fab was characterized using SDS-PAGE, Western blotting, indirect ELISA, competitive ELISA, and the fluorescent antibody virus neutralization test (FAVN), respectively, and examined in a Kunming mouse challenge model *in vivo*.
Results: A recombinant vector was constructed. The Fab was expressed in soluble form in *E coli* Top10F′. Specific binding of the Fab to rabies virus was confirmed by indirect ELISA and immunoprecipitation (IP). The neutralizing antibody titer of Fab was 10.26 IU/mL. The mouse group treated with both vaccine and human rabies immunoglobulin (HRIG)/Fab091 (32 IU/kg) showed protection against rabies, compared with the control group ($P<0.05$, Logrank test).
Conclusion: The antibody fragment Fab was shown to be a neutralizing antibody against RABVG. It can be used together with other monoclonal antibodies for post-exposure prophylaxis of rabies virus in future studies.

Keywords: rabies; Fab engineered antibody; neutralizing antibodies

Acta Pharmacologica Sinica (2011) 32: 329–337; doi: 10.1038/aps.2010.209; published online 31 Jan 2011

Introduction

Rabies is one of the most fatal central nervous system diseases and is a threat to humans and other mammals. The rabies virus (RABV) belongs to the *Rhabdoviridae* family and constitutes the prototype of the lyssa viruses[1]. Rabies kills more than 50000 people and millions of animals worldwide every year[2]. The progress of infection is rapid, and the mortality rate is nearly 100%. The glycoprotein of the rabies virus (RABVG) has been studied extensively for many years. It is a crucial protein for determining the neurovirulent nature of the rabies virus and is an important antigen for inducing protective immunity[3]. Among the different antibodies elicited after immunization, neutralizing antibodies specific to the RABVG are thought to provide protection[4]. We screened out a human anti-RABVG single-chain variable fragment (scFv) from an immune phage antibody library[5]. Based on the discrepancies between the native conformations of scFv and IgG, if the scFv was shown to be a neutralizing antibody, we would not consider the IgG, for scFv having the same neutralizing activity. In addition, the small molecular weight, short half-life, and expression type of the inclusion body also restrained the therapeutic application of the scFv[6].

In the present study, the scFv was transformed into a Fab fragment with a larger molecular weight and longer half-life. Fab has the same native conformation as IgG. Accordingly, exploration of the immunological activity of Fab will be helpful in preparing the human IgG. In this study, we transformed the human anti-RABVG scFv into a Fab fragment and to analyze its immunological activity.

Materials and methods

The rabies virus strain CTN was provided by the Wuhan

---

*To whom correspondence should be addressed.
E-mail zjsimmons@yahoo.com.cn (Jin ZHU);
xhguan@163.com (Xiao-hong GUAN)
Received 2010-05-31 Accepted 2010-11-14

Institute of Biologic Products, Wuhan, China. The rabies virus strains (CVS-11 and CVS-24) and BHK-21 cells were obtained from the Veterinary Institute of the Academy of Military Medical Sciences, Changchun, China. The XL1-Blue and Top10F′ *Escherichia coli* strains were obtained from the Medical Research Council, Lab of Molecular Biology, University of Cambridge, Cambridge, UK. The plasmids pComb3XSS and pComb3Xλ were obtained from the Barbas Laboratory, TSRI, La Jolla, CA, USA. The horseradish peroxidase-conjugated goat anti-human IgG (Fab specific) was obtained from Sigma, St Louis, MO, USA. The competitive ELISA kit (20080526) was purchased from the Veterinary Institute of the Academy of Military Medical Sciences, Changchun, China. The Kunming mice were provided by the Medical College of Jilin University, Changchun, China. In addition, all the *in vivo* experiments were approved by the Ethics Committee on Laboratory Animals of Nanjing Medical University.

Construction of human anti-RABV antibody Fab fragment

The human V_H and V_L genes were amplified from the anti-RABVG scFv plasmid by PCR. The forward primer of V_H was V_HF: 5′-*GCTGCCCAACCAGCCATGGCC*CAGGTGCAGCTGGTGCAGTCTGG-3′, which contained 21 complementary bases to the reverse primer of human IgG1 C_L (italicized). The reverse primer of V_H was V_HR: 5′-*CGATGGGCCCTTGGTGGAGGC*TGAGGAGACGGTGACCAGGGTTCC-3′, which contained 21 complementary bases to the forward primer of human IgG1 C_H1 (italicized) for overlap PCR. The V_L gene was amplified using the forward primer V_LF: 5′-GGGCCCAGGCGGCCCAGTCTGCCCTGACTCAGCCTCGCTCAGTGTCCGGG-3′, which contained the restriction endonuclease *Sfi* I site (underlined), and the reverse primer V_LR: 5′-*CGAGGGGGCAGCCTTGGGCTG*ACCTAGGACGGTCAGCTTGGTCCCTCCGCCGAAAACCAC-3′, which contained 21 complementary bases to the forward primer of human IgG1 C_L (italicized) for overlap PCR. The human IgG constant domains C_H1 and C_L were amplified from a recombinant vector pComb3Xλ. The PCR conditions were repeated for 25 cycles at 94 °C for 30 s, 60 °C for 30 s, and 72 °C for 1 min, followed by a final extension time of 10 min at 72 °C. The genes of C_H1 (human IgG1) and V_H were used as templates for generation of the Fd fragment by overlap PCR with a pair of primers — FdF: 5′-GCTGCCCAACCAGCCATGGCCCTCGAGGTGAAGCTGGTGGAGTC-3′ and FdR: 5′-AGAAGCGTAGTCCGGAACGTC-3′. The assembly of V_H and C_H1 was performed by PCR for 15 cycles of 94 °C for 15 s, 56 °C for 15 s, and 72 °C for 2 min, followed by a final extension time of 10 min at 72 °C. Similarly, human C_L and V_L fragments were joined to generate the light chain with the pair of primers LF: 5′-GGGCCCAGGCGGCCGAGCTCGACATTGTGATGCACAGTC-3′ and LR: 5′-GGCCATGGCTGGTTGGGCAGC-3′. In the third round of PCR, the Fd and L chains were mixed in equal parts to generate the overlap full-length Fab products. The conditions for PCR was 6 cycles without primers at 94 °C for 50 s, 56 °C for 30 s, 72 °C for 3 min, and then 20 cycles with a pair of human primers — FabF: 5′-GGGCCCAGGCGGCCGAGCTCGACATTGTGATGACACAGTC-3′ and FabR: 5′-AGAAGCGTAGTCCGGAACGTC-3′ [7].

Construction of recombinant plasmid

A phagemid pComb3XSS was used for expression of the Fab fragment[8]. The vector pComb3XSS and the Fab fragments were digested by the restriction endonuclease *Sfi* I (New England Biolabs, Ipswich, MA, USA)[9, 10] and ligated to create recombinants. The recombinants were transformed into competent *E coli* XL1-Blue cells by standard chemical methods ($CaCl_2$/heat shock)[11]. After overnight incubation, the clones were checked for the presence of the insert by colony PCR and DNA sequencing.

Expression and purification of Fab fragment

The recombinant phagemid, which was confirmed to contain the correct sequence by DNA sequencing, was transformed into *E coli* Top10F′ for expression by way of soluble protein expression[12]. The cells were harvested by centrifugation, and the cell pellet was suspended in PBS. The periplasmic extract was obtained by sonication and centrifugation of the suspended products. Twenty microliters of the samples were used for denaturing polyacrylamide gel analysis. The gels were analyzed by staining with Coomassie blue and Western blotting. The Fab fragment was purified from the supernatant (150 mL) by affinity chromatography using a HisTrap HP column (1 mL, GE Healthcare, Piscataway, NJ, USA) with a flow rate of 1 mL/min. The binding buffer was 20 mmol/L of phosphate buffer (pH 7.4) with 20 mmol/L imidazole and 500 mmol/L NaCl. The Fab was eluted using 20 mmol/L phosphate buffer (pH 7.4) with imidazole at different concentrations (50, 100, 200, 300, 400, and 500 mmol/L). The eluted Fab fractions were concentrated using an Amicon Ultra centrifugal filter device (10 kDa cut-off, Millipore, Bedford, MA, USA) and dissolved in PBS. The purified Fab fragment was named Fab091.

SDS-PAGE and Western blot analysis

The purified Fab091 fragment was resolved by 12% SDS-PAGE under reducing conditions with β-mercaptoethanol (β-ME). For Western blot analysis, Fab091 was detected by HRP-conjugated goat anti-human IgG (1:2000), and the blot was developed using the DAB/H_2O_2 system.

Antigen binding assays for Fab091

Indirect ELISA

A 96-well microplate (Costar, Washington, DC, USA) was coated with 2 μg/mL of rabies virus strain CTN. The Fab091 fragment (0.2 mg/mL) and *E coli*-negative supernatant was added to antigen-coated wells in serial two-fold dilutions (1:5, 1:10, 1:20, 1:40, 1:80, 1:160, 1:320, and 1:640), and bound antibodies were detected by HRP-conjugated goat anti-human IgG (1:5000). Each sample had two duplicate wells. PBS was used as a blank control, and its OD_{450} value was assigned as 0.

Competitive ELISA (C-ELISA) of Fab091 and scFv

Fab091 (0.5 mg/mL) was added into a 96-well microplate plate coated with RABV. Then the original anti-RABVG scFv was added at dilution ratios of 1:1, 1:5, 1:25, and 1:125 and incubated in these wells for 1 h at room temperature. After washing five times with PBST (20 mmol/L PBS, 0.05% Tween 20), HRP-conjugated mouse anti-human IgG (Fab specific) was added to the wells and incubated for 1 h at room temperature. An anti-Met scFv antibody[13] was used as a negative control in lieu of anti-RABVG scFv, and the blank control lacked scFv. The final results were expressed as percentages of inhibition (PI). The PI values for the Fab091 were calculated with the following formula:

$$PI = 1–(OD_b–OD_s)/OD_b×100\%$$

(s: sample, b: blank control)

A competitive ELISA kit was used to detect the neutralizing titer of Fab091. For the ELISA, the standard serum was obtained from volunteers who had been inoculated with rabies vaccine. The titers of neutralizing antibodies in the serum were detected by the FAVN method, and the serum was diluted to 0.25, 0.5, 1.0, 2.0, 4.0, and 8.0 IU/mL. The neutralizing antibodies in the ELISA were murine monoclonal antibodies against RABVG conjugated with horseradish peroxidase. One hundred microliters of HRP-conjugated antibodies against RABVG were mixed with 100 μL of different titers of standard serum (0.25, 0.5, 1.0, 2.0, 4.0, and 8.0 IU/mL) and added to a RABVG-coated ELISA microplate. Meanwhile, 100 μL of HRP-conjugated antibodies and 100 μL of Fab091 were mixed in the coated microplate. Every sample had two duplicate wells. Following incubation for 45 min at 37 °C, the plates were washed, and a tetramethylbenzidine (TMB) substrate solution was added. After incubation for 15 min at 37 °C, the reaction was stopped by adding 2.0 mol/L sulfuric acid, and the OD_{450} was measured by a Multiskan Spectrum Microplate Photometer. The neutralizing antibody titer of Fab091 was calculated according to the OD_{450} values and the titers of the standard samples[14, 15].

Immunoprecipitation (IP) and mass spectrometry (MS)

A mixture of 20 μL of Fab091 and 40 μL of CTN was resuspended in 1 mL of PBS and incubated for 1 h at 4 °C. Protein G magnetic beads (30 μL) were added to the mixture for immunoprecipitation (IP). The mixture was whirled gently and incubated with agitation at 4 °C for 12 h. The beads were collected by centrifugation at 4000×*g* for 5 min and then washed three times with PBS. The supernatant was removed. Finally, the beads were resuspended with loading buffer and boiled, and the proteins were resolved by 12% SDS-PAGE. The resolved proteins were transferred onto a nitrocellulose membrane and detected by Rab-50 (sc-57994, Santa Cruz, CA, USA), which is a mouse monoclonal anti-RABVG antibody. After blocking in 5% milk in PBST for 30 min and washing three times with PBST, the membrane was incubated with the HRP-conjugated goat anti-mouse IgG (Sigma, St Louis, MO, USA). Finally, the blot was developed using the DAB/H_2O_2 system. The band that corresponded to the blot (67 kDa) on a separate polyacrylamide gel stained with Coomassie blue was analyzed by mass spectrometry (MS). Detected spots were excised from the gels, which were stained with Coomassie Brilliant blue. The gel chips were excised and destained with a solution containing 100 mmol/L NH_4HCO_3 and 50% ethane nitrile (pH 8.0). After hydrating with ethane nitrile and drying, the gel chips were hydrated in a minimal volume of trypsin (Promega Corporation, Madison, WI, USA) solution and incubated at 37 °C overnight. The gel pieces were extracted with 50% acetonitrile/2.5% trifluoroacetic acid at 37 °C for one hour with sonication, and the supernatant was removed. The extraction was repeated twice. A gel slice was dissolved in 0.1% trifluoroacetic acid (Sigma, St Louis, MO, USA), desalted, and concentrated using ZipTips (Millipore, Bedford, MA, USA). The peptide solution (0.5 μL) was mixed with 0.5 μL of matrix (5 mg/mL α-cyano-4-hydroxycinnamic acid in 30% acetonitrile/0.1% TFA), spotted on a target disk, and allowed to air-dry. Samples were analyzed by MS (Bruker Daltonics, Leipzig, Germany). Protein database searching was performed with the MASCOT search engine (http://www.matrix science.com; Matrix Science, UK)[16].

Affinity analysis by surface plasmon resonance (SPR)

SPR was performed on a BIAcore T100 (GE, Piscataway, NJ, USA) analytical system. RABV was diluted to 5 μg/mL with acetate buffer (10 mmol/L sodium acetate, pH 5.5, GE, Piscataway, NJ, USA) and immobilized on the surface of a CM5 sensor chip (GE, Piscataway, NJ, USA) to capture purified Fab091. Fab091 was diluted by HBS-EP buffer (GE, USA) at concentrations ranging from 31.25 to 1000 nmol/L and performed at a constant flow rate of 30 μL/min for 3 min at 25 °C. The association time was 180 s, and the dissociation time was 600 s. The constants for association (k_a) and dissociation rate (k_d) and the equilibrium constant for dissociation (K_D, $K_D=k_d/k_a$) were obtained using global fittings from the Langmuir binding model (1:1 binding model). The sensor grams were evaluated using the BIAcore T100 evaluation software (GE, Piscataway, NJ, USA).

Detection of Fab091 neutralizing activity

To perform the FAVN test, BHK-21 cells and the RABV strain CVS-11 were used. The positive control serum against RABV was obtained from adult dogs vaccinated with rabies vaccine. The neutralizing antibody titers were determined by the Weybridge Laboratory (UK), a rabies reference laboratory of OIE, the World Organization for Animal Health. The serum was then diluted to 0.5 IU/mL and used as a standard serum. Serial three-fold dilutions of the positive and negative control sera and the Fab091 were made in 100-μL volumes in microplate wells. Each sample was added to four adjacent wells and serially diluted five times using a multichannel pipette. Fifty-microliter challenge virus suspensions containing 100 $TCID_{50}$ were added to each well. The microplates were incubated for one hour at 37 °C in a humidified incubator with 5% CO_2. Following incubation, $2×10^4$ BHK-21 cells in 50 μL of culture medium were added to each well, and the plates were incubated for another 48 h. Thereafter, the medium was discarded, and the plates were rinsed in PBS (pH 7.2) and in acetone (80% in distilled water). The plates were then fixed in 80% acetone for 30 min at room temperature and air-dried. The staining was carried out by adding 50 μL of fluorescein-isothiocyanate-conjugated anti-rabies serum. After incubation for 30 min at 37 °C, the plates were washed twice with PBS. The FAVN result was assessed with a fluorescence microscope (image A.l; Zeiss, Germany). The total area of each well was examined. The well was considered positive if one or more fluorescent cells were observed; otherwise, it was considered negative. The 50% endpoint of the antibody (D_{50}) content of the test sample and virus titers (TCID$_{50}$) were calculated according to the Spearman-Karber method[17]. The neutralizing titer of Fab091 was calculated based on the number of negative wells and their dilutions, compared with those of the standard serum included in the test[18].

Animals and inoculation

A lethal animal model mimicking rabies exposure was used as described elsewhere[19–21]. The mice were treated as described in Table 1. Four-week-old pathogen-free Kunming mice (10–12 g, 8 mice/group, 9 groups) were infected with 100 LD$_{50}$/0.05 mL CVS-24 on d 0 and d 7. The mice were inoculated in the hind limb with rabies vaccine (Sanofi-PASTEUR SA, France). In addition, human rabies immunoglobulin (HRIG, Taibang Health, Taian, China) at 20 IU/kg and Fab091 (treated with 32, 20, 8, 2, and 0.5 IU/kg) were administered on d 0. The mice were evaluated for 28 d for clinical signs of neurology and death. In the control group, the mice were injected with 100 LD$_{50}$/0.05 mL of the CVS-24 strain. The experiments using the CVS-24 strain were performed in a Biosafety Level 3 Laboratory (BSL-3)[22].

Table 1. Rabies virus postexposure prophylactic trial.

Treatment	Vacc	Fab091+vacc					Fab091	HRIG+ vacc	PBS
dose	A	B	C	D	E	F	G	H	I
(IU/kg)	0	0.5	2	8	20	32	20	20	0
Virus	+	+	+	+	+	+	+	+	+
Vaccine	+	+	+	+	+	+	–	+	–
Fab091	–	+	+	+	+	+	+	–	–
HRIG	–	–	–	–	–	–	–	+	–
PBS	–	–	–	–	–	–	–	–	+

+, disposed; –, undisposed; HRIG, human rabies immunoglobulin; PBS, phosphate-buffered saline.

Statistical analysis

Kaplan-meier method was used for survival analysis of Kunming mice after rabies virus challenge. Statistical analyses were performed with SPSS 11.5 statistical software package (SPSS Inc, Chicago, IL, USA). A *P* value <0.05 was accepted as statistically significant.

Results

Amplification of the human anti-RABV antibody Fab gene fragment and construction of the expression vector

The human anti-RABV antibody Fab gene fragment was amplified in three rounds of PCR, as described in Materials and methods. The cloning strategy is shown in Figure 1.

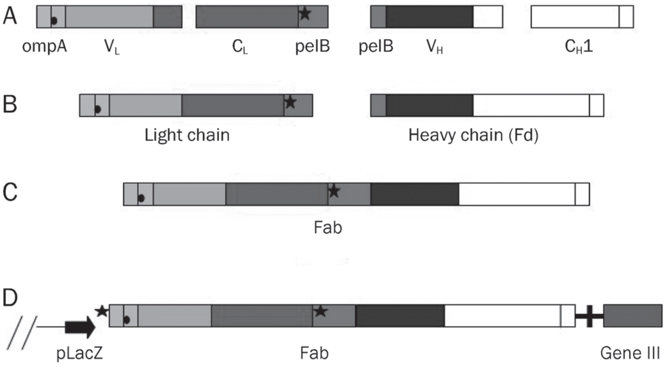

Figure 1. Construction of plasmid pComb3XSS-Fab for the production of Fab antibody fragments in *E coli*. Genes of light-chain and heavy-chain Fd fragments were fused by overlap-extension PCR, and cloned directionally by using two asymmetric sites of the rare cutter *Sfi* I. Fab was transcribed as a single transcript under the control of one LacZ promoter. The amber stop codon (cross) between the antibody genes and bacteriophage gene III enables the production of soluble Fab fragments in a non suppressor strain of *E coli*. (A) The genes for the variable and constant regions were amplified separately. (B) Heavy-chain Fd and light chain DNA were assembled by variable regions and their constant counterpart respectively by using overlap PCR. (C) Fd and light chain were fused to form Fab-encoding sequences by overlap PCR. Fab genes were directionally cloned into pComb3XSS phagemid by using the *Sfi* I site. (D) Both L chain fragment and Fd fragment were transported to the periplasm of *E coli*.

Purification and detection of soluble Fab fragment

Purified Fab091 was resolved by 12% SDS-PAGE under reducing conditions. Both the Fd (34 kDa) and L chains (26 kDa) were detected in the monomeric form (Figure 2A). The expression of Fab091 was confirmed using Western blotting (Figure 2B).

Specific binding of Fab091 fragment to RABV

Binding of the Fab091 fragment to RABV was detected by indirect ELISA as shown in Figure 3. The OD_{450} values showed a gradient change that was accompanied by a decreasing concentration of Fab091.

In the competitive ELISA, as shown in Figure 4A, the PI of Fab091 ranged from 73.65% to 11.83% concomitant with the decreasing concentration of scFv. Less than 10% inhibition was observed for the anti-Met scFv negative control.

A standard curve for the competitive ELISA is shown in Figure 4B. The range of the standard curve was 0 to 8 IU/mL. If the OD_{450} value was between 0 to 8 IU/mL, the neutralizing antibody titers could be read from the curve. In Figure 4B, the titers of standard serum decreased with increasing OD_{450} val-

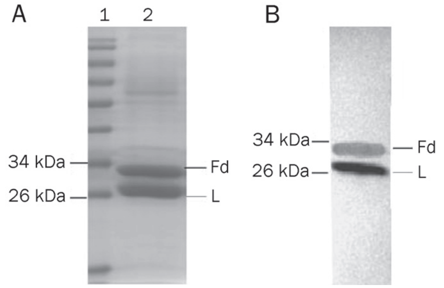

Figure 2. SDS-PAGE and Western blot of the purified Fab091 fragment after purification. The purified Fab091 was resolved in 12% SDS-PAGE under reducing conditions and stained with Coomassie blue. The heterodimer was dissociated into light chain (26 kDa) and Fd (34 kDa). (A) Lane 1: protein marker (#0671, Fermantas, Burlington, Ontario, Canada); Lane 2: the purified Fab091 fragment. (B) Electrobloted Fab091 fragments were detected by goat anti-human IgG-HRP conjugate (1:2000 dilution).

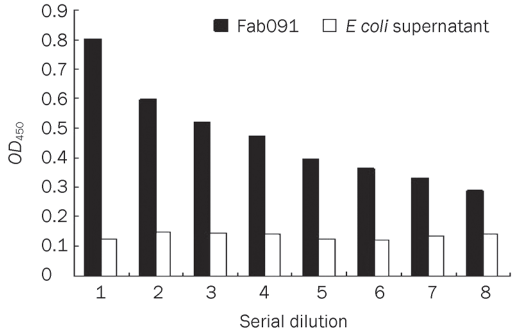

Figure 3. Indirect ELISA of the different dilutions of Fab091 fragment. The ELISA plate was coated with rabies virus strain CTN at 2 μg/mL. (1–8): The virus reacted with Fab091 which was in serial two-fold dilution (1:5, 1:10, 1:20, 1:40, 1:80, 1:160, 1:320, and 1:640) and incubated for 2 h at room temperature. *E coli* Top10F′ supernatant was used as control. The plate was washed five times with PBST, followed by incubation with goat anti-human IgG HRP-conjugated (1:5000).

ues. The OD_{450} of the test sample was 1.022, so the result was negative.

IP was also used for the detection of the specific binding of Fab to the rabies virus strain CTN (Figure 5A). Four peptide sequences (Table 2) matched with RABVG by MS analysis (Figure 5B) were found when the identified peptides were compared with the known sequences of RABVG in the SWISS PROT database. Mass tolerance was allowed within 0.05%.

Table 2. Amino-acid residue sequences of matched peptides.

	Relative intensity	Amino-acid residue
1	983.431	TCGFVDER
2	1070.575	STQHGLGGTGR
3	2118.972	YEESLHNPYPDYHWLR
4	2708.251	YVLMSAGVLIALMLTIFLMTCCR

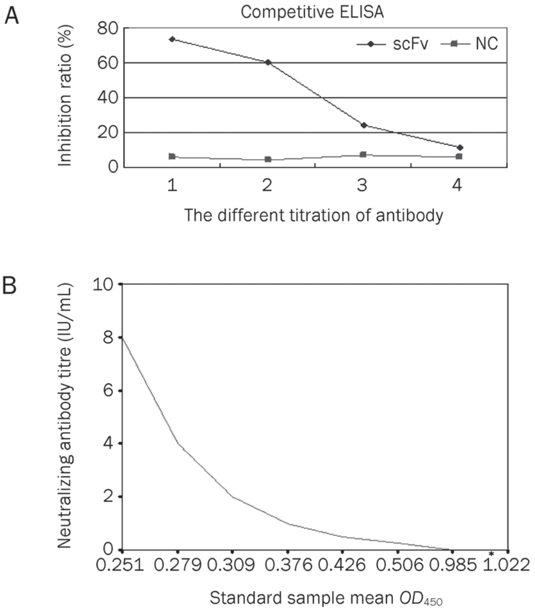

Figure 4. Competitive ELISA detection. (A) The rabies virus strain CTN was used as coated antigen for Competitive ELISA of scFv and Fab091. (1–4): The scFv was diluted to 1:1, 1:5, 1:25, 1:125, and incubated with Fab091. PI of Fab091 ranged from 73.65% to 11.83% (73.65%, 60%, 24.95%, and 11.83%) with decreasing concentration of scFv. Less than 10% inhibition was observed for negative anti-Met scFv. (B) Standard curve for Competitive ELISA: The 96-well microplate was coated with RABVG. HRP-conjugated antibodies against RABVG were mixed with different titers of standard serum (0.25, 0.5, 1.0, 2.0, 4.0, and 8.0 IU/mL). Meanwhile, HRP-conjugated antibodies and Fab091 were mixed in the coated microplate and incubated. The mean OD_{450} value of Fab091 well was 1.022, according to the standard curve ranging from 0 to 8 IU/mL, so the corresponding titre was 0.

Protein matching with a MASCOT score of >69 was considered statistically significant ($P<0.05$).

Affinity assay of Fab091

The binding affinities between rabies protein and purified Fab091 were analyzed by Biacore T100 (GE, Piscataway, NJ, USA). Fab091 had a high affinity with a K_D of 6.268E-10 M. (χ^2=1.09, U=5). The interaction between Fab091 and rabies virus is shown in Figure 6.

Neutralizing activity of Fab091

In the FAVN, no fluorescence was seen in the wells until the standard serum was diluted nine times. There were still two negative wells when the serum concentration was at 1:27 dilution. For the test sample Fab091, no fluorescence was seen until the wells were diluted to 1:81 (12 μg/mL). There was only one negative well at 1:243 dilution. According to the dilution rates and the total number of negative wells, compared with the standard serum (0.5 IU/mL), the neutralizing antibody titer of Fab091 was calculated to be 10.26 IU/mL.

Activity identification *in vivo*

The number of deaths observed in Kunming mice after infec-

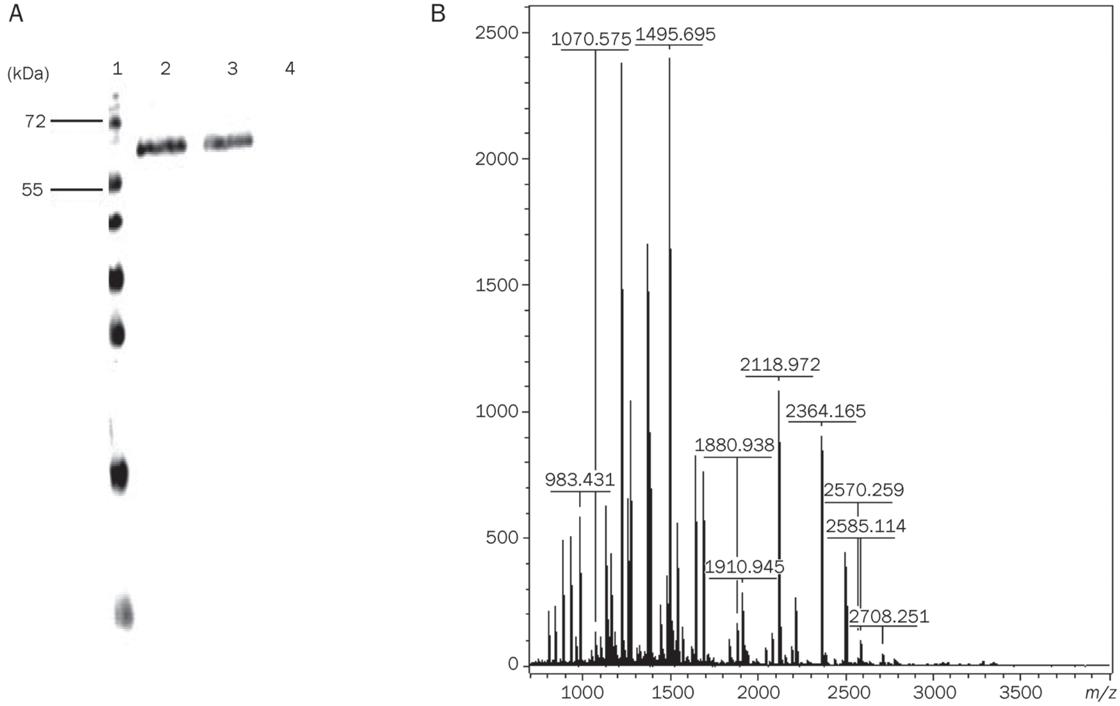

Figure 5. IP and MS analysis of RABVG. (A) Proteins immunoprecipitated by Fab091 were separated by SDS-PAGE and probed with RAB-50 by Western blot. (1): Protein marker; (2–3): One protein was recognized by RAB-50. The molecular weight of the protein was about 67 kDa. (4): BHK-21 lysate was used as the negative control to replace Fab091 in the IP. (B) The corresponding 67 kDa band on the polyacrylamide gel was analyzed by mass spectrometry, which was identified as RABVG. MS spectrums of fragment ions were from the 67 kDa protein. Four major (*m/z*=983.431, 1070.575, 2118.972, 2708.251) ions were detected.

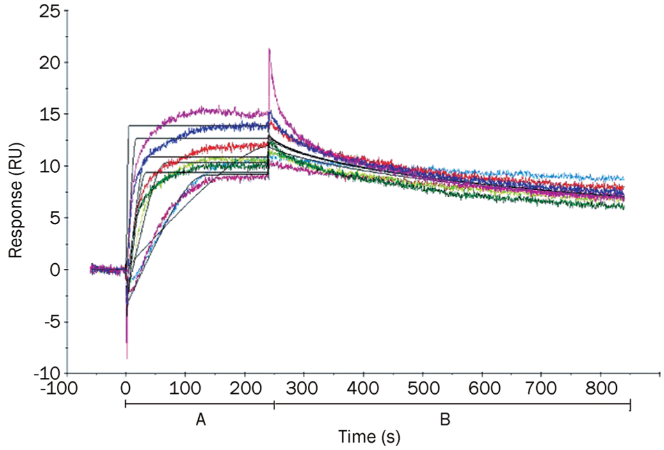

Figure 6. SPR analysis of Fab091 and rabies virus interaction. Fab091 (1 mg/mL) was subjected to SPR analysis. CM5 sensor chip was activated by the injection of 1-ethyl-3-(3-dimethylaminopropyl)-carbodiimide hydrochloride (EDC)/*N*-hydroxysuccinimide (NHS). Rabies virus was coated on the CM5 chip, and the surface was washed with 10 mmol/L HEPES (pH 7.4) for 200 s and then Fab091 was injected. Dilution rates of Fab091 were 31.25, 62.5, 125, 250, 500, 1000 nmol/L (Chi^2=1.09, U=5, R_{max}=13.05 RU). (A) Association stage; (B) Dissociation stage.

tion with CVS-24 at 28 d is shown in Table 3, and a survival curve is shown in Figure 7 for the Kunming mice, according to the Kaplan-Meier method. A survival rate of 12.5% (1/8) was observed in the group with CVS-24 infection. A survival rate of 25% (2/8) was observed in the control group, which

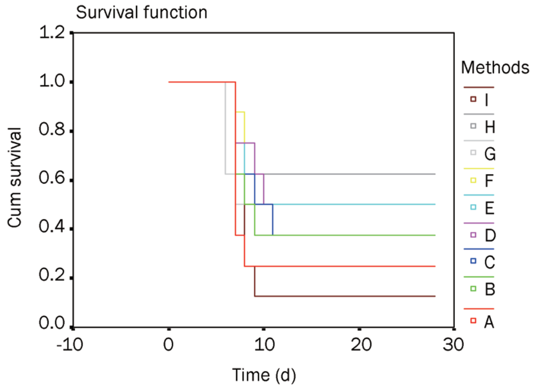

Figure 7. Kaplan-Meier survival curve for Kunming mice after rabies virus challenge. Mice (*n*=8 per group) were challenged with CVS-24 strain on d 0. Three hours later (d 0), the mice in treatment groups were inoculated with rabies vaccine and treated either with 32, 20, 8, 2, 0.5 IU/kg Fab091 or 20 IU/kg HRIG. The treatment groups also included 20 IU/kg Fab91 group. The mice in control groups received only PBS. The mice were evaluated twice daily and were sacrificed when neurological signs appeared. Kaplan-Meier survival curves were shown for d 0 to d 28. (A) Vaccine; (B) Vaccine+0.5 IU/kg Fab091; (C) Vaccine+2 IU/kg Fab091; (D) Vaccine+8 IU/kg Fab091; (E) Vaccine+20 IU/kg Fab091; (F) Vaccine+32 IU/kg Fab091 (*P*<0.05, Logrank test); G: 20 IU/kg Fab091; H: Vaccine+20 IU/kg HRIG (*P*<0.05, Logrank test); I: PBS.

Table 3. Deaths of Kunming mice after infected with CVS-24 in 28 d.

	Vaccine	Fab091+vaccine					Fab091	HRIG+vaccine	PBS
Days	A	B	C	D	E	F	G	H	I
	0	0.5	2	8	20	32	20	20	0
0	0	0	0	0	0	0	0	0	0
1	0	0	0	0	0	0	0	0	0
2	0	0	0	0	0	0	0	0	0
3	0	0	0	0	0	0	0	0	0
4	0	0	0	0	0	0	0	0	0
5	0	0	0	0	0	0	0	0	0
6	0	0	0	0	0	0	3	0	4
7	5	3	3	2	2	1	1	1	2
8	1	2	0	0	0	1	0	2	1
9	0	1	1	1	1	1	1	0	0
10	0	0	0	1	1	1	0	0	0
11	0	0	1	1	0	0	0	0	0
12–28	0	0	0	0	0	0	0	0	0

A: vaccine; B–F: vaccine+Fab091 (different dilution rates from 0.5 to 32 IU/kg); G: Fab091; H: vaccine+HRIG (20 IU/kg); I: PBS

received vaccine only. The group treated with vaccine and HRIG had a survival rate of 62.5% (5/8). The survival rates were 50% (4/8), 50% (4/8), 37.5% (3/8), 37.5% (3/8), and 25% (2/8) when the mice were treated with 32, 20, 8, 2, and 0.5 IU/kg Fab091, respectively, and vaccine. The groups that received vaccine and 32 IU/kg Fab091 (Figure 7) or vaccine and 20 IU/kg HRIG (Figure 7) were provided with a level of protection against the rabies virus compared to the PBS group (P=0.0485 and P=0.038, respectively; Logrank test).

Discussion

Equine anti-RABV immunoglobulin (ERIG) and human anti-RABV immunoglobulin (HRIG) have been used for passive rabies immunotherapy. However, ERIG can lead to allergic reactions and blood diseases, and HRIG is expensive and often in short supply[23–25]. Recombinant DNA technology and bacterial expression systems used to obtain active antibodies were very attractive compared to hybridoma technology, and antibody molecules can be further engineered to increase their binding affinity. Smaller antibody fragments (such as Fab and scFv) can be effectively used for diagnostic and therapeutic application due to their low immunogenicity and better tissue penetration[26]. ScFv fragments are composed of V_H and V_L with a connecting peptide link. Fab fragments are more stable due to an additional domain-domain interface resulting from the C_H1-C_L association. This structure resulted in higher affinity of purified antibodies[27–30].

Expression of heterologous proteins in bacterial systems can be influenced by many factors such as codon usage, DNA-protein interactions, regulatory factors for transcription and translation, and culture conditions. In the present study, the amber stop codon (cross) enabled the production of soluble Fab fragments in a non-suppressor strain of *E coli*. We optimized the expression conditions and found that Fab could be expressed in a soluble form at room temperature (22 to 25 °C). If the inducing temperature was 30 or 37 °C, Fab was most often expressed in the form of inclusion bodies. In the process of purification, it was found that the amount of purified Fd fragments was less than that of the light chain. This result was possibly due to the pH value of the binding or washing buffer used for purification being unsuitable for purification of the Fd fragment. Furthermore, we found that the Fab091 fragment was easily eluted by phosphate buffer with a concentration of 100 mmol/L imidazole and that the eluted protein had a higher purity. In Figure 3, OD_{450} values showed a gradient change that was accompanied by a decreasing concentration of Fab091, which illustrated the high specificity of Fab091 against the RABV. Furthermore, IP and MS analysis results also demonstrated that Fab091 binds specifically to RABVG. The competitive ELISA indicated that Fab091 and the original scFv shared the same epitope. The neutralizing antibodies in the ELISA kit had different epitopes against RABVG from Fab091.

The most critical property of Fab091 was its neutralizing potency to inhibit the entry of CVS-11 into BHK-21 cells. A sufficient level of antibody to inhibit entry is considered to be 0.5 IU/mL, according to the recommendations of the World Health Organization and the Centers for Disease Control and Prevention[31]. Compared with the reported neutralizing concentrations of FabRV01 and FabRV02, which neutralized the CVS-11 at 146 μg/mL[32], Fab091 was used to neutralize the virus at a concentration of only 12 μg/mL. FabRV01, FabRV02, and FabRV03 were isolated from a recombinant immune antibody library, differing from the altered Fab091, which was from scFv. These results may provide insight into the neutralization activity of recombinant antibodies.

Vaccination alone in the *in vivo* study was not sufficient to protect mice from rabies, whereas the treatment of mice with both vaccine and HRIG (20 IU/kg)/Fab091 (32 IU/kg) provided better protection against rabies than vaccine alone (P<0.05, Logrank test). However, the survival rates of the groups treated with vaccine and Fab091 (32 IU/kg) were lower than that of the vaccine and HRIG (20 IU/kg)-treated group. This result could be interpreted as follows. First, the *in vivo* clearance of RABV is a complicated process. Compared with small-molecular-weight antibodies, the IgG antibody (HRIG), with antibody-dependent cellular cytotoxicity and complement-mediated cytotoxicity, has a greater scavenging capacity *in vivo*[33, 34]. The neutralizing activity of Fab is usually less than that of full-length IgG because of the monovalence of the Fab fragments and the lack of Fc fragment on an IgG molecule. Human Fab may exhibit even greater functional activity when converted into IgG[35]. Second, HRIG consists of polyclonal antibodies from human plasma with a number of epitopes of RABVG, and the function of each epitope is independent of the others. Antibodies can effectively neutralize free virus by macrophage phagocytosis or complement-mediated cytotoxicity. However, Fab091, a monoclonal antibody, can only bind to a single epitope, limiting its ability to remove the virus.

In future studies, the Fab091 and human IgG Fc fragments could be fused and expressed in eukaryotic cells. The reconstitution of Fab091 to IgG is a strategy that could be used for future passive immunotherapy against RABV infection[36–39]. Although Fab091 is different from scFv and IgG in biological function, tissue penetration, and half-life, the three together will not only retain the same binding specificity but also play complementary functional roles. They, together with other monoclonal antibodies, in accordance with the WHO-recommended "cocktail" therapy, can be used for post-exposure prophylaxis of rabies virus.

Acknowledgements

This investigation was supported by the National High Technology Research and Development Program, China (No 2007AA02Z418). We would like to thank Chun-yan GU for valuable technical assistance and Johnson HUANG for revising the manuscript.

Author contribution

Chen LI carried out the molecular biology experiments and drafted the manuscript. Jin ZHU designed the study. Zhen-qing FENG and Xiao-hong GUAN were involved in the design of the study, and Feng ZHANG, Hong LIN, Jin ZHU, Zhong-can WANG, Xin-jian LIU, Zhen-qing FENG, and Xiao-hong GUAN helped to draft the manuscript.

References

1 Komarova AV RE, Borman AM, Brocard M, England P, Tordo N, Hershey JW, *et al*. Rabies virus matrix protein interplay with eIF3, new insights into rabies virus pathogenesis. Nucleic Acids Res 2007; 35: 1522–32.
2 Margalith M VA. Sustained protective rabies neutralizing antibody titers after administration of cationic lipid-formulated pDNA vaccine. Genet Vaccines Ther 2006; 4: 2.
3 Irie T KA. Studies on the different conditions for rabies virus neutralization by monoclonal antibodies #1-46-12 and #7-1-9. J Gen Virol 2002; 83: 3045–53.
4 Bordignon J CF, Ferreira SC, Caporale GM, Lima Filho JH, Zanetti CR. Calculating rabies virus neutralizing antibodies titres by flow cytometry. Rev Inst Med Trop Sao Paulo 2002; 44: 151–4.
5 Li C, Lin H, Liu XJ, Wang ZC, Zhou ZX, Chen LR, *et al*. Construction and screening of human immunized phage-display antibody libraries against rabies virus. Acta Univ Med Nanjing (Natural Sci) 2010; 30: 575–8.
6 Kovalskaya N HR. Expression and functional characterization of the plant antimicrobial snakin-1 and defensin recombinant proteins. Protein Expr Purif 2009; 63: 12–7.
7 Zhu J, Zhao P, Jiao YJ, Wang X, Cao BL, Feng ZQ, *et al*. Affinity Maturation and characterization of internalized human anti-Met recombinant antibody Fab. Prog Biochem Biophys 2007; 34: 73–9.
8 Barbas CF 3rd, Kang AS, Lerner RA, Benkovic SJ. Assembly of combinatorial antibody libraries on phage surfaces: the gene III site. Proc Natl Acad Sci USA 1991; 88: 7978–82.
9 Bellamy SR, Milsom SE, Kovacheva YS, Sessions RB, Halford SE. A switch in the mechanism of communication between the two DNA-binding sites in the *Sfi* I restriction endonuclease. J Mol Biol 2007; 373: 1169–83.
10 Corisdeo S WB. Functional expression and display of an antibody Fab fragment in *Escherichia coli*: study of vector designs and culture conditions. Protein Expr Purif 2004; 34: 270–9.
11 Sam brook J RD. Molecular Cloning: A Laboratory Manual. 3 ed. Cold Spring Harbor, New York: Cold Spring Harbor Laboratory Press; 2001.
12 Chatterjee DK ED. Enhanced soluble protein expression using two new fusion tags. Protein Expr Purif 2006, 46: 122–9.
13 Xiong L, Zhang AX, Li YQ, Zhang DW, Cao BL, Zhu J, *et al*. Reconstitution of human anti-Met genetic engineering antibody scFv. Acta Univ Med Nanjing (Natural Sci) 2009; 29: 605–17.
14 Zhao MP, Li YZ, Guo ZQ, Zhang XX, Chang WB. A new competitive enzyme-linked immunosorbent assay (ELISA) for determination of estrogenic bisphenols. Talant 2002; 57: 1205–10.
15 Tai HC, Campanile N, Ezzelarab M, Cooper DK, Phelps C. Measurement of anti-CD154 monoclonal antibody in primate sera by competitive inhibition ELISA. Xenotransplantation 2006; 13: 566–70.
16 Li WH MX, Qi ZT, Ni W, Zhu SY, Fang F. Proteomic analysis of differently expressed proteins in human hepatocellular carcinoma cell lines HepG2 with transfecting hepatitis B virus X gene. Chin Med J (Engl) 2009; 122: 15–23.
17 Cliquet F AM, Sagné L. Development of a fluorescent antibody virus neutralisation test (FAVN test) for the quantitation of rabies-neutralising antibody. J Immunol Methods 1998; 212: 79–87.
18 Zhang SF, Cao L, Zhang F, Li HT, Li QZ, Zhang RL. Establishment and application of hybridomas producing anti-rabies nucleoprotein McAb and fluorescent antibody virus neutralization test. Chin J Lab Med 2006; 29: 554–7.
19 Goudsmit J MW, Weldon WC, Niezgoda M, Hanlon CA, Rice AB, Kruif J, *et al*. Comparison of an anti-rabies human monoclonal antibody combination with human polyclonal anti-rabies immuneglobulin. J Infect Dis 2006, 193: 796–801.
20 de Kruif J BA, Marissen WE, Kramer RA, Throsby M, Rupprecht CE, Goudsmit J. A human monoclonal antibody cocktail as a novel component of rabies postexposure prophylaxis. Annu Rev Med 2007; 58: 359–68.
21 Prosniak M FM, Hanlon CA, Rupprecht CE, Hooper DC, Dietzschold B. Development of a cocktail of recombinant-expressed human rabies virus-neutralizing monoclonal antibodies for postexposure prophylaxis of rabies. J Infect Dis 2003; 188: 53–6.
22 Bakker AB, Marissen WE, Kramer RA, Rice AB, Weldon WC, Niezgoda M, *et al*. Novel human monoclonal antibody combination effectively neutralizing natural rabies virus variants and individual *in vitro* escape

mutants. J Virol 2005; 79: 9062–8.

23 Bakker AB, Python C, Kissling CJ, Pandya P, Marissen WE, Brink MF, *et al*. First administration to humans of a monoclonal antibody cocktail against rabies virus: safety, tolerability, and neutralizing activity. Vaccine 2008; 26: 5922–7.

24 Goudsmit J MW, Weldon WC, Niezgoda M, Hanlon CA, Rice AB, Kruif J, *et al*. Comparison of an anti-rabies human monoclonal antibody combination with human polyclonal anti-rabies immuneglobulin. J Infect Dis 2006; 193: 796–801.

25 Satpathy DM, Sahu T, Behera TR. Equine rabies immunoglobulin: a study on its clinical safety. J Indian Med Assoc 2005; 103: 238, 241–2.

26 Ray K, Embleton MJ, Jailkhani BL, Bhan MK, Kumar R. Selection of single chain variable fragments (scFv) against the glycoprotein antigen of the rabies virus from a human synthetic scFv phage display library and their fusion with the Fc region of human IgG1. Clin Exp Immunol 2001; 125: 94–101.

27 Henderikx P, Coolen-van Neer N, Jacobs A, van der Linden E, Arends JW, Müllberg J, *et al*. A human immunoglobulin G1 antibody originating from an *in vitro*-selected Fab phage antibody binds avidly to tumor-associated MUC1 and is efficiently internalized. Am J Pathol 2002; 160: 1597–608.

28 Beran J, Honegr K, Banzhoff A, Malerczyk C. Potency requirements of rabies vaccines administered intradermally using the Thai Red Cross regimen: investigation of the immunogenicity of serially diluted purified chick embryo cell rabies vaccine. Vaccine 2005; 23: 3902–7.

29 Kelly MP, Lee FT, Tahtis K, Power BE, Smyth FE, Brechbiel MW, *et al*. Tumor targeting by a multivalent single-chain Fv (scFv) anti-Lewis Y antibody construct. Cancer Biother Radiopharm 2008; 23: 411–23.

30 Goncalvez AP, Chien CH, Tubthong K, Gorshkova I, Roll C, Donau O, *et al*. Humanized monoclonal antibodies derived from chimpanzee Fabs protect against Japanese encephalitis virus *in vitro* and *in vivo*. J Virol 2008; 82: 7009–21.

31 Mazor Y, Van Blarcom T, Iverson BL, Georgiou G. E-clonal antibodies: selection of full-length IgG antibodies using bacterial periplasmic display. Nat Protoc 2008; 3: 1766–77.

32 Mazor Y, Van Blarcom T, Mabry R, Iverson BL, Georgiou G. Isolation of engineered full-length antibodies from libraries expressed in *Escherichia coli*. Nat Biotechnol 2007; 25: 563–5.

33 Cardoso TC, Silva LH, Albas A, Ferreira HL, Perri SH. Rabies neutralizing antibody detection by indirect immunperoxidase serum neutralization assay performed on chicken embryo related cell line. Mem Inst Oswaldo Cruz 2004; 99: 531–4.

34 Houimel M, Dellagi K. Isolation and characterization of human neutralizing antibodies to rabies virus derived from a recombinant immune antibody library. J Virol Methods 2009; 161: 205–15.

35 Bender E, Woof JM, Atkin JD, Barker MD, Bebbington CR, Burton DR. Recombinant human antibodies: linkage of a Fab fragment from a combinatorial library to an Fc fragment for expression in mammalian cell culture. Hum Antibodies Hybridomas 1993; 4: 74–9.

36 Cheung SC, Dietzschold B, Koprowski H, Notkins AL, Rando RF. A recombinant human Fab expressed in *Escherichia coli* neutralizes rabies virus. J Virol 1992; 66: 6714–20.

37 Thullier P, Lafaye P, Megret F, Deubel V, Jouan A, Mazie JC. A recombinant Fab neutralizes dengue virus *in vitro*. J Biotechnol 1999; 69: 183–90.

38 Barbas CF 3rd, Crowe JE Jr, Cababa D, Jones TM, Zebedee SL, Murphy BR, *et al*. Human monoclonal Fab fragments derived from a combinatorial library bind to respiratory syncytial virus F glycoprotein and neutralize infectivity. Proc Natl Acad Sci USA 1992; 89: 10164–8.

39 Lamarre A, Talbot PJ. Protection from lethal corona virus infection by immunoglobulin fragments. J Immunol 1995; 154: 3975–84.

npg Acta Pharmacologica Sinica (2011) 32: 338–344
www.nature.com/aps

Original Article

Sesquiterpenoids from myrrh inhibit androgen receptor expression and function in human prostate cancer cells

Xiao-ling WANG[1, 2], Feng KONG[1], Tao SHEN[3], Charles YF YOUNG[4], Hong-xiang LOU[3], Hui-qing YUAN[1, *]

[1]Institute of Biochemistry and Molecular Biology, School of Medicine, Shandong University, Ji-nan 250012, China; [2]the Second Hospital of Shandong University, Ji-nan 250033, China; [3]Department of Natural Product Chemistry, School of Pharmaceutical Sciences, Shandong University, Ji-nan 250012, China; [4]Department of Urology, Mayo Clinical College of Medicine, Mayo Clinic, Rochester, MN 55905, USA

Aim: To examine whether two naturally occurring sesquiterpenoids (ST1 and ST2) with anti-proliferative activity in prostate cancer cells inhibit androgen receptor (AR) signaling.
Methods: Human prostate cancer cell lines LNCaP and PC3 were used. The expression of AR, AR translocation into the nucleus, and expression levels of AR coactivators ARA70 and steroid receptor coactivator-1 (SRC-1) in LNCaP cells were examined using real-time PCR and Western blot. Changes in prostate-specific antigen (PSA) protein levels, PSA promoter activity, and androgen response element (ARE)-mediated reporter gene activity were examined using enzyme-linked immunoabsorbent assay (ELISA) and transient transfection assays. Co-immunoprecipitation was performed to analyze the interaction between AR and the AR coactivators in ST1- and ST2-treated cells.
Results: In LNCaP cells, ST1 and ST2 (40 μmol/L) led to a significant decrease in the expression of AR as well as a reduction of AR translocation into the nucleus, but had no effect on AR protein translation. ST1 and ST2 treatment also resulted in a significant decrease in the level of PSA protein secreted into the medium and was able to suppress PSA promoter-dependent and ARE-dependent luciferase activity. Furthermore, decreased expression of ARA70 and SRC-1 was observed when LNCaP cells were exposed to ST1 and ST2, which interfered with their ability to interact with AR.
Conclusion: The observations suggest that suppression of AR transactivation by ST1 and ST2 may be mediated, in part, by inhibiting AR nuclear translocation and/or interfering with the interaction between AR and its coactivators ARA70 and SRC-1. Therefore, sesquiterpenoids could be developed as novel therapeutic agents for treating prostate cancer.

Keywords: myrrh; germacrane sesquiterpenoids; androgen receptor; prostate carcinoma cell lines

Acta Pharmacologica Sinica (2011) 32: 338–344; doi: 10.1038/aps.2010.219

Introduction

The biological roles of androgens in the prostate are mediated through the androgen receptor (AR), which is a ligand-activated transcription factor in the nuclear receptor superfamily that is required for normal development and maintenance of male sexual behavior[1]. Additionally, there is strong evidence demonstrating that androgen/AR signaling is involved in the development and progression of prostate cancer (PCa). The importance of AR in PCa is supported by numerous observations showing that AR has been detected and remains active during all stages of PCa, including in most hormone refractory prostate cancer (HRPC), suggesting that AR is improperly activated in the absence of or at post-castration levels of androgens[2–4]. Therefore, inhibition or reduction of aberrant AR activity is a major therapeutic goal for the management of metastatic disease[5].

Myrrh is a resinous substance obtained from *Commiphora* trees, which is believed to act as an anti-tumor agent and is also capable of relieving pain. It has been combined with gum resins in the anti-tumor prescription drug Xihuang wan (or Xihuang pill) for the treatment of cancer in China[6, 7]. Sesquiterpenoids, nonsteroidal compounds found in myrrh, possess diverse biological functions, including antibacterial, anesthetic, and anti-hyperglycemic activity[8–10]. Recent studies have shown that sesquiterpenoids may be anti-tumorigenic[11–13], but the molecular mode of action remains unknown. We

---

* To whom correspondence should be addressed.
E-mail lyuanhq@sdu.edu.cn

Received 2010-05-11 Accepted 2010-12-02

have previously reported that two sesquiterpenoids isolated from myrrh, 1(10)*E*,2*R*,4*R*-2-methoxy-8,12-epoxygermacra-1(10),7,11-trien-6-one (ST1) and 2-methoxy-5-acetoxy-furanogermacr-1(10)-en-6-one (ST2), inhibited the proliferation of LNCaP cells[14, 15]. In this study, we examined whether the anti-tumorigenic function of ST1 and ST2 occurred targeting the AR. Our results showed that ST1 and ST2 blocked AR expression and transcriptional activity and that this inhibition interfered with the interaction of AR and its coactivators ARA70 and SRC-1.

Materials and methods

Cell culture and treatments

Human prostate cancer cell lines LNCaP (obtained from the American Type Culture Collection, Rockville, MD, USA) and PC3 (purchased from the Cell Bank of Chinese Academy of Sciences, Shanghai) were seeded in RPMI-1640 medium supplemented with 10% fetal bovine serum (FBS; JRH, St Louis, MO, USA) and were kept in 5% carbon dioxide at 37 °C until they reached approximately 50% to 70% confluency. Cells were maintained in serum-free RPMI-1640 medium for 24 h to deplete endogenous steroid hormones and then treated with sesquiterpenoids (40 μmol/L) dissolved in RPMI-1640 medium containing 1% charcoal stripped FBS with or without 1 nmol/L synthetic androgen mibolerone (Mib). The sesquiterpenoids were dissolved in dimethyl sulfoxide (DMSO), which was also used as the control vehicle. The control group received the same volume of DMSO.

Western blot analysis

LNCaP cells were grown in 75-mL culture flasks using the same treatment described above. To test whether ST1 and ST2 affected AR protein translation, cells were pretreated simultaneously with cycloheximide (CHX, 20 μg/mL) and sesquiterpenoids (40 μmol/L) for 24 h. Removal of the media was followed by a brief rinse with cold PBS, and whole cell extracts were prepared as described previously[16]. Freshly prepared protease inhibitors [0.5 mmol/L phenylmethanesulfonyl fluoride (PMSF), 50 μg/mL aprotinin, 1 mmol/L sodium orthovanada te, 10 mmol/L sodium fluoride, and 10 mmol/L β-glycerolphosphate] were also added. The Bradford protein assay (Bio-Rad, Hercules, CA, USA) was employed for quantifying the protein content. Proteins were loaded onto an SDS polyacrylamide gel (8%) and electrotransferred onto a nitrocellulose membrane (PALL, Port Washington, NY, USA). The blots were blocked with 5% non-fat milk in TBST buffer (20 mmol/L Tris-HCl, 137 mmol/L NaCl, and 0.1% Tween 20, pH 8.0) prior to incubation with specific antibodies to AR (BD, Franklin Lakes NJ, USA), β-actin (Santa Cruz, CA, USA), ARA70 (Santa Cruz, CA, USA), and SRC-1 (Thermo, Rockford, IL, USA) for 1 h at room temperature. After three times of washing with TBST buffer, the membranes were incubated with an anti-rabbit or anti-mouse IgG secondary antibody conjugated to horseradish peroxidase (Santa Cruz, CA, USA) at room temperature and visualized using enhanced chemiluminescence substrate (ECL, Amersham Corporation, Piscataway, NJ, USA).

Nuclear extracts

After treatments with sesquiterpenoids for 24 h, the LNCaP cells were pelleted, and the nuclear extracts, with or without STs treatment, were prepared as described previously[16]. The protein concentrations of the nuclear extracts were determined using the Bradford protein assay and stored at -80 °C in small aliquots.

Quantitative PCR

After exposure to ST1 and ST2 for 24 h in 6-well plates, LNCaP cells were collected, and the total RNA was extracted using Trizol (Invitrogen, Carlsbad, CA, USA). Changes in the mRNA levels of AR following ST1 and ST2 treatment were quantified using real-time RT-PCR on the ABI 7000 Sequence Detection System (Applied BioSystems, Carlsbad, CA, USA). The AR transcript was detected from M-MLV reverse transcriptase-amplified cDNA, with one aliquot designated to receive no enzyme. Quantitative PCR (TaqMan PCR) was performed using Premix Ex Taq™ reagent, according to the manufacturer's recommended protocols (Takara Biotechnology, Dalian, China). For each 25-μL TaqMan PCR reaction, synthesized cDNA, corresponding to 100 ng total RNA as a template, a final concentration of 400 nmol/L primers, 120 nmol/L of probe, 2×TaqMan PCR Mix and PCR-grade water were mixed together. Sequence-specific primers for AR were 5′-AAGGCTATGAATGTCAGCCCA-3′ (sense) and 5′-CATTGAGGCTAGAGAGCAAGGC-3′ (antisense). Probes contained the fluorescence reporter FAM at the 5′-end and TAMRA at the 3′-end, FAM5′-TGTGTGCTGGACACGACAACAACC-3′TAMRA. Glyceraldehyde-3-phosphate dehydrogenase (GAPDH) was included as an internal control and ran in the same PCR reaction. The probe and primer combinations were as follows: FAM5′-AACAGCGACACCCACTCCTCCACC-3′TAMRA, 5′-CCAGGTGGTCTCCTCTGACTT-3′ (sense) and 5′-GTTGCTGTAGCCAAATTCGTTGT-3′ (antisense). All of the primers and probes were synthesized by Takara Biotech (Dalian, China). All of the PCR assays were performed in triplicate. The quality of each reaction was confirmed by comparing the triplicate RT *versus* the no-enzyme control. The amount of each target gene relative to GAPDH for each sample was analyzed using the $2^{-\Delta\Delta CT}$ method[17]. The values were indicated as the percentage of untreated control and set to 100%.

Transient transfection and reporter gene activity assays

The PC-3 and LNCaP cells were seeded in 24-well plates and grown under the conditions described above. A plasmid containing the AR promoter (-1380/+577) (AR 2 kb promoter, 0.8 μg/well), pGL3 basic vector with 6 kb of the PSA promoter (pGL3-PSA promoter, 0.8 μg/well), or pGL3-SV40 with three copies of the androgen response element (ARE) of the *hk2* gene (hk2-3ARE, 0.8 μg/well) were transfected into LNCaP cells using Lipofectamine™ 2000 (Invitrogen, Carlsbad, CA, USA). For transfection of DNA into PC3 cells, the human AR expression vector pSG5-AR (hAR, 0.2 μg/well) was included for cotransfection with the plasmids described above. The parental vectors pGL3 basic (0.8 μg/well) and pGL3-SV40 (0.8 μg/well) were used as controls. The phRL-TK vector (0.1 μg/well, Renilla luciferase, Promega, Madison, WI, USA) served as an internal control to normalize the transfection efficiency. After 24 h post-transfection, cells were either treated with sesquiterpenoids (40 μmol/L) or remained untreated in the presence or absence of 1 nmol/L Mib for an additional 24 h in medium containing 1% charcoal stripped serum. The cell extracts were prepared and used for luciferase assays (Dual-Luciferase Reporter Assay System, Promega, Madison, WI, USA). At least three independent transfection experiments were performed. Statistical analysis was done using two-tailed Student's *t*-test. $P<0.05$ was accepted as the level of significance.

Immunofluorescence staining

The LNCaP cells were cultured on slides. After sesquiterpenoid (40 μmol/L) treatment, LNCaP cells were fixed with 4% paraformaldehyde for 20 min. After washing with PBS, the cells were treated with 0.3% Triton X-100 in PBS for 15 min at room temperature to increase cellular permeability. Fixed cells were blocked with 10% normal goat serum in PBS at room temperature for 60 min, and then anti-AR antibody was applied at a dilution of 1:2 and incubated at 4 °C in a moist chamber overnight. The slides were then incubated with the FITC-conjugated goat anti-rabbit IgG (Zhongshan, China) for 60 min and examined under a fluorescence microscope (IX-71, Olympus, Tokyo, Japan). Negative control cells were incubated with preimmune rabbit serum instead of primary antibodies. The assays were repeated three times.

Measurement of secreted PSA protein

The LNCaP cells were cultured as described above and exposed to sesquiterpenoids in the absence or presence of Mib. After 24 h of incubation, the depleted media was harvested, and the levels of PSA in the depleted media were quantified with ELISA (Alpha Diagnostic, San Antonio, TX, USA). The cell density was measured using the 3-(4,5-dimethylthiazol-2-yl)-2,5-diphenyl-2Htetrazolium bromide (MTT; Sigma, St Louis, MO, USA) assay. The levels of PSA protein were normalized based on the cell density measurements.

Co-immunoprecipitation

The LNCaP cells were plated in 75-mL culture dishes and treated with sesquiterpenoids in the absence or presence Mib for 24 h. Whole cell lysates were prepared as described previously[16] and precleared with anti-mouse IgG and protein A-agarose (Santa Cruz ,CA, USA). Protein aliquots of 500 μg were incubated with 2 μg of antibody directed against AR (BD, Franklin Lakes, NJ, USA) in binding buffer (20 mmol/L HEPES, pH 7.9, 20% glycerol, 150 mmol/L KCl, 0.2 mmol/L EDTA, 0.5 mmol/L DTT, 0.5 mmol/L PMSF, 50 mg/mL aprotinin, 1 mmol/L sodium orthovanadate, 10 mmol/L sodium fluoride, and 10 mmol/L β-glycerolphosphate) at 4 °C overnight. The protein A-agarose beads were added and incubated for 6 h at 4 °C. The immunoprecipitates were washed four times with buffer containing 50 mmol/L Tris-HCl, pH 7.5, 0.5% IGEPAL CA-630, 150 mmol/L NaCl, 0.2 mmol/L EDTA, 0.5 mmol/L PMSF, 50 mg/mL aprotinin, 1 mmol/L sodium orthovanadate, 10 mmol/L sodium fluoride, and 10 mmol/L β-glycerolphosphate. Immunocomplexes were recovered by heating at 75 °C for 10 min in SDS sample buffer and analyzed by Western blot.

Results

ST1 and ST2 inhibit the expression of AR in LNCaP cells

We previously reported that ST1 and ST2 inhibited LNCaP cell proliferation by causing cell cycle arrest in the G_1 phase[15]. Because downregulation of AR resulted in significant suppression of prostate tumor cell growth[18, 19], we used Western blot analysis to determine whether the inhibition of cell growth by STs was due to a reduction in AR expression in LNCaP cells. As shown in Figure 1A, treatment of LNCaP cells with Mib led to a significant increase in the expression of AR, while Mib-mediated stimulation of AR protein levels was decreased by ST1 and ST2. Activated AR typically translocates to the nucleus to regulate transcription of target gene expression. The effect of ST1 and ST2 on AR nuclear translocation was further analyzed by Western blot analysis of the nuclear extracts. As shown in Figure 1A, Mib treatment also increased the level of AR protein expression in the nucleus. This increase was drastically reduced by treating LNCaP cells with ST1 and ST2. These results indicate that the inhibition of androgen-stimulated AR nuclear translocation by ST1 and ST2 treatments might attribute to the suppression of AR protein expression. In addition, immunocytochemistry was performed to determine the change in AR protein levels in LNCaP cells. Similarly, in the absence of Mib, AR protein levels were reduced (Figure 1B), whereas Mib treatment caused a significant increase in the expression of AR in these cells. Furthermore, most of the AR was located in the nucleus. Consistent with the Western blot results, the AR protein level was greatly reduced in cells exposed to ST1 and ST2.

To determine whether STs affect AR expression at the transcriptional level, we performed real-time PCR to monitor changes in the AR mRNA levels. Figure 1C showed that androgen-induced expression of the AR transcript was greatly reduced in cells exposed to STs compared with those treated with Mib alone. The inhibitory effect of STs on AR gene expression was further confirmed in LNCaP cells transfected with an AR promoter-luciferase construct. As shown in Figure 1D, increased AR promoter reporter activity was evident in response to Mib, and the luciferase activity was significantly inhibited by ST1 and ST2 in the presence of Mib, which is consistent with the data in Figures 1A, 1B, and 1C.

We next examined the effect of STs on AR protein synthesis using CHX, an inhibitor of protein synthesis. As shown in Figure 2, AR protein levels were decreased in the presence of CHX, whereas treatment with both CHX and STs caused no detectable changes in the AR protein expression, suggesting that STs may not regulate translation of the AR protein. These

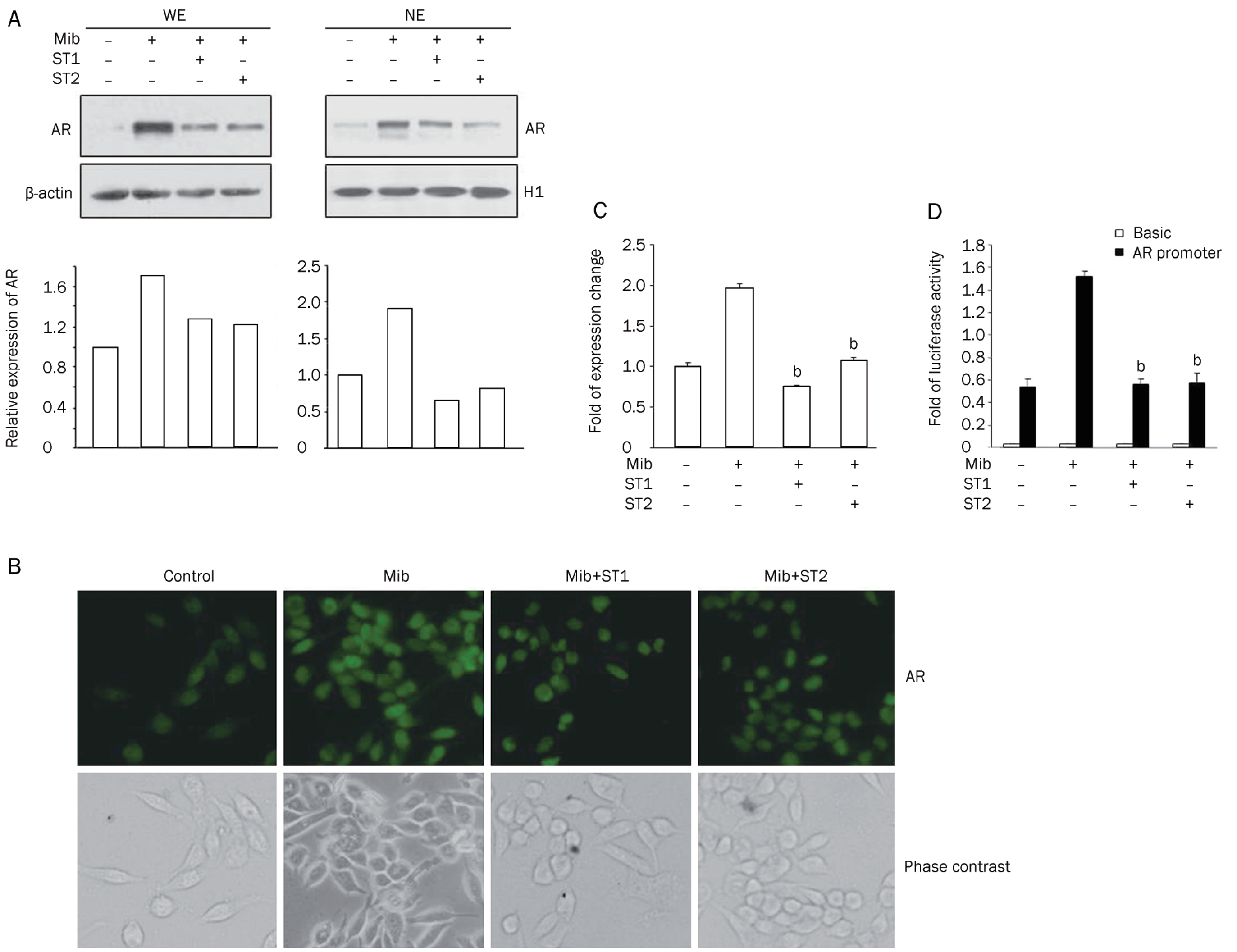

Figure 1. Effects of ST1 and ST2 on AR expression in LNCaP cells. (A) Western blot analysis of AR protein expression in whole cell lysates (WE) and nuclear extracts (NE) from LNCaP cells treated with or without STs was performed. Beta-actin and H1 bands represent protein loading and transferring efficiency controls. Histograms represent the densitometry analysis of Western blot. (B) Immunofluorescent staining of AR. (C) Changes in AR mRNA expression were determined by quantitative PCR. RNA from ST-treated and control cells were subjected to real-time PCR analysis using primers specific for AR or GAPDH, respectively. The data are shown as the mean±SD of three independent experiments, each performed in triplicate. $^{b}P<0.05$ *vs* Mib treatment. (D) Effect of ST1 and ST2 on AR promoter activity. Cell extracts from transfections were used for dual luciferase activity assays. The resulting luciferase activity was normalized to the activity of phRL-TK to show the equal transfection efficiency. The normalized relative luciferase activities (mean±SD) of at least three independent experiments are shown. $^{b}P<0.05$ *vs* Mib treatment.

results indicate that the suppression of AR protein levels by ST1 and ST2 is mediated by a reduction of the AR mRNA transcripts in the presence of androgen.

ST1 and ST2 repress AR transcriptional activity

PSA and *hk2* are androgen-inducible genes that contain AREs, which are AR-binding regions. The expression of the *PSA* and *hk2* genes are highly dependent upon the regulation of androgens through AR[20, 21]. To clarify whether the ST-mediated reduction in cellular AR protein levels was accompanied a decrease in the transcriptional activity of the AR, the secreted PSA protein level was examined in ST-treated LNCaP cells. As shown in Figure 3, the secreted PSA level was enhanced in the presence of Mib compared to the untreated control, while exposure of LNCaP cells to ST1 and ST2 for 24 h decreased the PSA protein levels in the presence of androgens. The inhibition of ST1 and ST2 on AR transactivity was further investigated using co-transfection experiments. A construct containing the PSA promoter linked to a luciferase gene was transfected into LNCaP cells to examine the AR transactivity following ST treatment. As shown in Figure 4A, Mib stimulated the induction of the reporter gene, which was detected by examining the activity of luciferase, while ST1 and ST2 suppressed the androgen induction of the PSA promoter. We next transfected the PSA promoter-luciferase reporter, with an AR expression vector, into PC-3 cells lacking AR protein

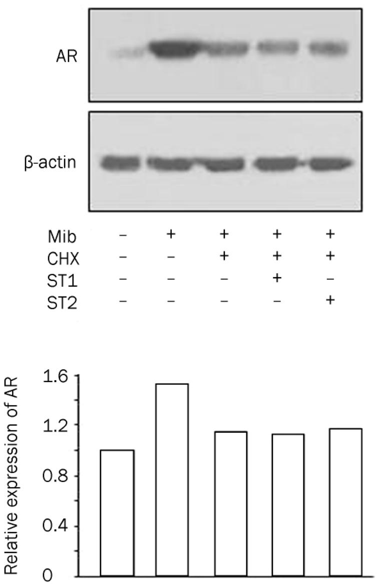

Figure 2. Effects of ST1 and ST2 on AR protein synthesis in LNCaP cells. AR in LNCaP cells exposed to ST1 and ST2 in the presence or absence of CHX was analyzed using Western blot. Beta-actin is the protein loading and transferring efficiency control. Histograms show the densitometry analysis of Western blot.

expression to confirm the ST-mediated inhibitory effect on AR transcriptional function. As shown in Figure 4B, the PSA promoter caused a strong androgenic induction of luciferase activity in Mib-treated cells. However, ST1 and ST2 treatments abolished the androgenic-mediated induction of the PSA promoter. Because ARE is necessary for AR-mediated gene transactivation, we used the luciferase reporter linked to three repeats of ARE from the *hk2* gene to test whether specific DNA sequence dependent AR transcriptional activity could be affected by ST treatments. The luciferase activity of hk2-3ARE was reduced by ST1 and ST2 in the presence of Mib (Figure 4B). Additionally, the results in Figure 4D further established the efficacy of ST1 and ST2 by specifically blocking AR actions in PC3 cells. Thus, ST1 and ST2 treatments significantly suppressed AR expression and the androgen-stimulated AR transcriptional activity.

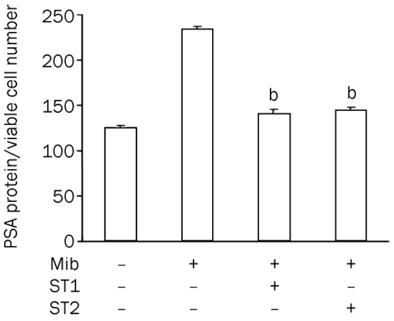

Figure 3. Effects of ST1 and ST2 on PSA expression in LNCaP cells. The PSA protein levels were normalized to cell density using the MTT assay. Error bars indicate the standard error of three separate experiments. $^{b}P<0.05$ *vs* Mib treatment.

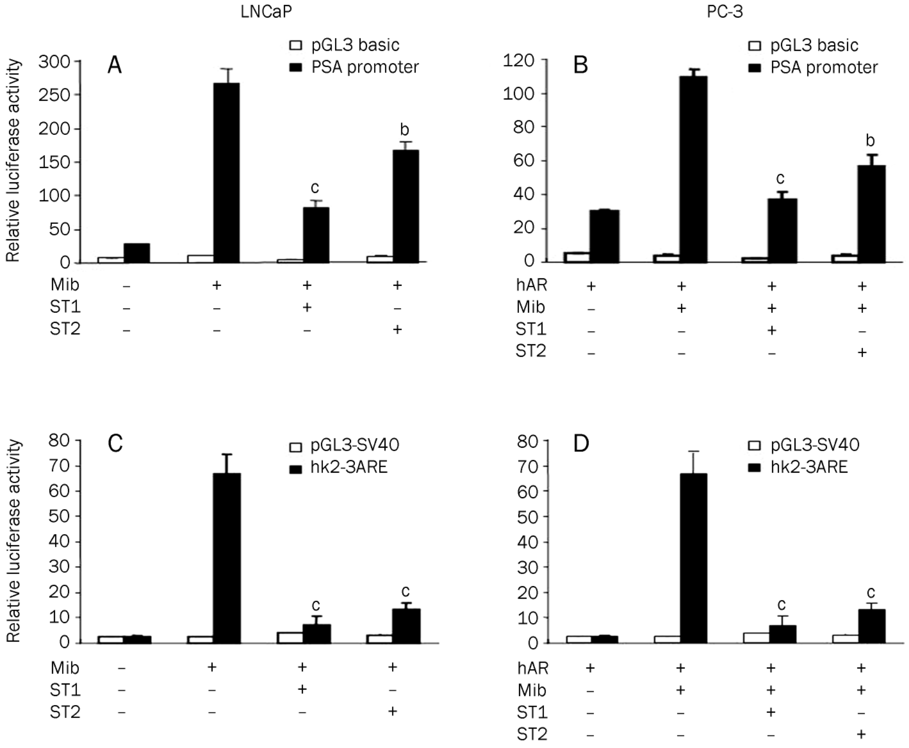

Figure 4. Effects of ST1 and ST2 on the AR transcriptional activity in LNCaP cells (A) Luciferase activity in LNCaP cells transfected with the pGL3-PSA 6 kb promoter luciferase reporter following treatment with STs for 24 h. (B) Luciferase activity in PC3 cells co-transfected with the pGL3-PSA 6 kb promoter reporter and a human AR expression construct following exposure to STs as indicated for 24 h. (C) Luciferase activity in LNCaP cells transfected with the pGL3-SV40-hk2-3ARE reporter following treatment with STs for 24 h. (D) Luciferase activity in PC3 cells co-transfected with the pGL3-SV40-hk2-3ARE reporter and a human AR expression construct following treatment with STs as indicated for 24 h. $^{b}P<0.05$, $^{c}P<0.01$ *vs* Mib treatment. The parental vectors pGL3 basic vector and pGL3-SV40 were included as controls. The phRL-TK, co-transfected in each transfection, was the internal control for normalization. The normalized relative luciferase activity (mean±SD) of at least three independent experiments is shown.

ST1 and ST2 weaken the interaction between AR and its coactivators SRC-1 and ARA70 in LNCaP cells

It is well documented that the AR intrinsic ligand-dependent activity is potentiated through its interaction with coactivators, including SRC-1 and ARA70[22]. Because ST1 and ST2 repressed the AR transcriptional activity and subsequently led to a reduction in the expression of PSA protein and promoter activity, it is likely that ST1 and ST2 suppressed AR transactivation by interrupting the function of AR coactivators. Alterations in the expression of ARA70 and SRC-1 were analyzed in response to ST1 and ST2 by Western blot. As shown in Figure 5, Mib treatment resulted in elevated expression of both ARA70 and SRC-1; however, protein abundance of these two coactivators was greatly reduced in LNCaP cells treated with ST1 and ST2. Co-immunoprecipitation was performed to further analyze the interaction between AR and its coactivators. Proteins potentially associated with AR were first precipitated with anti-AR antibody and subsequently detected using AR antibody, ARA70 antibody or SRC-1 antibody. As indicated in Figure 6, endogenous ARA70 and SRC-1 bands were detected in anti-AR-precipitated complexes from cells treated with Mib (line 2), and very weak signals were observed in ST1- and ST2-treated cells (lines 3 and 4). No detectable proteins were shown in immunocomplexes precipitated with normal IgG. Together, these data indicate that the ST1- and ST2-mediated reduction in the levels of AR coactivators ARA70 and SRC-1 also plays a role in the ST-induced suppression of AR transactivity, mainly through their inhibition of expressions of these two coactivators, and leading to interference with the interactions with the AR.

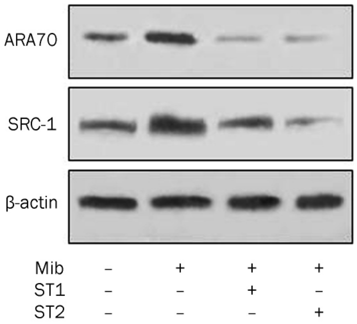

Figure 5. Effects of ST1 and ST2 on AR coactivators SRC-1 and ARA70. The AR coactivators ARA70 and SRC-1 in LNCaP cells exposed to ST1 and ST2 were analyzed using Western blot.

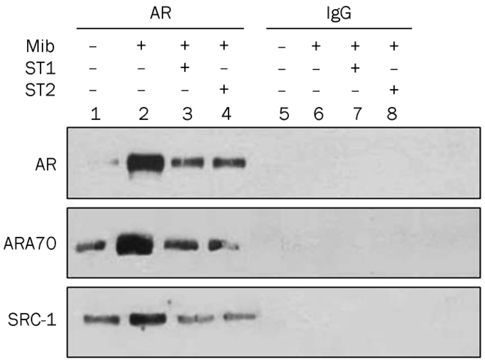

Figure 6. Effects of ST1 and ST2 on the interactions between AR and AR coactivators SRC-1 and ARA70. The association of AR and AR coactivators SRC-1 and ARA70 was analyzed using co-immunoprecipitation. Normal IgG was used as the negative control. Input represents 10% of the whole cell extracts used in the above experiments.

Discussion

The present work is an initial study aimed at identifying novel, natural nonsteroidal modulators targeting androgen/AR signaling from traditional oriental medicines. Based on previous studies using petroleum extract from myrrh, we discovered two sesquiterpenoids, ST1 and ST2, that inhibited prostate cancer cell proliferation. In this study, we demonstrated that the sesquiterpenoids suppressed AR promoter transcription, mRNA and protein expression levels and decreased androgen-stimulated PSA promoter activity and protein secretion. These observations indicated that ST-mediated suppression of AR function was at least partly due to a reduction of AR expression in the nucleus.

To regulate the transcription of target genes, AR must recruit a series of coactivator proteins that generally do not directly bind to DNA. These proteins are recruited to gene-promoter regions through protein–protein interactions with AR, and this interaction occurs usually in a ligand-dependent manner. Therefore, a decrease in the expression levels of AR coactivators or the interruption of their interaction with AR in prostate cancer cells could contribute to AR signaling inhibition. The first identified member of the coactivator family that regulated steroid receptor action was SRC-1[23], which is functional in many different tissue types, enhances transcriptional activity of the AR in a ligand-dependent manner[22], and is involved in the negative regulation of AR activity by sesquiterpenoids. Sesquiterpenoids significantly decreased the expression of SRC-1 and interfered with the interaction between the AR and SRC-1 in the presence of androgens. In addition, ARA70 has been reported to be a relatively AR-specific coactivator[22]; however, other studies contradict this idea. The expression of ARA70 is increased in high-grade prostate cancer tissues as well as in hormone-refractory LNCaP xenografts and other prostate cancer cell lines. High levels of ARA70 may induce agonist activity of anti-androgens in LNCaP and other hormone-refractory prostate cancer cells[24, 25]. The molecular mechanisms by which ARA70 enhances AR transactivation involve increasing AR expression, protein stability, and nuclear translocation. In this study, when cells were exposed to the sesquiterpenoids, ARA70 protein expression was inhibited, and the interaction between AR and ARA70 was also interfered. Further studies are necessary to test if the sesquiterpenoids, by inhibiting ARA70, can enhance the anti-androgen treatment of the advanced stages of prostate cancer.

As sesquiterpenoids can decrease ARA70 and SRC-1 levels and interfere with the interaction between AR and its coactivators, our data support the idea that the inhibition of AR transcriptional activity by these two compounds occurred in an androgen-dependent manner. However, it remains to be clarified whether sesquiterpenoids can block androgen binding to AR and inhibit AR translocation into the nucleus, preventing the transcription of AR-responsive target genes.

Our results suggest that the anti-androgen/AR effects of sesquiterpenoids are mediated through a reduction of AR expression, inhibition of AR translocation into the nucleus, reduction of the expression of ARA70 and SRC-1, and interference with the interaction between AR and ARA70 and SRC-1, leading to the inhibition of AR transactivity. Additional studies in animals as well as clinical trials will be necessary to evaluate the potential benefit of utilizing these sesquiterpenoids in the treatment of prostate cancer.

Acknowledgements

This work was supported by the National Natural Science Foundation of China (No 30772594); Shandong Scientific Reward Funding Program (No 2006BS03006); and the Independent Innovation Foundation of Shandong University, IIF-SDU.

Author contribution

Hui-qing YUAN designed the research; Xiao-ling WANG and Feng KONG performed the research; Tao SHEN and Hong-xiang LOU contributed to the isolation and determination of chemicals; Xiao-ling WANG analyzed the data; and Xiao-ling WANG, Charles YF YOUNG, and Hui-qing YUAN wrote the paper.

References

1 Feldman BJ, Feldman D. The development of androgen-independent prostate cancer. Nat Rev Cancer 2001; 1: 34–45.
2 Edwards J, Krishna NS, Grigor KM, Bartlett JM. Androgen receptor gene amplification and protein expression in hormone refractory prostate cancer. Br J Cancer 2003; 89: 552–6.
3 Kung HJ, Evans CP. Oncogenic activation of androgen receptor. Urologic Oncology 2009; 27: 48–52.
4 Dehm SM, Tindall DJ. Androgen receptor structural and functional elements: role and regulation in prostate cancer. Mol Endocrinol 2007; 21: 2855–63.
5 Taplin ME, Balk SP. Androgen receptor: a key molecule in the progression of prostate cancer to hormone independence. J Cell Biochem 2004; 91: 483–90.
6 Li LF, Chen RS, Liu XM. Xihuangwan induce Bel-7402 cell apoptosis and the change of intracellular-free calcium level in the process. Chin J Clin Hepatol 2003; 19: 362–3.
7 Xiong Y, Kong XY, Chen RS, Jin QW, Liu XM. The morphological study on the induction of apoptosis *in vitro* by Chinese herbal medicine Xihuangwan. Chin J Clin Gastroenterol 2001; 13: 82–4.
8 Ubillas RP, Mendez CD, Jolad SD, Luo J, King SR, Carlson TJ, *et al.* Antihyperglycemic furanosesquitterpens from *Commiphora* myrrha. Planta Med 1999; 65: 778–9.
9 Dolara P, Corte B, Ghelardini C, Pugliese AM, Cerbai E, Menichetti S, *et al*. Local anaesthetic, antibacterial and antifungal properties of sesquiterpenes from myrrh. Planta Med 2000; 66: 356–8.
10 Zhu N, Kikuzaki H, Sheng S, Sang S, Rafi MM, Wang M, *et al*. Furanosesquiterpenoids of *Commiphora* myrrha. J Nat Prod 2001; 64: 1460–2.
11 Tipton DA, Lyle B, Babich H, Dabbous MKh. *In vitro* cytotoxic and anti-inflammatory effects of myrrh oil on human gingival fibroblasts and epithelial cells. Toxicol *In Vitro* 2003; 17: 301–10.
12 El Ashry ES, Rashed N, Salama OM, Saleh A. Components, therapeutic value and uses of myrrh. Pharmazie 2003; 58: 163–8.
13 Shoemarker M, Hamilton B, Dairkee SH, Cohen I, Campbell MJ. *In vitro* anticancer activity of twelve Chinese medicinal herbs. Phytother Res 2005; 19: 649–51.
14 Ji K, Kong F, Shen T, Wang XL, Xu AH, Yuan HQ, *et al*. Separation and identification of myrrh sesquiterpenoids and their anti-proliferation effect on tumor cells. J Shandong Univ (Health Sciences) 2008; 46: 344–8.
15 Wang XL, Kong F, Ji K, Cai J, Ren K, Gong L, *et al*. Overexpression of p21$^{WAF/CIP1}$ is involved in sesquiterpenoids-mediated inhibitory effect on proliferation of prostate cancer cells. Weisheng Dulixue Zazhi 2008; 22: 10−3.
16 Yuan HQ, Gong AY, Young CYF. Involvement of transcription factor Sp1 in quercetin-mediated inhibitory effect on the androgen receptor in human prostate cancer cells. Carcinogenesis 2005; 26: 793–801.
17 Livak KJ, Schmittgen TD. Analysis of relative gene expression data using real-time quantitative PCR and the $2^{-\Delta\Delta CT}$ method. Methods 2001; 25: 402–8.
18 Scher HI, Buchanan G, Gerald W, Butler LM, Tilley WD. Targeting the androgen receptor: improving outcomes for castration resistant prostate cancer. Endocr Relat Cancer 2004; 11: 459–76.
19 Zegarra-Moro OL, Schmidt LJ, Huang H, Tindall DJ. Disruption of androgen receptor function inhibits proliferation of androgen-refractory prostate cancer cells. Cancer Res 2002; 62: 1008–13.
20 Kim J, Coetzee GA. Prostate specific antigen gene regulation by androgen receptor. J Cell Biochem 2004; 93: 233–41.
21 Mitchell SH, Murtha PE, Zhang S, Zhu W, Young CY. An androgen response element mediates LNCaP cell dependent androgen induction of the hK2 gene. Mol Cell Endocrinol 2000; 168: 89–99.
22 Heinlein CA, Chang C. Androgen receptor (AR) coregulators: an overview. Endocr Rev 2002; 23: 175–200.
23 Oñate SA, Tsai SY, Tsai MJ, O'Malley BW. Sequence and characterization of a coactivator for the steroid hormone receptor superfamily. Science 1995; 270: 1354–7.
24 Rahman MM, Miyamoto H, Takatera H, Yeh S, Altuwaijri S, Chang C. Reducing the agonist activity of antiandrogens by a dominant-negative androgen receptor coregulator ARA70 in prostate cancer cells. J Biol Chem 2003; 278: 19619–26.
25 Hu YC, Yeh S, Yeh SD, Sampson ER, Huang J, Li P, *et al*. Functional domain and motif analyses of androgen receptor coregulator ARA70 and its differential expression in prostate cancer. J Biol Chem 2004; 279: 33438–46.

Acta Pharmacologica Sinica (2011) 32: 345–353
© 2011 CPS and SIMM All rights reserved 1671-4083/11 $32.00
www.nature.com/aps

Original Article

Ginsenoside Rh2 inhibits glioma cell proliferation by targeting microRNA-128

Nan WU, Guo-cai WU, Rong HU, Mei LI, Hua FENG*

Department of Neurosurgery, Southwest Hospital, Third Military Medical University, Chongqing 400038, China

Aim: To examine the influence of ginsenoside Rh2 (Rh2), a triterpene saponin extracted from the traditional medicinal plant ginseng, on the expression of miRNAs in human glioma cells.
Methods: The expression profile of miRNA (miR) was analyzed in human U251, T98MG and A172 glioma cells using a miRNA array and quantitative real-time PCR. Cell viability was assessed using a colorimetric assay (cell counting kit-8). Transfection of miR-128 was performed using Lipofectamine 2000. Caspase 3 activity was determined using a caspase colorimetric assay kit. Apoptosis was assessed using annexin V and propidium iodide staining. Protein expression was determined with Western blot analysis. miRNA-128 targeting activity was measured using a luciferase reporter assay.
Results: In U251 cells treated with Rh2 (12 μg/mL), 14 of 452 human miRNAs were up-regulated and 12 were down-regulated as detected with the miRNA array assay. The up-regulation of miR-128 by Rh2 was further verified in human U251, T98MG and A172 cells using quantitative real-time PCR. In U251 cells, transfection of a miR-128 inhibitor (50 nmol/L) prevented the overexpression of miR-128 by Rh2, and significantly blunted Rh2-induced cytotoxicity, apoptosis, caspase 3 activation, transcriptional activation of E2F3a, a miR-128 target gene, as well as E2F3a protein expression.
Conclusion: The anti-proliferative effect of Rh2 in human glioma cells was mediated in part through up-regulation of miRNA-128 expression.

Keywords: ginsenoside Rh2; triterpene saponin; glioma cell; microRNA; miR-128; apoptosis; apoptosis cell proliferation; caspase 3; E2F3a

Acta Pharmacologica Sinica (2011) 32: 345–353; doi: 10.1038/aps.2010.220

Introduction

Gliomas are the most common brain tumors in humans. Even when treated with surgery, radiotherapy, chemotherapy, and other intensive regimens, malignant gliomas are incurable[1]. The tumors are characterized by rapid cell growth and diffuse cellular infiltration into adjacent normal tissues[2]. Although a number of genetic and molecular lesions have been correlated with glioma progression, a complete understanding of the molecular basis and therapy of these tumors remains elusive.

One novel approach to characterizing the molecular and therapeutic targets of gliomas is based on the expression profiling of miRNAs[3]. These small RNA molecules are a class of endogenously expressed small noncoding RNA, 18-25 nucleotides in length[4]. To date, more than 700 miRNAs have been identified in humans[5]. miRNAs are known to be important in the regulation of many fundamental cellular processes, such as cell proliferation, differentiation and apoptosis[6, 7]. Following binding to the 3′-untranslated regions (UTRs) of specific mRNAs, miRNAs regulate target gene expression by inducing translational repression or mRNA degradation[8]. It is estimated that up to 30% of human genes may be regulated by miRNAs[8]. Moreover, approximately 50% of the known miRNAs were reported to be located in cancer–associated genomic regions[9, 10] and miRNA dysregulation has been detected in various cancer cells[11]. Therefore, aberrations in miRNA expression patterns are thought to be involved in the progression of human cancers[12]. Since the first report of abnormal miRNA expression in glioblastomas in 2005, there has been an increasing number of reports each year describing miRNA dysregulation and function in various brain tumors[13–17]. These findings not only provide new insights into the molecular pathogenesis of gliomas, but also are useful in identifying miRNAs as potential targets in therapeutic intervention.

Ginsenoside Rh2 is a biologically active phytochemical extracted from Ginseng, a commonly used alternative drug taken orally in traditional herbal medicines in China, Korea, Japan and some Western countries[18]. It is a triterpene saponin, consisting of a steroid nucleus and a sugar moiety[18].

---

* To whom correspondence should be addressed.
E-mail fenghua8888@yahoo.com.cn
Received 2010-07-02 Accepted 2010-12-02

Rh2 has been reported to have a variety of biological effects, such as reducing blood glucose[19] and ameliorating ischemic brain injury[20]; in addition, it has antiallergic activity[21] and antiproliferative effects[22]. The ability of Rh2 to suppress cell growth has also been observed in glioma cells[22, 23]. Because Rh2 promotes neoplastic cells to return to a normal cell phenotype, it is expected to be a new type of anticancer agent[23]. It displays low toxicity, is associated with only a few side effects and is generally regarded as an anticancer nutrient[23]. Although extensive investigations have shown that Rh2 exerts its antiproliferative effects through induction of an apoptotic pathway[24], the role of miRNAs in this process has not yet been explored.

Using an miRNA array to examine miRNA expression in Rh2-treated human glioma cells, we found that Rh2 altered the miRNA expression in human glioma U251 cells. We verified the observed up-regulation of the brain-enriched miR-128 by quantitative real-time PCR in human U251, T98MG and A172 glioma cells. To further investigate the role of miR-128 in Rh2-mediated antiproliferation, we transfected miR-128 inhibitor into glioma cells and observed an abrogation of Rh2-induced miR-128 overexpression, causing significant inhibition of Rh2-induced cytotoxicity, apoptosis, caspase-3 activation, transcriptional activation of E2F3a, a miR-128 target gene, and the expression of E2F3a protein.

Materials and methods

Reagents

Ginsenoside Rh2 (20R-form, >99% purity, HPLC pure) was purchased from the National Institute for the Control of Pharmaceutical and Biological Products (Beijing, China). The chemical structure of ginsenoside Rh2 is shown in Figure 1.

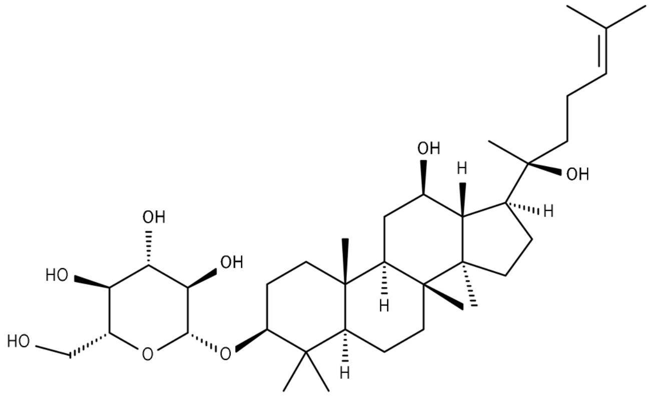

Figure 1. Chemical structure of ginsenoside Rh2 (20R-form).

Cell lines and culture conditions

Human U251, T98MG and A172 glioma cells were purchased from the Cell Bank of Shanghai Institutes for Biological Sciences, Chinese Academy of Sciences (Shanghai, China). The cells were maintained in RPMI-1640 medium (Gibco Life Technologies, Grand Island, NY, USA), supplemented with 10% fetal bovine serum (Sijiqing, Hangzhou, China), 100 U/mL penicillin and 100 mg/mL streptomycin. All cells were routinely passaged and maintained in a humidified incubator of 5% CO_2 at 37 °C.

Cell proliferation assay

Cell viability was assessed colorimetrically using the cell counting kit-8 (CCK-8, Dojindo Laboratories, Tokyo, Japan)[25]. Human glioma U251 cells (1×10^5) were seeded in each well of a 96-well plate and incubated for 24 h prior to treatment with different dosages of Rh2 or vehicle. After treatment, 10 μL of the CCK-8 solution was added into each well, and the cells were incubated for an additional 2 h. The absorbance value (A) at 470 nm was read using a microplate reader (Bio-Rad, CA, USA) with a reference wavelength of 630 nm.

miRNA microarray analysis

The U251 cells were cultured for 24 h and then incubated with 12 μg/mL Rh2 for 24 h. Total cellular RNA was isolated from Rh2-treated and –untreated cells using TRIzol reagent (Invitrogen™, Carlsbad, CA, USA) according to the manufacturer's protocol. Five micrograms of total RNA was labeled at the 3′-end with Hy3™ using miRCURY Array Labeling kit (Exiqon, Vedback, Denmark) for 1 h at 0 °C.

The labeled RNA was purified using a Miniprep Kit (QIAgen, Valencia, CA, USA). The resulting sample was diluted with hybridization buffer, and 20 μL of the diluted sample was loaded onto the spotted area of the array and covered with a Bioarray LifterSlip coverslip. The chamber was rotated in a 60 °C water bath for 14 h. The miRCURY LNA miRNA Array 8.1 contained probes for 452 mature human miRNAs printed in quadruplicate. Next, the slides were washed in wash buffer A (2×SSC/0.2% SDS) at 60 °C until the Bioarray LifterSlip coverslip fell off. Then the slides were washed with wash buffer B (1×SSC) twice and wash buffer C (0.2×SSC) once. After drying by centrifugation for 5 min at 1000 round per minute, the slides were scanned with a Genepix 4000B laser scanner (Molecular Devices) and digitized by Genepix Pro 6.0. The resulting ratios of miRNA spots to background were calculated. The data were analyzed by subtracting out the background and normalizing the signals using global Lowess (locally weighted scatter plot smoothing) regression algorithm. All miRNAs having a ratio of 2.0 or greater were included.

Quantitative real-time PCR for miRNA expression

To confirm the miRNA levels obtained from the microarray results, miRNA expression was assessed using quantitative real-time PCR (qRT-PCR). Total cellular RNA was extracted from each of the experimental groups. Reverse transcription was performed using gene specific primers. The sequences of the primer pairs were as follows: miR-128: forward 5′-CGCGCTCACAGTGAACCG-3′ and reverse 5′-GTGCAGGGTCCGAGGT-3′; miR-15b: forward 5′-TAGCAGCACATCATGGTTTACA-3′ and reverse 5′-TCGTGCCAGCGGCTCG-3′; miR-21: forward 5′-CGGGATCCTGGGGTTCGATCTTAACAGGC-3′ and reverse 5′-CGGAATCCCCA-

CAATGCAGCTTAGTTTTCC-3′; miR-25: forward 5′-GTGTTGAGAGGGCGGAGACTT-3′ and reverse 5′-TCAGACCGAGACAAGTGCAA-3[14–17]. U6 was taken as an internal control (forward 5′-GCTTCGGCAGCACATATACTAAAAT-3′ and reverse 5′-CGCTTCACGAATTTGCGTGTCAT-3′). qRT-PCR was performed using a Rotor-Gene 3000 real-time SYBR-green PCR system. The reactions were carried out in a 96-well optical plate at 95 ºC for 10 min and then amplified for 10 s at 90 ºC, followed by 1 min at 60 ºC for 40 cycles. The relative value of each miRNA to U6 RNA was calculated using the $2^{-\triangle\triangle Ct}$ method, where Ct is the number of cycles at which the application reaches a threshold, as determined by SDS software v1.2 (Applied Biosystems Inc). Thermal denaturation was administered at the conclusion of the PCR to determine the number of the products that were present in the reaction. Each reverse transcription and PCR assay were performed in triplicate.

miR-128 inhibitor transfection

The miR-128 inhibitor 5′-AAAGAGACCGGUUCACUGUGA-3′ and miR-128 inhibitor control 5′-CAGUACUUUUGUGUAGUACAAA-3′ were purchased from RiboBio Co Ltd, China. U251 cells in a volume of 100 μL DMEM medium were plated in each well of a 96-well plate. After 24 h of culture, the cells were transfected with 50 nmol/L miR-128 inhibitor or inhibitor control for 48 h using Lipofectamine 2000 (Invitrogen). After transfection, the wells were treated with Rh2 for different lengths of time in order to study cell proliferation, apoptosis, as well as caspase 3 and E2F3a expression.

Luciferase assay

A E2F3a 3′-untranslated region (UTR) reporter plasmid (pmiR-RB-REPORT™ 3′-UTR) was purchased from RiboBio Co Ltd, China. This vector was constructed by ligating a 1127-bp fragment to the type E2F3a 3′-UTR, which encompassed the target sequence for miR-128. The E2F3a 3′-UTR (accession number: NM0019490) was amplified from the genomic DNA using the following primers: forward 5′-AAACAATGCCAGGGTGTCTC-3′, reverse 5′-GCTCACACACGAAATGGCTA-3′. The empty plasmid containing only the E2F3a 3′-UTR was used as a control. The U251 cells were transfected with 50 nmol/L E2F3a 3′-UTR plasmid or empty E2F3a 3′-UTR plasmid for 48 h using Lipofectamine 2000 (Invitrogen). After transfection, the cells were treated with Rh2 for 24 h, and the luciferase assay was performed using TECAN Genios multifunctional microplate reader.

Western blotting

Cells were harvested and lysed in a buffer containing 50 mmol/L Tris-HCI, pH 8.0, 150 mmol/L NaCl, 1% NP40 and protease inhibitors (2 μg/mL leupeptin, 2 μg/mL pepstatin, 2 μg/mL aprotinin and 2 μg/mL PMSF, Sigma) for 30 min on ice. Lysates were centrifuged at 12 000 round per minute at 4 ºC for 20 min, and the supernatants were collected. The protein concentrations were determined using the Bradford method. The proteins were separated using SDS-PAGE and transferred to a nitrocellulose membrane. The membranes were incubated with rabbit anti-human E2F3a (Santa Cruz Biotechnology, Santa Cruz, CA, USA) or mouse anti-human β-actin antibody (Sigma, USA).

Apoptosis assay

Apoptosis was determined by annexin V and propidium iodide (PI) staining using the apoptosis detection kit (Beyotime, China) according to the manufacturer's instructions. Briefly, U251 cells were transfected with 50 nmol/L miR-128 inhibitor or miR-128 inhibitor control for 48 h, and then with 12 μg/mL Rh2 for 48 h. After treatment, the cells were washed with 50 mmol/L cold phosphate buffer (pH 7.5), centrifuged at 1200×*g* for 5 min, and suspended in binding buffer. The treated cells were incubated with annexin V and propidium iodide for 15 min at room temperature, after which the samples were analyzed for annexin V binding affinity within 1 h by flow cytometry[26].

Caspase 3 activity assay

Caspase 3 activity was determined using a caspase colorimetric assay kit (BioVision Research Products, USA) according to manufacturer's protocol. The assay is based on spectrophotometric detection of the chromophore ρ-nitroanilide (ρNA) after cleavage from the labeled substrate DEVD-ρNA. Briefly, 1×10^6 cells were first treated with 50 nmol/L miR-128 inhibitor or miR-128 inhibitor control for 48 h and then with a different dosage of Rh2 for various time. The cells were collected, washed with ice-cold PBS, and lysed in a lysis buffer. Cell lysates were measured for protease activity using a caspase-specific peptide conjugated with the color molecule ρNA. The caspase-cleaved chromophore ρNA was quantitated with a spectrophotometer at a wavelength of 405 nm[27].

Statistical analysis

The results were analyzed by one-way ANOVA or Student's *t* test. Both analyses were performed using SPSS 13.0 statistical software. A value of $P<0.05$ was considered statistically significant. All values were expressed in terms of mean±SEM or mean±SD.

Results

Effects of ginsenoside Rh2 on miRNA expression in human glioma U251 cells

To identify the miRNAs involved in Rh2-induced cytotoxicity, total RNA was extracted from U251 cells treated with 12 μg/mL Rh2 for 24 h for miRNA microarray analysis. The Exiqon microarray (Exiqon, Vedback, Denmark) containing 452 mature human miRNA probes was used to identify the cellular miRNA expression profile. miRNAs up-regulated more than 2-fold or down-regulated by 2-fold by Rh2 treatment were classified as being up-regulated or down-regulated miRNAs, respectively. Table 1 summarizes the results of Rh2-regulated miRNAs and their chromosomal locations are summarized. Of the 452 human miRNAs tested the microarray, 14 miRNAs were up-regulated and 12 miRNAs were down-

Table 1. Microarray analysis of miRNA expression in human gliomas U251 cells treated with ginsenoside Rh2.

miRNA	Fold (Mean±SEM)	*P* value	Localization	Up-down regulation
miR-15b	3.15±0.18	0.015	17q23.1	up
let-7c	2.03±0.15	0.010	21q11.2	up
let-7d	2.97±0.25	0.024	7q22.1	up
miR-29b	2.32±0.21	0.017	6q23.31	up
miR-106b	2.26±0.17	0.005	7q22.1	up
miR-125b	2.88±0.30	0.020	11q24.1	up
miR-128	3.04±0.19	0.013	2q21.3	up
miR-129	2.54±0.24	0.014	7q32.1	up
miR-137	2.13±0.14	0.008	1q21.3	up
miR-138	2.29±0.11	0.009	3q21.33	up
miR-181a	2.41±0.22	0.011	1q32.1	up
miR-181b	2.62±0.26	0.021	1q32.1	up
miR-181c	2.35±0.23	0.017	19p13.3	up
miR-323	2.57±0.18	0.013	14q32.31	up
miR-16	0.41±0.07	0.001	21q11.2	down
miR-18	0.37±0.10	0.007	9q22.2	down
miR-21	0.17±0.04	0.000	17q23.1	down
miR-25	0.23±0.09	0.003	7q22.1	down
miR-32	0.43±0.18	0.009	11q24.1	down
miR-92	0.39±0.11	0.005	21q11.2	down
miR-107	0.37±0.13	0.006	7q32.1	down
miR-155	0.28±0.09	0.002	3p21.33	down
miR-210	0.45±0.11	0.005	11p15.5	down
miR-218	0.37±0.21	0.012	4p15.31	down
miR-328	0.42±0.12	0.007	16q22.1	down
miR-370	0.38±0.07	0.003	14q32.2	down

1. The results presented fold change of signal ratio of 12 μg/mL Rh2-treated cells to untreated control cells.
2. The raw data were normalized and analyzed with software of MatLab version7.4, which produced an average value of the four spot replications of each miRNAs.
3. Chromosome localization of microRNAs as refered in miRBase sequences (http://microrna.sanger.ac.uk).

regulated in the Rh2-treated U251 cells. To further confirm the miRNA array results, we randomly selected the following four miRNAs: the up-regulated miR-128 and miR-15b as well as the down-regulated miR-21 and miR-25, and measured their expression levels by quantitative RT-PCR. As shown in Figure 2A, the results of quantitative RT-PCR for the four selected miRNAs were consistent with the miRNA array results, indicating that the results of miRNA array are reliable. To determine whether Rh2-induced miRNA expression occurred in other glioma cells, we measured the expression of miR-128 and miR-21 in human glioma cell lines, T98MG and A172. We observed consistent results in these two glioma cells as compared to U251 cells (Figure 2B).

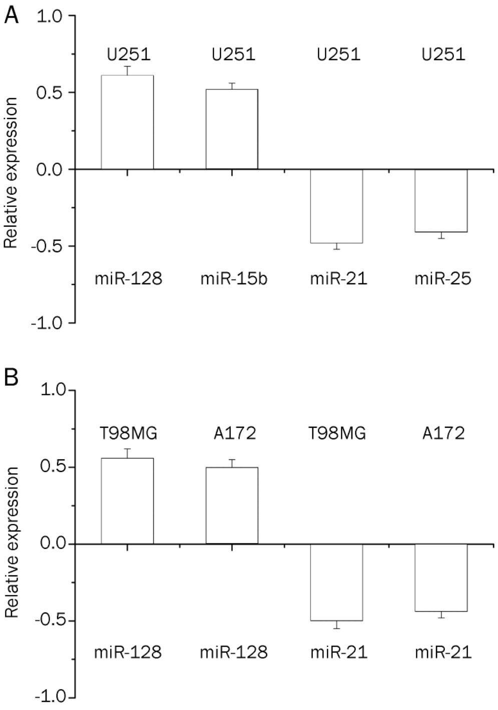

Figure 2. Validation of miRNA expression by quantitative real-time PCR. (A) The expressions of up-regulated miR-128 and miR-15b, as well as the down-regulated miR-21 and miR-25 in U251 cells were verified. The results of quantitative RT-PCR for the four selected miRNAs were consistent with the miRNA array results. (B) The expressions of miR-128 and miR-21 in human T98MG and A172 glioma cells were determined. The consistent results in these two giloma cells were observed as compared to U251 cells. The cells were treated with 12 μg/mL Rh2 for 24 h. Data were expressed as means±SEM of 3 independent experiments. Fold change of miRNA expression was presented in log 2 scale.

miRNA-128 mediated Rh2-induced growth inhibition in glioma cells

Given that miR-128 has been reported to inhibit glioma cell proliferation[17], we sought to further investigated its role in Rh2-induced cytotoxicity. We first investigated the effect of miR-128 inhibitor on miR-128 overexpression induced by Rh2 in human U251, T98MG and A172 glioma cells with qRT-PCR. As shown in Figure 3, inhibition of miR-128 significantly suppressed Rh2-induced miR-128 overexpression, as compared with miR-128 inhibitor control. These results demonstrate that anti-miR-128 treatment was effective for inhibition of miR-128 overexpression.

We next examined the antiproliferative effect of Rh2 in human glioma U251 cells. As shown in Figure 4, Rh2 treatment (6, 12, and 25 μg/mL) of U251 cells resulted in a dose-dependent inhibition of cell growth. In a time course study, 12 μg/mL Rh2 resulted in increasing levels of inhibition of cell growth up to 72 h, as measured by the cell counting kit-8 assay.

To investigate whether miR-128 could be involved in Rh2-induced growth inhibition, we transfected U251 cells with 50 nmol/L miR-128 inhibitor or inhibitor control for 48 h and then examined the alteration of Rh2-induced cell growth inhibition. Knockdown of miR-128 following transfection of miR-128 inhibitor significantly increased the proliferation of U251

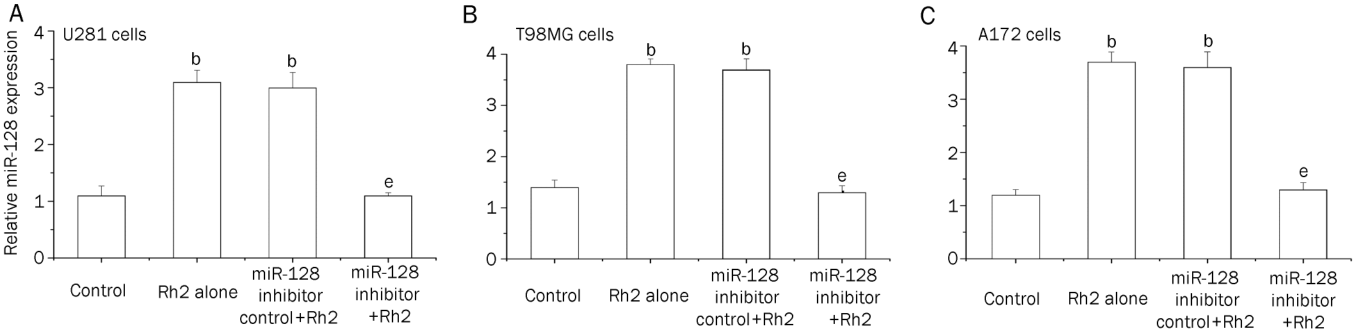

Figure 3. Transfection of miR-128 inhibitor significantly suppressed Rh2-induced miR-128 over-expression in U281 cells (A), T98MG cells (B), and A172 cells (C). The effects of miR-128 inhibitor transfection on Rh2-induced miR-128 overexpression in human U251, T98MG and A172 glioma cells were determined using qRT-PCR. The cells were transfected with 50 nmol/L miR-128 inhibitor or inhibitor control for 48 h, and then with Rh2 (12 μg/mL) for 24 h. The experiment was performed three times, each in triplicate. Data were expressed as means±SEM. $^{b}P<0.05$ compared with control. $^{e}P<0.05$ compared with Rh2 alone or miR-128 inhibitor control+Rh2.

cells treated with Rh2, as compared with the cells transfected with a miR-128 inhibitor control (Figure 5).

miRNA-128 mediated Rh2 induction of apoptosis in glioma U251 cells

Rh2 is known to exert its tumor growth inhibitory effect through the induction of apoptosis[28, 29]. We further examined whether Rh2-induced overexpression of miR-128 was able to inhibit apoptosis induced by this compound. The rate of apoptosis was measured by flow cytometry with annexin V and PI staining following Rh2 treatment. U251 cells were treated with 50 nmol/L miR-128 inhibitor or miRNA-128 inhibitor control for 48 h prior to treatment with 12 μg/mL Rh2 for 48 h. Transfection of the miR-128 inhibitor significantly prevented Rh2-induced apoptosis in U251 cells. The percentages of early apoptosis cells were 6.78%±2.11%, 25.77%±4.10%, 27.36%±5.33% and 11.25%±2.89% in the control, Rh2 alone, Rh2+miR-128 inhibitor control, and Rh2+miR-128 inhibitor group, respectively (Figure 6 A–D, the lower right quadrant). The percentages of late apoptotic cells were 7.62%±2.34%, 27.84%±3.56%, 28.07%±5.92% and 14.77%±3.62% in the control, Rh2 alone, Rh2+miR-128 inhibitor control, and Rh2+miR-128 inhibitor group, respectively (Figure 6 A–D, the upper right quadrant).

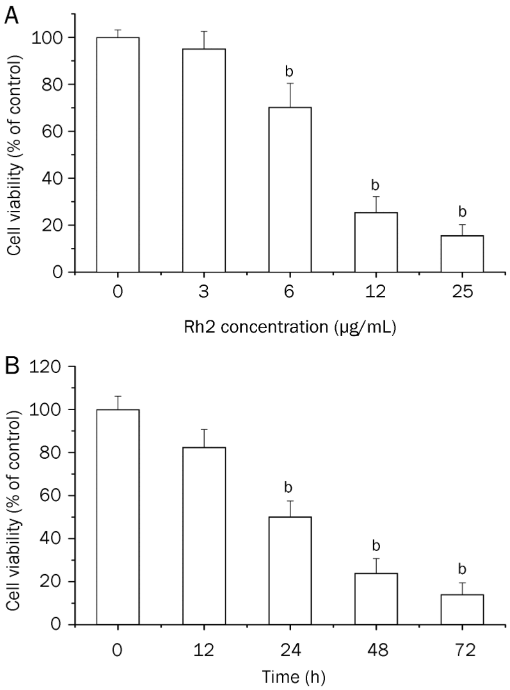

Figure 4. Rh2 inhibited viability of human glioma U251 cells determined using a CCK-8 assay. (A) Dose-dependent response. U251 cells were treated with Rh2 (3, 6, 12 and 25 μg/mL) for 48 h. (B) Time-dependent response. U251 cells were treated with Rh2 (12 μg/mL) for 12, 24, 48 and 72 h. The results represented three independent experiments. Data were expressed as means±SEM. $^{b}P<0.05$ compared with control.

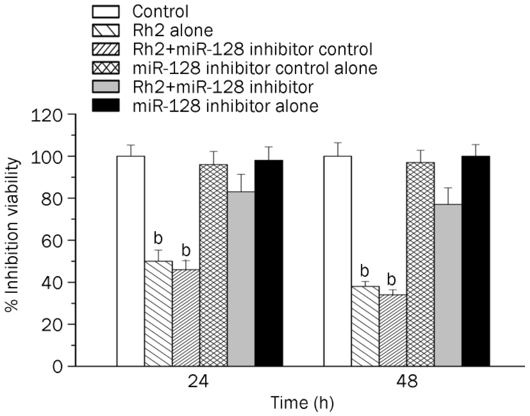

Figure 5. Transfection of miR-128 inhibitor prevented Rh2-induced cytotoxicity in glioma U251 cells. U251 cells were transfected with 50 nmol/L miR-128 inhibitor to knockdown miR-128. A miR-128 inhibitor control was used as negative control. At 48 h after transfection, the cells were treated with 12 μg/mL Rh2 for 24 or 48 h. Cell proliferation was determined using CCK-8 assay. $^{b}P<0.05$ compared with Rh2+miR-128 inhibitor. The experiment was performed three times, each in triplicate.

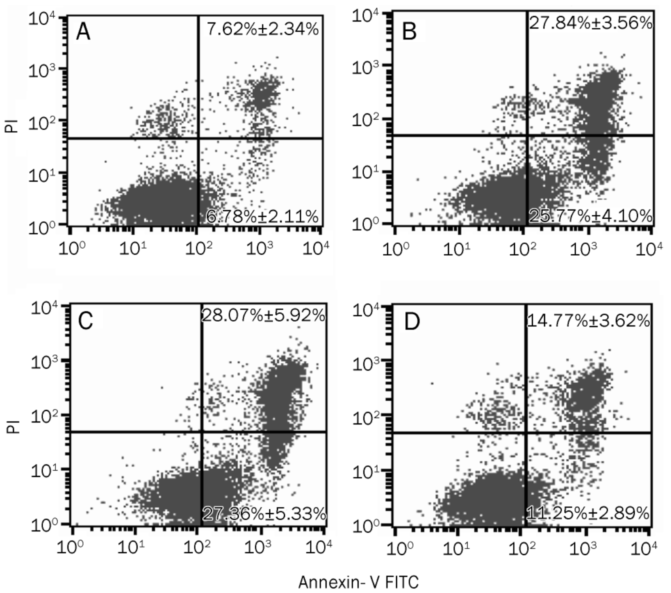

Figure 6. Transfection of miR-128 inhibitor inhibited Rh2-induced apoptosis in U251 cells. The cells were transfected with 50 nmol/L miR-128 inhibitor or inhibitor control for 48 h and then with Rh2 (12 μg/mL) for 48 h. Apoptosis was evaluated by annexin V and propidium iodide staining. The LR and UR quadrants indicated the percentage of early and late apoptotic cells, respectively, in control (A), Rh2 alone (B), Rh2+miR-128 inhibitor control (C) and Rh2+miR-128 inhibitor group (D). The experiment was performed three times, each in triplicate. Each point represented the means±SEM. There were significant differences between Rh2 alone or Rh2+miR-128 inhibitor control and control group, as well as between Rh2 alone and Rh2+miR-128 inhibitor group ($P<0.05$).

miRNA-128 mediated Rh2 induction of caspase 3 activity in glioma U251 cells

The previous studies have shown that the process of Rh2-induced apoptosis requires the activation of caspase 3 protease[28]. To assess whether miR-128 overexpression is involved in Rh2-induced caspase 3 activation in U251 cells, we measured caspase 3 activities after the cells were treated with Rh2 alone or Rh2 plus miR-128 inhibitor. Results from the colorimetric assay demonstrated that caspase 3 activity increased significantly in a dose- and time-dependent manner in Rh2-treated U251 cells (Figure 7). We also found that the knockdown of miR-128 by transfection of a miR-128 inhibitor significantly inhibited Rh2-induced caspase 3 activation, as compared to cells treated with miR-128 inhibitor control (Figure 7).

Rh2 suppressed the activity of luciferase reporter containing the E2F3a-3'-UTR and the level of E2F3a protein in glioma U251 cells

E2F3a is a validated target of miR-128, and has been reported to mediate miR-128-induced glioma cell growth inhibition[17]. To investigate whether overexpression of miR-128 induced by Rh2 affects E2F3a expression, the activity of a luciferase reporter containing the E2F3a-3′-UTR sequence was determined in U251 cells. The protein level of E2F3a was also assessed in U251 cells. We found that cells treated with 12 and 25 μg/mL Rh2 had suppressed luciferase activity (Figure 8A), indicative of transcriptional inhibition, as well as decreased the E2F3 protein expression in U251 cells (Figure 8B). To further explore whether miR-128 inhibitor prevents Rh2-induced inhibition of E2F3a expression, cells were transfected with 50 nmol/L miR-128 inhibitor for 48 h prior to 12 μg/mL Rh2 for 24 h. We also found that transfection of miR-128 inhibitor prevented Rh2-induced inhibition of E2F3a expression, as compared with cells transfected with miR-128 inhibitor control (Figure 8B).

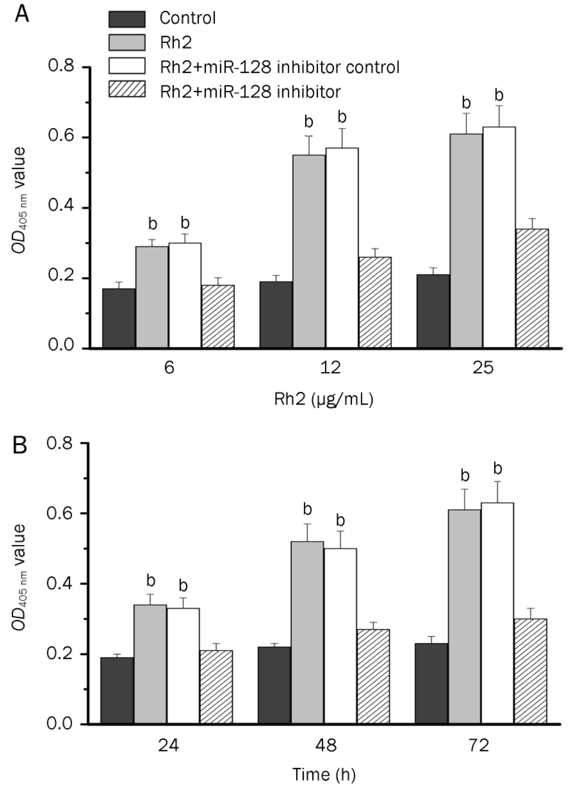

Figure 7. Transfection of miR-128 inhibitor inhibited Rh2-induced caspase 3 activation in U251 cells. (A) Transfection of miR-128 inhibitor inhibited the caspase 3 activation induced by treatment with 6, 12, and 25 μg/mL Rh2 for 48 h. The cells were transfected with 50 nmol/L miR-128 inhibitor or inhibitor control for 48 h, and then with Rh2 for 48 h. (B) Transfection of miR-128 inhibitor inhibited the caspase 3 activation induced by treatment with 12 μg/mL Rh2. The cells were transfected with 50 nmol/L miR-128 inhibitor or inhibitor control for 48 h, and then with Rh2 for 24, 48, and 72 h. Caspase 3 avtivity was determined using colorimetric assay. The experiment was performed three times each in triplicate. Mean±SEM. ${}^{b}P<0.05$ compared with control or miR-128 inhibitor+Rh2.

Discussion

Many miRNAs have been reported to have an oncogenic or a tumor suppressor function and to be involved in cell prolif-

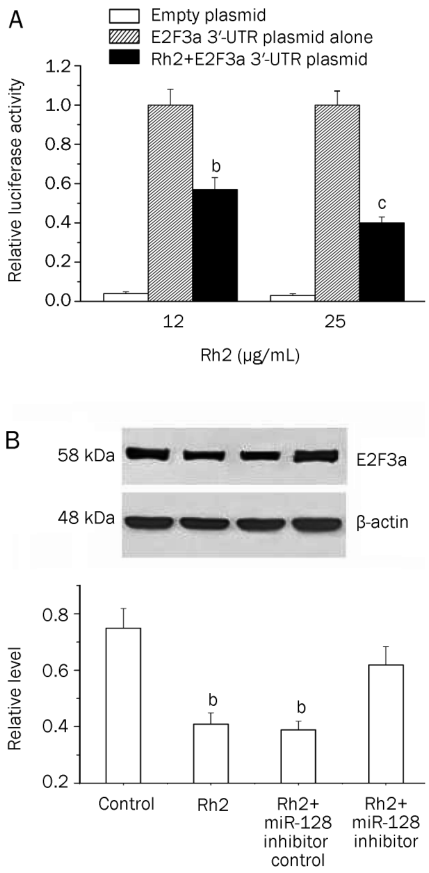

Figure 8. Rh2 suppressed the activity of luciferase reporter containing the E2F3a-3′-UTR and the level of E2F3a protein in U251 cells. (A) Rh2 inhibited the luciferase activity of E2F3a-3′-UTR. The activity of luciferase reporter containing the E2F3a-3′-UTR sequence was measured by TECAN Genios multifunctional microplate reader. The cells were transfected with 50 nmol/L E2F3a 3′-UTR plasmid or empty E2F3a 3′-UTR plasmid for 48 h using Lipofectamine 2000 (Invitrogen). After transfection, the cells were treated with Rh2 for 24 h, and the luciferase assay was performed. The experiment was performed three times, each in triplicate. Mean±SEM. $^{b}P<0.05$, $^{c}P<0.01$ compared to E2F3a 3′-UTR plasmid alone. (B) Transfection of miR-128 inhibitor prevented Rh2-induced inhibition of E2F3a protein expression in U251 cells, as compared with Rh2+miR-128 inhibitor control. The cells were transfected with 50 nmol/L miR-128 inhibitor for 48 h and then with 12 μg/mL Rh2 for 24 h. β-actin was used as a loading control in Western blot. $^{b}P<0.05$ as compared to control or Rh2+miR-128 inhibitor.

eration, growth and apoptosis[11, 30]. However, little is known about the ralationship between miRNA expression and Rh2-induced anti-proliferation. The present study demonstrated that Rh2, a natural glycoside from the Ginseng, altered miRNA expression in human glioma U251 cells, including 14 up-regulated and 12 down-regulated miRNAs. We verified that miR-128 was up-regulated in human U251, T98MG and A172 glioma cells by quantitative real-time PCR. Among the miRNAs regulated by Rh2, some have been reported to be tumor suppressors. For instance, miR-128 and miR-181 function as tumor suppressors and trigger growth inhibition in human glioma cells. In addition, knockdown or reduction of miR-21 led to glioma cell apoptosis and cell growth inhibition, reduced invasiveness and suppressed tumorigenicity[31]. Our findings indicate that miRNAs play important roles in Rh2-induced antiproliferation in glioma cells.

miR-128 is a brain-enriched miRNA whose overexpression inhibits glioma cell proliferation[17]. In our study, miR-128 was up-regulated by Rh2. To further investigate miR-128's role in Rh2-induced cytotoxicity, a miR-128 inhibitor was used to diminish miR-128 overexpression induced by Rh2 and led to an increase in U251 cell proliferation. Our study demonstrated that Rh2 could inhibit the proliferation of glioma U251 cells in a dose- and time-dependent manner. Moreover, we found that miR-128 inhibitor significantly inhibited miR-128 up-regulation and restored cell viability in Rh2-treated cells, implying that miR-128 overexpression is one of the principal mechanisms by which Rh2 mediates anti-proliferation in U251 cells.

Activation of apoptotic pathways is a key mechanism by which chemotherapeutic drugs kill cancer cells. Rh2 has been reported to induce apoptosis in glioma cells[28]. Here, we demonstrated that Rh2 could induce apoptosis of glioma U251 cells in a dose- and time-dependent manner, illustrated by annexin V and propidium iodide staining. Moreover, we found that treatment with a miR-128 inhibitor markedly inhibited Rh2-induced apoptosis in these cells. Previous studies have shown that Rh2 could induce apoptosis through activation of the caspase pathway in human neuroblastoma[28]. Consistent with the previous finding, our results showed that Rh2 significantly increased caspase 3 activity in U251 cells. We also found that knockdown of miR-128 expression prevented Rh2-induced caspase 3 activation. These results suggest that miR-128-mediated apoptosis is a key mechanism in Rh2-induced cytotoxicity in U251 cells.

In addition, our results showed that knockdown of Rh2-induced miR-128 overexpression by transfection of miR-128 inhibitor only partially prevented Rh2-induced anti-proliferation in glioma U251 cells. However, in our initial experiments, we transfected a miR-128 mimic into U251 cells and observed a reduced proliferation of the cells. In cells treated with a miR-128 mimic in addition to Rh2, the compound did have an anti-proliferation effect, although there was no significant difference compared with miR-128 mimic control (data not shown). These results suggest that there may be additional miRNAs that also mediate Rh2-induced cytotoxicity in glioma cells. For instance, miR-21 has been found to function as an oncogene and to be abundant and up-regulated in glioma cells[32, 33]. Taken together with our findings, these results suggest that the fold change values of miR-21 was larger than those of miR-128. In fact, the expression levels of miR-128 were lower than those of miR-21 in our microarray results. Therefore, miR-21 appears to be a better candidate for study. In the present study, we focused on miR-128 because it is a brain-enriched miRNA and has strong anti-proliferative roles in glioma development. However, our results do not exclude the involvement of miR-21 in Rh2-induced cytotoxicity. Further studies are needed to investigate the molecular mechanism of miR-21 in Rh2-induced anti-proliferative effects.

Computational algorithms showed several hundreds of putative targets of miR-128 (http://www.microrna.org). A recent study also showed that the transcription factor E2F3a is a direct target of miR-128[17]. Considering that overexpression of miR-128 can inhibit proliferation of glioma cells by targeting E2F3a, we wondered whether Rh2 could affect E2F3a via induction of miR-128 overexpression. We found that Rh2 inhibited E2F3a protein expression using Western blotting, an effect that was reversed following treatment with an miR-128 inhibitor. These results suggest that Rh2-induced inhibition of glioma cell proliferation may be mediated by negatively regulating the expression of E2F3a, a miR-128 target gene. E2F3a has been found to stimulate cell proliferation, apoptosis and carcinogenesis in a transgenic mouse model[34]. E2F3a protein expression negatively correlated with the expression level of miR-128 in glioma cells[17]. The sequence of miR-128 and its target site in the 3′-UTR of E2F3a is shown in Figure 9, as predicted by Miranda software (http://www.microrna.org). The 5′-end of miR-128 is complementary to the 3′-UTR of E2F3a, which mediates post-transcriptional negative regulation of E2F3a via RNA duplex formation.

```
human E2F3a 3′-UTR 2018: 5′-UUAAGUGCCUACUGGAAAUGCACUGUG-3′
                              |||  |    ||  ||    |  |||||||
                miR-128: 3′-UUUUCUC ......UGGCC ...... AAGUGACAC-5′
```

Figure 9. Sequence of miR-128 and its target site in the 3’-UTR of E2F3a.

Except for E2F3a, miR-128 has been reported to exert its anti-proliferative and stem cell self-renewal effects in glioma cells through targeting Bmi-1, a stem cell renewal factor[33]. In our study, we could not investigate the effect of Rh2 on Bmi-1 and stem cell self-renewal effects in glioma cells. Therefore, it would be interesting to examine the effects of Rh2 has on stem cell self-renewal through miR-128-mediated Bmi-1 pathway in human glioma neurosphere cultures that possess features of glioma "stem-like" cells.

In conclusion, the present study shows that ginsenoside Rh2 exerts its anti-proliferative effect in U251 glioma cells in part by up-regulation of miRNA-128 expression. This finding provides new insight into the understanding of the molecular mechanism of Rh2-mediated cytotoxicity.

Acknowledgements

This work was supported by the National Natural Science Foundation of China (No̲ 30872660).

Author contribution

Hua FENG and Nan WU designed research; Nan WU and Guo-cai WU performed research; Rong HU and Mei LI contributed new analytical tools and reagents; Rong HU and Mei LI analyzed data; and Nan WU wrote the paper.

References

1 Franceschi E, Tosoni A, Bartolini S, Mazzocchi V, Fioravanti A, Brandes AA. Treatment options for recurrent glioblastoma: pitfalls and future trends. Expert Rev Anticancer Ther 2009; 9: 613−9.

2 Claes A, Idema AJ, Wesseling P. Diffuse glioma growth: a guerilla war. Acta Neuropathol 2007; 114: 443−58.

3 Pang JC, Kwok WK, Chen Z, Ng HK. Oncogenic role of microRNAs in brain tumors. Acta Neuropathol 2009; 117: 599−611.

4 Mendes ND, Freitas AT, Sagot MF. Current tools for the identification of miRNA genes and their targets. Nucleic Acids Res 2009; 37: 2419−33.

5 Novakova J, Slaby O, Vyzula R, Michalek J. MicroRNA involvement in glioblastoma pathogenesis. Biochem Biophys Res Commun 2009; 386: 1−5.

6 Croce CM, Calin GA. miRNAs, cancer, and stem cell division. Cell 2005; 122: 6−7.

7 Hagen JW, Lai EC. microRNA control of cell-cell signaling during development and disease. Cell Cycle 2008; 7: 2327−32.

8 Lewis BP, Burge CB, Bartel DP. Conserved seed pairing, often flanked by adenosines, indicates that thousands of human genes are microRNA targets. Cell 2005; 120: 15−20.

9 Calin GA, Sevignani C, Dumitru CD, Hyslop T, Noch E, Yendamuri S, *et al*. Human microRNA genes are frequently located at fragile sites and genomic regions involved in cancers. Proc Natl Acad Sci USA 2004; 101: 2999−3004.

10 Zhang L, Huang J, Yang N, Greshock J, Megraw MS, Giannakakis A, *et al*. microRNAs exhibit high frequency genomic alterations in human cancer. Proc Natl Acad Sci USA 2006; 103: 9136−41.

11 Cho WC. OncomiRs: the discovery and progress of microRNAs in cancers. Mol Cancer 2007; 6: 60.

12 Stahlhut Espinosa CE, Slack FJ. The role of microRNAs in cancer. Yale J Biol Med 2006; 79: 131−40.

13 Ciafre SA, Galardi S, Mangiola A, Ferracin M, Liu CG, Sabatino G, *et al*. Extensive modulation of a set of microRNAs in primary glioblastoma. Biochem Biophys Res Commun 2005; 334: 1351−8.

14 Chen Y, Liu W, Chao T, Zhang Y, Yan X, Gong Y, *et al*. MicroRNA-21 down-regulates the expression of tumor suppressor PDCD4 in human glioblastoma cell T98G. Cancer Lett 2008; 272: 197−205.

15 Li Y, Tan W, Neo TW, Aung MO, Wasser S, Lim SG, *et al*. Role of the miR-106b-25 microRNA cluster in hepatocellular carcinoma. Cancer Sci 2009; 100: 1234−42.

16 Xia H, Qi Y, Ng SS, Chen X, Chen S, Fang M, *et al*. MicroRNA-15b regulates cell cycle progression by targeting cyclins in glioma cells. Biochem Biophys Res Commun 2009; 380: 205−10.

17 Zhang Y, Chao T, Li R, Liu W, Chen Y, Yan X, *et al*. MicroRNA-128 inhibits glioma cells proliferation by targeting transcription factor E2F3a. J Mol Med 2009; 87: 43−51.

18 Shibata S. Chemistry and cancer preventing activities of ginseng saponins and some related triterpenoid compounds. J Korean Med Sci 2001; 16 Suppl: S28−37.

19 Lai DM, Tu YK, Liu IM, Chen PF, Cheng JT. Mediation of beta-endorphin by ginsenoside Rh2 to lower plasma glucose in streptozotocin-induced diabetic rats. Planta Med 2006; 72: 9−13.

20 Park EK, Choo MK, Oh JK, Ryu JH, Kim DH. Ginsenoside Rh2 reduces ischemic brain injury in rats. Biol Pharm Bull 2004; 27: 433−6.

21 Park EK, Choo MK, Kim EJ, Han MJ, Kim DH. Antiallergic activity of ginsenoside Rh2. Biol Pharm Bull 2003; 26: 1581−4.

22 Kim HE, Oh JH, Lee SK, Oh YJ. Ginsenoside RH-2 induces apoptotic cell death in rat C6 glioma via a reactive oxygen- and caspase-dependent but Bcl-X(L)-independent pathway. Life Sci 1999; 65: PL33−40.

23 Zeng XL, Tu ZG. *In vitro* induction of differentiation by ginsenoside Rh2 in SMMC-7721 hepatocarcinoma cell line. Pharmacol Toxicol 2003; 93: 275−83.

24 Cheng CC, Yang SM, Huang CY, Chen JC, Chang WM, Hsu SL. Molecular mechanisms of ginsenoside Rh2-mediated G_1 growth arrest and apoptosis in human lung adenocarcinoma A549 cells. Cancer Chemother Pharmacol 2005; 55: 531−40.

25 Wen XY, Wu SY, Li ZQ, Liu ZQ, Zhang JJ, Wang GF, *et al*. Ellagitannin (BJA3121), an anti-proliferative natural polyphenol compound, can regulate the expression of MiRNAs in HepG2 cancer cells. Phytother Res 2009; 23: 778−84.

26 Wang Q, Li J, Gu J, Huang B, Zhao Y, Zheng D, *et al*. Potentiation of (−)-epigallocatechin-3-gallate-induced apoptosis by bortezomib in multiple myeloma cells. Acta Biochim Biophys Sin (Shanghai) 2009; 41: 1018−26.

27 Liu JJ, Liu WD, Yang HZ, Zhang Y, Fang ZG, Liu PQ, *et al*. Inactivation of PI3k/Akt signaling pathway and activation of caspase-3 are involved in tanshinone I-induced apoptosis in myeloid leukemia cells *in vitro*. Ann Hematol 2010; 89: 1089-97.

28 Kim YS, Jin SH. Ginsenoside Rh2 induces apoptosis via activation of caspase-1 and -3 and up-regulation of Bax in human neuroblastoma. Arch Pharm Res 2004; 27: 834−9.

29 Kim YS, Jin SH, Lee YH, Kim SI, Park JD. Ginsenoside Rh2 induces apoptosis independently of Bcl-2, Bcl-xL, or Bax in C6Bu-1 cells. Arch Pharm Res 1999; 22: 448−53.

30 Hagen JW, Lai EC. microRNA control of cell-cell signaling during development and disease. Cell Cycle 2008; 7: 2327−32.

31 Zhou X, Zhang J, Jia Q, Ren Y, Wang Y, Shi L, *et al*. Reduction of miR-21 induces glioma cell apoptosis via activating caspase 9 and 3. Oncol Rep 2010; 24: 195−201.

32 Shi L, Chen J, Yang J, Pan T, Zhang S, Wang Z. MiR-21 protected human glioblastoma U87MG cells from chemotherapeutic drug temozolomide induced apoptosis by decreasing Bax/Bcl-2 ratio and caspase-3 activity. Brain Res 2010; 1352: 255−64.

33 Godlewski J, Nowicki MO, Bronisz A, Williams S, Otsuki A, Nuovo G, *et al*. Targeting of the Bmi-1 oncogene/stem cell renewal factor by microRNA-128 inhibits glioma proliferation and self-renewal. Cancer Res 2008; 68: 9125−30.

34 Paulson QX, McArthur MJ, Johnson DG. E2F3a stimulates proliferation, p53-independent apoptosis and carcinogenesis in a transgenic mouse model. Cell Cycle 2006; 5: 184−90.

npg
Acta Pharmacologica Sinica (2011) 32: 354–360

www.nature.com/aps

Original Article

The role of *Med19* in the proliferation and tumorigenesis of human hepatocellular carcinoma cells

Shao-wu ZOU, Kai-xing AI, Zhi-gang WANG, Zhou YUAN, Jun YAN, Qi ZHENG*

General Surgery Department, Shanghai Jiao Tong University Sixth People's Hospital, Shanghai 200233, China

---

Aim: To explore the role of *Med19*, a component of the Mediator complex that coactivates DNA-binding transcription factors, in the proliferation and tumorigenesis of human hepatocellular carcinoma cells.
Methods: The human hepatocellular carcinoma cell lines HepG2 and Hep3B were infected with lentiviral vectors encoding interfering RNA (RNAi) targeting the *Med19* gene. To further confirm the inhibitory effects of RNAi vectors on *Med19* gene expression, quantitative real-time RT-PCR and Western blotting assays were used. The proliferation of HepG2 and Hep3B cells after transduction with the *Med19*-RNAi-Lentivirus vector was evaluated by MTT conversion, BrdU incorporation, colony formation, and cell-cycle assays *in vitro*. In addition, the ability of the *Med19*-RNAi-Lentivirus vector-infected Hep3B cells to form tumors after inoculation into nude mice was determined.
Results: Recombinant lentiviral vectors expressing small interfering RNA (siRNA) against *Med19* were constructed and were found to efficiently downregulate *Med19* mRNA and protein levels in HepG2 and Hep3B cells. Furthermore, the inhibition of *Med19* by RNAi dramatically reduced hepatocellular carcinoma cell proliferation, induced cell-cycle arrest in the G_0/G_1 phase, and suppressed tumor formation.
Conclusion: These results provide new evidence of an important role for *Med19* in the development of hepatocellular carcinomas, suggesting that lentivirus-mediated RNAi to target *Med19* is a potential tool for inhibiting cancer cell proliferation and tumorigenesis.

Keywords: hepatocellular carcinoma; *Med19*; RNAi; lentivirus vector; proliferation; tumorigenesis

---

Acta Pharmacologica Sinica (2011) 32: 354–360; doi: 10.1038/aps.2010.223

Introduction

Hepatocellular carcinoma (HCC) is a malignant tumor type with a high rate of relapse and metastasis; it is the third leading cause of cancer-related deaths worldwide. The incidence of HCC has been increasing at an alarming rate on a global scale over the past two decades[1–5]. Despite a recent improvement in long-term survival rates, the prognosis of HCC is still poor. Therefore, it is necessary to find new therapeutic molecular targets and therapeutic strategies for the prevention and treatment of HCC. The recent discovery of RNA interference (RNAi), a powerful tool to induce loss-of-function phenotypes through the posttranscriptional silencing of gene expression, has provided new possibilities for cancer therapy[6–8].

As a multi-protein coactivator, the Mediator (Med) complex is an essential component of the RNA polymerase II (pol II)-mediated transcription complex and is required for the transcriptional activation of pol II-transcribed genes by transcription factors[9, 10]. In addition to stimulating basal transcription, the Mediator complex plays a crucial role in the activation and repression of eukaryotic mRNA synthesis[11, 12]. The Mediator complex, which consists of at least 20 subunits with multiple activities, including Rox3 (Med19), was first characterized through biochemical and genetic studies in *Saccharomyces cerevisiae* in the early 1990s[13, 14].

In the human genome, the Mediator complex subunit 19 (*Med19*) gene, also known as lung cancer metastasis-related protein 1 (LCMR1), is located at chr11q12.1. The Med19 protein can modulate both basal and heat-shock gene transcription, which are capabilities of a distinct functional module (head) within the Mediator complex. The *Med19* gene was first cloned from a human lung large-cell carcinoma cell line through differential display reverse-transcription PCR by researchers at the Chinese General Hospital of the People's Liberation Army, Beijing, China, in 2003. However, the function of *Med19* in the progression of hepatocellular carcinomas has not been investigated.

---

* To whom correspondence should be addressed.
E-mail shqizheng@163.com
Received 2010-06-21 Accepted 2010-12-08

To study the role of *Med19* in HCC cells, *Med19* was silenced in HepG2 and Hep3B cells by small interfering RNA (siRNA), expressed by recombinant lentiviral vectors[15]. The effect of *Med19* knockdown on cancer cell proliferation, cell-cycle arrest, and tumorigenesis was investigated. In addition, the expression of cell-cycle-related proteins in *Med19*-RNAi-Lentivirus vector-infected cells was analyzed to elucidate the possible mechanism of HCC cell proliferation.

Materials and methods

Lentiviral vectors encoding small interfering RNAs targeting *Med19*

The small interfering RNA (siRNA) sequences targeting the human *Med19* gene (GenBank accession number NM_153450) were designed by Genechem Co, Ltd, Shanghai, China. Lentiviral vectors encoding *Med19* siRNA and green fluorescent protein (GFP) (Genechem Co, Ltd, Shanghai, China) were constructed. After screening to validate potential siRNAs, the *Med19* siRNA target sequence (5'-GGTGAAGGAGAAGCTAAGT-3') was selected. The recombinant lentivirus particles encoding siRNA targeting *Med19* (*Med19*-RNAi-Lentivirus) and the negative-control lentivirus (pGC-SIL-GFP) were packaged. To confirm the specificity of the RNAi experiment, *Med19* gene expression was rescued with a cDNA containing silent third-codon point mutations in the targeted region, which made the cDNA resistant to silencing by the siRNA targeting *Med19*.

Cell culture and lentivirus infection

The human hepatocellular carcinoma cell lines HepG2 and Hep3B were purchased from the Cell Bank Type Culture Collection of the Chinese Academy of Sciences (Shanghai, China) and maintained in Dulbecco's modified Eagle's medium (DMEM, Gibco BRL, Grand Island, NY, USA) with 10% fetal bovine serum (FBS, Gibco BRL, Grand Island, NY, USA) at 37 ºC in a humidified atmosphere of 5% CO_2. HepG2 and Hep3B cells were seeded in 6-well plates (at a density of 5×10^4 cells/well) and infected with lentivirus at an MOI (multiplicity of infection) of 20 when the cells reached 30% confluency. After 24 h of infection at 37 ºC, the medium was replaced by fresh DMEM and incubated for another 48 h.

Real-time RT-PCR

Total RNA was extracted from naïve cells and lentivirus-infected cells with Trizol (Life Technologies, Inc, Grand Island, NY, USA) according to the manufacturer's instructions. The first-strand cDNA was synthesized using 2 μg of total RNA, 10 units of M-MLV reverse transcriptase (Promega, Madison, WI, USA), and 0.5 μg of oligo (dT) primer in a reaction volume of 20 μL.

Next, 1 μL of the cDNA reaction product was used for quantitative real-time PCR with SYBR Master Mixture (Takara, Otsu, Japan) on IQ5 (BioRad, Hercules, CA, USA), with reaction conditions consisting of an initial denaturation at 95 ºC for 15 s, followed by 45 cycles at 95 ºC for 5 s and 60 ºC for 30 s. The PCR primer sequences for the *Med19* target gene and the beta-actin internal control gene are listed in Table 1. The relative quantity of *Med19* mRNA, normalized to beta-actin and relative to a calibrator, was calculated as $2^{-\Delta\Delta CT}$, where $\Delta\Delta CT=(CT_{Med19} - CT_{\text{beta-actin}})$ sample – $(CT_{Med19} - CT_{\text{beta-actin}})$ calibrator[16].

Table 1. Base sequence of primers for quantitative real-time RT-PCR.

	Primers	Base sequence
Med19	Forward	5'-TGACAGGCAGCACGAATC-3'
	Reverse	5'-CAGGTCAGGCAGGAAGTTAC-3'
Beta-actin	Forward	5'-GGCGGCACCACCATGTACCCT-3'
	Reverse	5'-AGGGGCCGGACTCGTCATACT-3'

Western blotting

Cells from each group were lysed on d 7 after infection by using pre-cooled lysis buffer. Next, 30 μg of lysates were loaded into each well and run on a 10% polyacrylamide gel at 30 mA for 2 h, followed by semidry transfer for a further 2 h. After being blocked with 5% non-fat dry milk for 1 h at room temperature, the membrane was probed with protein-specific antibodies overnight at 4 °C. Next, the membrane was washed with TBST three times and incubated for 2 h with the secondary antibody at room temperature. Following another round of washing with TBST, the membrane was developed using enhanced chemiluminescence (ECL) (Amersham Life Sciences, Amersham, UK). The primary antibodies for Med19 (Abcam, Cambridge, UK) and GAPDH (Santa Cruz Biotechnology, Santa Cruz, CA, USA) were employed at dilutions of 1:200 and 1:6000, and the secondary antibodies were utilized at working concentrations of 1:5000 and 1:6000 for anti-goat IgG and anti-mouse IgG (Santa Cruz Biotechnology, Santa Cruz, CA, USA), respectively.

Cell proliferation assay

Cell viability was assessed by methyl thiazol tetrazolium (MTT) assay, as in a previous report[17], and the absorbance was measured at 570 nm (Sigma-Aldrich Corp, St Louis, MO, USA). Analysis of DNA synthesis, as measured by 5'-bromodeoxyuridine (BrdU, Sigma-Aldrich Corp, St Louis, MO, USA) incorporation, was performed according to a previous report[18]. Results of the BrdU assay were recorded at 490 nm at 24 and 48 h after the seeding of cells.

Colony-forming assay

Cells from the normal control, infected with *Med19*-RNAi-Lentivirus vector and negative-control lentivirus vector, were collected by trypsinization and suspended in complete growth medium, and 200 cells from each group were then seeded onto 6-well plates for each well. After being cultured at 37 ºC for 2 weeks, visible colonies were detected with a fluorescence microscope. After fixation in paraformaldehyde, the colonies were stained with Giemsa for 10 min and photographed with a digital camera. Finally, the number of colonies formed by each group of cells was counted.

Cell-cycle assay and analysis of cell-cycle-related proteins

Hep3B cells were cultured on 6-well plates and infected with the *Med19*-RNAi-Lentivirus vector and the negative-control lentivirus vector. After reaching 90% confluency, cells were harvested for cell-cycle detection by propidium-iodide staining and were subsequently analyzed by flow cytometry.

The expression of the cell-cycle-related proteins CDKN1A (cyclin-dependent kinase inhibitor 1A, p21), CDC25A (cell division cycle 25A), CDC25B (M-phase inducer phosphatase 2), and CDC45L (cell division control protein 45 homolog) in *Med19*-RNAi-Lentivirus-infected Hep3B cells was detected by Western blotting analysis. The following antibodies were used: rabbit polyclonal to p21 (Abcam, Cambridge, UK; ab7960), rabbit polyclonal to CDC25A (Novus Biologicals, Littleton, CO, USA; NB100-213), rabbit polyclonal to CDC25B (Novus Biologicals, Littleton, CO, USA; NB100-91690), and mouse monoclonal to CDC45L (Abcam, Cambridge, UK; ab56476).

Tumor formation in nude mice

To assay tumor formation in nude mice, parental cells and Hep3B cells infected with the *Med19*-RNAi-Lentivirus vector and the negative-control lentivirus vector were trypsinized, counted, and resuspended in PBS. One hundred microliters of PBS containing 1×10^6 cells were then injected into 4- to 5-week-old female nude mice (n=8 per group). Tumor volumes were assessed every other day by measuring two perpendicular diameters with vernier calipers and was calculated using the formula $(L\times W^2)/2$, where L is the long diameter and W is the short diameter. The mice were sacrificed 30 d after injection and were examined for subcutaneous tumor growth.

Statistical analysis

The expression of *Med19* was considered reduced if its relative mRNA level ($2^{-\Delta\Delta CT}$) was less than 1.0; otherwise, *Med19* expression was determined to be preserved. When the 95% confidence interval (CI) of the sample did not overlap that of its calibrator, we considered the result statistically significant. When the P-value was less than 0.05, we considered the difference statistically significant.

Results

GFP expression of cells infected with recombinant lentivirus

We constructed a lentiviral vector system to express siRNA targeting *Med19* and to express GFP as a reporter gene. To determine whether the recombinant lentiviruses were able to infect human HCC cell lines, cells infected with the *Med19*-RNAi-Lentivirus (pKD) vector and the negative-control lentivirus (pNC) vector were observed under a fluorescence microscope. Seventy-two hours postinfection, more than 80% of the cells expressed GFP (Figure 1A), which indicated high-efficiency infection by the *Med19*-RNAi-Lentivirus vector.

Silencing of the *Med19* gene by RNAi

To verify that the *Med19* gene was silenced by the pKD vector's siRNA, we determined the mRNA levels in uninfected, pNC-infected, and pKD-infected cells through real-time RT-PCR. Cells infected with pKD exhibited significantly reduced levels of *Med19* mRNA compared with pNC-infected cells and uninfected cells ($P<0.05$, Figure 1B).

Inhibition of *Med19* protein levels by RNAi

After verifying the reduction in *Med19* mRNA levels in pKD-infected cells, we detected Med19 protein levels in cell lysates using Western blot analysis with GAPDH as an internal control. Compared with that of uninfected and pNC-infected cells, the Med19 protein levels in cells infected with the pKD vector decreased greatly (Figure 1C).

Effects of *Med19* knockdown on cell proliferation

To investigate the effect of *Med19* knockdown on cell proliferation, MTT and BrdU assays were performed. The growth

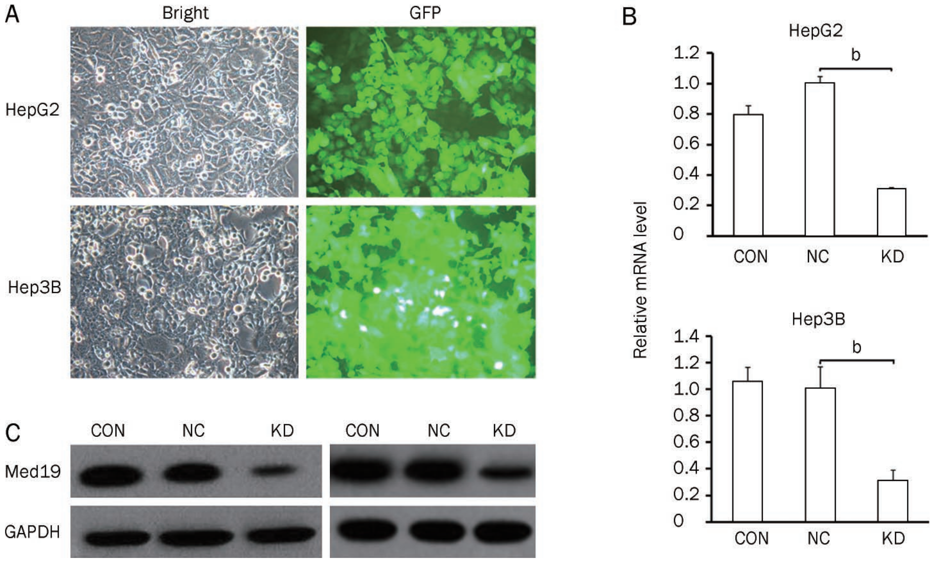

Figure 1. Determination of infection efficiency in the human hepatocellular carcinoma cell lines HepG2 and Hep3B. (A) Images recorded under a fluorescence microscope. Expression analyses of *Med19* mRNA (B) and protein (C) levels by quantitative real-time RT-PCR and Western blot analysis in uninfected HepG2 and Hep3B cells (CON), cells infected with the pNC vector (NC), and cells infected with the pKD vector (KD). The beta-actin gene and the GAPDH protein are the internal controls for quantitative real-time RT-PCR and Western blot analysis, respectively. Significant difference from NC ($^bP<0.05$).

curve obtained from the MTT assay indicated that the proliferative ability of pKD-infected cells was significantly decreased when compared with that of pNC-infected cells (*P*<0.05, Figure 2A and 2B). In the BrdU incorporation assay, the DNA synthesis capacity of pKD-infected HepG2 and Hep3B cells was significantly reduced (*P*<0.05 *vs* pKD infected, Figure 2C and 2D). The results of these experiments suggest that the depletion of endogenous *Med19* expression in HCC cells correlates with impaired cell growth and DNA synthesis and demonstrate that Med19 is a key factor in cancer cell proliferation. More importantly, when Hep3B cells was treated with a vector encoding a *Med19* wobble mutant (Rescue-*Med19*), which preserves the same amino acid sequence as pKD but contains three point mutations in the target nucleotide sequence, cell proliferation was substantially rescued (*P*<0.05 *vs* pKD infected, Figure 2E). The above results indicate that the knockdown of endogenous *Med19* by RNAi inhibited the proliferation in HCC cells, and the rescued *Med19* expression validated the specificity of the siRNA targeting.

Effect of *Med19*-RNAi on the colony-forming ability of HCC cells

To detect whether *Med19* has a significant effect on the colony-forming capacity of human HCC cells, a colony-forming experiment was performed on HepG2 and Hep3B cells. Our data indicated that the number and size of colonies formed from pKD-infected cells were strongly decreased when compared with those of uninfected and pNC-infected cells (Figure 3A and 3B), suggesting that the reduced expression of *Med19* could significantly inhibit colony formation in human HCC cells.

Effect of *Med19* knockdown on cell-cycle distribution

To elucidate whether the pKD-mediated knockdown of *Med19* has any impact on the cell-cycle status of HCC cells, all three groups of Hep3B cells were subjected to a flow cytometry assay 7 d after infection. pKD-infected Hep3B cells exhibited a greater proportion of cells in the G_0/G_1 phase when compared with pNC-infected cells (*P*<0.05, Figure 4A). We next explored the expression of cell cycle-related proteins to investigate the possible role of Med19 in the control of mitotic cellular process. As shown in Figure 4B, the expression of CDKN1A was increased, whereas the expression of CDC25A, CDC25B, and CDC45L was diminished, in pKD-infected Hep3B cells.

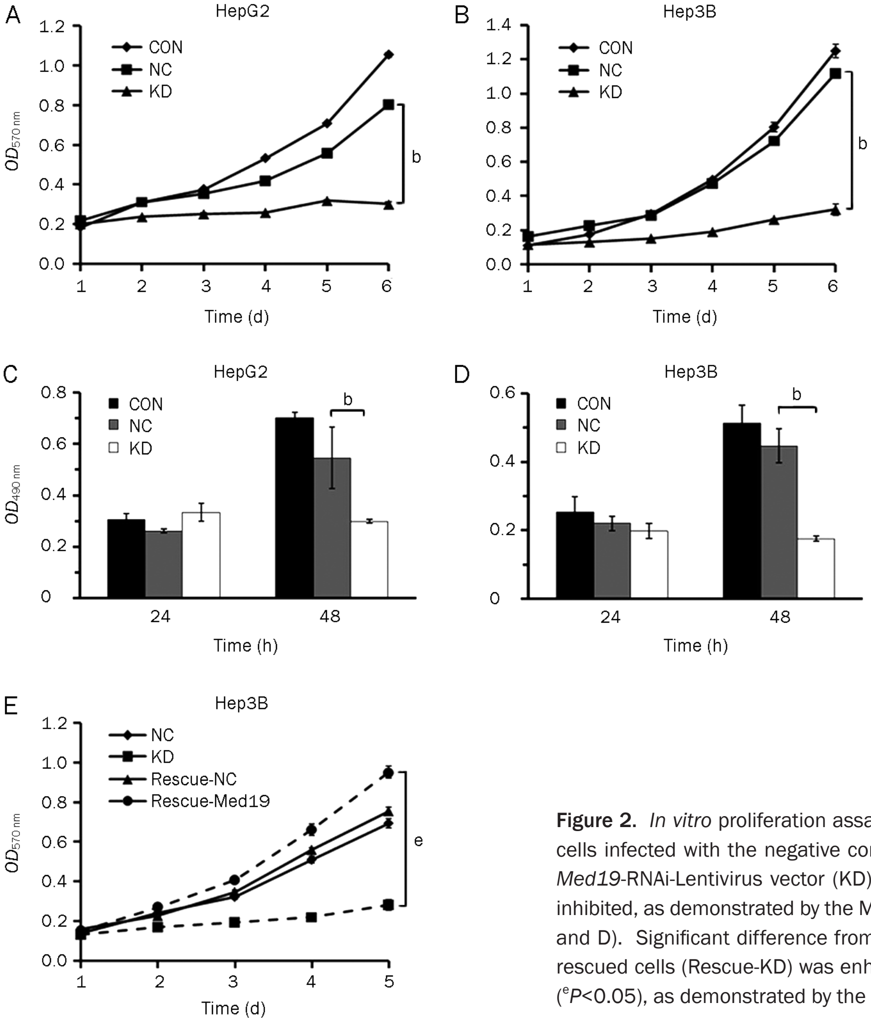

Figure 2. *In vitro* proliferation assays of HepG2 and Hep3B cells without infection (CON), cells infected with the negative control lentivirus vector (NC), and cells infected with the *Med19*-RNAi-Lentivirus vector (KD). Cell proliferation in the KD groups was significantly inhibited, as demonstrated by the MTT assay (A and B) and the BrdU incorporation assay (C and D). Significant difference from NC ($^{b}P<0.05$). (E) The proliferation of *Med19* siRNA-rescued cells (Rescue-KD) was enhanced significantly when compared with the KD group ($^{e}P<0.05$), as demonstrated by the MTT assay.

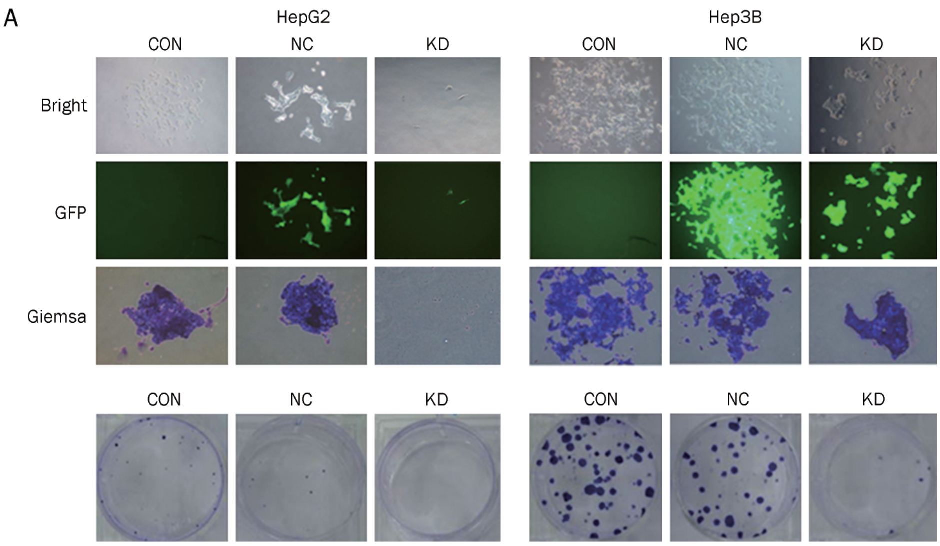

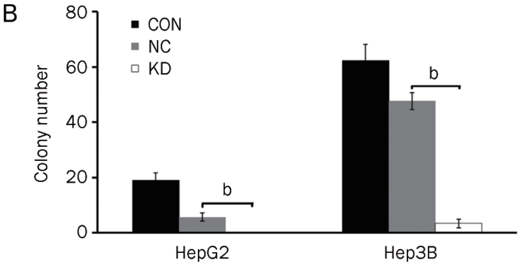

Figure 3. *Med19*-RNAi-Lentivirus infection inhibits the colony-forming ability of HepG2 and Hep3B cells. (A) Images recorded under a fluorescence microscope, representing the size and number of colonies in each group of cells; (B) Statistical analysis of the number of colonies with Giemsa staining. CON: cells without infection; NC: cells infected with the negative-control vector; KD: cells infected with the *Med19*-RNAi-Lentivirus vector. Significant difference from NC ($^{b}P<0.05$).

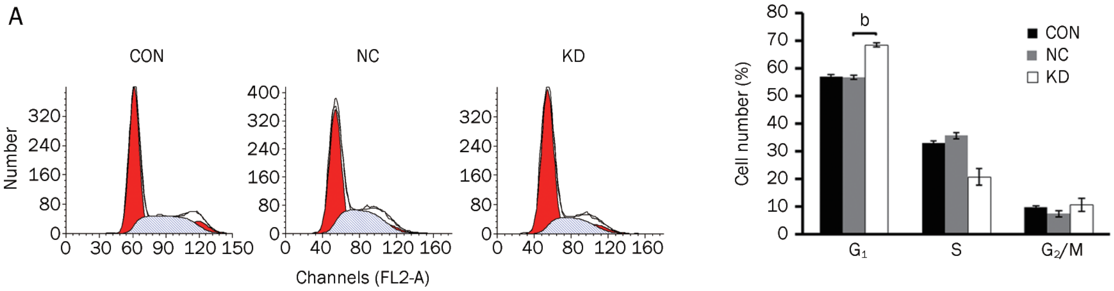

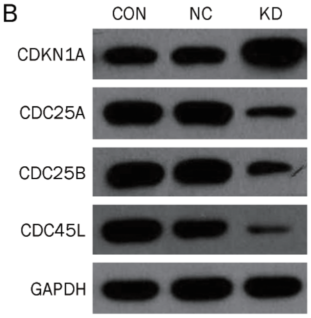

Figure 4. *Med19*-RNAi-Lentivirus infection induces cell-cycle arrest at G_0/G_1 phase and affects the expression of cell-cycle-related proteins in Hep3B cells. (A) Increased cell population in G_0/G_1 phase in the *Med19*-RNAi-Lentivirus-infected group (KD); (B) Increased expression of CDKN1A (cyclin-dependent kinase inhibitor 1A) and diminished expression of CDC45L (cell division control protein 45 homolog), CDC25A (cell division cycle 25A), and CDC25B (M-phase inducer phosphatase 2) in Med19-RNAi-Lentivirus-infected Hep3B cells. Significant difference from NC ($^{b}P<0.05$).

Effects of *Med19* knockdown on tumorigenesis

Tumor formation in *Med19*-silenced Hep3B cells was then evaluated *in vivo*, and the results are shown in Figure 5. With regard to changes in tumor volume and tumor weight, no significant difference was found between the pNC-infected cells and uninfected cells. However, pKD infection had a significant inhibitory effect on tumor volume ($P<0.05$ *vs* pNC infected) and tumor weight ($P<0.05$ *vs* pNC infected). Repre-

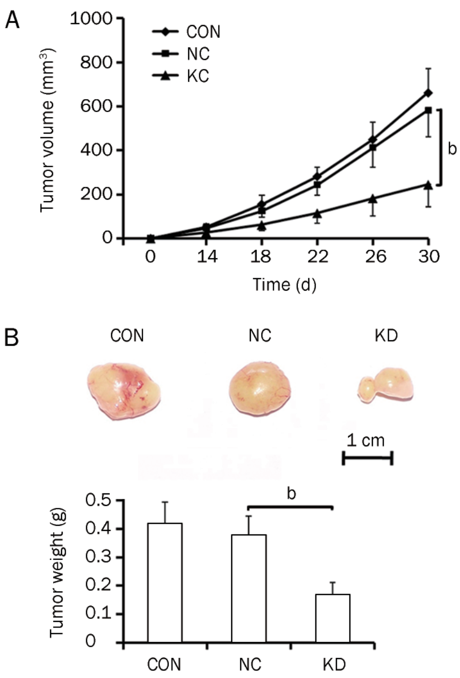

Figure 5. *In vitro* tumorigenesis assay in mice inoculated with uninfected Hep3B cells (CON), cells infected with the negative-control lentivirus vector (NC), and cells infected with the *Med19*-RNAi-Lentivirus vector (KD). (A) Tumor volume growth curve. (B) Picture of excised tumor in each group and quantitative measurement of tumor weights. Significant difference from NC ($^bP<0.05$).

sentative pictures of tumors on d 30 can be seen in Figure 5B. The tumors in the uninfected and pNC-infected groups were large, whereas the tumors in the pKD-infected group exhibited a reduced tumorigenic capacity.

Discussion

Conventional gene-suppression technologies, such as chemical inhibitors, antisense technology, ribozymes, and deoxyribozymes, often evoke nonspecific side effects and/or offer only transient and partial suppression of the gene of interest[19, 20]. Recently emerging as an important tool for silencing specific genes, RNAi is more potent in inhibiting gene expression than other methods and carries less risk of toxicity[21–23]. More importantly, with the effectiveness and relative ease with which dsRNA can be introduced into cells and tissues, RNAi has a significant therapeutic potential for targeting human carcinomas. Therefore, RNAi-mediated gene silencing, as a novel tool to arrest tumor growth and kill cancer cells, may open new avenues in cancer therapy[24–27].

Malignant tumor cells have the ability to migrate into surrounding tissue and/or distal organs — a phenomenon known as metastasis. In the complex and multi-step process of metastasis, cancer cells first detach from the primary tumor position, then invade adjacent lymph nodes and tissue, enter the circulatory system, migrate through the vasculature, and, finally, proliferate from microscopic growths into macroscopic secondary tumors in a distant tissue[7]. To date, several studies have revealed that many genes, such as oncogenes and tumor-suppressor genes, could be involved in complex metastatic processes, including tumor cell proliferation. For example, a few transcription factors that program many biological cell changes are required for executing the initial steps of the tumor invasion-metastasis cascade[28–33]. Med19 is a component of the Mediator complex, which is a coactivator for DNA-binding factors that activate transcription via RNA polymerase II[9]. Med19 is also known as "lung cancer metastasis-related protein 1" (LCMR1) in the human genome. However, there is no report on the effect of Med19 on proliferation and tumorigenesis in HCC.

In our study, lentivirus-mediated RNAi was used to silence Med19 in the human HCC cell lines HepG2 and Hep3B. The siRNA targeting *Med19*, expressed from the recombinant lentivirus, induced efficient and specific inhibition of endogenous *Med19* mRNA and protein expression in both cell lines. Simultaneously, inhibition of *Med19* expression led to decreased colony formation and tumorigenic capacity in these cells. Thus, this study is to observe and confirm a crucial role of Med19 in the progression of HCC, showing that the *Med19* gene may act as an oncogene to promote HCC development.

Moreover, our results indicated that the downregulation of *Med19* expression significantly inhibits cell proliferation and induces G_1-phase delay in HCC cells, indicating that *Med19* is a proliferation regulator in HCC and may be involved in the control of mitotic cellular processes. Next, the detection of cycle-related proteins was performed on *Med19*-silenced Hep3B cells. As shown in Figure 4B, the expression of CDKN1A was increased, whereas the expression levels of CDC25A, CDC25B, and CDC45L were diminished in *Med19*-RNAi-Lentivirus vector-infected Hep3B cells. The cyclin-dependant kinase inhibitors are well known to prevent cyclin D/cdk4, 6, and cyclin E/cdk2-mediated phosphorylation of the retinoblastoma protein (Rb) and to block progression of the cell cycle in the G_1 phase. However, CDC25A is required for progression from the G_1 to the S phase of the cell cycle, whereas CDC25B activates the cyclin-dependent kinase CDC2 and is required for entry into mitosis. In addition, CDC45L is required for the initiation of chromosomal DNA replication (which occurs during the S phase). Taken as a whole, the enhanced CDKN1A expression and suppressed CDC25A, CDC25B, and CDC45L expression in *Med19*-silenced HCC cells contributed to arrested cell cycling at G_0/G_1 phase. These data support the hypothesis that *Med19* acts as an oncogene to promote human hepatocellular carcinoma growth by regulating cell-cycle progression. However, further experiments are needed to elucidate the detailed mechanism of cell proliferation.

In conclusion, knockdown of human *Med19* gene expression with RNAi successfully reduced tumor-cell proliferation and suppressed tumor formation in HepG2 and Hep3B cells *in vitro* and *in vivo*. These results provide new evidence for the involvement of *Med19* in carcinogenesis and the development of HCC and suggest that RNAi-directed *Med19* silencing may be a potent therapeutic tool for the treatment of HCC, especially in inhibiting or preventing cancer cell proliferation and tumorigenesis.

Acknowledgements

This work was supported by a grant from the National Natural Science Foundation of China (No 30872512).

Author contribution

Shao-wu ZOU, Kai-xing AI, and Qi ZHENG conceived and designed the experiments; Shao-wu ZOU, Kai-xing AI, Zhigang WANG, and Zhou YUAN performed the experiments; Shao-wu ZOU, Kai-xing AI, and Qi ZHENG analyzed the data; Zhou YUAN and Jun YAN contributed reagents, materials, and analytical tools; and Shao-wu ZOU and Qi ZHENG wrote the manuscript.

References

1 Okuda K. Natural history of hepatocellular carcinoma including fibrolamellar and hepato-cholangio carcinoma variants. J Gastroenterol Hepatol 2002; 17: 401–5.
2 Bosch FX, Ribes J, Cleries R, Diaz M. Epidemiology of hepatocellular carcinoma. Clin Liver Dis 2005; 9: 191–211.
3 El-Serag HB. Hepatocellular carcinoma: Recent trends in the United States. Gastroenterology 2004; 127: S27–34.
4 McKillop IH, Schrum LW. Alcohol and liver cancer. Alcohol 2005; 35: 195–203.
5 Farazi PA, De Pinho RA. Hepatocellular carcinoma pathogenesis: from genes to environment. Nat Rev Cancer 2006; 6: 674–87.
6 Elbashir SM, Harborth J, Lendeckel W, Yalcin A, Weber K, Tuschl T. Duplexes of 21-nucleotide RNAs mediate RNA interference in cultured mammalian cells. Nature 2001; 411: 494–8.
7 Fidler IJ. The pathogenesis of cancer metastasis: the ‘seed and soil’ hypothesis revisited. Nature Rev Cancer 2003; 3: 453–8.
8 Westhof E, Filipowicz W. From RNAi to epigenomes: how RNA rules the world. Chembiochem 2005; 6: 441–3.
9 Sato S, Tomomori-Sato C, Parmely TJ, Florens L, Zybailov B, Swanson SK, *et al*. A set of consensus mammalian mediator subunits identified by multidimensional protein identification technology. Mol Cell 2004; 14: 685–91.
10 Kornberg RD. Mediator and the mechanism of transcriptional activation. Trends Biochem Sci 2005; 30: 235–9.
11 Conaway RC, Sato S, Tomomori-Sato C, Yao T, Conaway JW. The mammalian Mediator complex and its role in transcriptional regulation. Trends Biochem Sci 2005; 30: 250–5.
12 Casamassimi A, Napoli C. Mediator complexs and eukaryotic transcription regulation: An overview. Biochimie 2007; 89: 1439–46.
13 Myers LC, Kornberg RD. Mediator of transcriptional regulation. Annu Rev Biochem 2000; 69: 729–49.
14 Baidoobonso SM, Guidi BW, Myers LC. Med19 (Rox3) regulates intermodule interactions in the *Saccharomyces cerevisiae* mediator complex. J Biol Chem 2007; 282: 5551–9.
15 Naldini L, Gallay P, Gallay P. *In vivo* gene delivery and stable transduction of nondividing cells by a lentiviral vector. Science 1996; 272: 263–7.
16 Livak KJ, Schmittgen TD. Analysis of relative gene expression data using real-time quantitative PCR and the $2^{-\Delta\Delta CT}$ method. Methods 2001; 25: 402–8.
17 Xu Y, Wang Z, Wang J, Li J, Wang H, Yue W. Lentivirus-mediated knockdown of cyclin Y (CCNY) inhibits glioma cell proliferation. Oncol Res 2010; 18: 359–64.
18 Lengronne A, Pasero P, Bensimon A, Schwob E. Monitoring S phase progression globally and locally using BrdU incorporation in TK^+ yeast strains. Nucleic Acids Res 2001; 29: 1433–42.
19 McCaffrey AP, Meuse L, Pham TT, Conklin DS, Hannon GJ, Kay MA. RNA interference in adult mice. Nature 2002; 418: 38–9.
20 Xia H, Mao Q, Paulson HL, Davidson BL. siRNA-mediated gene silencing *in vitro* and *in vivo*. Nat Biotechnol 2002; 20: 1006–10.
21 Schweinitz A, Steinmetzer T, Banke IJ, Arlt MJ, Stürzebecher A, Schuster O, *et al*. Design of novel and selective inhibitors of urokinase-type plasminogen activator with improved pharmacokinetic properties for use as antimetastatic agents. J Biol Chem 2004; 279: 33613–22.
22 D’Alessio S, Margheri F, Pucci M, Del Rosso A, Monia BP, Bologna M, *et al*. Antisense oligodeoxynucleotides for urokinase plasminogen activator receptor have anti-invasive and anti-proliferative effects *in vitro* and inhibit spontaneous metastases of human melanoma in mice. Int J Cancer 2004; 110: 125–33.
23 Arens N, Gandhari M, Bleyl U, Hildenbrand R. *In vitro* suppression of urokinase plasminogen activator in breast cancer cells — a comparison of two antisense strategies. Int J Oncol 2005; 26: 113–9.
24 Woessmann W, Damm-Welk C, Fuchs U, Borkhardt A. RNA interference: new mechanisms for targeted treatment? Rev Clin Exp Hematol 2003; 7: 270–91.
25 Jiang M, Rubbi CP, Milner J. Gel-based application of siRNA to human epithelial cancer cells induces RNAi-dependent apoptosis. Oligonucleotides 2004; 14: 239–48.
26 Rye PD, Stigbrand T. Interfering with cancer: a brief outline of advances in RNA interference in oncology. Tumour Biol 2004; 25: 329–36.
27 Wilda M, Fuchs U, Wossmann W, Borkhardt A. Killing of leukemic cells with a BCR/ABL fusion gene by RNA interference (RNAi). Oncogene 2002; 21: 5716–24.
28 Cano A, Pérez-Moreno MA, Rodrigo I, Locascio A, Blanco MJ, del Barrio MG, *et al*. The transcription factor snail controls epithelial-mesenchymal transitions by repressing E-cadherin expression. Nat Cell Biol 2000; 2: 76–83.
29 Comijn J, Berx G, Vermassen P, Verschueren K, van Grunsven L, Bruyneel E, *et al*. The two-handed E box binding zinc finger protein SIP1 downregulates E-cadherin and induces invasion. Mol Cell 2001; 7: 1267–78.
30 Bolós V, Peinado H, Pérez-Moreno MA, Fraga MF, Esteller M, Cano A. The transcription factor Slug represses E-cadherin expression and induces epithelial to mesenchymal transitions: a comparison with Snail and E47 repressors. J Cell Sci 2003; 116: 499–511.
31 Yang J, Mani SA, Donaher JL, Ramaswamy S, Itzykson RA, Come C. Twist, a master regulator of morphogenesis, plays an essential role in tumor metastasis. Cell 2004; 117: 927–39.
32 Hartwell KA, Muir B, Reinhardt F, Carpenter AE, Sgroi DC, Weinberg RA. The Spemann organizer gene, Goosecoid, promotes tumor metastasis. Proc Natl Acad Sci USA 2006; 103: 18969–74.
33 Mani SA, Yang J, Brooks M, Schwaninger G, Zhou A, Miura N, *et al*. Mesenchyme Forkhead 1 (FOXC2) plays a key role in metastasis and is associated with aggressive basal-like breast cancers. Proc Natl Acad Sci USA 2007; 104: 10069–74.

Acta Pharmacologica Sinica (2011) 32: 361–367
© 2011 CPS and SIMM All rights reserved 1671-4083/11 $32.00
www.nature.com/aps

Original Article

Expression of elongation factor-2 kinase contributes to anoikis resistance and invasion of human glioma cells

Li ZHANG[1, #], Yi ZHANG[1, #], Xiao-yuan LIU[1], Zheng-hong QIN[1], Jin-ming YANG[2, *]

[1]Department of Pharmacology, College of Pharmaceutical Science, Soochow University, Suzhou 215123, China; [2]Department of Pharmacology and Penn State Hershey Cancer Institute, the Pennsylvania State University College of Medicine, Hershey, PA, USA

Aim: To determine whether elongation factor-2 kinase (eEF-2 kinase) contributes to the malignant phenotype of glioblastoma multiforme by promoting the migration and invasion of glioma cells. The mechanism involved was also explored.
Methods: Human glioma cell lines T98G and LN-229 were used. The expression of eEF-2 kinase was silenced using siRNA, and the invasive potential of tumor cells was assessed using a wound-healing assay and a Matrigel invasion assay. Apoptosis was determined using propidium iodide (PI) staining and Western blot analysis of cleaved caspase-3.
Results: Silencing the expression of eEF-2 kinase by siRNA significantly suppressed both the migration and invasion of human glioma cells. Silencing eEF-2 kinase expression also sensitized glioma cells to anoikis, thereby decreasing tumor cell viability in the absence of attachment. Treatment of tumor cells with the caspase inhibitor z-VAD-fmk down-regulated Bim accumulation and abolished glioma cell sensitivity to anoikis.
Conclusion: The results suggest that the expression of eEF-2 kinase contributes to migration and invasion of human glioma cells by protecting them from anoikis. eEF-2 kinase expression may serve as a prognostic marker and a novel target for cancer therapy.

Keywords: eEF-2 kinase; migration; invasion; anoikis; glioma

Acta Pharmacologica Sinica (2011) 32: 361–367; doi: 10.1038/aps.2010.213; published online 31 Jan 2011

Introduction

Elongation factor-2 kinase (eEF-2 kinase, also known as calmodulin-dependent protein kinase III) is a unique calmodulin/calcium-dependent enzyme that inhibits protein synthesis. Expression of eEF-2 kinase has been reported to be up-regulated in several types of malignancies, including gliomas[1, 2]. eEF-2 kinase phosphorylates eEF-2, a 100-kDa protein that promotes ribosomal translocation from the A to the P site in eukaryotic tissues, which induces movement of mRNA along the ribosome during translation[3]. Phosphorylation of eEF-2 at Thr56 by eEF-2 kinase decreases the affinity of eEF-2 for ribosomes and terminates peptide elongation, thereby inhibiting protein synthesis.

The role of protein synthesis in the growth and survival of cancer cells has gained widespread attention. For example, mitotic cells show a 20%–40% decrease in protein synthesis compared to cells in inter-phase. In addition, a transient decrease in protein synthesis is characteristically observed at the G_1/S interface[4, 5]. Altered protein synthesis can transform cells by interfering with the expression and activity of translation factors such as eIF2 alpha and its specific protein kinase, PKR[6]. There is also abundant evidence suggesting that the downstream effects of growth factors require transient inhibition of protein synthesis[7]. In fact, a variety of processes important to cell proliferation, such as polyamine transport[8]; ATP turnover[9]; expression of early growth response genes, such as *c-fos* and *c-jun*[10]; and activation of the ribosomal protein, S6 kinase[11], as well as specific signaling molecules, such as MAP kinase[12] and JNK/SAPK kinase[13], are stimulated by inhibitors of protein synthesis[14]. In addition, exposure of 3T3 cells to cycloheximide or puromycin results in the induction of DNA synthesis and cell division[15]. Connolly *et al*[16] demonstrated that the protein expression level of eEF-2 kinase in non-transformed cells is kept low by proteasomal degradation. In contrast, as cells transform from immortalized to highly malignant, the expression level of eEF-2 kinase increases. These results are consistent with our

---

[#] These two authors contributed equally to this study.
[*] To whom correspondence should be addressed.
E-mail juy16@psu.edu

Received 2010-10-04 Accepted 2010-11-29

original reports demonstrating that eEF-2 kinase is regulated by ubiquitin-mediated proteasomal degradation[17], and that eEF-2 kinase is constitutively up-regulated in cancer cell lines and tumor specimens[18, 19]. Connolly *et al* also reported that hypoxic breast epithelial cells down-regulate protein synthesis by disrupting the proteasome-mediated degradation of eEF-2 kinase and activation of 4EBP-1[16]. In contrast, breast cancer cells have constitutively activated eEF-2 kinase. These studies suggest that eEF-2 kinase might have a role in promoting cancer cell survival by favoring their growth and dissemination. Anchorage-independent growth and the capacity to invade are characteristics of glioma cells. Migration and invasion of glioma cells is a complex process that involves multiple biological features such as tumor cell adhesion and motility, secretion of proteases by tumor cells, and the ability to survive in the absence of anchorage[20, 21]. We report here that the expression of eEF-2 kinase in glioma cells confers resistance to anoikis, a form of apoptosis triggered by the loss of cell-to-cell or cell-to-matrix anchorage, and favors migration and invasion of human glioma cells. Our results provide new evidence that eEF-2 kinase might be an effective target in brain cancer therapy.

Materials and methods

Cell lines and culture

The human glioblastoma cell lines T98G and LN-229 were obtained from the Shanghai Institutes for Biological Sciences. The glioma cells were cultured in DMEM supplemented with 10% fetal bovine serum, 100 units/mL penicillin, and 100 μg/mL streptomycin. Cells were maintained at 37 °C in a humidified atmosphere containing 5% CO_2 and 95% air.

Antibodies and reagents

The antibodies used in this study were as follows: monoclonal anti-eEF-2 kinase antibody (NOVUS), polyclonal cleaved caspase-3 antibody and polyclonal caspase-3 antibody recognizing the full-length pro-enzyme (Sigma), polyclonal anti-Bim antibody (H-191; Santa Cruz), monoclonal anti-β-actin antibody (Santa Cruz), caspase inhibitor z-VAD-fmk (Sigma), eEF-2 kinase-siRNA (Shanghai Gene-Pharma Co, China), and poly-HEMA (Sigma).

siRNA preparation and transfection

The siRNA sequence used to target eEF-2 kinase mRNA corresponded to amino acids 144 to 164 (5′-AAGCTCGAACCA-GAATGTC-3′) of the coding region relative to the start codon. The siRNA duplex with the following sense and antisense sequences was used, 5′-AAGCUCGAACCAGAAUGUCTT-3′ (sense) and 5′-GACAUUCUGGUUCGAGCUUTT-3′ (antisense) (prepared by Shanghai Genepharma Research, Inc). For transfection, cells in the exponential phase of growth were plated in 60-mm tissue culture dishes at 5×10^5 cells per dish, grown for 24 h, and then transfected with siRNA using oligofectamine and Opti-MEMI–Reduced Serum medium following the manufacturer's protocol.

Wound-healing assay

Cells (5×10^5 cells in 2 mL per well) were transfected with an eEF-2 kinase-targeted siRNA or a non-targeting scrambled siRNA and then plated onto standard 6-well tissue culture plates cultured in medium containing 10% FBS to nearly confluent cell monolayers. Cell monolayers were then carefully wounded using a 200-μL sterile pipette tip, and any cellular debris was removed by washing with PBS. The wounded monolayers were then incubated in medium containing 10% FBS for 24 h and photographed using a phase-contrast microscope (Eclipse TE 200, Nikon Inc, Melville, NY, USA). The experiments were performed in triplicate wells and repeated at least three times.

Invasion assay

Invasion assays were carried out in modified Boyden chambers with filter inserts with 8-μm pores in 24-well plates (Corning, NY, USA). The surfaces of the filters were coated with 50 mg/L ice-cold Matrigel (Matrigel basement membrane matrix, BD Bioscience, NJ, USA). The lower chamber was filled with medium containing 10% serum. Cells were transfected with an eEF-2 kinase-targeted siRNA or a non-targeting scrambled siRNA. Sixty hours later, the cells were seeded into the upper chamber of a 24-well chemotaxis chamber transwell. Cells (1×10^5 cells/well) were washed with PBS twice, re-suspended in 200 μL of serum-free medium, and then transferred into the upper chamber. After a 24-h incubation, the filters were gently removed from the chambers, and the cells on the upper surface were removed by wiping with a cotton swab. Cells that had invaded to the lower surface areas were fixed with ice-cold methanol, stained with crystal violet, and counted in 10 randomly selected fields under a microscope (100×). Results shown are representative of three independent experiments.

Anoikis assay

Cells (5x10^5 cells in 2 mL per well) were transfected with an eEF-2 kinase siRNA or a non-targeting scrambled siRNA. Sixty hours later, cells were plated onto standard 6-well tissue culture plates or poly-HEMA-coated plates to prevent attachment. Following a 24-h incubation at 37 °C in a humidified atmosphere containing 5% CO_2 and 95% air, viability of the cells was determined using the trypan blue exclusion method. Apoptosis was determined by propidium iodide (PI) staining and Western blot analysis of cleaved caspase-3. To stain apoptotic nuclei with PI, cells were stained with a PI dye solution at 4 °C in the dark for 30 min, and then the samples were analyzed on a FC500 Beckman-Counter flow cytometer. Active caspase-3, which is present in cells undergoing apoptosis, was detected by Western blot analysis using a polyclonal anti-caspase-3 antibody that recognizes the cleaved active caspase-3.

Western blot analysis

Cell lysates were prepared in TNT buffer (20 mmol/L Tris-HCl, pH 7.4, 200 mmol/L NaCl, 1% Triton X-100, 1 mmol/L phenylmethylsulfonyl fluoride, and 1% aprotinin), and proteins were resolved by SDS-PAGE. The blots were incubated in blocking solution consisting of 5% skim milk in 10 mmol/L Tris-HCl, pH 8.0, 150 mmol/L NaCl, and 0.1% Tween 20 at room temperature for 1 h and then immuno-blotted with the indicated antibodies. Proteins were detected using the enzyme-linked chemiluminescence (ECL) method. β-Actin was used as a loading control.

Statistical analysis

Data were shown as mean±SD. Differences between individual groups were analyzed using student's *t*-test. All *P* values were 2-sided; $P<0.05$ was considered significant. Analyses were performed using the GraphPad Prism 4.0 package (GraphPad, San Diego, CA, USA).

Results

Effect of eEF-2 kinase on glioma cell migration and invasion

To determine the role of eEF-2 kinase in the malignant phenotype of glioma, we utilized an siRNA approach to inactivate this enzyme. Human glioma cell lines, T98G and LN229, transfected with eEF-2 kinase-targeted siRNA showed an 85%–90% reduction in eEF-2 kinase protein expression 60 h after transfection when compared with the cells transfected with a non-targeting siRNA (Figure 1).

We next compared the invasive potentials and migrating capabilities of T98G and LN229 cells with or without silencing of eEF-2 kinase expression. Invasion was assessed using a Matrigel chamber assay, and the ability to migrate was examined using a wound-healing assay. As shown in Figure 2A, wound healing after 24 h was significantly inhibited in T98G and LN229 cells when eEF-2 kinase was knocked down in cells compared with control cells that were transfected with a non-targeting siRNA. Consistent with the wound-healing assay, the invasiveness of the glioma cells in which eEF-2 kinase expression was silenced also decreased considerably compared with control cells (Figure 2B). These results suggest that the expression of eEF-2 kinase plays an important role in the invasion and migration of glioma cells.

Effect of eEF-2 kinase on cell viability in the absence of matrix attachment

To determine whether eEF-2 kinase affects the survival of glioma cells in the absence of matrix attachment, we determined the viability of T98G and LN229 cells grown either as monolayers attached to plastic or in suspension on poly-HEMA. Figures 3C and 3D show that the viability of glioma cells cultured in suspension was significantly reduced in eEF-2 kinase knock-down cells when compared with control cells. In contrast, reduction of eEF-2 kinase expression had no effect on the viability of cells grown attached to a matrix (Figure 3A and 3B). These results suggest that expression of eEF-2 kinase has a role in the survival of human glioma cells in the absence of anchorage.

Expression of eEF-2 kinase confers resistance to anoikis

To determine whether the pro-survival function of eEF-2 kinase, as evidenced in Figure 3, was mediated through the inhibition of anoikis, we compared the apoptotic properties of T98G and LN229 cells with or without silencing of eEF-2 kinase expression. As shown in Figure 4, silencing of eEF-2 kinase expression by siRNA resulted in the activation of caspase-3 in T98G and LN229 cells cultured in suspension on poly-HEMA but had a barely detectable effect on cells grown as monolayers attached to plastic (Figure 4A and 4B). The PI apoptotic assay also demonstrated that when cultured in suspension on poly-HEMA, there was an increase in the sub-diploid peak of apoptotic nuclei in the DNA histogram in the glioma cells with silencing of eEF-2 kinase expression when compared with that of the cells transfected with a non-targeting siRNA (Figure 4B), indicating an induction of apoptosis. The caspase inhibitor z-VAD-fmk abolished the sub-diploid DNA peak observed in the cells transfected with an eEF-2 kinase-targeted siRNA (Figure 4B). These results suggest a role for eEF-2 kinase in the inhibition of anoikis in tumor cells.

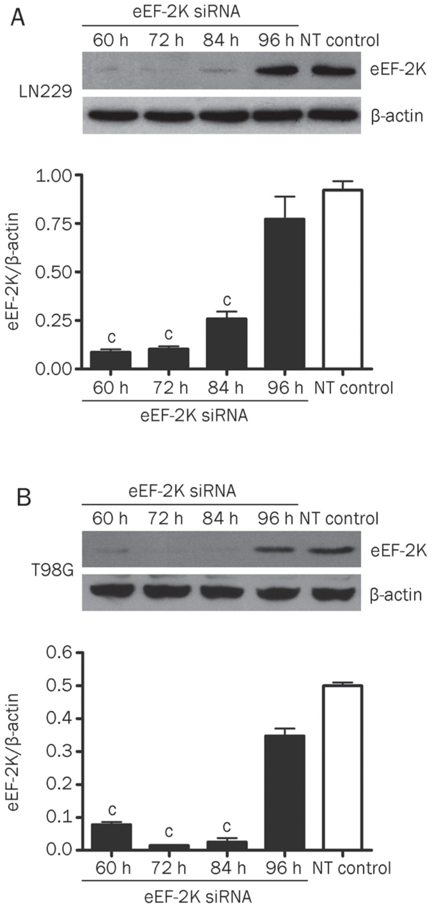

Figure 1. eEF-2 kinase expression was silenced by siRNA. Human glioma cell lines LN229 and T98G were transfected with an eEF-2 kinase-targeted siRNA. Expression of eEF-2 kinase was analyzed by Western blot analysis. Each bar represents mean±SE of three separate experiments. *P*-values were determined by *t*-test. $^{c}P<0.01$ *vs* NT control.

Down-regulation of Bim correlates with the anoikis resistance conferred by eEF-2 kinase

We next explored the possible mechanism involved in anoi-

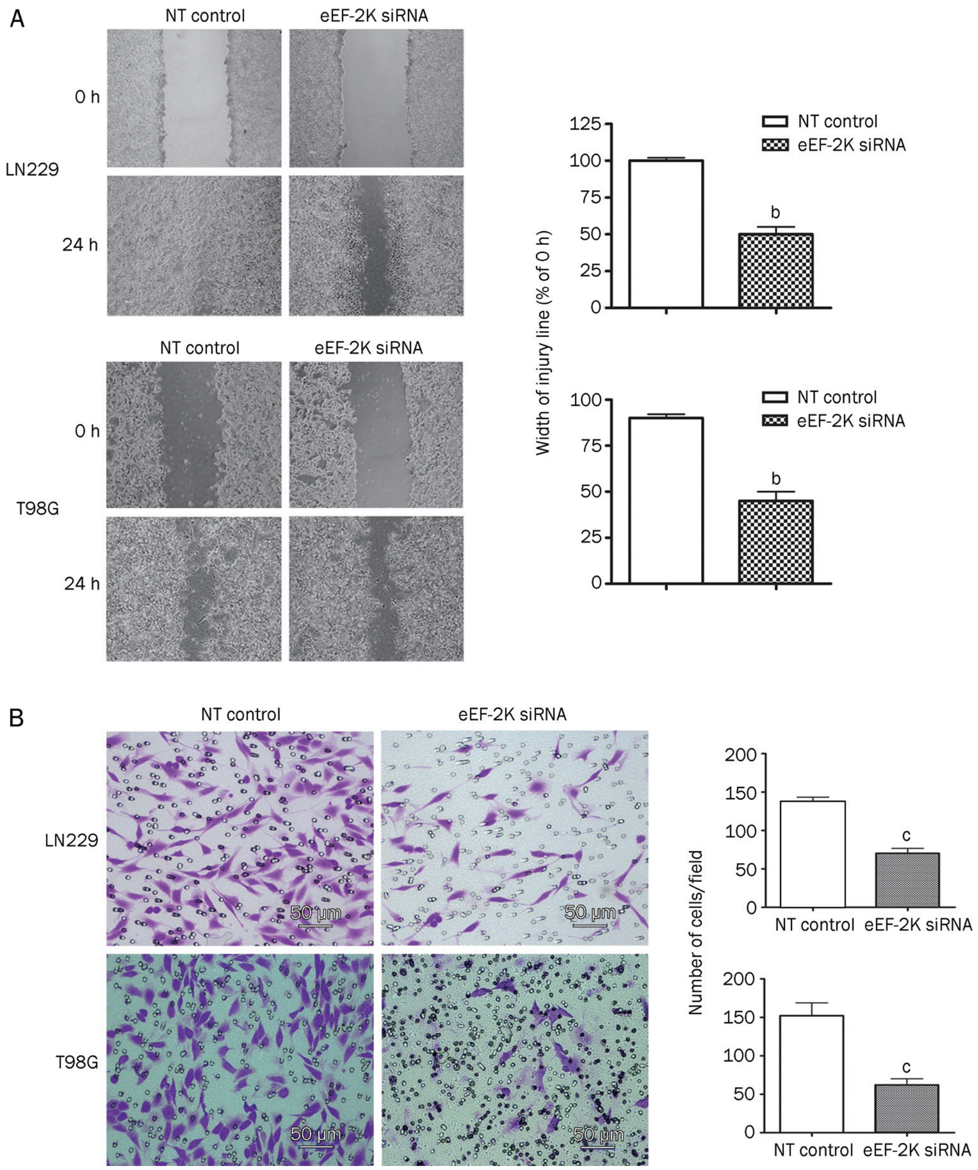

Figure 2. Effect of eEF-2 kinase expression on migration and invasion of glioma cells. LN229 and T98G cells were transfected with an eEF-2 kinase-targeted siRNA or a scrambled siRNA, and their ability to migrate and invade was determined as described in Materials and methods. (A) Migration; (B) Invasion. *P*-values were determined by *t*-test. $^{b}P<0.05$, $^{c}P<0.01$ compared with NT control.

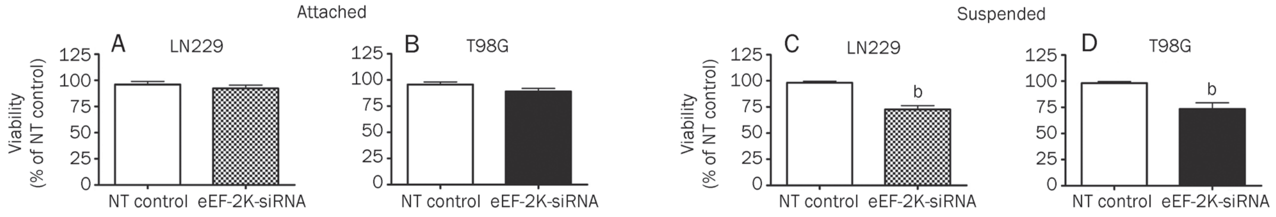

Figure 3. Effect of eEF-2 kinase expression on cell viability in the absence of attachment. LN229 and T98G cells transfected with an eEF-2 kinase siRNA or a scrambled siRNA were seeded on plastic (attached) or on poly-HEMA (suspended) for 24 h, and then cell viability was determined by trypan blue assay. Each bar represents mean±SEM of three experiments. *P*-values were determined by *t*-test. $^{b}P<0.05$ compared with scrambled cells.

kis resistance associated with eEF-2 kinase expression. We determined whether resistance to anoikis in glioma cells was associated with a down-regulation of Bim, a pro-apoptotic BH3-only protein that plays a crucial role in regulating anoikis[22]. As demonstrated in Figure 5, silencing of eEF-2 kinase expression caused an increase of Bim in glioma cells, and this increase in the Bim protein level was more remarkable when the eEF-2 kinase siRNA-treated cells were grown in suspension on poly-HEMA (Figure 5). These observations suggest that the enhanced sensitivity to anoikis caused by the silencing

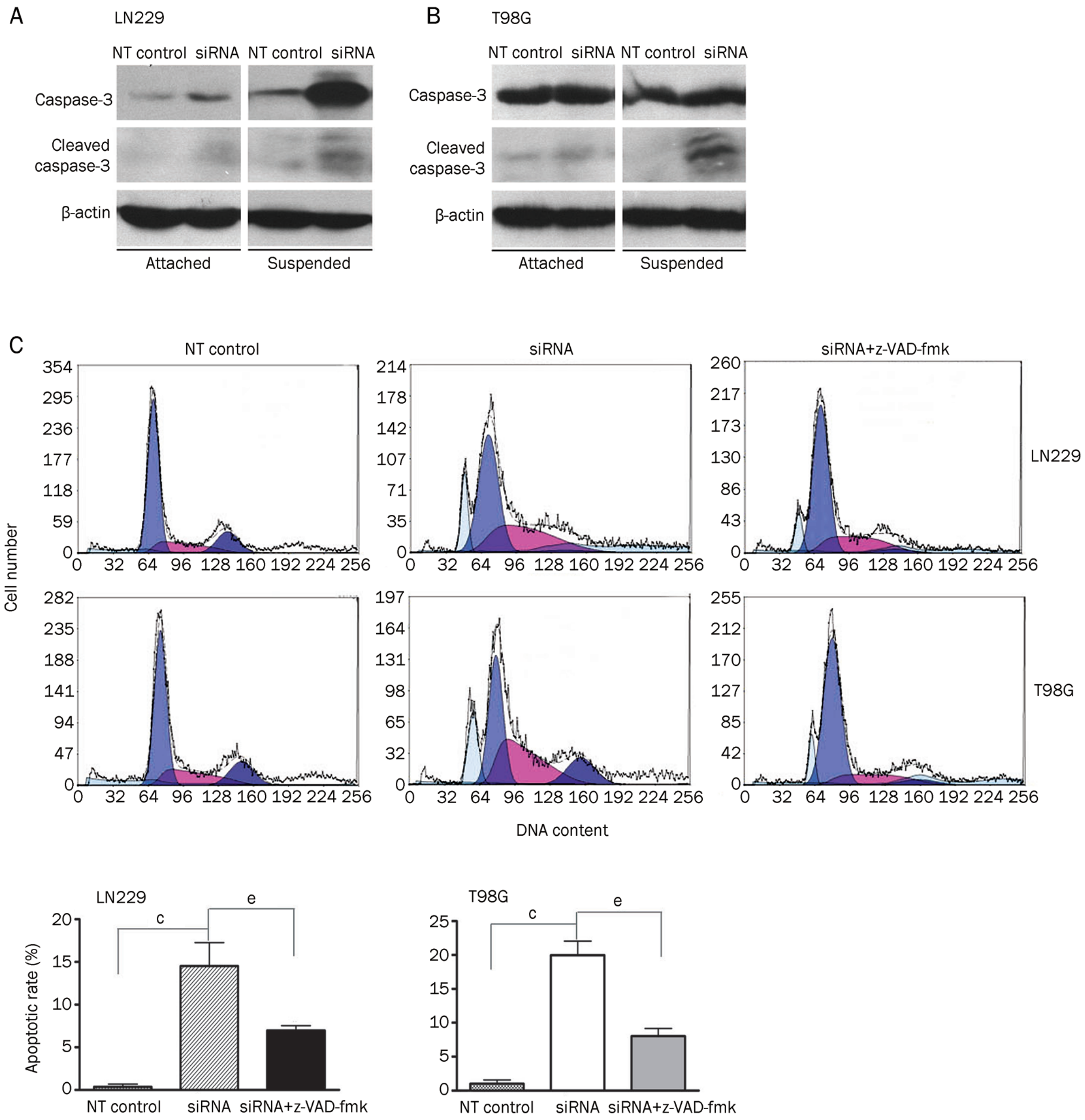

Figure 4. Effect of eEF-2 kinase expression on glioma cell sensitivity to anoikis. (A and B) LN229 and T98G cells transfected with an eEF-2 kinase siRNA or scrambled siRNA were seeded on plastic (attached) or on poly-HEMA (suspended) for 24 h. The levels of caspase-3 and cleaved caspase-3 were examined by Western blot analysis. β-Actin was used as a loading control. (C) LN229 and T98G cells transfected with an eEF-2 kinase siRNA or a scrambled siRNA were seeded on plastic (attachment), poly-HEMA (suspension), followed by treatment with caspase inhibitor, z-VAD-fmk, for 24 h. Apoptosis was determined by flow cytometric analysis of PI-stained apoptotic nuclei. Each bar represents mean±SEM of three separate experiments. *P*-values were determined by *t*-test. [c]*P*<0.01 *vs* NT control group. [e]*P*<0.05 *vs* siRNA group.

of eEF-2 kinase expression might be due to the up-regulation of Bim protein expression.

Discussion

Previous studies showed that activation of eEF-2 kinase promotes autophagy and survival in cancer cells[23]. In the current study, we sought to determine a role for eEF-2 kinase in the malignant phenotype of glioblastoma multiforme, one of the most common childhood malignancies and a cancer of increasing significance in adults. The results of our study suggest a role for eEF-2 kinase in the progression of glioma, as expression of this kinase appears to promote migration and invasion of glioma cells (Figure 2), protect viability when tumor cells lose anchorage (Figure 3), and render cells resistant to anoikis (Figure 4), a form of apoptosis induced by loss of matrix or cellular attachment, which is often defective in tumor cells. Moreover, we demonstrate that down-regulation of Bim is involved in the resistance to anoikis in tumor cells expressing high levels of eEF-2 kinase (Figure 5).

Migration and invasion involves the spread of glioma cells

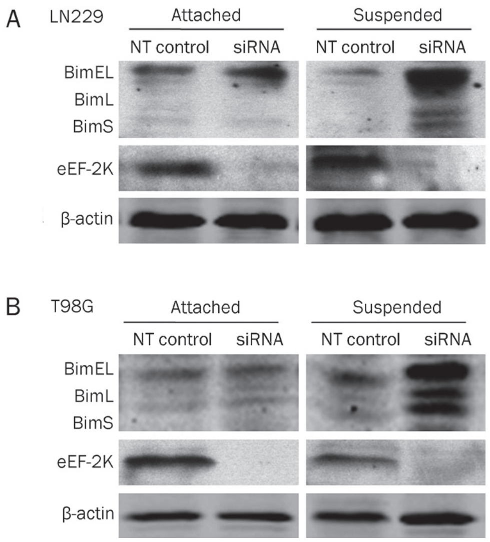

Figure 5. Effect of silencing of eEF-2 kinase expression on Bim protein expression level in glioma cells cultured in suspension or as an attached monolayer. (A) LN229 and (B) T98G cells transfected with an eEF-2 kinase-targeted siRNA or a scrambled siRNA were seeded on plastic (attached) or on poly-HEMA (suspended) for 24 h. Cell lysates were prepared from monolayer or suspension cultures, and Bim (BimEL, BimL, and BimS) and eEF-2 kinase proteins were detected by Western blot analysis. β-Actin was used as a loading control.

from a primary tumor site to the surrounding normal tissues. These processes involve the coordination of several signal-transduction pathways that allow cancer cells to proliferate, remodel their surrounding environment, invade to distant sites and re-establish the tumor[24]. Recently, studies have shown that initiation of several pro-survival genes that maintain growth can enhance cell migration[25]. In this study, we found that eEF-2 kinase plays an important role in tumor migration and invasion, which is consistent with the role of this kinase in cell survival, as reported by us and others[23, 26].

Resistance to apoptosis (anoikis) is a hallmark of migrating and invasive glioma cells. Here, we show that expression of eEF-2 kinase in human glioma cells can suppress anoikis (Figures 3 and 4). In the absence of anchorage, human glioma cells have high viability (Figure 3) and low rates of apoptosis (Figure 4). Silencing of eEF-2 kinase expression in glioma cells produces lower viability and higher rates of apoptosis (Figures 3 and 4). These observations indicate that in the absence of attachment, promotion of glioma cell survival by eEF-2 kinase may be the result of inhibition of anoikis. Bim, a BH3-only pro-apoptotic protein belonging to the Bcl-2 family, plays a critical role in triggering anoikis. For example, inhibition of Bim induction has been found to be the mechanism responsible for the anoikis deficiency caused by G_1/S cell cycle arrest[27]. In addition, Bim has been shown to be a tumor suppressor and a key determinant of paclitaxel sensitivity in epithelial tumors[28]. We found a converse relationship between eEF-2 kinase expression and Bim accumulation (Figure 5); Bim is reduced in cells with high expression of eEF-2 kinase, and silencing of eEF-2 kinase expression results in the up-regulation of Bim expression levels (Figure 5).

In summary, the current study identified eEF-2 kinase as a regulator of glioma cell migration and invasion and as a suppressor of anoikis. Because the ability of glioma cells to invade and migrate and to develop resistance to treatment represents two critically important malignant characteristics, and defective anoikis likely contributes to both of these features, re-establishing sensitivity to anoikis may represent a novel therapeutic strategy for malignant glioma. Thus, the results reported here provide support for further studying eEF-2 kinase as a target for cancer therapy.

Acknowledgements

This project was supported by the National Natural Sciences Foundation of China (K113416510) and Natural Science Foundation of Jiangsu Province of China (BK2010224) and US Public Health Service R01CA135038.

Author contribution

Jin-ming YANG designed research; Li ZHANG, Yi ZHANG, Xiao-yuan LIU performed research; Li ZHANG and Yi ZHANG analyzed data; Zheng-hong QIN contributed new analytical and tools; Li ZHANG and Yi ZHANG wrote the paper.

References

1 Serfass L, Van Herpen C, Saghatchian M. Molecular targets and cancer therapeutics. Eur J Cancer 2007; 43: 1494–5.
2 Wu H, Yang JM, Jin S, Zhang H, Hait WN. Elongation factor-2 kinase regulates autophagy in human glioblastoma cells. Cancer Res 2006; 66: 3015–23.
3 Ryazanov AG, Rudkin BB, Spirin AS. Regulation of protein synthesis at the elongation stage. New insights into the control of gene expression in eukaryotes. FEBS Lett 1991; 285: 170–5.
4 Hait WN, Wu H, Jin S, Yang JM. Elongation factor-2 kinase: its role in protein synthesis and autophagy. Autophagy 2006; 2: 294–6.
5 Celis JE, Madsen P, Ryazanov AG. Increased phosphorylation of elongation factor 2 during mitosis in transformed human amnion cells correlates with a decreased rate of protein synthesis. Proc Natl Acad Sci USA 1990; 87: 4231–5.
6 Donze O, Jagus R, Koromilas AE, Hershey JW, Sonenberg N. Abrogation of translation initiation factor eIF-2 phosphorylation causes malignant transformation of NIH 3T3 cells. Embo J 1995; 14: 3828–34.
7 Herschman HR. Primary response genes induced by growth factors and tumor promoters. Annu Rev Biochem 1991; 60: 281–319.
8 Xu CS, Chang CF. Expression profiles of the genes associated with metabolism and transport of amino acids and their derivatives in rat liver regeneration. Amino Acids 2008; 34: 91–102.
9 Nunes PH, Calaza Kda C, Albuquerque LM, Fragel-Madeira L, Sholl-Franco A, Ventura AL. Signal transduction pathways associated with ATP-induced proliferation of cell progenitors in the intact embryonic retina. Int J Dev Neurosci 2007; 25: 499–508.
10 Edwards DR, Mahadevan LC. Protein synthesis inhibitors differentially superinduce *c-fos* and *c-jun* by three distinct mechanisms: lack of evidence for labile repressors. Embo J 1992; 11: 2415–24.
11 Clark DE, Errington TM, Smith JA, Frierson HF Jr, Weber MJ, Lannigan

DA. The serine/threonine protein kinase, p90 ribosomal S6 kinase, is an important regulator of prostate cancer cell proliferation. Cancer Res 2005; 65: 3108–16.

12 Zinck R, Cahill MA, Kracht M, Sachsenmaier C, Hipskind RA, Nordheim A. Protein synthesis inhibitors reveal differential regulation of mitogen-activated protein kinase and stress-activated protein kinase pathways that converge on Elk-1. Mol Cell Biol 1995; 15: 4930–8.

13 Cano E, Hazzalin CA, Mahadevan LC. Anisomycin-activated protein kinases p45 and p55 but not mitogen-activated protein kinases ERK-1 and -2 are implicated in the induction of *c-fos* and *c-jun*. Mol Cell Biol 1994; 14: 7352–62.

14 White-Gilbertson S, Kurtz DT, Voelkel-Johnson C. The role of protein synthesis in cell cycling and cancer. Mol Oncol 2009; 3: 402–8.

15 Kaczmarek L, Surmacz E, Baserga R. Cycloheximide or puromycin can substitute for PDGF in inducing cellular DNA synthesis in quiescent 3T3 cells. Cell Biol Int Rep 1986; 10: 455–63.

16 Connolly E, Braunstein S, Formenti S, Schneider RJ. Hypoxia inhibits protein synthesis through a 4E-BP1 and elongation factor 2 kinase pathway controlled by mTOR and uncoupled in breast cancer cells. Mol Cell Biol 2006; 26: 3955–65.

17 Arora S, Yang JM, Hait WN. Identification of the ubiquitin-proteasome pathway in the regulation of the stability of eukaryotic elongation factor-2 kinase. Cancer Res 2005; 65: 3806–10.

18 Bagaglio DM, Cheng EH, Gorelick FS, Mitsui K, Nairn AC, Hait WN. Phosphorylation of elongation factor 2 in normal and malignant rat glial cells. Cancer Res 1993; 53: 2260–4.

19 Parmer TG, Ward MD, Yurkow EJ, Vyas VH, Kearney TJ, Hait WN. Activity and regulation by growth factors of calmodulin-dependent protein kinase III (elongation factor 2-kinase) in human breast cancer. Br J Cancer 1999; 79: 59–64.

20 Salhia B, Tran NL, Symons M, Winkles JA, Rutka JT, Berens ME. Molecular pathways triggering glioma cell invasion. Expert Rev Mol Diagn 2006; 6: 613–26.

21 Giese A, Bjerkvig R, Berens ME, Westphal M. Cost of migration: invasion of malignant gliomas and implications for treatment. J Clin Oncol 2003; 21: 1624–36.

22 Reginato MJ, Mills KR, Paulus JK, Lynch DK, Sgroi DC, Debnath J, *et al*. Integrins and EGFR coordinately regulate the pro-apoptotic protein Bim to prevent anoikis. Nat Cell Biol 2003; 5: 733–40.

23 Wu H, Yang JM, Jin S, Zhang H, Hait WN. Elongation factor-2 kinase regulates autophagy in human glioblastoma cells. Cancer Res 2006; 66: 3015–23.

24 Reddy KB, Nabha SM, Atanaskova N. Role of MAP kinase in tumor progression and invasion. Cancer Metastasis Rev 2003; 22: 395–403.

25 Yoeli-Lerner M, Toker A. Akt/PKB signaling in cancer: a function in cell motility and invasion. Cell Cycle 2006; 5: 603–5.

26 Chen Y, Matsushita M, Nairn AC, Damuni Z, Cai D, Frerichs KU, *et al*. Mechanisms for increased levels of phosphorylation of elongation factor-2 during hibernation in ground squirrels. Biochemistry 2001; 40: 11565–70.

27 Collins NL, Reginato MJ, Paulus JK, Sgroi DC, Labaer J, Brugge JS. G_1/S cell cycle arrest provides anoikis resistance through Erk-mediated Bim suppression. Mol Cell Biol 2005; 25: 5282–91.

28 Tan TT, Degenhardt K, Nelson DA, Beaudoin B, Nieves-Neira W, Bouillet P, *et al*. Key roles of BIM-driven apoptosis in epithelial tumors and rational chemotherapy. Cancer Cell 2005; 7: 227–38.

npg
Acta Pharmacologica Sinica (2011) 32: 368–374
© 2011 CPS and SIMM All rights reserved 1671-4083/11 $32.00
www.nature.com/aps

Original Article

Attenuated *Salmonella typhimurium* carrying shRNA-expressing vectors elicit RNA interference in murine bladder tumors

Nan YANG[#], Sheng-hua LI[#], Yun-zhe LÜ, Li-shan CHEN, Da-ming REN*

Instititute of Genetics, School of Life Sciences, Fudan University, Shanghai 200433, China

Aim: To examine whether attenuated *Salmonella typhimurium* (*S typhimurium*) could be used as an anti-cancer agent or a tumor-targeting vehicle for delivering shRNA-expressing pDNA into cancer cells in a mouse tumor model.
Methods: Mouse bladder transitional cancer cell line (BTT-T739) expressing GFP was used, in which the GFP expression level served as an indicator of RNA interference (RNAi). BTT-T739-GFP tumor-bearing mice (4–6 weeks) were treated with *S typhimurium* carrying plasmids encoding shRNA against gfp or scrambled shRNA. The mRNA and protein expression levels of GFP were assessed 5 d after the bacteria administration, and the antitumor effects of *S typhimurium* were evaluated.
Results: In BTT-T739-GFP tumor-bearing mice, *S typhimurium* (1×10^9 cfu, *po*) preferentially accumulated within tumors for as long as 40 d, and formed a tumor-to-normal tissue ratio that exceeded 1000/1. *S typhimurium* carrying plasmids encoding shRNA against gfp inhibited the expression of GFP in tumor cells by 73.4%. Orally delivered *S typhimurium* significantly delayed tumor growth and prolonged the survival of tumor-bearing mice.
Conclusion: This study demonstrates that attenuated *S typhimurium* can be used for both delivering shRNA-expressing vectors into tumor cells and eliciting RNAi, thus exerting anti-tumor activity, which may represent a new strategy for the treatment of solid tumors.

Keywords: RNA interference; *Salmonella typhimurium*; shRNA-expressing pDNA; mouse bladder transitional cancer cell; tumor therapy

Acta Pharmacologica Sinica (2011) 32: 368–374; doi: 10.1038/aps.2010.224

Introduction

RNA interference (RNAi) is a naturally occurring gene silencing event in which small interfering RNA (siRNA) initiates the degradation of target mRNA that contains a sequence complementary to the siRNA. Since the original discovery of RNAi in *Caenorhabditis elegans*[1], there has been an increasing interest in harnessing this endogenous mechanism to treat a variety of diseases in which aberrant expression of mRNA is problematic. The first clinical trial to test siRNA in the treatment of age-related macular degeneration (AMD) commenced in 2004[2]. However, systemic siRNA therapy is hampered by barriers that prevent siRNA from reaching their intended targets in the cytoplasm and exerting their stable gene silencing activity. DNA vectors that transcribe short hairpin RNA (shRNA) provide another way to elicit RNAi. Previous studies have shown that the extent by which target gene expression is repressed is nearly identical between siRNA and shRNA-expressing plasmid DNA (pDNA)[3]. However, the gene-silencing effect induced by shRNA-expressing pDNA lasts significantly longer than gene silencing induced by siRNA[4]. pDNA must be delivered into the nucleus of target cells to transcribe shRNA. The shRNA is then transported to the cytosol and processed into siRNA. As gene therapy studies have previously demonstrated, nuclear delivery is one of the biggest challenges in transfection, and limited transgene expression has largely hampered the clinical application of therapeutic DNA[5]. By hijacking a variety of cellular mechanisms, viruses have evolved strategies to transport their genomic material into the nucleus[6, 7]. However, the safety concerns surrounding viral vectors have not been resolved.

In cancer research, efforts have been made to find a magic bullet that could selectively target and destroy malignant cells. More than 100 years ago, the German physician W Busch induced a bacterial infection in a woman with an inoperable sarcoma and observed a reduction in the size of the primary tumor[8]. Recently, both the presence and the selective growth of anaerobic bacteria in human tumors have

---

[#] These two authors contributed equally to this work.
* To whom correspondence should be addressed.
E-mail dmren@fudan.edu.cn
Received 2010-09-09 Accepted 2010-12-08

garnered attention. The conditions that permit anaerobic bacterial growth, such as impaired circulation and extensive necrosis, are found in many tumors. Therefore, bacteria may be a viable therapeutic option for a variety of malignancies. *Salmonella typhimurium* (*S typhimurium*), a facultative anaerobe, has been exploited as an anti-tumor agent that is capable of preferentially targeting tumors. The bacteria then amplify within the tumor and inhibit its growth[9, 10]. Tumor targeting bacteria have been harnessed to deliver exogenous genes that facilitate anti-tumor effects[11, 12]. To this end, our group has reported that *S typhimurium* can transfer plasmids expressing cytokines[13] and prodrug converting enzymes[14] across phylogenetic borders to mammalian cancer cells, thereby exerting anti-tumor effects. Given the tumor-targeting capacity of *S typhimurium*, we examined the ability of attenuated *Salmonella* to serve as an anti-cancer agent and a tumor-targeting vehicle that would deliver shRNA-expressing pDNA into tumor cells in a mouse model. The results indicated that attenuated *S typhimurium* SL3261 mediated the trans-kingdom gene transfer of shRNA-expressing pDNA into tumors to silence gene expression. This proof of principle study suggests that the combination of tumor-targeting and repressive actions by *S typhimurium,* as well as the therapeutic potential of RNA interference using *S typhimurium* carrying shRNA-expressing plasmids, can be exploited as a novel therapeutic approach for the treatment of cancers.

Materials and methods

Plasmids and bacteria

The plasmid pSuper (Oligoengine, Halo-Bio RNAi Therapeutics, Inc, USA) was used to express shRNA under the control of the H1 RNA polymerase gene promoter. The general strategy for constructing the RNAi plasmid involved subcloning an inverted repeat into pSuper. shRNA targeting green fluorescent protein (GFP) was designed using the online siRNA Selection Program (http://jura.wi.mit.edu/bioc/siRNAext/reference.php) according to Tuschl's siRNA user guide (http://www.rockefeller.edu/labheads/tuschl/sirna.html). Forward and reverse oligos for *gfp* were: (forward) 5′- GATCCCC **GGAGCGCACCATCTTCTTC** TTCAAGAGA **GAAGAAGATGGTGCGCTCC** TTTTTGGAAA-3′ and (reverse) 5′-AGCTTTTCCAAAAA **GGAGCGCACCATCTTCTTC** TCTCTTGAA **GAAGAAGATGGTGCGCTCC** GGG-3′. Oligos were annealed, cloned into pSUPER and designated as pGFPi. A similar method was used to construct the pscrGFP negative control that contained the same nucleotide composition as the *gfp* targeting shRNA but had no match to the *gfp* coding sequence. Two sequences were blasted against the mouse genome database and the EST database to exclude the possibility of off-target effects. Plasmids were transformed into *S typhimurium* LB5000 (LT2 Trp Met Erpsl flaA R^-M^+) and SL3261 (WARY hisG 46 aroA$^-$ Del 407 Fusaricres R^+M^+) (provided by Bruce AD STOCKER, Stanford University) as previously described[13].

Cell lines and mice

Mouse bladder transitional cancer cells (BTT-T739) were derived from BBN-(*N*-butyl-*N*-(4-hydroxybutyl) nitrosamine) exposed T739 mice[15]. The GFP-expressing cell line BTT-T739-GFP was generously provided by Prof Qian WANG and Feng HUANG from the Central Experimental Laboratory of the First People's Hospital in Shanghai, China. Cells were cultured in RPMI-1640 medium (Gibco BRL) supplemented with 100 units/mL penicillin, 100 μg/mL streptomycin and 10% FBS.

Four- to six-week-old female T739 mice were used for tumor growth models and infection studies. T739 adult mice were purchased from B&K Universal Ltd (Shanghai, China), and all animal experiments were performed according to the institutional animal care and use protocol.

Bacterial infection assay *in vitro*

BTT-T739-GFP cells were plated at a density of 5.0×10^5 cells in 12-well culture plates and incubated overnight without antibiotics. Bacteria in late log phase were washed and diluted in RPMI-1640 and then added to the BTT-T739-GFP cells (1.25×10^8 bacteria/well). After 3 h, the cells were washed and incubated in RPMI-1640 containing 100 units/mL of penicillin and 100 μg/mL of streptomycin until harvested.

Flow cytometry analysis

GFP expression was assessed using fluorescence activated cell sorting (FACS). Cultured cells were harvested, washed and resuspended in PBS. Ten thousand events per sample of cultured cells were captured. The geometric mean fluorescence was used as a measure of the relative intensity of green fluorescence.

Animal tumor model and *in vivo* bacterial tumor targeting assay

BTT-T739-GFP cells (5×10^5) were implanted subcutaneously in mice before bacterial administration. Treatments were initiated 15 d after tumor inoculation. Groups of 15–20 tumor-bearing mice were orally administrated with 1×10^9 cfu of *Salmonella* (SL3261/pGFPi or SL3261/pscrGFP) or saline. All mice were monitored for tumor growth and survival as previously described[16, 17].

Groups of 3–5 mice were sacrificed to investigate bacteria distribution at various time points after bacteria treatment. Tumors, blood, livers and spleens from the mice were collected, weighed and homogenized in 2 mL of ice-cold sterile PBS. The homogenates were plated onto L broth (Sigma) agar plates containing ampicillin (100 μg/mL), and bacterial counts were performed. To assess GFP expression levels, tumor cells were filtered through 0.22 μm meshes, resuspended in PBS and processed as described above for cultured cells. Tumor samples from T739 mice were homogenized in liquid nitrogen and stored for future semi-qRT-PCR analysis.

Extraction of total RNA and DNA and semi-qRT-PCR assay

Total DNA and RNA from cultured cells and mouse tumors were prepared using TRIzol reagent (Invitrogen), and cDNA was synthesized using oligo(dT) with the AccessQuick™ RT-PCR System (Promega). Total RNA (100 ng) was subjected to cDNA synthesis. The RT-PCR method was used to analyze GFP expression levels in different samples, and β-actin was used for normalization. Semi-qRT-PCR was performed as previously described[18] using 100 ng of cDNA in a 25 μL reaction volume. The expression level of each gene was determined by semi-qRT-PCR method. The primers for β-actin amplification were 5′-CCCAGAGCAAGAGAGGTATC-3′ (forward) and 5′-GACCAGAGGCATACAGGGAC-3′ (reverse). The primers used for GFP amplification were 5′-GAGCGCACCATCTTCTTC-3′ (forward) and 5′-CGTCTAGATTACTTGTACAGCTCGTC-3′ (reverse). β-actin and GFP were amplified using 27 and 35 cycles, respectively. The parameters for each cycle were 94 °C for 30 s, 55 °C for 30 s, and 72 °C for 45 s. The amplified fragments were separated by 1% agarose gel electrophoresis. Images of the semi-qRT-PCR products stained with ethidium bromide were analyzed with Dolphin-1D software (WEALTEC Corp, Sparks, NV, USA). The band intensity of GFP was normalized to β-actin.

Statistical analysis

Statistical analysis was performed using the SPSS statistic software package (SPSS, Chicago, IL, USA). All results are expressed as means±SEM, and $P<0.05$ was considered significant.

Results

Silencing of *gfp* expression by SL3261/pGFPi in tumor cells *in vitro*

To test whether shRNA-expressing pDNA can be delivered from *S typhimurium* to mammalian tumor cells and induce gene specific RNAi, BTT-T739-GFP cells were infected with SL3261/pGFPi, SL3261/pSUPER, and SL3261/pscrGFP. As shown in Figure 1A, different levels of green fluorescence protein (GFP) expression were detected in tumor cells infected with SL3261/pGFPi or SL3261/pscrGFP at 48 h after bacterial infection. GFP protein levels were analyzed by FACS at 72 or 96 h post-infection. At 96 h post-infection, GFP protein expression in the SL3261/pGFPi treated group was reduced by 40.2% and 33.9% compared to that of SL3261/pSUPER- and SL3261/pscrGFP-infected groups, respectively (Figure 1B). Collectively, these results demonstrate that eukaryotic shRNA-expressing plasmids can be transferred to, and expressed in, tumor cells using attenuated *S typhimurium* as a gene delivery vehicle.

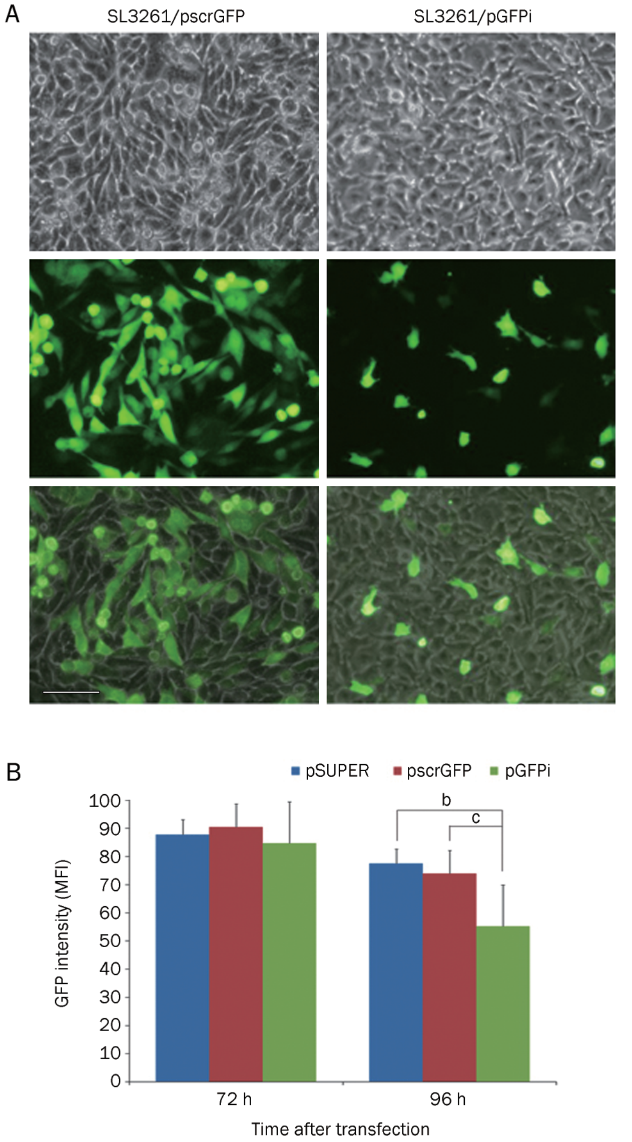

Figure 1. SL3261/pGFPi suppressed GFP expression in BTT-T739-GFP cells *in vitro*. (A) Different levels of GFP expression between SL3261/pGFPi and SL3261/pscrGFP treated groups were directly detected by fluorescence microscopy at 48 h following bacterial infection. The scale bar indicates 100 μm. (B) Protein levels of GFP were analyzed by FACS at 72 and 96 h post-bacterial infection. The overall expression of GFP was reduced because the cultures deteriorated several days after bacterial infection. Notably, GFP expression was significantly decreased by SL3261/pGFPi compared with SL3261/pSUPER and SL3261/pscrGFP. $^{b}P<0.05$, $^{c}P<0.01$.

Preferential accumulation of attenuated S *typhimurium* in tumors

To determine the localization of orally administered attenuated *S typhimurium* in BTT-739T-GFP tumor-bearing mice, we monitored bacterial burdens in the blood, liver, spleen and tumor at various time points after oral infection. As shown in Figure 2A, SL3261 (regardless of the plasmid it harbors) was detected in the blood, liver, spleen and tumor at 36 h after bacterial administration. By the 7th d, SL3261 had selectively accumulated within tumors, such that the tumor-to-normal tissue ratios were greater than 1000:1, and bacteria in the blood had been almost completely cleared. Notably, SL3261, while retained in the tumors, was undetectable in the spleens or livers of the mice by 21 d (Figure 2A, 2B). At 40 d after oral administration, bacteria were still present in tumors but were undetectable in the livers and spleens, as confirmed by

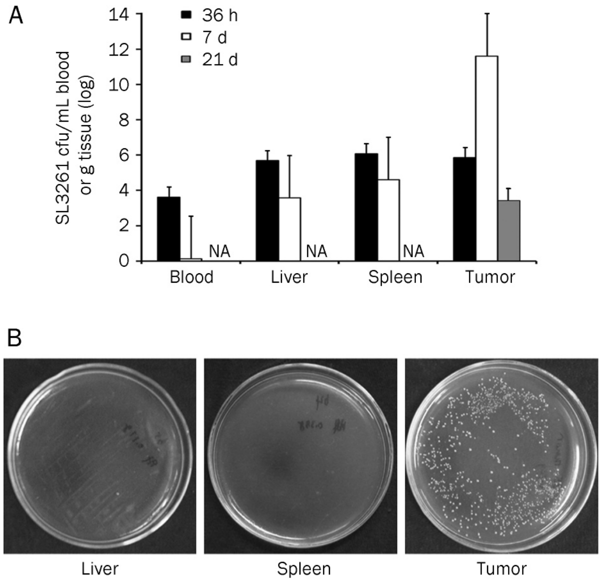

Figure 2. Preferential accumulation of *S typhimurium* in mouse bladder tumors. Tumor-bearing mice received the three different *Salmonella* treatments once tumors reached a predetermined size. (A) The amount of SL3261 in the tumors, livers and spleens was determined at 36 h, 7 d and 21 d post-infection. Data are shown as means±SEM. *n*=5. (B) Liver, spleen or tumor tissue (0.3 g each) was harvested from tumor-bearing mice on d 21 post-infection and homogenized and resuspended in 50 μL PBS. The suspension was spread on LB agar plates containing ampicillin.

PCR using primer pairs specific to a region of *S typhimurium* genomic DNA (data not shown). Previous studies from our lab also investigated bacteria distribution in mouse lung, heart, brain and kidney. Bacterial was undetectable in the brain at 36 h after oral administration, and by 72 h the *Salmonella* were eliminated from all other organs (unpublished). Collectively, these results show that *S typhimurium*, when orally administered to mice bearing established tumors, preferentially accumulates in tumors and is retained for as long as 40 d.

Downregulation of *gfp* expression in mouse tumors treated with SL3261/pGFPi

We have shown that attenuated *S typhimurium* transferred shRNA-expressing plasmids to tumors and that shRNA was successfully expressed. Attenuated *S typhimurium* preferentially accumulated, and was retained in large amounts, within the tumors. Thus, we next examined *gfp* mRNA and protein levels in mice to determine whether attenuated *Salmonella* could deliver shRNA-expressing pDNA and induce RNAi in tumor cells *in vivo*. Compared to the SL3261/pscrGFP treated group, we observed considerably reduced *gfp* mRNA and protein expression in the tumors of SL3261/pGFPi treated mice at 5 d after bacteria administration. Gene silencing specificity was confirmed by the lack of change in β-actin expression. Representative results from this experiment are shown in Figure 3A, 3B. We next examined the presence of attenuated *S typhimurium* and shRNA-expressing pDNA in tumor tissues. For this, tumors were dissected, and dissociated tumor cells were incubated with medium containing kanamycin to eliminate extracellular bacteria before extracting total DNA and performing PCR to detect SL3261 and pSUPER. As shown in Figure 3C (a, b), attenuated *S typhimurium* was localized in tumors, and shRNA-expressing pDNA was transferred into tumor cells 5 d after bacterial treatment. Previous studies have shown that plasmid instability may result in its loss from *Salmonella in vivo*. Therefore, we streaked the tumor cell suspension on LB agar plates and performed colony PCR using pSUPER specific primers. As shown in Figure 3C (c), *S typhimurium* in the tumor cells retained the shRNA-expressing plasmids. These results indicate that shRNA-expressing plasmids delivered by oral administration of attenuated *S typhimurium* can efficiently induce gene specific silencing in tumor cells.

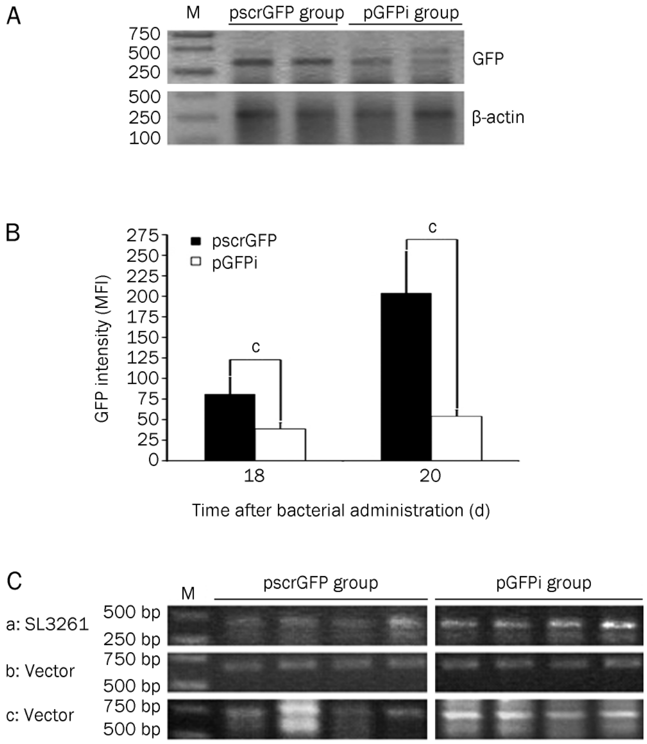

Figure 3. SL3261/pGFPi suppressed GFP expression in BTT-T739-GFP cells *in vivo*. Tumor cell suspensions were collected at 3 d and 5 d after bacterial treatment. GFP mRNA and protein levels were analyzed by semi-qRT-PCR (A) and FACS (B). Oral administration of SL3261/pGFPi significantly decreased GFP expression in tumor cells compared with SL3261/pscrGFP. (C) Dissociated tumor cells were treated with kanamycin to kill extracellular *Salmonella*, and the total DNA and RNA from tumor cells were extracted. Plasmid containing *Salmonella* was confirmed in tumor cells by PCR using *Salmonella* specific primers (a) and pSUPER specific primers (b). Tumor cell suspensions were dispersed onto ampicillin containing plates to confirm the presence of the different plasmids in the bacteria using colony PCR with pSUPER specific primers (c). $^{c}P<0.01$.

Inhibition of tumor growth by *S typhimurium* oral administration

Despite its accumulation in diverse tumor subtypes, *Salmonella* has been show to exhibit minimal, if any, impact on tumor growth[19]. We next investigated whether SL3261 has therapeutic effects on bladder tumor progression in mice and whether the shRNA-expressing plasmids would interfere with its antitumor activity. Tumor volumes and survival time were examined in tumor-bearing mice treated with SL3261, SL3261/pGFPi, or SL3261/pscrGFP. SL3261 treatment significantly inhibited tumor growth compared to saline controls (Figure 4). SL3261/pGFPi and SL3261/pscrGFP exhibited antitumor effects similar to SL3261. This suggests that SL3261 can be used as both a shRNA-expressing pDNA delivery vehicle and an antitumor agent. The average tumor volume in the SL3261, SL3261/pGFPi, and SL3261/pscrGFP treated groups was significantly smaller than that in the saline control (P<0.001) at d 30 and 35 post-tumor inoculation. We also recorded the survival rate of SL3261/pGFPi and SL3261/pscrGFP treated groups *versus* the saline treated group at different time points. SL3261/pGFPi and SL3261/pscrGFP treatment increased the life span by 35.7% (P<0.001) compared to saline treatment, as determined by ED_{50} (day at which 50% of the mice were dead). Gross adverse effects, such as loss of body weight, were observed during the experimental periods (data not shown). Different antitumor activities were not observed between SL3261, SL3261/pGFPi, and SL3261/pscrGFP treatments because the shRNA-expressing pDNA targets GFP rather than endogenous genes critical for tumor development. Collectively, these results suggest that oral administration of a shRNA-expressing plasmid containing *S typhimurium* can significantly suppress tumor growth and prolong the life span of tumor-bearing mice.

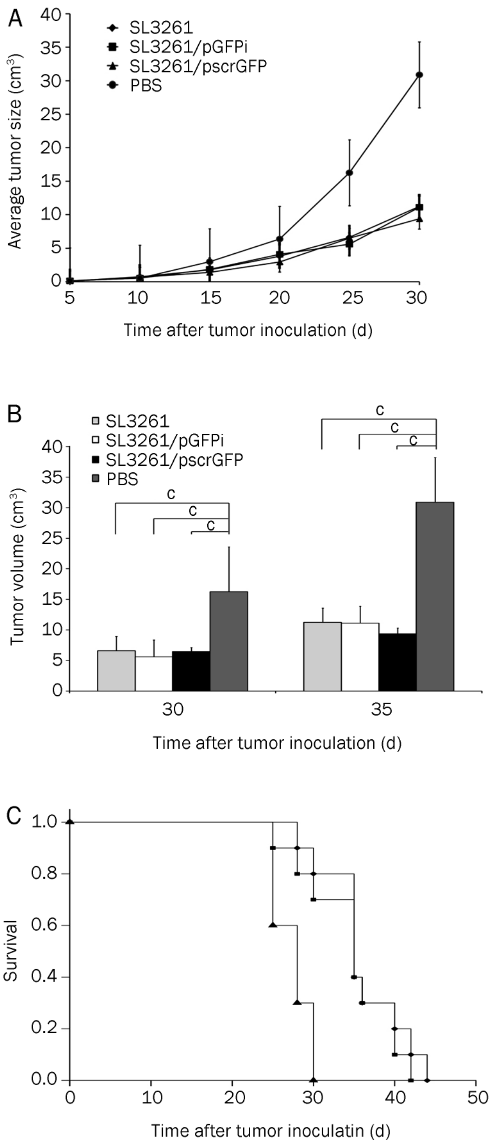

Figure 4. Antitumor effect of SL3261, SL3261/pGFPi, and SL3261/pscrGFP in the tumor-bearing mice. (A) Tumor growth curves of different treatment groups. On the 15th d after tumor inoculation, SL3261 (♦), SL3261/pGFPi (■), SL3261/pscrGFP (▲), or PBS (●) was orally administered. Tumor diameters were measured at a regular interval for more than 30 d, and the tumor volume was calculated. Results represent the mean±SEM (n=5–6). (B) Comparison of tumor volumes on d 30 and 35. Compared to PBS, SL3261 alone, or SL3261 carrying either plasmid, exhibited an anti-tumor effect (P<0.01). (C) Kaplan-Meier survival curves of tumor-bearing mice receiving the various treatments described in (A). SL3261/pGPFi or SL3261/pscrGFP treatment increased the life span by 35.7% (P<0.01) compared to saline treatment, as evidenced by ED_{50}. ^cP<0.01.

Discussion

We examined the potential of attenuated *S typhimurium* to be used as a gene transfer vehicle to mediate vector-based RNA interference in a mouse tumor model. We demonstrated that orally administered *S typhimurium* preferentially accumulated within tumors and mediated the trans-kingdom gene transfer of shRNA-expressing plasmids from bacteria to mammalian cells. The RNAi that was observed was presumably due to shRNAs produced from the plasmids.

In the past decade, there has been an increased interest in RNA interference, which is an evolutionarily ancient method of genome defense in many organisms. RNA interference is a widespread natural phenomenon that has the power to produce gene-specific inhibition. The sequence-mediated specificity and potency of RNAi make it a promising therapeutic strategy to treat diseases caused by aberrant gene expression. However, both siRNA and shRNA-expressing pDNA are negatively charged hydrophilic molecules that do not easily cross the cell membrane. Effective delivery of these molecules is perhaps the greatest challenge that needs to be overcome for RNAi to be translated to the clinic. Preclinical data have revealed multiple ways to deliver RNAi, including the injection of naked siRNAs into target organs, such as the lung and eye, or the systemic delivery of siRNA in nanoparticles that are complexed to polycations, cholesterol groups or cell-surface receptors (reviewed by Daniela CASTANOTTO and John ROSSI[20]). These methods are not suitable for delivering shRNA-expressing pDNA due to their size. The genes encoding the hairpin structures are most commonly inserted into the backbones of viral vectors under the control of Pol II or Pol III promoters. Although some viruses are non-pathogenic, they are still potentially immunogenic and can cause insertional mutagenesis or trigger aberrant gene expression. A potential advantage of vector delivery is that a single treatment triggers long-term expression of the therapeutic RNAi. This is particularly appropriate for chronic viral diseases and makes it appealing to find a safer, yet efficient, way to deliver shRNA-expressing vectors to target cells.

The finding that genes of putative prokaryotic origins exist within the human genome strengthened the hypothesis that transfer of genomic information occurred during evolution. This suggested that bacteria could potentially be used to deliver DNA products into mammalian or human cells. The tumor may also provide an immunosuppressive environment that inhibits clearance of the bacteria. In addition to accumulating within tumors, attenuated *Salmonella* also exerts an inherent anti-tumor efficacy[21–24]. The *Salmonella*-induced anti-tumor effect may be due to competition for nutrients between cancer cells and the bacteria and/or secretion of bacterial enzymes, such as proteases and other hydrolases. Additionally, apoptosis via the type III secretion system, as seen with macrophages *in vitro*, may also explain the anti-tumor efficacy caused by *Salmonella*[25]. However, the precise mechanisms underlying the anti-tumor effects have not been fully elucidated.

Attenuated bacterial strains, such as *S typhimurium*[26–28], *Clostridium*[29], and *Bifidobacterium*[30], preferentially accumulate in tumors because the hypoxic and necrotic areas in solid tumors are conducive to the proliferation of anaerobic bacteria. We previously used an attenuated *S typhimurium* SL3261 as a delivery vehicle to carry eukaryotic expression vectors encoding cytokines[13] or pro-drug converting enzymes[14] as anticancer agents. We have confirmed these findings and extended them to the use of *S typhimurium* as a tumor-targeted anticancer agent. Our results showed that *S typhimurium* delivered shRNA-expressing pDNA into tumor cells via systemic administration, and this resulted in effective induction of RNAi. Because *S typhimurium* preferentially colonized in tumors and survived for approximately 40 d after inoculation, a more sustained release of shRNA-expressing pDNA in tumor cells could potentially be achieved via *S typhimurium*-mediated gene transfer. Furthermore, *S typhimurium* has been genetically engineered to improve its ability to target tumors and to reduce toxicity[24]. Because bacteria have served as a well-validated system in molecular biology and biotechnology and *Salmonella* grow well in an oxygen-rich environment, versatile RNAi vectors for therapeutic applications can be easily constructed, stored, and amplified in *S typhimurium*. Compared with synthetic siRNA, *S typhimurium*-mediated vector-based RNAi may result in a higher targeting specificity, a more sustained RNAi effect, and a more economical treatment method. Despite the fact that our shRNA was designed to target GFP, rather than an endogenous tumor-related gene, orally administered SL3261 carrying a pGFPi or pscrGFP plasmid showed antitumor effects. This indicates that synergistic antitumor effects may be achieved using *S typhimurium* to deliver shRNA-expressing pDNA targeting genes critical for tumor development. It has been 30 years since trans-kingdom gene transfer was first observed by Walter SCHAFFNER[31], and extensive studies have examined the potential use of bacteria as a gene delivery method in tumor cells. However, little is known at the cellular level about the precise events involved in gene transfer between bacteria and target cells. Based on previous studies on the trans-kingdom gene transfer process (reviewed by Siegfried WEISS[32, 33], Christoph SCHOEN[34] and John PAWELEK[35]), it is known that *S typhimurium* containing shRNA-expressing vectors invade host cells, that the bacterial carriers are then lysed within the phagolysosomes, and that this results in the intraphagosomal release that transfers plasmid DNA into the cytosol. By a mechanism that is not fully understood[36], these plasmids cross the vesicular membrane and reach the nucleus of the host cell where they are expressed. This process can occur with very high frequency.

In addition to intracellular bacteria, other researchers reported that *Escherichia coli* encoding siRNA can induce gene silencing in human colon cancer xenografts in mice[37]. The plasmid used to make the siRNA was engineered to express the invasion gene *Inv* and the listeriolysin O gene *HlyA*, which are two bacterial factors that are essential for the transfer of siRNAs into mammalian cells. We had little problem with crosstalk between bacteria and mammalian cells because intracellular *S typhimurium* bacteria can circumvent host defense mechanisms. *S typhimurium* induce their own phagocytic uptake and avoid phagocyte-mediated death following internalization[36]. The pDNA is released and can enter the nucleus following intracellular breakdown of bacterial carriers.

In conclusion, we demonstrated the potential of using *S typhimurium* to mediate the gene transfer of a shRNA-expressing vector for RNAi-based cancer therapy. The benefits of this system include tumor targeting and repression by *S typhimurium* and the therapeutic potential of RNA interference. Thus, *S typhimurium* that carry shRNA-expressing vectors that produce siRNA against genes critical in tumor development may be a promising approach for cancer treatment.

Acknowledgements

We thank Fudan University State Key Laboratory of Genetic Engineering for technical support and Su-qin SHEN for her excellent technical assistance. We thank Prof Qian WANG and Feng HUANG for their generous offer of the cell line. We also thank Xiao WANG, Lu-biao HUANG, Meng-ning ZHOU, and Gao-feng LIU for their kind support and helpful suggestions regarding this project.

Author contribution

Nan YANG, Sheng-hua LI, and Da-ming REN designed research; Nan YANG and Sheng-hua LI performed research; Li-shan CHEN and Yun-zhe LÜ contributed new analytical tools and reagents; Nan YANG and Sheng-hua LI analyzed data; and Nan YANG wrote the paper.

References

1 Fire A, Albertson D, Harrison SW, Moerman DG. Production of antisense RNA leads to effective and specific-inhibition of gene-expression in *C elegans* muscle. Development 1991; 113: 503–14.

2 siRNA Therapeutics Inc. siRNA therapeutics commences phase I clinical trial for age-related macular degeneration at cleveland clinic. PR Newswire 2004 Nov 23. http://www.prnewswire.com/news-releases.

3 McAnuff M, Rettig G, Rice K. Potency of siRNA *versus* shRNA mediated knockdown *in vivo*. J Pharm Sci 2007; 96: 2922–30.

4 Takahashi Y, Yamaoka K, Nishikawa M, Takakura Y. Quantitative and temporal analysis of gene silencing in tumor cells induced by small interfering RNA or short hairpin RNA expressed from plasmid vectors. J Pharm Sci 2009; 98: 74–80.

5 Wagstaff KM, Jans D. Nucleocytoplasmic transport of DNA: enhancing non-viral gene transfer. Biochem J 2007; 406: 185–202.

6 Anderson JHope T. Intracellular trafficking of retroviral vectors: obstacles and advances. Gene Ther 2005; 12: 1667-78.

7 Ding W, Zhang L, Yan Z, Engelhardt J. Intracellular trafficking of adeno-associated viral vectors. Gene Ther 2005; 12: 873-80.

8 Stephen S HALL. A commotion in the blood: Life, death, and the immune system. New York: Henry Holt; 1997.

9 Pawelek J, Low K, Bermudes D. Tumor-targeted *Salmonella* as a novel anticancer vector. Cancer Res 1997; 57: 4537-44.

10 Pawelek J, Low K, Bermudes D. Bacteria as tumour-targeting vectors. Lancet Oncol 2003; 4: 548–56.

11 Lee C, Wu C, Shiau A. Systemic administration of attenuated *Salmonella choleraesuis* carrying thrombospondin-1 gene leads to tumor-specific transgene expression, delayed tumor growth and prolonged survival in the murine melanoma model. Cancer Gene Ther 2004; 12: 175–84.

12 Lee C, Wu C, Shiau A. Endostatin gene therapy delivered by *Salmonella choleraesuis* in murine tumor models. J Gene Med 2004; 6: 1382–93.

13 Li YH, Guo KY, Chen H, Xie YM, Song CY, Tang X, *et al.* Oral cytokine gene therapy against murine tumor using attenuated *Salmonella typhimurium*. Int J Cancer 2001; 94: 438-43.

14 Fu W, Lan H, Liang S, Gao T, Ren D. Suicide gene/prodrug therapy using *salmonella*-mediated delivery of *Escherichia coli* purine nucleoside phosphorylase gene and 6-methoxypurine 2′-deoxyriboside in murine mammary carcinoma 4T1 model. Cancer Sci 2008; 99: 1172–9.

15 Wen-sen W, Ke-zheng Y, Yue-ming H, Xiao-ming Z, Dong-shen Z, Da-luo H. Establishment and study of a transplantable bladder transitional cell carcinoma model (BTT739) in T739 inbred mice. Chin J Clin Oncol 1996; 23: 751-756.

16 Burfeind P, Chernicky CL, Rininsland F, Ilan J, Ilan J. Antisense RNA to the type I insulin-like growth factor receptor suppresses tumor growth and prevents invasion by rat prostate cancer cells *in vivo*. Proc Natl Acad Sci USA 1996; 93: 7263–8.

17 Hsieh J, Wu C, Lee C, Shiau A. Hepatitis B virus X protein sensitizes hepatocellular carcinoma cells to cytolysis induced by E1B-deleted adenovirus through the disruption of p53 function. Clin Cancer Res 2003; 9: 338–45.

18 Meadus W. A semi-quantitative RT-PCR method to measure the *in vivo* effect of dietary conjugated linoleic acid on porcine muscle PPAR gene expression. Biological Proced Online 2003; 5: 20–8.

19 Rosenberg S, Spiess P, Kleiner D. Antitumor effects in mice of the intravenous injection of attenuated *Salmonella typhimurium*. J Immunother 2002; 25: 218–25.

20 Castanotto D, Rossi J. The promises and pitfalls of RNA-interference-based therapeutics. Nature 2009; 457: 426–33.

21 Saltzman DA, Katsanis E, Heise CP, Hasz DE, Vigdorovich V, Kelly SM, *et al.* Antitumor mechanisms of attenuated *Salmonella typhimurium* containing the gene for human interleukin-2: A novel antitumor agent? J Pediatr Surg 1997; 32: 301–6.

22 Rosenberg SA, Spiess PJ, Kleiner DE. Antitumor effects in mice of the intravenous injection of attenuated *Salmonella typhimurium*. J Immunother 2002; 25: 218–25.

23 Luo X, Li ZJ, Lin S, Le T, Ittensohn M, Bermudes D, *et al.* Antitumor effect of VNP20009, an attenuated *Salmonella*, in murine tumor models. Oncol Res 2001; 12: 501–8.

24 Clairmont C, Lee KC, Pike J, Ittensohn M, Low KB, Pawelek J, *et al.* Biodistribution and genetic stability of the novel antitumor agent VNP20009, a genetically modified strain of *Salmonella typhimurium*. J Infect Dis 2000; 181: 1996–2002.

25 Hardt W, Urlaub H, Galán J. A substrate of the centisome 63 type III protein secretion system of *Salmonella typhimurium* is encoded by a cryptic bacteriophage. Proc Natl Acad Sci USA 1998; 95: 2574–9.

26 Graham F, Coleman P. Infection of a secondary carcinoma by *Salmonella montevideo*. Br Med J 1952; 1: 1116.

27 Gill GV, Holden A. A malignant pleural effusion infected with *Salmonella enteritidis*. Thorax 1996; 51: 104–5.

28 Johnson PH, Macfarlane JT. Commentary: pleural empyema and malignancy — another dimension. Thorax 1996; 51: 107–8.

29 Fox M, Lemmon M, Mauchline M, Davis T, Giaccia A, Minton N, *et al.* Anaerobic bacteria as a delivery system for cancer gene therapy: *in vitro* activation of 5-fluorocytosine by genetically engineered clostridia. Gene ther 1996; 3: 173–8.

30 Kimura N, Taniguchi S, Aoki K, Baba T. Selective localization and growth of *Bifidobacterium bifidum* in mouse tumors following intravenous administration. Cancer Res 1980; 40: 2061–8.

31 Schaffner W. Direct transfer of cloned genes from bacteria to mammalian cells. Proc Natl Acad Sci USA 1980; 77: 2163–7.

32 Weiss S, Krusch S. Bacteria-mediated transfer of eukaryotic expression plasmids into mammalian host cells. Biol Chem 2001; 382: 533–41.

33 Weiss S, Chakraborty T. Transfer of eukaryotic expression plasmids to mammalian host cells by bacterial carriers. Curr Opin Biotechnol 2001; 12: 467–72.

34 Schoen C, Stritzker J, Goebel W, Pilgrim S. Bacteria as DNA vaccine carriers for genetic immunization. Int J Med Microbiol 2004; 294: 319–35.

35 Pawelek JM, Low KB, Bermudes D. Bacteria as tumour-targeting vectors. Lancet Oncol 2003; 4: 548–56.

36 Finlay BB, Brumell JH. *Salmonella* interactions with host cells: *in vitro* to *in vivo*. Philos Trans R Soc Lond B Biol Sci 2000; 355: 623–31.

37 Xiang SL, Fruehauf J, Li CJ. Short hairpin RNA-expressing bacteria elicit RNA interference in mammals. Nat Biotechnol 2006; 24: 697–702.

Acta Pharmacologica Sinica (2011) 32: 375–384
© 2011 CPS and SIMM All rights reserved 1671-4083/11 $32.00
www.nature.com/aps

Original Article

MicroRNA-221 inhibits CDKN1C/p57 expression in human colorectal carcinoma

Kai SUN*, Wei WANG, Jun-jie ZENG, Cheng-tang WU, Shang-tong LEI, Guo-xin LI

Department of General Surgery, Nanfang Hospital of Southern Medical University, Guangzhou 510515, China

---

Aim: To investigate the regulatory effect of microRNA-221 (miR-221) on CDKN1C/p57 expression in colorectal carcinoma (CRC).
Methods: Thirty four CRC and adjacent non-tumorous tissue samples were collected individually. Total RNA and protein were isolatedand from these samples and four human CRC-derived cell lines (including HT-29, Lovo, SW-480 and Caco2). MiR-221 expression was examined using real-time RT-PCR. CRC cells were treated with or without anti-p57-siRNA prior to the addition of pre-miR-221 or anti-miR-221. The mRNA and protein levels of CDKN1C/p57 were examined using semi-quantitative RT-PCR and Western blot, respectively. CRC cell proliferation and apoptosis were assessed using MTT assay and flow cytometry, respectively. The CDKN1C/p57 3′-UTR fragment was amplified using PCR from the genomic DNA of human colon cells and inserted into a luciferase reporter construct. The reporter construct was then transfected into CRC cells together with pre-miR-221 or anti-miR-221, and the luciferase activity in the transfected cells was examined.
Results: MiR-221 expression was significantly up-regulated in 90% of CRC samples compared to that in the adjacent non-tumorous tissue, and the expression level was positively correlated to an advanced TNM stage and local invasion. There was no significant difference in CDKN1C/p57 mRNA expression between CRC and corresponding non-tumorous tissues, whereas CDKN1C/p57 protein expression was markedly decreased in the CRC samples. A significant inverse correlation between miR-221 and CDKN1C/p57 expression was found in CRC cells. Moreover, a miR-221-specific inhibitor significantly increased CDKN1C/p57 protein expression in CRC cells. Anti-miR-221 markedly inhibited CRC cell proliferation and induced apoptosis. This inhibitory effect was abolished by pretreatment with anti-p57-siRNA, suggesting that the inhibition was mediated by CDKN1C/p57. A significant increase of the luciferase activity was observed in CRC cells co-transfected with the luciferase reporter construct and anti-miR-221.
Conclusion: MiR-221 binds to the target site in the 3′-UTR of the CDKN1C/p57 mRNA to inhibit CDKN1C/p57 expression by post-transcriptional gene silencing to promote CRC occurrence and progress, therefore serving as a potential therapeutic target for the prevention and treatment of CRC.

Keywords: colorectal carcinoma; microRNA-221; CDKN1C/p57; proliferation; apoptosis

---

Acta Pharmacologica Sinica (2011) 32: 375–384; doi: 10.1038/aps.2010.206; published online 31 Jan 2011

Introduction

Colorectal carcinoma (CRC) is one of the most frequently occurring cancers and a common cause of cancer-related death worldwide, with an increasing incidence expected in the next decades[1]. The overall incidence of CRC is 5% in the general population, and the 5-year survival rate ranges from 40% to 60%[2]. So far, prognosis largely relies on descriptive staging systems based on tumor morphology and histopathology[3]. However, morphologically similar tumors may differ in their underlying molecular changes and tumorigenic potential. CRC development from normal epithelial cells to malignant carcinomas is a multi-step process. It involves the accumulation of both genetic and epigenetic changes, leading to a temporal activation of oncogenes and an inactivation of tumor suppressor genes that confer a selective advantage to cells harboring these alterations[4]. CRC screening allows early diagnosis of the malignancy and reduces mortality. With the advent of new chemotherapeutic agents, such as angiogenesis inhibitors and TGF-α inhibitors, there is growing interest in identifying new prognostic biomarkers and therapeutic targets for this disease[5].

MicroRNAs (miRNAs) are a class of small noncoding RNAs that regulate target gene expression by translational repression and mRNA cleavage/decay[6]. Genome-wide studies have demonstrated that miRNA genes are frequently located at cancer-associated genomic regions, within minimal regions of loss of heterozygosity or of amplifications, and at common breakpoint regions, indicating the potential roles of miRNAs

---

* To whom correspondence should be addressed.
E-mail sunkai9602@sina.com
Received 2010-08-27 Accepted 2010-11-08

in tumorigenesis[7]. MiRNAs have been demonstrated to play an important role in the multi-step process of carcinogenesis, functioning as either oncogenes or tumor suppressors. The role of miRNAs has been studied in many types of tumors, including CRC tumors. Those studies suggest that miRNAs may be potential diagnostic or prognostic tools for cancer and that identifying their target mRNAs is a key step for assessing the role of aberrantly expressed miRNAs in human cancer[8].

MiR-221, encoded in tandem from a gene cluster located on chromosome X, is a recently discovered miRNA involved in tumor development by regulating cell proliferation. Fornari *et al*[9] demonstrated that miR-221 overexpression promotes hepatocellular carcinoma cell proliferation, most likely through its ability to modulate cyclin dependent kinase inhibitors (CDKIs), including CDKN1C/p57 and CDKN1B/p27. However, miR-221 expression and its targets in CRC have not been reported. CDKN1C/p57, an important regulator of cell-cycle progression, belongs to the kinase inhibitor protein (CIP/KIP) family, which has become a research focus in recent years because it can negatively regulate cell cycle progression by arresting cell proliferation in the G_0/G_1 phase[10]. CDKN1C/p57 down-regulation in CRC has been shown to correlate with high biological aggressiveness, advanced stage, poor differentiation, large tumor size, and high proliferative activity. Furthermore, low CDKN1C/p57 expression is associated with poor prognosis and low disease-free survival after surgery, suggesting that CDKN1C/p57 down-regulation might contribute to CRC progression by regulating cell growth[11]. Under both physiological and pathological conditions, CDKN1C/p57 is mostly regulated at a post-transcriptional level[12]. Therefore, we inferred that miR-221 is up-regulated in CRC and promotes carcinogenesis by inhibiting CDKN1C/p57 expression. To test this hypothesis, we investigated the regulatory effect of miR-221 on CDKN1C/p57 expression in CRC and provided new insight into the pathogenesis, diagnosis, and treatment of CRC.

Materials and methods

Patients

In total, 34 samples of CRC and matched non-tumorous tissue were harvested from patients who underwent operations in our hospital from September 2008 to May 2009 with diagnosis confirmed by postoperative pathological examination. Patients' characteristics regarding gender, age, tumor site, TNM stage, local invasion, vessel invasion, differentiation and sera carcinoembryonic antigen (CEA) were obtained from surgical and pathological records. The mean age was 52.5 years (ranging from 32 to 74 years). Local invasion was classified as tumor invading the submucosa (T1), the muscularis propria (T2), through the muscularis propria into the subserosa or nonperitonealized pericolic or perirectal tissues (T3), and through the muscularis propria into other organs or structures and/or perforated visceral peritoneum (T4). Differentiation was graded as better (including well and moderately differentiated tumors) and worse (including poorly differentiated, mucinous and signet-ring cell carcinoma). Non-tumorous tissue was harvested from the intestinal mucosa 5 cm from the tumor site, whereas normal controls were the intestinal mucosa over 10 cm from the tumor site. No patients received radiotherapy or chemotherapy before the operation. The samples were snap frozen in liquid nitrogen after collection and stored at -80 °C. All participants of this study signed an informed consent approved by the Institutional Review Board.

MiRNA target prediction

The analysis of predicted miR-221 targets was performed using the algorithms TargetScan (http://targetscan.org/), PicTar (http://pictar.mdc-berlin.de/), and miRanda (http://www.microrna.org/microrna/home.do) website tools.

Cell culture and transfection

Human CRC-derived cell lines, including HT-29, Lovo, SW-480 and Caco2, and control human umbilical vein endothelial cells (HUVEC), provided by Shanghai Institutes for Biological Science, were resuscitated and resuspended with RPMI-1640 supplemented with 10% (*v/v*) fetal bovine serum (FBS, provided by Hyclone, USA), 100 U/mL penicillin G and 100 mg/mL streptomycin. The cells were then plated in 25 cm^2 culture bottles and incubated in a 5% CO_2 humidified atmosphere at 37 °C. The media were changed every 3 d, and the cells were trypsinized using trypsin-edetic acid when they reached 80% to 90% confluence. Cells aged at passages 4 to 8 were used for experiments. The day before transfection, cells were seeded in antibiotic-free medium at a density of 1×10^4 cells/well in 96-well plates, incubated for 24 h, and then transfected with 80 nmol/L anti-p57 SMARTpool siRNAs or the control siRNA (Dharmacon) using Oligofectamine (Invitrogen, Carlsbad, CA, USA). Secondary transfection was performed 24 h after the first transfection, using 50 nmol/L negative control, anti-miR-221 negative control, pre-miR-221 or anti-miR-221, respectively (Shanghai GenePharma Co Ltd). MiRNA transfection was performed using Lipofectamine 2000 according to the manufacturer's instructions (Invitrogen). The experiment was repeated at least three times.

Detection of miR-221 expression by real-time RT-PCR

Total RNA was extracted using Trizol (Invitrogen, Carlsbad, CA, USA). The precipitation was dissolved in DEPC-treated water. A nucleic acid protein analyzer (Beckman Coulter, USA) was used to determine the RNA concentration. The purity and integrity of RNA were evaluated in formaldehyde denaturing gel electrophoresis based on two criteria: $A_{260\ nm}/A_{280\ nm}\geq1.8$ and a band ratio of 28S RNA to 18S RNA≥1.5. Mature miR-221 was accurately quantified using the TaqMan MicroRNA Assay (hsa-miR-221, N/P: 4373077; Applied Biosystems, Foster City, CA, USA). Briefly, the reverse transcription reaction was performed with 10 ng of total RNA using the looped primers. Real-time PCR was performed on an iCycler iQ Real-Time PCR Detection System (Bio-Rad) according to the standard TaqMan MicroRNA Assay protocol. The 20-μL PCR reaction included 1.33 μL of reverse transcription product, 1×TaqMan Universal PCR

Master Mix, No AmpErase UNG (P/N 4324018; Applied Biosystems), 0.2 μmol/L TaqMan probe, 1.5 μmol/L forward primer, and 0.7 μmol/L reverse primer. The reactions were incubated in a 96-well plate at 95 °C for 10 min, followed by 40 cycles of 95 °C for 15 s and 60 °C for 1 min. MiR-221 expression was measured using Ct (threshold cycle). The Ct is the fractional cycle number at which the fluorescence of each sample passes a fixed threshold. The ΔΔCt method for relative quantification of gene expression was used to determine miR-221 expression. The ΔCt was calculated by subtracting the Ct of RNU6B from that of miR-221. The ΔΔCt was calculated by subtracting the ΔCt of the reference sample from that of each tested sample. Fold change was calculated using the equation of $2^{-\Delta\Delta Ct}$. The TaqMan MicroRNA Assay for U6 RNA (RNU6B, P/N: 4373381; Applied Biosystems) was used to normalize the relative abundance of miR-221. The experiment was repeated at least three times.

Detection of CDKN1C/p57 mRNA expression by semi-quantitative RT-PCR

Briefly, 3 μg of total RNA was used as the template for RT-PCR analysis according to the instructions of the RNA PCR Kit Ver 3.0 of TaKaRa Company. The PCR parameters were as follows: 94 °C for 2 min; 30 cycles of 94 °C for 30 s, 55 °C for 30 s, and 72 °C for 1 min; and 72 °C for 10 min. Of the PCR products, 10 μL was loaded on a 1.5% agarose gel stained with ethidium bromide (0.5 g/L). The signal was quantitated by densitometry using the Image Master VDS system and the associated software (Pharmacia, USA) as follows: relative mRNA content=integral absorbance value of the target gene band/integral absorbance value of the internal reference GAPDH. The experiment was repeated at least three times[13].

Detection of CDKN1C/p57 protein expression by Western blot

The tissues and cells were rinsed twice with cold PBS buffer and lysed in an ice-cold lysis buffer containing 150 mmol/L NaCl, 50 mmol/L Tris-HCl (pH 7.6), 0.1% SDS, 1% Nonidet P-40, and a protease inhibitor cocktail (Boehringer Mannheim, Lewes, UK). The samples were cleared by centrifugation at 13 000×*g* for 10 min; 50 μg of protein from the tissue samples was subjected to sodium dodecyl sulfate-polyacrylamide gel electrophoresis (SDS-PAGE) and electrotransferred to polyvinylidene fluoride (PVDF) membranes (Immobilon, Bedford, MA). After being blocked in 20 mmol/L Tris-HCl, pH 7.6 (containing 150 mmol/L NaCl, 0.1% Tween-20, and 5% non-fat dry milk), the membranes were incubated with primary antibodies against CDKN1C/p57 or β-actin (used as a loading control) overnight at 4 °C and then incubated with a horseradish peroxidase-conjugated secondary antibody. The blot was developed using an ECL detection kit (Amersham Pharmacia Biotech), according to the manufacturer's instructions, and the protein imprinting band was obtained. The experiment was repeated at least three times.

Cell proliferation analysis of transfected cells by the MTT assay

Cell proliferation was determined by the 3-(4,5-dimethylthiazol-2-yl)-2,5-diphenyl tetrazolium bromide (MTT provided by Amresco, USA) assay. Briefly, exponentially growing CRC cells were adjusted to 1.5×10^4 cells/mL with RPMI-1640, plated in 96-well plates (Corning, USA) at 200 μL/well and then incubated for 12 h. After being transfected with 50 nmol/L miR-221 or anti-miR-221 and incubated for 48 h (five duplicate wells for each sample), 20 μL/well MTT (5 g/L) was added to each well. The medium was then removed after a 4-h incubation, and 100 μL/well dimethyl sulfoxide (DMSO) was added to dissolve the reduced formazan product. Subsequently, the plate was read in an enzyme-linked immunity implement (BIO-RAD2550, USA) at 490 nm. Cellular proliferation inhibition rate (CPIR) was calculated according to the following formula: CPIR=(1–average A value of the experimental group/average A value of the control group)×100%. The experiment was repeated at least three times.

Cell-cycle and apoptosis analyses of transfected cells by flow cytometry

The effects of miR-221 on cell cycle and apoptosis in CRC cells were examined by flow cytometry. In brief, pretreated CRC cells were harvested and washed twice with PBS buffer, fixed with 70% ethanol at -20 °C for 30 min and stored at 4 °C overnight. The cells were then washed with PBS again, treated with 100 mL of 100 mg/L RNase at 37 °C for 30 min and stained with Annexin V-FITC and PI at 4 °C for 30 min in darkness. Cell cycle and apoptotic rate were measured using an EPICS XL Flow Cytometer (Coulter, USA) at 488 nm, and the data were analyzed using the CELL Quest Software. The percentages of G_0/G_1 phase, S phase and the apoptotic rate were measured by calculating the ratio of the number of corresponding cells and that of total cells. For each sample, 10 000 cells were measured. The experiment was repeated at least three times.

Luciferase activity assay

The human 3'-untranslated region (3'-UTR) of the CDKN1C/p57 gene was amplified by PCR and cloned into the XbaI site of the pGL3-Control vector (Promega, Madison, WI, USA), downstream of the luciferase gene, to generate the vector pGL3-p57. For the luciferase assay, the CRC cells were cultured in 24-well plates and were transfected with 500 ng of either pGL3-p57 or the pGL3 control vector and 50 pmol of miR-221, anti-miR-221 or negative controls. Transfection was performed using Lipofectamine 2000 (Invitrogen) according to the manufacturer's instructions. At 24 h after transfection, the firefly luciferase activity was measured using the Dual-Luciferase Reporter Assay (Promega). The experiment was repeated at least three times.

Statistical analysis

The relative expression of target genes was analyzed using REST-XL (Relative Expression Software Tool, available at http://www.gene-quantification.de/rest.html). All data were presented as the average±standard deviation (Mean±SD). Comparisons between groups were performed by one-way

ANOVA and Student-Newman-Keuls *q* test using SPSS 13.0 (SPSS Inc, Chicago, IL, USA). *P* values less than 0.05 were considered statistically significant.

Results

CDKN1C/p57 mRNA expression is down-regulated in some CRC samples

To investigate the regulatory effect of miR-221 on CDKN1C/p57 protein expression in CRC, we examined CDKN1C/p57 mRNA expression in 34 CRC samples by semi-quantitative RT-PCR. The data showed that in four CRC samples, CDKN1C/p57 mRNA expression significantly decreased compared with the adjacent non-tumorous tissue (Figure 1A). These cases were excluded from the following experiments, whereas the remaining thirty samples (whose CDKN1C/p57 mRNA expression showed no significant difference between CRC and the adjacent non-tumorous tissue) were used for the following study (selective cases were shown in Figure 1B).

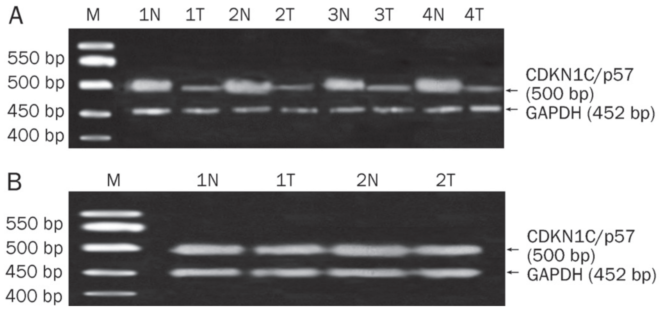

Figure 1. Semi-quantitative RT-PCR analysis showing CDKN1C/p57 mRNA expression in several CRCs and adjacent non-tumorous tissues. A reduction of CDKN1C/p57 mRNA levels can be observed in four CRC samples compared with adjacent non-tumorous tissues (A). The remaining thirty samples showed no significant difference of CDKN1C/p57 mRNA expression in CRC and adjacent non-tumorous tissues (selective cases were reported in (B). Equal loading was confirmed by using GAPDH as a loading control. M: Marker; N, T represented the patients' non-tumorous tissues (N) and CRCs (T), respectively.

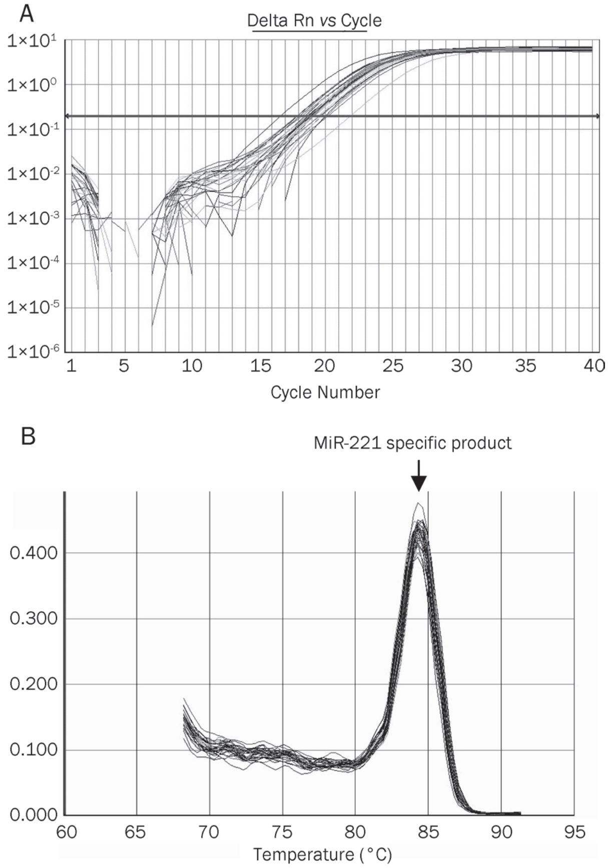

Figure 2. Real-time RT-PCR analysis detecting miR-221 expression in CRCs and adjacent non-tumorous tissues. (A) miR-221 cDNA concentrations' Log value as ordinate, Ct value as abscissa. (B) Tm of miR-221 was 84.26 °C.

MiR-221 is aberrantly overexpressed in CRC tissues and CRC-derived cell lines

To study the expression pattern of miR-221 in CRC, we used real-time RT-PCR to examine miR-221 expression in thirty CRC samples and the adjacent non-tumorous tissue, as well as in four CRC-derived cell lines. The data showed that the miR-221 cDNA level exponentially increased and reached the plateau phase. Its amplification curve displayed a typical reverse S pattern (Figure 2A), indicating high amplification efficiency. The miR-221 PCR product was 73 bp in length, and the corresponding Tm was 84.26±0.56 °C. The melting temperature was even, and the shape of the peak was sharp (Figure 2B). Of the 30 cases, 27 (90%) showed significantly up-regulated miR-221 expression in CRC compared with that in the non-tumorous tissue (2.041±1.401 *vs* 0.706±0.341, $P<0.01$). As shown in Table 1, miR-221 expression was related to TNM stage ($P=0.032$) and local invasion ($P=0.021$). MiR-221 expression was higher in tumors at a more advanced TNM stage and with deeper invasions. The expression levels of miR-221 in HT-29, Lovo, SW-480, and Caco2 were 4.094±0.208, 1.122±0.138, 3.927±0.232, and 1.831±0.149, respectively. Significant miR-221 overexpression was observed in all four CRC cell lines compared to the miR-221 level in HUVEC (0.223±0.047, $P<0.01$). The Caco2 cell line was chosen for both miR-221 and anti-miR-221 transfection in the subsequent experiment because of its intermediate miR-221 expression level among the four tested cell lines.

CDKN1C/p57 is a target of miR-221 in CRC

To confirm the regulatory effect of miR-221 on CDKN1C/p57 in CRC, we selected a group of samples with similar CDKN1C/p57 mRNA expressions between CRC and the matched non-tumorous tissue to avoid the 20%–25% of CRC cases in which CDKN1C/p57 is affected by aberrant methylation at chromosome 11p15.5. Among the 34 initial samples of CRC and matched non-tumorous tissue, 30 cases were selected because they displayed similar CDKN1C/p57 mRNA levels.

Table 1. Relationship between miR-221 expression and clinicopathological features in CRC patients.

Variable	NO	miR-221 (Mean±SD)	*P* value
Gender			0.096
Male	16	2.154±1.620	
Female	14	1.800±0.714	
Age			0.605
≤50	11	1.898±0.976	
>50	19	2.145±1.457	
Site			0.586
Colon	12	1.935±0.577	
Rectum	18	2.037±1.033	
TNM stage			0.032
I+II	11	1.185±0.392	
III+IV	19	2.658±1.437	
Local invasion			0.021
T1+T2+T3	23	1.275±0.445	
T4	7	2.833±1.498	
Differentiation			0.767
Better	16	2.168±1.128	
Worse	14	1.974±0.824	
CEA (μg/L)			0.429
≤5	10	2.020±0.321	
>5	20	2.213±0.647	

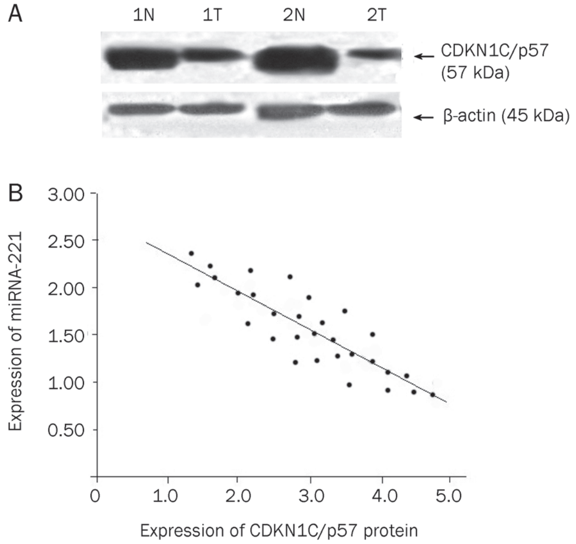

Figure 3. Inverse correlation between miR-221 and CDKN1C/p57 in CRC samples. (A) CDKN1C/p57 protein levels in CRC and matched non-tumorous tissues. A reduction of CDKN1C/p57 protein levels can be observed in several CRCs (total proteins, from the same samples utilized for RT-PCR in Figure 1B, were analyzed by Western-blot with anti-p57 antibodies. β-actin was used as house-keeping gene to normalize CDKN1C/p57 protein expression). Note: N, T represented the patients' non-tumorous tissues (N) and CRCs (T), respectively. (B) Inverse correlation between miR-221 and CDKN1C/p57 in CRC tissues. MiR-221 quantitation was obtained by real-time RT-PCR, whereas CDKN1C/p57 protein expression was evaluated by Western-blot analysis. A statistically significant inverse correlation between miR-221 and CDKN1C/p57 protein levels was observed ($P<0.01$).

To assess the correlation between miR-221 expression and the CDKN1C/p57 protein level in CRC, we examined miR-221 expression by real-time RT-PCR and analyzed CDKN1C/p57 protein expression by Western blot in the 30 matched samples of CRC and adjacent non-tumorous tissue, among which 27 (90%) showed down-regulation of CDKN1C/p57 protein expression in CRC compared to that in the matched non-tumorous tissue (3.019±1.708 *vs* 0.972±0.31, $P<0.01$). Interestingly, the down-regulation was not observed at the mRNA level, indicating that the protein was down-regulated at a post-transcriptional level (selective cases were shown in Figure 3A). As shown in Figure 3B, when CDKN1C/p57 protein expression was plotted against miR-221 expression, an inverse correlation was observed ($r^2=0.904$, $P<0.01$). Together, these results suggest that miR-221 may negatively regulate CDKN1C/p57 in CRC cells.

We further examined the effect of miR-221 on CDKN1C/p57 expression in CRC cells by ectopic expression of miR-221. Briefly, we transfected pre-miR-221 or its inhibitor, a specific 2′-methoxy-modified RNA oligonucleotide (anti-miR-221), into Caco2 cells, and we examined CDKN1C/p57 protein expression by Western blot. Ectopic expression of miR-221 caused a significant increase of miR-221 expression (2.915±0.442) and a decrease of CDKN1C/p57 protein expression. Conversely, anti-miR-221 induced a significant decrease of miR-221 expression (0.541±0.206) and an increase of CDKN1C/p57 protein expression (Figure 4A). Interestingly, no significant changes in CDKN1C/p57 mRNA expression were observed in the

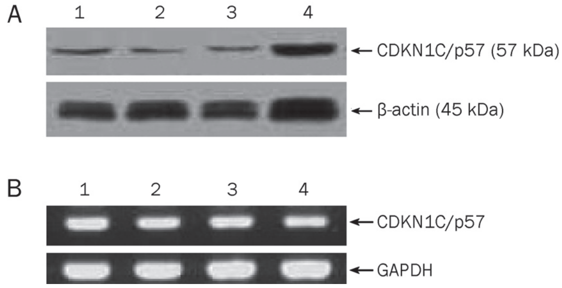

Figure 4. MiR-221 regulates the expression of CDKN1C/p57 in CRC-derived cells. (A) Western-blot analysis showing CDKN1C/p57 protein expression in Caco2 cells. β-actin was used as house-keeping gene to normalize CDKN1C/p57 protein expression. (B) Semi-quantitative RT-PCR analysis showing CDKN1C/p57 mRNA expression in Caco2 cells. The transfected cells showed no significant difference of CDKN1C/p57 mRNA expression. Equal loading was confirmed by using GAPDH. Note: lane 1, negative control; lane 2, anti-miR-221 negative control; lane 3, miR-221; lane 4, anti-miR-221. The results are representative of three independent experiments.

cells transfected with either miR-221 or anti-miR-221 (Figure 4B). These results strongly indicate that miR-221 regulates CDKN1C/p57 protein expression at a post-transcriptional level but does not cause CDKN1C/p57 mRNA degradation.

MiR-221 interacts with the 3′-UTR of the CDKN1C/p57 mRNA

Most miRNAs are thought to regulate gene expression by base-pairing with the miR-recognizing elements (miR-RE) in their target mRNAs. Therefore, we used all of the three currently available major prediction programs, including TargetScan, Miranda and PicTar, to analyze the potential interaction between miR-221 and CDKN1C/p57. The CDKN1C/p57 mRNA was predicted as a miR-221 target by at least two of the algorithms, and a potential miR-221 target site was predicted in its 3′-UTR region (Figure 5A). To confirm that the direct interaction between miR-221 and the CDKN1C/p57 mRNA was responsible for the decreased CDKN1C/p57 expression, we cloned a 262-bp CDKN1C/p57 3′-UTR fragment, including the potential target site for miR-221, downstream of the pGL3 luciferase reporter gene to generate the pGL3-p57 vector. This vector was co-transfected with miR-221 or anti-miR-221 into Caco2 cells. The luciferase activity in Caco2 cells co-transfected with the pGL3-p57 vector and miR-221 markedly decreased compared with that in the negative control. On the contrary, the luciferase activity in Caco2 cells transfected with anti-miR-221 significantly increased compared with that in the negative control (Figure 5B). These results support the bioinformatic prediction indicating the 3′-UTR of CDKN1C/p57 mRNA as a miR-221 target.

MiR-221 increases cell proliferation and inhibits apoptosis in CRC cells

Because CDKN1C/p57 plays a key role in cell cycle progression, particularly in cell growth arrest at the G_1/S transition, we further tested if the growth of stably transfected CRC cells expressing miR-221was affected as a result of the demonstrated CDKN1C/p57 reduction. First, to evaluate the effect of miR-221 on CRC cell proliferation, we transfected Caco2 cells with miR-221 or anti-miR-221. At 48 h after transfection, cell proliferation was determined by the MTT assay. We observed a significant increase in the proliferation rate after the transfection of miR-221. In contrast, anti-miR-221 significantly decreased cell proliferation (Figure 6A, P<0.01). These data indicate that increased miR-221 expression significantly promotes cell proliferation in Caco2 cells. Second, we investigated the cell cycle phase distribution in CRC after the transfection of miR-221 or anti-miR-221 by flow cytometry. The results showed a significant increase in the S-phase population and a decrease in the G_0/G_1 population in Caco2 cells overexpressing miR-221 compared with the cells transfected with the negative control. On the contrary, anti-miR-221 significantly decreased the S-phase population and increased the G_0/G_1 population (Figure 6B, P<0.01). Third, we investigated the effect of anti-miR-221 on cell apoptosis by flow cytometry and found that cell apoptosis dramatically increased in Caco2 cells after transfection with anti-miR-221, suggesting that anti-miR-221 may function as a strong apoptosis inducer in human CRC cells (Figures 6C–6D). These results strongly support the potential oncogenic activity of miR-221 in CRC.

CRC cell proliferation suppression by anti-miR-221 is mediated by CDKN1C/p57

If the suppression of CRC cell proliferation by anti-miR-221 is indeed mediated by CDKN1C/p57, we would expect the suppression effect to be abolished by the CDKN1C/p57-specific irreversible antagonist anti-p57-siRNA. To test this hypothesis, we measured the effect of miR-221 and anti-miR-221 on cell proliferation in CRC cells previously transfected with anti-p57-siRNA. The aim of this experiment was to address if and how the CDKN1C/p57-depleted cellular environment responds to miR-221 or anti-miR-221 overexpression. Briefly, Caco2 cells were pretreated with or without anti-p57-siRNA (80 nmol/L) for 24 h prior to the addition of pre-miR-221 (50 nmol/L) or anti-miR-221 (50 nmol/L). Cell proliferation was determined by MTT assay. The data showed that CDKN1C/p57 down-regulation by means other than miR-221 overexpression led to an analogous outcome: when Caco2 cells were transfected with anti-p57-siRNA, caus-

A

Target gene	TargetScan prediction	Predicted consequential pairing of target region (top) and miRNA (bottom)	Seed match
CDKN1C	Position 86-92 of CDKN1C 3′-UTR hsa-miR-221	5′ … CGGCUGGGACCGUUCAUGUAGCA … 3′ CUUUGGGUCGUCUGU —— UACAUCGA	8 mer

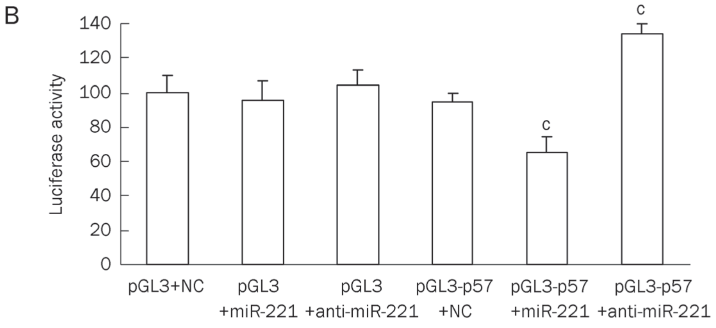

Figure 5. Direct regulation of CDKN1C/p57 mRNA by miR-221. (A) CDKN1C/p57 3′-UTR site potentially targeted by miR-221 as predicted by TargetScan. (B) Luciferase activity assay showing direct interaction between miR-221 and CDKN1C/p57 3′-UTR site. Firefly luciferase reporter activity on the presence of both pGL3-p57 vector and miR-221 or anti-miR-221 were compared with those of the controls. Luciferase activity in Caco2 cells co-transfected with pGL3-p57 vector and miR-221 was decreased markedly compared with negative control. On the contrary, luciferase activity in Caco2 cells transfected with anti-miR-221 was increased significantly compared with negative control. n=3. Mean±SD. ^cP<0.01 *vs* control group.

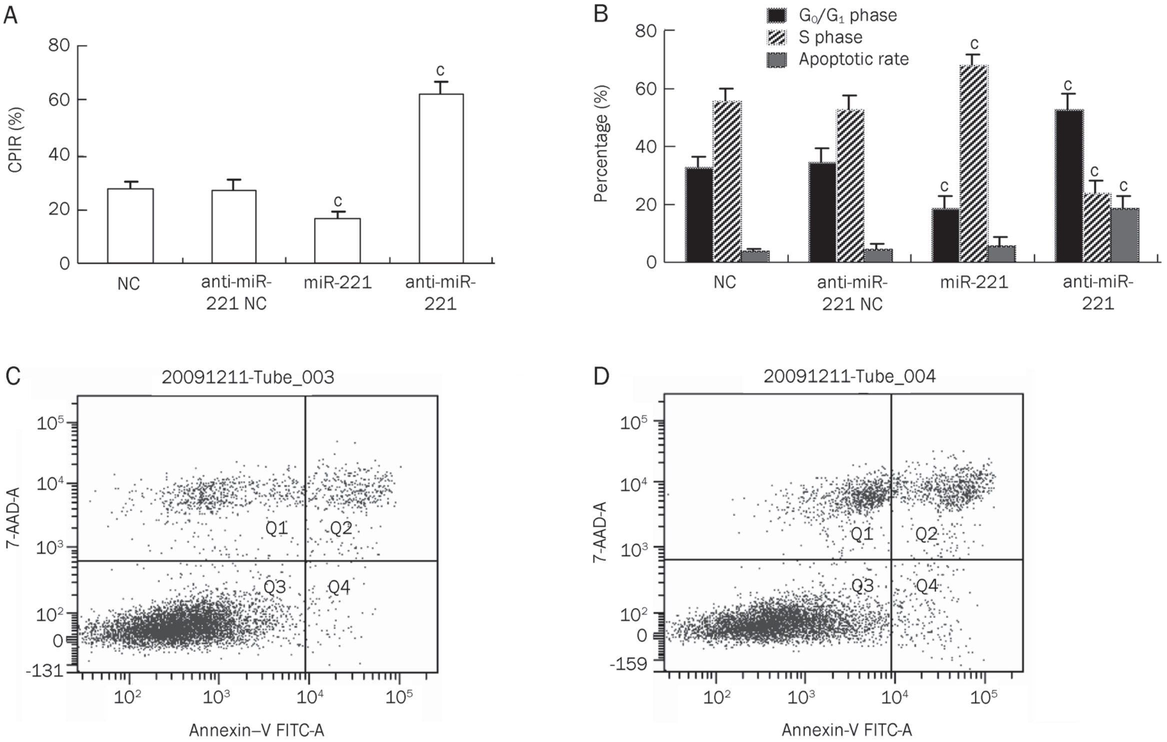

Figure 6. Effects of miR-221 and anti-miR-221 on cell proliferation and apoptosis in CRC cells. (A) The status of cell proliferation was determined by MTT assay. CPIR on the presence of miR-221 or anti-miR-221 was compared with those of the controls. *n*=6. Mean±SD. $^{c}P<0.01$ *vs* control group. (B) Effects of miR-221 and anti-miR-221 on cell-cycle in Caco2 cells. The percentages of G_0/G_1 phase, S phase and apoptotic rate were measured by computing the ratio of the number of corresponding cells and that of total cells. *n*=3. Mean±SD. $^{c}P<0.01$ *vs* control group. (C, D) Cell apoptosis analysis of transfected cells by flow cytometer. Note: C, NC group; D, anti-miR-221 group. The right-down quadrant ($FITC^{+}/PI^{-}$) was shown as apoptotic cells.

ing about 70% down-regulation of CDKN1C/p57 at both the mRNA and the protein levels (Figure 7A-7B), we observed a marked increase in cell proliferation compared with the negative control (Figure 7C). Thus, reducing CDKN1C/p57 protein expression in CRC cells, by either miR-221 overexpression or anti-p57-siRNA transfection, promoted cell proliferation at a comparable level.

When miR-221 was transfected into Caco2 cells previously treated with anti-p57-siRNA, we observed that, at 48 h after miR-221 transfection, anti-p57-siRNA and miR-221 seemed to cooperate to increase the growth rate (Figure 7C). Conversely, when anti-miR-221 was transfected into Caco2 cells previously treated with anti-p57-siRNA, we observed that, at 48 h after anti-miR-221 transfection, the suppression of cell proliferation by anti-miR-221 was largely abrogated by anti-p57-siRNA (Figure 7C). These results indicate that the inhibitory effect of anti-miR-221 on CRC cell growth is largely, but not completely, mediated by CDKN1C/p57, suggesting that anti-miR-221 may also activate CDKN1C/p57-independent signaling pathways to inhibit CRC cell growth.

Discussion

In this study, we identified CDKN1C/p57 as a direct target of miR-221 in CRC. The data have shown that in CRC, miR-221 is up-regulated and CDKN1C/p57 protein expression is down-regulated. A significant inverse correlation between miR-221 and CDKN1C/p57 was observed in CRC. CDKN1C/p57 modulation by miR-221 was demonstrated by *in vitro* transfection experiments in CRC-derived cell lines and by confirming the direct interaction between miR-221 and the CDKN1C/ p57 3′-UTR target site using the luciferase assay.

MiR-221 is a newly discovered miRNA that is up-regulated in multiple malignancies such as hepatocellular carcinoma, bladder cancer, and pancreatic cancer[14–16]. It promotes tumor cells entering the S phase from the G_0/G_1 phase by inhibiting CDKI expression[17, 18]. Therefore, miR-221 is an attractive candidate for selective treatment using miR-221-specific inhibitors. A few published reports have begun to reveal the mechanisms that may link miR-221 up-regulation to cancer; however, the exact underlying molecular mechanisms remain unclear. CDKN1C/p57 is a negative regulatory factor of cell cycle dependent kinases that belong to the CIP/KIP family. It was first cloned using a two-hybrid system by Matsuoka *et al*[19] in 1995 and was located within the region of about 22 kb in length between D11S648 and D11S679 on chromosome 11p15.5. The α2 helix domain at the amino terminus of its product, the $p57^{kip2}$ protein, can form homodimers, which in turn interact with the cyclin2-CDK4 complex and inhibit

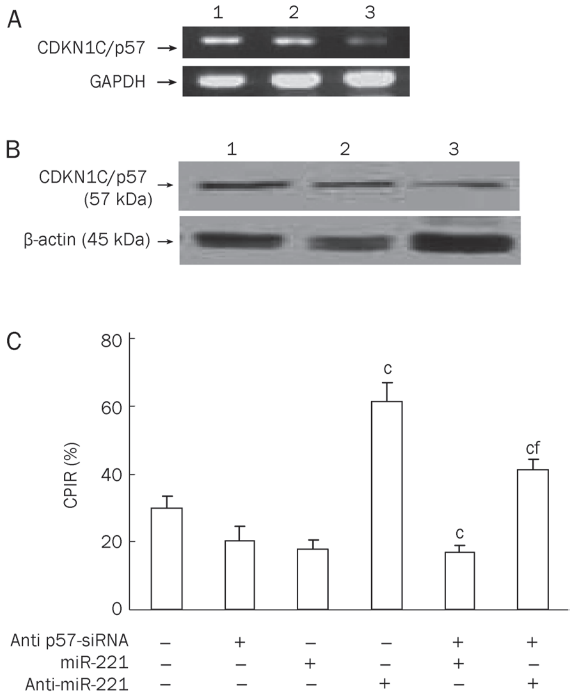

Figure 7. Ectopic expression of miR-221 affects the growth of CRC cells by targeting CDKN1C/p57. Caco2 cells were pretreated with or without anti-p57-siRNA (80 nmol/L) for 24 h prior to the addition of pre-miR-221 (50 nmol/L) or anti-miR-221 (50 nmol/L). Semi-quantitative RT-PCR and Western-blot analysis showing that both CDKN1C/p57 mRNA (A) and protein (B) reduced markedly after transfection with anti-p57-siRNA. Equal loading was confirmed by using GAPDH or β-actin. Note: lane 1, negative control; lane 2, Caco2 cells transfected with control siRNA; lane 3, Caco2 cells transfected with anti-p57-siRNA. (C) The status of cell proliferation was determined by MTT assay. The suppression of Caco2 cell proliferation by anti-miR-221 was largely, but not completely, abrogated by anti-p57-siRNA (CPIR from 61.4% to 41.2%). *n*=3. Mean±SD. $^cP<0.01$ *vs* negative control group. $^fP<0.01$ *vs* sole anti-miR-221 group.

the complex function to prevent cell cycle progression from the G_0/G_1 phase to the S phase. Indeed, reduced or absent CDKN1C/p57 expression has been shown in many types of human cancers to correlate with tumor aggressiveness, poor prognosis and high recurrence rate. Soejima *et al*[20] have demonstrated that the loss of imprinting (LOI) of the methylation of the maternal allele at the KvDMR1 locus occurs in about 20% to 25% of malignant cells and that the KvDMR1 locus is also at chromosome 11p15.5, which is the locus of the CDKN1C/p57 gene that causes CDKN1C/p57 down-regulation. In the present study, we found that CDKN1C/p57 protein expression is down-regulated in about 90% of unscreened CRC samples in our preliminary experiment, suggesting that CDKN1C/p57 down-regulation might have additional outcomes other than aberrant methylation. Moreover, the regulation of CDKN1C/p57 expression and function essentially occurs at the post-transcriptional level[21]. With the application of bioinformatic predictions using TargetScan, PicTar and miRanda, we found that miR-221 and the CDKN1C/p57 mRNA 3′-UTR have complementary binding sites, suggesting that CDKN1C/p57 might be a novel target of miR-221 in CRC that has not yet been reported.

In this study, we showed that CDKN1C/p57 mRNA expression was low in about 11.8% (4/34) of CRC cases, in agreement with the previous hypothesis of loss of imprinting of the maternal gene allele methylation in tumor cells and the down-regulation of CDKN1C/p57 mRNA expression at the transcriptional level. However, the subsequent down-regulation of CDKN1C/p57 protein expression is probably not caused by the post-transcriptional gene silencing of miR-221. These samples were excluded from the study; therefore, the subsequent experiments can more accurately reflect the regulatory role of miR-221. Real-time RT-PCR analysis of the remaining samples demonstrated that miR-221 expression is up-regulated in 90% of CRC samples, and it may be expected that miR-221 targets belong to the class of tumor suppressor genes or genes encoding proteins with potential tumor suppressor functions. Moreover, miR-221 expression is related to not only TNM stage but also tumor invasiveness. The level of miR-221 expression at TNM stages III and IV is higher than that at stages I and II, and the tumors invading adjacent tissues or organs display higher miR-221 levels than those limited to the wall of the colon and the rectum. Thus, miR-221 is likely to be an important oncomiR that can cleave or inhibit the target tumor suppressor mRNAs and that plays a role in CRC progression. In our study, CDKN1C/p57 protein expression is down-regulated in CRC, which was confirmed by Western blot analysis. Thus, it could be inferred that miR-221 binds to the 3′-UTR of the CDKN1C/p57 mRNA in an incomplete complementary pairing pattern. Therefore, it could only inhibit the further translation of the CDKN1C/p57 mRNA without inducing complete degradation, consistent with the result that the CDKN1C/p57 mRNA levels in CRC and non-tumorous tissues are not significantly different, whereas CDKN1C/p57 protein expression decreases in CRC. It could also be inferred that tumor cells probably gain a proliferative advantage through miR-221-mediated post-transcriptional silencing of CDKN1C/p57. Therefore, our data indicate the presence of more than one mechanism regulating CDKN1C/p57 expression in CRC.

Our results also demonstrated that miR-221 is dramatically up-regulated in four human CRC-derived cell lines compared with that in HUVEC, and this is in accordance with the results from clinical samples. Indeed, CDKN1C/p57 is down-regulated in response to miR-221 transfection in CRC cells, and a significant up-regulation of CDKN1C/p57 occurs in response to anti-miR-221 transfection. A direct interaction between miR-221 and the target site in the 3′-UTR of the CDKN1C/p57 mRNA was also demonstrated by the luciferase assay. By controlling CDKN1C/p57 expression, miR-221 up-regulation promotes the growth of CRC cells by increasing the S-phase population. Conversely, miR-221 inhibition represses CRC cell growth and induces cell apoptosis. Cell cycle progression and cell apoptosis are usually closely associated. Cells failing to progress to the mitosis phase are destined for apoptosis. Aside from cell cycle arrest, the inhibition of cell growth by anti-miR-221 observed in CRC cells may also result from increased apoptosis. In this study, at 48 h anti-miR-221 transfection, cells were arrested at the G_0/G_1 phase and blocked from entering the S phase. As seen in other tumor cells, we demonstrate that anti-miR-221 induces significant apoptosis in CRC cells.

Recently, it has been reported that there are CDKN1C/p57-independent effects of miR-221 in tumorigenesis[22]. Moreover, miR-221 possesses many oncogenic functions other than serving as a CDKN1C/p57 inhibitor[23]. In this study, we showed that a miR-221-specific inhibitor, anti-miR-221, can inhibit CRC cell proliferation. Using a CDKN1C/p57-specific antagonist, anti-p57-siRNA, we demonstrated that the inhibitory effect of anti-miR-221 on CRC cell growth is largely, but not completely, mediated by CDKN1C/p57, suggesting that miR-221 might regulate CDKN1C/p57-independent signaling pathways to promote CRC growth. It has been previously shown that CDKN1B/p27 is also a miR-221 target and that CDKN1B/p27 expression consistently inversely correlates with miR-221 overexpression in most cancers, which may explain why the inhibition of anti-miR-221 on CRC cell growth is only partly abrogated by anti-p57-siRNA[24]. Interestingly, it has also been reported that c-Kit, a common oncogene, is a miR-221 target in thyroid papillary carcinoma[25]. However, the role of c-Kit expression in CRC cell proliferation and carcinogenesis remains undefined. Our results, which identified CDKN1C/p57 as a miR-221 target in CRC cell lines, perfectly fit the dynamic view of the miRNA-mediated regulation of gene expression: the relationship between miRNAs and target mRNAs is not a “one to one” connection because the same mRNA can be regulated by more than one miRNA, and the choice of how many and which miRNAs target an individual 3′-UTR is largely determined by the specific cellular environment[26]. A miRNA that regulates target genes playing opposite roles in regulating cell proliferation may act as a tumor suppressor in some cancers but as an oncogene in others, depending on which targets are driving tumorigenesis in that specific cellular milieu.

In summary, we identified miR-221 as a direct regulator of CDKN1C/p57 expression in CRC, demonstrating a new mechanism for CDKN1C/p57 down-regulation in CRC. These findings further emphasize the importance of miR-221 in CRC carcinogenesis. However, it is noteworthy that the results in this study are based on cultured CRC cells that might not necessarily comprehensively reflect the *in vivo* situations. Therefore, further experiments are required to elucidate the anti-tumor mechanisms of anti-miR-221 in *in vivo* systems.

Acknowledgements

This work was supported by the Natural Science Foundation of Guangdong Province (No 8451051501000390), the Medical Scientific Research Foundation of Guangdong Province (No B2010190) and the Chief Foundation of Nanfang Hospital of Southern Medical University (No 2008C005).

Author contribution

Dr Kai SUN designed the research, analyzed the data, wrote the manuscript and revised the paper; Wei WANG, Jun-jie ZENG, Cheng-tang WU, and Shang-tong LEI performed the experiments; Guo-xin LI assisted with the experiments.

References

1 Motoyama K, Inoue H, Takatsuno Y, Tanaka F, Mimori K, Uetake H, *et al*. Over- and under-expressed microRNAs in human colorectal cancer. Int J Oncol 2009; 34: 1069–75.

2 Wang CJ, Zhou ZG, Wang L, Yang L, Zhou B, Gu J, *et al*. Clinicopathological significance of microRNA-31, -143 and -145 expression in colorectal cancer. Dis Markers 2009; 26: 27–34.

3 Yantiss RK, Goodarzi M, Zhou XK, Rennert H, Pirog EC, Banner BF, *et al*. Clinical, pathologic, and molecular features of early-onset colorectal carcinoma. Am J Surg Pathol 2009; 33: 572–82.

4 Guarnieri DJ, DiLeone RJ. MicroRNAs: a new class of gene regulators. Ann Med 2008; 40: 197–208.

5 Cheng HY, Obrietan K. Revealing a role of microRNAs in the regulation of the biological clock. Cell Cycle 2007; 6: 3034–5.

6 La Rocca G, Badin M, Shi B, Xu SQ, Deangelis T, Sepp-Lorenzinoi L, *et al*. Mechanism of growth inhibition by MicroRNA 145: the role of the IGF-I receptor signaling pathway. J Cell Physiol 2009; 220: 485–91.

7 Shin S, Cha HJ, Lee EM, Jung JH, Lee SJ, Park IC, *et al*. MicroRNAs are significantly influenced by p53 and radiation in HCT116 human colon carcinoma cells. Int J Oncol 2009; 34: 1645–52.

8 Yamamichi N, Shimomura R, Inada K, Sakurai K, Haraguchi T, Ozaki Y, *et al*. Locked nucleic acid in situ hybridization analysis of miR-21 expression during colorectal cancer development. Clin Cancer Res 2009; 15: 4009–16.

9 Fornari F, Gramantieri L, Ferracin M, Veronese A, Sabbioni S, Calin GA, *et al*. MiR-221 controls CDKN1C/p57 and CDKN1B/p27 expression in human hepatocellular carcinoma. Oncogene 2008; 27: 5651–61.

10 Diaz-Meyer N, Day CD, Khatod K, Maher ER, Cooper W, Reik W, *et al.* Silencing of CDKN1C(p57/KIP2) is associated with hypomethylation at KvDMR1 in Beckwith-Widemann syndrome. J Med Genet 2003; 40: 797–801.

11 Vlachos P, Joseph B. The Cdk inhibitor p57(Kip2) controls LIM-kinase 1 activity and regulates actin cytoskeleton dynamics. Oncogene 2009; 28: 4175–88.

12 Bartels CL, Tsongalis GJ. MicroRNAs: novel biomarkers for human cancer. Clin Chem 2009; 55: 623–31.

13 Sun K, Wang Q, Huang XH. PPAR gamma inhibits growth of rat hepatic stellate cells and TGF beta-induced connective tissue growth factor expression. Acta Pharmacol Sin 2006; 27: 715–23.

14 Mirnezami AH, Pickard K, Zhang L, Primrose JN, Packham G. MicroRNAs: key players in carcinogenesis and novel therapeutic targets. Eur J Surg Oncol 2009; 35: 339–47.

15 Baffa R, Fassan M, Volinia S, O'Hara B, Liu CG, Palazzo JP, *et al*. MicroRNA expression profiling of human metastatic cancers identifies cancer gene targets. J Pathol 2009; 219: 214–21.

16 Schetter AJ, Harris CC. Plasma microRNAs: a potential biomarker for colorectal cancer? Gut 2009; 58: 1318–9.

17 Ahmed FE, Jeffries CD, Vos PW, Flake G, Nuovo GJ, Sinar DR, *et al*. Diagnostic microRNA markers for screening sporadic human colon cancer and active ulcerative colitis in stool and tissue. Cancer Genomics Proteomics 2009; 6: 281–95.

18 Glinskii AB, Ma J, Ma S, Grant D, Lim CU, Sell S, *et al*. Identification of intergenic trans-regulatory RNAs containing a disease-linked

SNP sequence and targeting cell cycle progression/differentiation pathways in multiple common human disorders. Cell Cycle 2009; 8: 3925–42.

19 Matsuoka S, Edwards MC, Bai C, Parker S, Zhang P, Baldini A, *et al*. p57KIP2, a structurally distinct member of the p21CIP1 Cdk inhibitor family, is a candidate tumor suppressor gene. Genes Dev 1995; 9: 650–62.

20 Soejima H, Nakagawachi T, Zhao W, Higashimoto K, Urano T, Matsukura S, *et al*. Silencing of imprinted CDKN1C gene expression is associated with loss of CpG and histone H3 lysine 9 methylation at DMR-LIT1 in esophageal cancer. Oncogene 2004; 23: 4380–8.

21 Galardi S, Mercatelli N, Giorda E, Massalini S, Frajese GV, Ciafrè SA, *et al*. MiR-221 and miR-222 expression affects the proliferation potential of human prostate carcinoma cell lines by targeting p27Kip1. J Biol Chem 2007; 282: 23716–24.

22 Felli N, Fontana L, Pelosi E, Botta R, Bonci D, Facchiano F, *et al*. MicroRNAs 221 and 222 inhibit normal erythropoiesis and erythroleukemic cell growth via kit receptor down-modulation. Proc Natl Acad Sci USA 2005; 102: 18081–6.

23 Le Sage C, Nagel R, Egan DA, Schrier M, Mesman E, Mangiola A, *et al*. Regulation of the p27(Kip1) tumor suppressor by miR-221 and miR-222 promotes cancer cell proliferation. EMBO J 2007; 26: 3699–708.

24 Visone R, Russo L, Pallante P, De Martino I, Ferraro A, Leone V, *et al.* MicroRNAs (miR)-221 and miR-222, both overexpressed in human thyroid papillary carcinomas, regulate p27Kip1 protein levels and cell cycle. Endocr Relat Cancer 2007; 14: 791–8.

25 He H, Jazdzewski K, Li W, Liyanarachchi S, Nagy R, Volinia S, *et al.* The role of microRNA genes in papillary thyroid carcinoma. Proc Natl Acad Sci USA 2005; 102: 19075–80.

26 Meltzer PS. Cancer genomics: small RNAs with big impacts. Nature 2005; 435: 745–6.

Acta Pharmacologica Sinica (2011) 32: 385–392
© 2011 CPS and SIMM All rights reserved 1671-4083/11 $32.00
www.nature.com/aps

Original Article

Establishment and characterization of primary lung cancer cell lines from Chinese population

Chao ZHENG[1, #], Yi-hua SUN[2, #], Xiao-lei YE[1], Hai-quan CHEN[2, *], Hong-bin JI[1, *]

[1]Institute of Biochemistry and Cell Biology, Shanghai Institute for Biological Sciences, Chinese Academy of Sciences, Shanghai 200031, China; [2]Department of Thoracic Surgery, Shanghai Cancer Center, Department of Oncology, Shanghai Medical College, Fudan University, Shanghai 200032, China

Aim: To establish and characterize primary lung cancer cell lines from Chinese population.
Methods: Lung cancer specimens or pleural effusions were collected from Chinese lung cancer patients and cultured *in vitro* with ACL4 medium (for non-small cell lung carcinomas (NSCLC)) or HITES medium (for small cell lung carcinomas (SCLC)) supplemented with 5% FBS. All cell lines were maintained in culture for more than 25 passages. Most of these cell lines were further analyzed for oncogenic mutations, karyotype, cell growth kinetics, and tumorigenicity in nude mice.
Results: Eight primary cell lines from Chinese lung cancer patients were established and characterized, including seven NSCLC cell lines and one SCLC cell line. Five NSCLC cell lines were found to harbor epidermal growth factor receptor (EGFR) kinase domain mutations.
Conclusion: These well-characterized primary lung cancer cell lines from Chinese population provide a unique platform for future studies of the ethnic differences in lung cancer biology and drug response.

Keywords: lung cancer; primary cell lines; epidermal growth factor receptor; small cell lung carcinomas; non-small cell lung carcinomas

Acta Pharmacologica Sinica (2011) 32: 385–392; doi: 10.1038/aps.2010.214

Introduction

Lung cancer is one of the most common causes of cancer-related death worldwide[1, 2], with a five year survival rate of approximately 15%. In China, the situation is even worse. The vast majority of lung cancers are carcinomas derived from epithelial cells and are pathologically divided into two major types: non-small cell lung carcinomas (NSCLC) (~80%) and small cell lung carcinomas (SCLC) (~20%).

Lung cancer cell lines are crucial for translational and biomedical research. Lung cancer cells were successfully cultured approximately 25 years after the establishment of a human cervical carcinoma (HeLa) cell line[3, 4]. Since then, many attempts have been made to establish permanent lung cancer cell lines[5–10]. The emergence of lung cancer cell lines reached a peak after serum-free chemically defined media (for example, ACL4, C-based medium, and HITES) were introduced[11, 12]. Since then, more than 200 lung cancer cell lines have been successfully established. These permanent cell lines, derived from either primary or metastatic cancers, provide important experimental systems for studying the genetic changes and biology associated with tumor initiation and progression. As a pure cancer cell population, the global using of *in vitro* permanent cell lines over the past several decades has led to great achievements, including elucidating the molecular and translational biology of cancer and further drug screening[3, 13]. To date, more than 9000 citations, including several important biomedical discoveries, have resulted from the usage of these lines[3]. However, it is noteworthy that among all of the widely used cell lines, almost none have a Chinese genetic background.

Studies demonstrate that ethnic differences in genetic background are important in defining cancer biology as well as in drug toxicity[14–21]. For example, the epidermal growth factor receptor (EGFR) kinase domain mutations occur in approximately 10% of NSCLC patients in the Caucasian population[22], but occur in 30%–50% of NSCLC patients from East Asian populations[15, 17, 18, 21, 23]. Ethnic differences in the expression of allelic variants may produce altered pharmacokinetics and

---

[#] These authors contributed equally to this work.
[*] To whom correspondence should be addressed.
E-mail hqchen1@yahoo.com (Hai-quan CHEN);
hbji@sibs.ac.cn (Hong-bin JI)

Received 2010-09-20 Accepted 2010-11-29

result in differential toxicity for the same anticancer treatments[19, 20]. Understanding the causes of ethnic differences in cytotoxic metabolism may help to improve cancer treatment in the clinic. From this standpoint, the establishment of lung cancer cell lines from Chinese genetic background is urgently needed.

We have worked to establish Chinese lung cancer cell lines. A total of eight primary Chinese lung cancer cell lines were successfully established, including seven NSCLC cell lines and one SCLC cell line. We characterized most of these cell lines for oncogenic mutations, growth kinetics, karyotype, and tumorigenicity in nude mice. These cell lines provide a very useful platform for studying the ethnic differences in cancer biology and drug response in the future.

Materials and methods

Collection of clinical specimens

All patients were from the Chinese population and underwent surgery for potentially curative resections. The lung cancer specimens or pleural effusions were collected with patient consent. Solid tumors were immediately immersed in ice-cold RPMI-1640 supplemented with P/S (1000 U/mL penicillin G and 1000 mg/L streptomycin), while pleural effusions were kept on ice. Samples were transported to the laboratory for primary cell culturing within one hour of collection.

Preparation of lung cancer cells from resected samples

Solid tumor specimens were rinsed twice with PBS supplemented with P/S and finely minced with scissors. Both necrotic tissue and apparently normal tissue were discarded. Tumor fragments were then immersed into ACL4 medium (for NSCLC)[24, 25] or HITES medium (for SCLC)[11, 12] supplemented with 5% fetal bovine serum (FBS) and P/S, and they were pipetted more than 50 times. The cell suspension was then transferred to a collagen-coated flask. The pleural effusions were subjected to red blood cell lysis and then to Ficoll gradient separation to remove lymphocytes. The interface was collected and washed three times with PBS plus P/S. Cells were suspended in ACL4 medium with 5% FBS and P/S and then cultured in a collagen-coated flask. The medium was changed every 3 d. A cell scraper was used to remove visible fibroblast growth whenever it occurred. Once the cells were confluent, they were digested with 0.05% EDTA-trypsin for passage. All established cell lines were maintained in culture for more than 25 passages.

Karyotype analysis

Cells were seeded and cultured for 70 h or until confluence. Colchicine was added to cells with a final concentration of 0.2 μg/mL. Cells were incubated for another 2 h and then digested using 0.05% EDTA-trypsin and resuspended in 0.075 mol/L KCl. After fixation in 3:1 methanol/glacial acetic acid, cell suspensions were dropped onto ice-cold slides, which were then stained by Giemsa for 8 min. Chromosome ploidy was estimated from at least 29 metaphases per cell line under a microscope.

EGFR and KRAS mutation detection

Detection of EGFR and KRAS mutations was previously described[18, 21]. Briefly, genomic DNA and RNA were extracted from Chinese lung cancer cell lines per standard protocol (RNeasy Mini Kit, and QIAamp DNA Mini Kit, Qiagen, Hilden, Germany). Total RNA was reverse transcribed into single-stranded cDNA using a RevertAid™ First Strand cDNA Synthesis Kit (Fermentas, EU, USA) and sequenced. The cDNA regions of EGFR (exons 18–22) and KRAS (exons 2–3) were then PCR amplified and sequenced. All mutations found from the cDNA sequencing were further confirmed by genomic DNA sequencing.

Fluorescence *in situ* hybridization (FISH)

Cells were applied onto slides as described in Karyotype analyses. Slides were then incubated in 0.01% pepsin solution (pH 2.0) for 10 min at 37 °C and then fixed in 1% formaldehyde for another 10 min at room temperature. Vysis EGFR probe (Abbott Laboratories, Des Plaines, IL, USA) was applied to the targeted area, and slides were sealed with rubber cement. Slides were then incubated at 83 °C for 5 min, followed by another 16 h at 37 °C. Slides were washed with 0.4×SSC/0.3% NP-40 at 73 °C for 4 min and then 2×SSC/0.1% NP-40 at ambient temperature for 2 min. Chromatin was counterstained with 4′,6-diamidino-2-phenylindole. Fluorescence was analyzed in more than 50 cells per cell line for both EGFR and chromosome 7 centromere signals. We divided the EGFR copy number variation into 6 categories (disomy, low trisomy, high trisomy, low polysomy, high polysomy, gene amplification) as previously described[26].

Cell growth assay

Cells were seeded in 96-well plates with ACL4 plus 5% FBS (5000 cells per well for cell lines SH-437, SH-450; 7000 cells per well for cell lines SH-416, SH-289). Cell growth kinetics were assessed by MTT (3-(4,5-Dimethylthiazol-2-yl)-2,5-diphenyltetrazolium bromide) assay daily as previously described[27].

Soft agar assay

To assess soft agar colony formation, each of the cell lines (SH-224, SH-289, SH-416, SH-437, and SH-450. CRL-5803 serves as a control, which was obtained from ATCC) was suspended in a top layer of RPMI 1640 containing 10% FBS and 0.4% Select agar at 5000 cells per well in 6-well plates and plated on a bottom layer of RPMI-1640 containing 10% FBS and 1% Select agar. Cells were stained with 0.5 mL crystal violet for 1 h.

Tumor formation in nude mice

Cells (5×10^6 to 1×10^7) were mixed with matrigel and then transplanted subcutaneously in nude mice. The animals were killed after 2 weeks, and the tumors were fixed in formalin for hematoxylin-eosin staining and pathological analysis.

Results

Establishment of the primary Chinese lung cancer cell lines

From 2008 to 2010, we collected and used 179 fresh lung cancer specimens for the establishment of primary Chinese lung cancer cell lines. Eventually, eight cell lines were successfully established and maintained in cell culture for more than 25 passages. Some cell lines even exceed 40 passages. Among these cell lines, seven are NSCLC cell lines, including three from adenocarcinomas, one from squamous cell carcinoma, one from adeno-squamous carcinoma, one from large cell carcinoma and one from poorly differentiated carcinoma (Figure 1, Table 1). All NSCLC cell lines were cultured using ACL4 medium with 5% FBS. Three cell lines including SH-543, SH-450, and SH-437 can also be maintained in RPMI-1640 with 10% FBS. Because SCLC patients seldom go through surgery and very few tumor specimens are available, we have established only one SCLC cell line.

The clinical and pathologic details for all the patients from whom the cell lines were derived are summarized in Table 1. Most lines were established from primary solid tumors, with typical pathological images shown in Figure 1, except SH-289, which was derived from pleural effusions. All of the patients were from the Chinese population with an age range from 49 to 71 years old and with different stages of disease.

Morphological appearance of primary Chinese lung cancer cell lines

Five NSCLC cell lines, including SH-224, SH-289, SH-416, SH-437, and SH-450, grow in cell culture as an attached monolayer (Figure 2). Adherent cells were, in general, large, and they exhibited characteristic epithelioid 'cobble-stone' morphology and were occasionally multi-nucleated or vacuolated. SH-450 cells were slightly unique due to their unconstrained growth and foci formation even after they reach 100% confluence. Another two NSCLC cell lines, SH-405 and SH-543, grew in suspension like SCLC cell lines. This is not common because the majority of NSCLC cell lines are adherent cells. Only 5% (8 of 154) of NSCLC cell lines grow as suspension cells, and none has been established before in a Chinese genetic background. Typical suspension cell growth was seen in the SCLC cell line SH-498, which grows as either single cell or cell clusters.

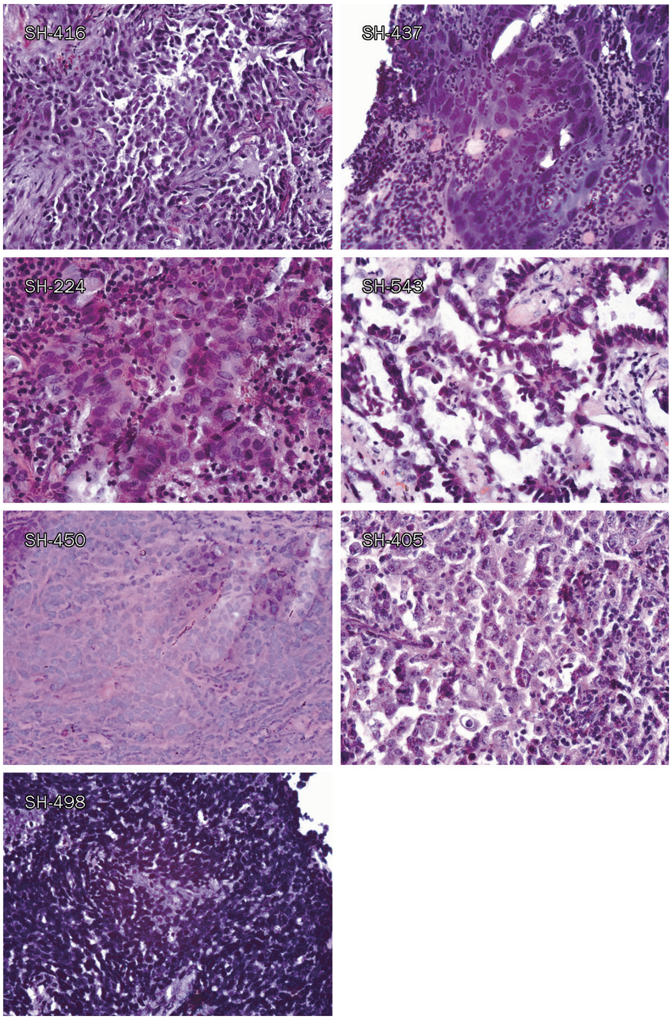

Figure 1. Typical pathological images of the tumor tissues used to establish primary Chinese lung cancer cell lines. Typical pathological images of the original tumors of primary Chinese lung cancer cell lines are shown, including SH-416 (SCC), SH-437 (LC), SH-224 (Ad), SH-543 (Ad), SH-450 (AS), SH-405 (PDE), SH-498 (SCLC).

Table 1. Clinical and pathologic summary of the established primary Chinese lung cancer cell lines.

Cell lines	Gender	Age (Year-old)	Pathology	Staging	Origin	EGFR mutations Tumor	EGFR mutations Cell line	EGFR CNV
SH-224	Female	71	Ad	III	Primary tumor	Exon 19 deletion	Exon 19 deletion	High polysomy
SH-289	Female	58	Ad	IV	Pleural fluid	Exon 19 deletion	Exon 19 deletion	Amplification
SH-543	Female	62	Ad	I	Primary tumor	WT	WT	Disomy
SH-416	Female	57	SCC	III	Primary tumor	Exon 19 deletion	Exon 19 deletion	Amplification
SH-450	Male	59	AS	III	Primary tumor	Exon 19 deletion	Exon 19 deletion	High polysomy
SH-437	Male	49	LC	II	Primary tumor	Exon 21 P848L	Exon 21 P848L	High polysomy
SH-405	Male	63	PDE	IIIa	Primary tumor	WT	WT	NA
SH-498	Male	53	SCLC	LS	Primary tumor	WT	WT	NA

Ad: Adenocarcinoma; SCC: Squamous cell carcinoma; LC: Large cell carcinoma; AS: Adeno-squamous carcinoma; PDE: Poorly differentiated carcinoma; WT: wild type; SCLC: Small cell lung carcinoma; LS: Limited stage; NA: not available; CNV: Copy number variation.

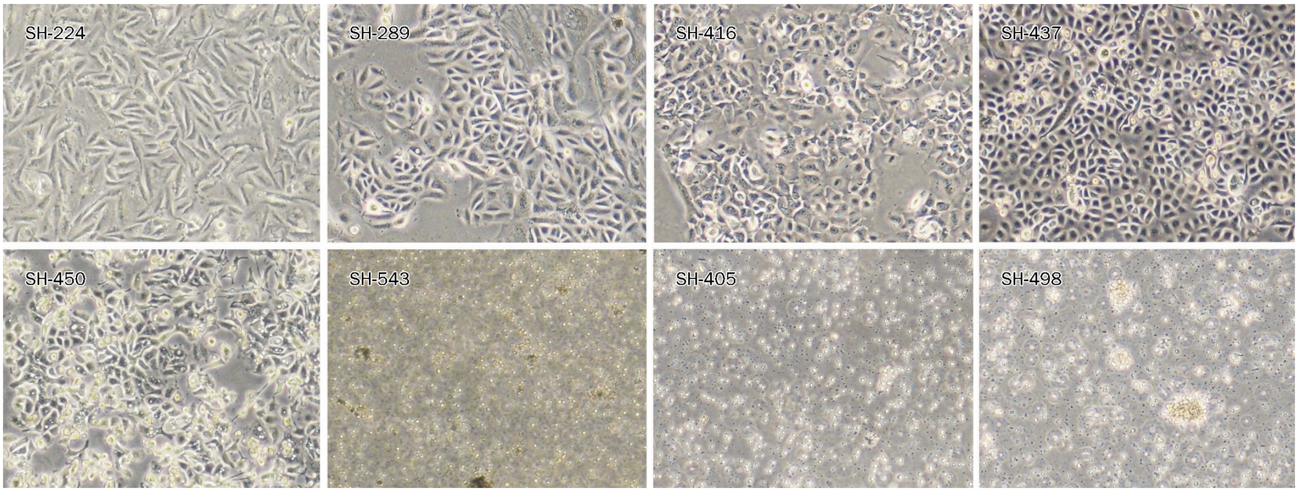

Figure 2. Representative morphology of primary Chinese lung cancer cell lines under light microscope. Typical morphology of cell lines is shown, including SH-224 (Ad), SH-289 (Ad), SH-416 (SCC), SH-437 (LC), SH-450 (AS), SH-543 (Ad), SH-405 (PDE), and SH-498 (SCLC).

Karyotype of the primary Chinese lung cancer cell lines

We have performed karyotype for the cell lines, except for SH-498 and SH-405, which grow very slow in suspension. The human origin of these cell lines is confirmed by a peak on nearly 46 chromosomes (Figure 3A). Most of the cell lines are aneuploid, consistent with their tumor origin. Significant subpopulations with both lower and higher chromosome ploidy were shown in all analyzed cell lines, with their modal chromosome numbers ranging from 36 to 107 (Figure 3B). SH-416 and SH-289 cells harbor a wide range of chromosomes number, while the suspension cell line SH-543 displayed almost uniformed diploidy (Figure 3A, 3C).

Status of EGFR mutations and gene amplification in the primary Chinese lung cancer cell lines

The EGFR kinase domain mutations, which are frequently associated with clinical tyrosine kinase inhibitor response, often occur in NSCLC patients from East Asia including China. We then asked if any of the above established cell lines harbor EGFR mutations, which may be useful for drug response studies. Using cDNA sequencing of the EGFR tyrosine kinase domain region, we found that five lines harbor EGFR mutations — four among them have exon 19 deletions (SH-224, SH-289, SH-416, and SH-450) and one has an exon 21 point mutation (SH-437) (Figure 4A). We further checked the gene amplification of EGFR allele, and the results from FISH analyses showed that all 5 cell lines displayed various degree of gene copy number increase (Table 1). Three cell lines (SH-224, SH-437, and SH-450) showed high polysomy, while another two (SH-289 and SH-416) showed gene amplification (Figure 4B).

Cell growth of the primary Chinese lung cancer cell lines in two dimension and soft agar

Five adherent NSCLC cell lines were used for further MTT assay and soft agar assay for testing their cell growth ability. Three cell lines with EGFR mutations SH-224, SH-437, and SH-450 grow faster than SH-289 and SH416 (Figure 5A).

Consistently, all the three cell lines (SH-224, SH-437, and SH-450) growing faster in two-dimension culture formed recognizable colonies in soft agar. In contrast, no colonies were seen in the two slow-growing cell lines SH-416 and SH-289 (Figure 5B).

Tumorigenicity of primary Chinese NSCLC cell lines

We further checked the tumor formation ability of these NSCLC cell lines in nude mice. Cell lines SH-224, SH-437, and SH-450 readily formed subcutaneous tumors in nude mice 2 weeks following transplantation. Surprisingly, SH-416, the cell line that failed to form colonies in soft agar, could also form a visible graft in nude mice at a low rate (1/4) (Figure 6A, 6B). This may somehow reflect the difference between *in vitro* and *in vivo* systems. Nonetheless, these data also suggest that SH-289 and SH-416 may have a low potential for tumor formation. The tumors grew locally as compact masses. In each instance the histological appearance of the tumors closely resembled the original tumors from which they were derived (Figure 1, 6C).

Discussion

The *in vitro* cell line model system has contributed significantly to cancer research and resulted in several seminal biomedical discoveries. However, the majority of these cancer cell lines are from Western populations, thus dramatically constraining the studies focusing on ethnic differences in cancer biology, drug response or toxicity between Chinese and Caucasian populations. In this study, we have established eight lung cancer cell lines from a Chinese genetic background. These well-characterized cell lines will provide an ideal platform for stimulating studies in the future.

In general, it is considered much more difficult to establish lung cancer cell lines in comparison with other types of epi-

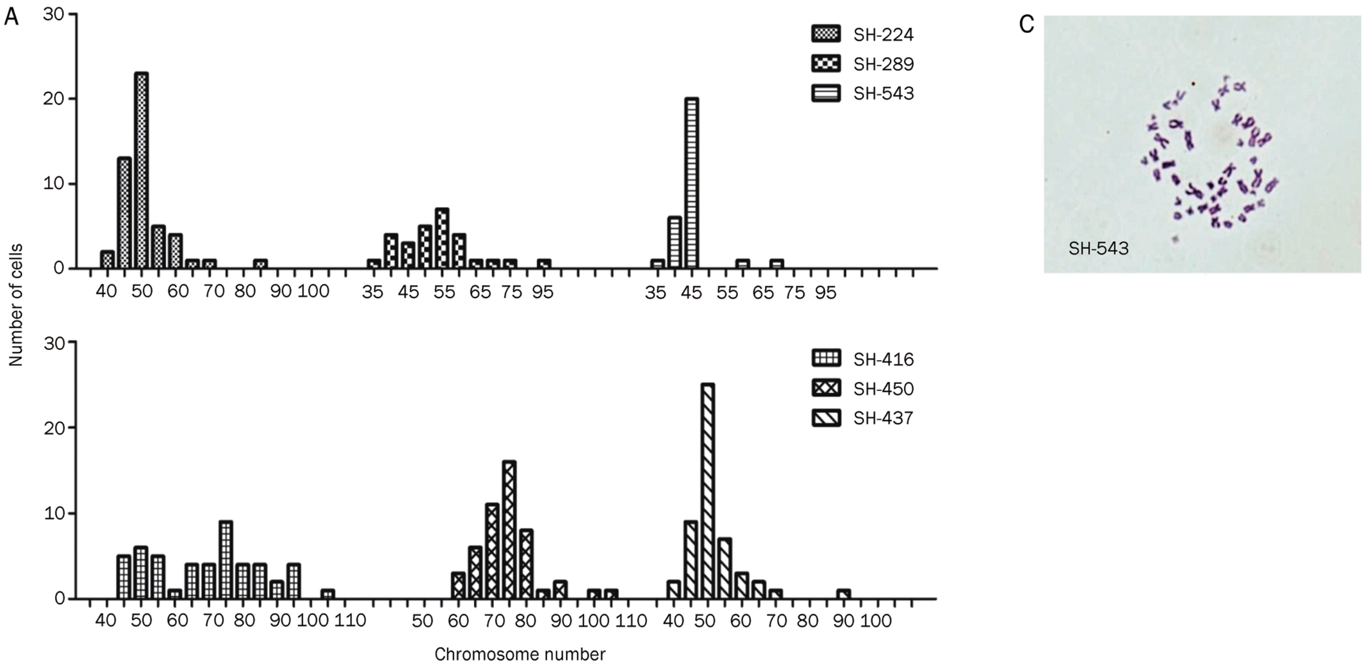

B

Cell line	Number of counted cells	Ploidy distribution	Mean
SH-224	50	40–84	50.9
SH-289	28	37–85	53.54
SH-543	29	36–72	45.31
SH-416	49	45–107	69.76
SH-450	49	58–107	74.39
SH-437	50	39–92	51.28

Figure 3. Ploidy and cytogenetic analyses of primary Chinese lung cancer cell lines. (A) Ploidy distribution of six Chinese NSCLC cell lines. (B) The summary of chromosome counting in the six Chinese NSCLC cell lines. (C) The karyotype of SH-543 is shown as one example.

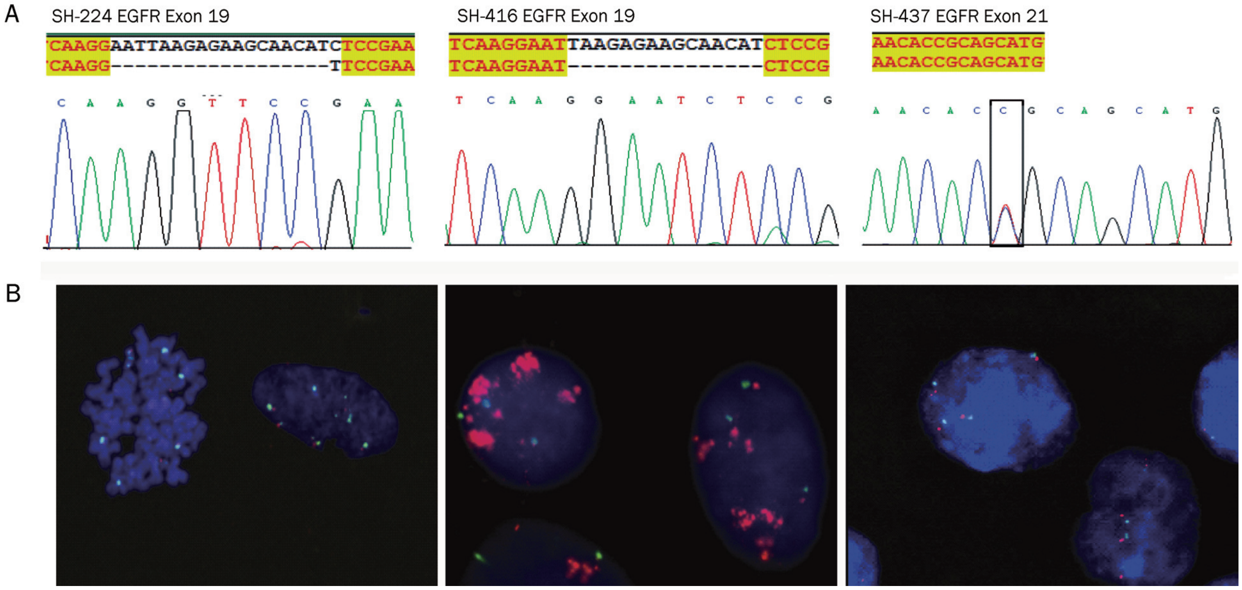

Figure 4 . Status of EGFR mutation and gene amplification in primary Chinese lung cancer cell lines. (A) DNA sequencing results showed EGFR mutations in the indicated cell lines. (B) FISH analyses showed either EGFR high polysomy or gene amplification in the indicated cell lines. Green: chromosome 7 centromere; Red: EGFR.

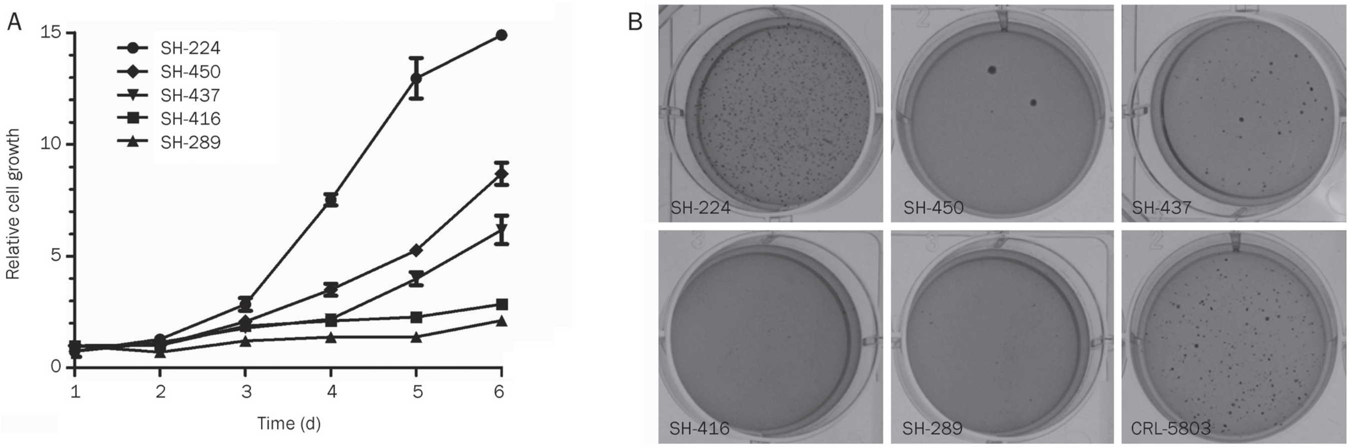

Figure 5. Cell growth of primary Chinese lung cancer cell lines in two dimension and soft agar. (A) The cell growth kinetics of the five adherent NSCLC cell lines are indicated. (B) The anchorage-independent cell growth of the five NSCLC cell lines. CRL-5803 serves as the control.

A

	Soft agar (Y/N)	Xenograft (tumor/total)
SH-224	Y	4/4
SH-450	Y	4/4
SH-437	Y	4/4
SH-416	N	1/4

Figure 6. Tumor formation ability of primary Chinese NSCLC cell lines in nude mice. (A) The summary of tumorigenicity in four Chinese NSCLC cell lines in nude mice. (B) Representative photos are shown for the xenografts; (C) H&E staining of the tumors from xenografts.

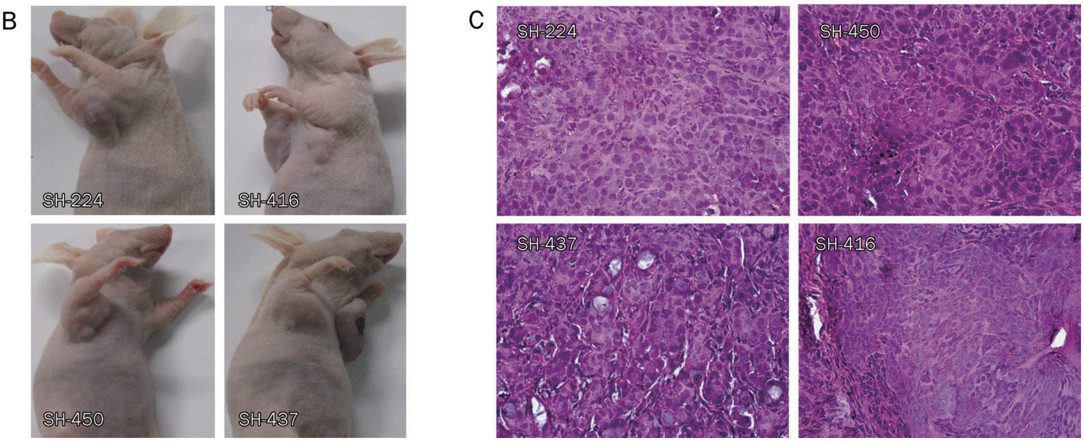

thelia-originated cell lines[28]. Chemically defined media such as ACL3, ACL4, and HITES were first used for primary lung cancer cell culture with success. We tried here to add 5% FBS to the chemically defined medium ACL4, which stimulates the growth of not only the cancer cells but also the fibroblast. With great effort to eliminate fibroblast growth using scraping methods, we have successfully established eight Chinese lung cancer cell lines. It is possible that serum played an important role in making the floating cells attach to a culture dish. However, the success rate in our study still remains low (4.5%, Table 2). Further work is warranted to optimize the chemically defined medium.

To our surprise, five of the seven NSCLC cell lines we established harbor EGFR mutations as well as EGFR polysomy or allele amplification. EGFR mutations in all established Chinese NSCLC cell lines reach 71%. Through several decades of efforts, 21 lung cancer cell lines with EGFR kinase domain mutations have been developed worldwide: 12 with exon 19 deletions and 7 with the exon 21 mutation L858R and/or drug-resistant exon 20 mutation T790M (Table 3). Two uncommon mutations L861Q and G719S are also seen. Among these EGFR mutant cell lines, nine are from Caucasian populations,

Table 2. Summary of the success rate of all primary cell lines from different lung cancer subtypes.

Pathology	Success	Total	Success rate
Ad	3	83	3.6%
SCC	1	43	2.3%
AS	1	6	16.7%
LC	1	4	25%
PDE	1	11	9.1%
SCLC	1	4	25%
Others	0	28	0
Summary	8	179	4.5%

Table 3. Previously established lung cancer cell lines with EGFR kinase domain mutations.

Cell line	Pathology	EGFR mutation status	References
H1650	Ad	Exon 19 deletion (746–750)	[29]
HCC827	Ad	Exon 19 deletion (746–750)	[30]
HKULC 3	Ad	Exon 19 deletion (756–760)	[31]
PC3	Ad	Exon 19 deletion (747–749), A750P	[32]
PC9	Ad	Exon 19 deletion (746–750)	[33]
PC-14	Ad	Exon 19 deletion (746–750)	[32]
HCC2935	Ad	Exon 19 deletion (746–751), S752I	[34]
HCC4006	Ad	Exon 19 deletion (747–749), A750P	[35]
H820	Ad	Exon 19 deletion (746–751), T790M	[36]
HCC2279	Ad	Exon 19 deletion (746–750)	[37]
RERF-LC-Ad2	Ad	Exon 19 deletion (747–749), A750P	[32]
H1975	Ad	L858R and T790M	[29, 38]
H3255	Ad	L858R	[39]
HCC4011	Ad	L858R	[34]
11-18	Ad	L858R	[32]
LCSC#1*	Ad	L858R	[32]
LC2/Ad	Ad	L858R	[32]
KTA-7	Ad	L861Q	[32]
PC-7	Ad	G719S	[32]
RERF-LC-A1	SCC	L858R	[32]
KTSq-1	SCC	Exon 19 deletion (746–750)	[32]

eleven from Japan and one from Hong Kong. Here, we have established a comparable number of NSCLC cell lines with EGFR mutations in a Chinese genetic background. It is noteworthy that the majority of the previously established EGFR mutant cell lines are from lung adenocarcinomas, while two are from squamous cell carcinomas, which are not commonly used. In contrast, our collection of cell lines is composed of various pathologies including adenocarcinoma (3), squamous cell carcinoma (1), adeno-squamous cell carcinoma (1) and large cell carcinoma (1) (Table 1). In addition, SH-437 harbors an exon 21 point mutation P848L, which has not been previously reported in any cell line. Taken together, our effort to establish Chinese lung cancer cell lines was a very successful small step toward our long-term goal of establishing more than 30 Chinese lung cancer cell lines. These cell lines will provide important tools for studying the ethnic differences in lung cancer biology as well as in drug treatment between Chinese and Caucasian populations in the future.

Acknowledgements

This work was supported by the National Basic Research Program of China (2010CB912102), the National Natural Science Foundation of China (30871284 and 30971461), the Chinese Academy of Sciences (KSCX1-YW-22), and the Science and Technology Commission of Shanghai Municipality (08PJ14105, 09JC1416300). Hong-bin JI is a scholar of the Hundred Talents Program of the Chinese Academy of Sciences.

Author contribution

Hong-bin JI and Hai-quan CHEN designed the research; Chao ZHENG, Yi-hua SUN, and Xiao-lei YE performed the research; Hong-bin JI and Chao ZHENG wrote the paper.

References

1 Jemal A, Siegel R, Ward E, Hao Y, Xu J, Thun MJ. Cancer statistics, 2009. CA Cancer J Clin 2009; 59: 225–49.

2 Jemal A, Siegel R, Xu J, Ward E. Cancer statistics, 2010. CA Cancer J Clin 2010; 60: 277–300.

3 Gazdar AF, Girard L, Lockwood WW, Lam WL, Minna JD. Lung cancer cell lines as tools for biomedical discovery and research. J Natl Cancer Inst 2010; 102: 1310–21.

4 Masters JR. HeLa cells 50 years on: the good, the bad and the ugly. Nat Rev Cancer 2002; 2: 315–9.

5 Lieber M, Smith B, Szakal A, Nelson-Rees W, Todaro G. A continuous tumor-cell line from a human lung carcinoma with properties of type II alveolar epithelial cells. Int J Cancer 1976; 17: 62–70.

6 Masuda N, Fukuoka M, Takada M, Kudoh S, Kusunoki Y. Establishment and characterization of 20 human non-small cell lung cancer cell lines in a serum-free defined medium (ACL-4). Chest 1991; 100: 429–38.

7 Loh PM, Clamon GH, Robinson RA, White ML, Hukku B, Rossi NP, *et al*. Establishment and characterization of four new human non-small cell lung cancer cell lines. Cancer Res 1984; 44: 3561–9.

8 Anger B, Bockman R, Andreeff M, Erlandson R, Jhanwar S, Kameya T, *et al*. Characterization of two newly established human cell lines from patients with large-cell anaplastic lung carcinoma. Cancer 1982; 50: 1518–29.

9 Baillie-Johnson H, Twentyman PR, Fox NE, Walls GA, Workman P, Watson JV, *et al*. Establishment and characterisation of cell lines from patients with lung cancer (predominantly small cell carcinoma). Br J Cancer 1985; 52: 495–504.

10 Carney DN, Gazdar AF, Bepler G, Guccion JG, Marangos PJ, Moody TW, *et al*. Establishment and identification of small cell lung cancer cell lines having classic and variant features. Cancer Res 1985; 45: 2913–23.

11 Simms E, Gazdar AF, Abrams PG, Minna JD. Growth of human small cell (oat cell) carcinoma of the lung in serum-free growth factor-supplemented medium. Cancer Res 1980; 40: 4356–63.

12 Oie HK, Russell EK, Carney DN, Gazdar AF. Cell culture methods for the establishment of the NCI series of lung cancer cell lines. J Cell Biochem Suppl 1996; 24: 24–31.

13 Gazdar AF, Gao B, Minna JD. Lung cancer cell lines: Useless artifacts

or invaluable tools for medical science? Lung Cancer 2010; 68: 309–18.

14 Jang TW, Oak CH, Chang HK, Suo SJ, Jung MH. EGFR and KRAS mutations in patients with adenocarcinoma of the lung. Korean J Intern Med 2009; 24: 48–54.

15 Pao W, Miller VA. Epidermal growth factor receptor mutations, small-molecule kinase inhibitors, and non-small-cell lung cancer: current knowledge and future directions. J Clin Oncol 2005; 23: 2556–68.

16 Riely GJ, Marks J, Pao W. KRAS mutations in non-small cell lung cancer. Proc Am Thorac Soc 2009; 6: 201–5.

17 Sun YH, Fang R, Gao B, Han XK, Zhang JH, Pao W, *et al*. Comparable rate of EGFR kinase domain mutation in lung adenocarcinomas from Chinese male and female never-smokers. Acta Pharmacol Sin 2010; 31: 647–8.

18 Gao B, Sun Y, Zhang J, Ren Y, Fang R, Han X, *et al*. Spectrum of LKB1, EGFR, and KRAS mutations in chinese lung adenocarcinomas. J Thorac Oncol 2010; 5: 1130–5.

19 Phan VH, Moore MM, McLachlan AJ, Piquette-Miller M, Xu H, Clarke SJ. Ethnic differences in drug metabolism and toxicity from chemotherapy. Expert Opin Drug Metab Toxicol 2009; 5: 243–57.

20 Sekine I, Yamamoto N, Nishio K, Saijo N. Emerging ethnic differences in lung cancer therapy. Br J Cancer 2008; 99: 1757–62.

21 Sun Y, Ren Y, Fang Z, Li C, Fang R, Gao B, *et al*. Lung adenocarcinoma from east asian never smokers is a disease largely defined by targetable oncogenic mutant kinases. J Clin Oncol 2010; 28: 4616-20.

22 Haber DA, Bell DW, Sordella R, Kwak EL, Godin-Heymann N, Sharma SV, *et al*. Molecular targeted therapy of lung cancer: EGFR mutations and response to EGFR inhibitors. Cold Spring Harb Symp Quant Biol 2005; 70: 419–26.

23 Yang CH. EGFR tyrosine kinase inhibitors for the treatment of NSCLC in East Asia: present and future. Lung Cancer 2008; 60: S23–30.

24 Gazdar AF, Oie HK. Cell culture methods for human lung cancer. Cancer Genet Cytogenet 1986; 19: 5–10.

25 Brower M, Carney DN, Oie HK, Gazdar AF, Minna JD. Growth of cell lines and clinical specimens of human non-small cell lung cancer in a serum-free defined medium. Cancer Res 1986; 46: 798–806.

26 Cappuzzo F, Hirsch FR, Rossi E, Bartolini S, Ceresoli GL, Bemis L, *et al*. Epidermal growth factor receptor gene and protein and gefitinib sensitivity in non-small-cell lung cancer. J Natl Cancer Inst 2005; 97: 643–55.

27 Ali S, Banerjee S, Schaffert JM, El-Rayes BF, Philip PA, Sarkar FH. Concurrent inhibition of NF-kappaB, cyclooxygenase-2, and epidermal growth factor receptor leads to greater anti-tumor activity in pancreatic cancer. J Cell Biochem 2010; 110: 171–81.

28 Sugaya M, Takenoyama M, Osaki T, Yasuda M, Nagashima A, Sugio K, *et al*. Establishment of 15 cancer cell lines from patients with lung cancer and the potential tools for immunotherapy. Chest 2002; 122: 282–8.

29 NCI-Navy Medical Oncology Branch cell line supplement. J Cell Biochem Suppl 1996; 24: 1-291.

30 Girard L, Zochbauer-Muller S, Virmani AK, Gazdar AF, Minna JD. Genome-wide allelotyping of lung cancer identifies new regions of allelic loss, differences between small cell lung cancer and non-small cell lung cancer, and loci clustering. Cancer Res 2000; 60: 4894–906.

31 Lam DC, Girard L, Suen WS, Chung LP, Tin VP, Lam WK, *et al*. Establishment and expression profiling of new lung cancer cell lines from Chinese smokers and lifetime never-smokers. J Thorac Oncol 2006; 1: 932–42.

32 Nagai Y, Miyazawa H, Huqun, Tanaka T, Udagawa K, Kato M, *et al*. Genetic heterogeneity of the epidermal growth factor receptor in non-small cell lung cancer cell lines revealed by a rapid and sensitive detection system, the peptide nucleic acid-locked nucleic acid PCR clamp. Cancer Res 2005; 65: 7276-82.

33 Noro R, Gemma A, Kosaihira S, Kokubo Y, Chen M, Seike M, *et al*. Gefitinib (IRESSA) sensitive lung cancer cell lines show phosphorylation of Akt without ligand stimulation. BMC Cancer 2006; 6: 277.

34 Kubo T, Yamamoto H, Lockwood WW, Valencia I, Soh J, Peyton M, *et al*. MET gene amplification or EGFR mutation activate MET in lung cancers untreated with EGFR tyrosine kinase inhibitors. Int J Cancer 2009; 124: 1778-84.

35 Shigematsu H, Takahashi T, Nomura M, Majmudar K, Suzuki M, Lee H, *et al*. Somatic mutations of the HER2 kinase domain in lung adenocarcinomas. Cancer Res 2005; 65: 1642-6.

36 Shimamura T, Li D, Ji H, Haringsma HJ, Liniker E, Borgman CL, *et al*. Hsp90 inhibition suppresses mutant EGFR-T790M signaling and overcomes kinase inhibitor resistance. Cancer Res 2008; 68: 5827-38.

37 Lu Y, Liang K, Li X, Fan Z. Responses of cancer cells with wild-type or tyrosine kinase domain-mutated epidermal growth factor receptor (EGFR) to EGFR-targeted therapy are linked to downregulation of hypoxia-inducible factor-1 alpha. Mol Cancer 2007; 6: 63.

38 Sordella R, Bell DW, Haber DA, Settleman J. Gefitinib-sensitizing EGFR mutations in lung cancer activate anti-apoptotic pathways. Science 2004; 305: 1163-7.

39 Tracy S, Mukohara T, Hansen M, Meyerson M, Johnson BE, Jänne PA. Gefitinib induces apoptosis in the EGFRL858R non-small-cell lung cancer cell line H3255. Cancer Res 2004; 64: 7241-4.

Acta Pharmacologica Sinica (2011) 32: 393–398
© 2011 CPS and SIMM All rights reserved 1671-4083/11 $32.00
www.nature.com/aps

Original Article

Down-regulation of ALKBH2 increases cisplatin sensitivity in H1299 lung cancer cells

Shuang-shuang WU, Wei XU, Shan LIU, Bo CHEN, Xue-li WANG, Yan WANG, Shi-feng LIU, Jian-qing WU*

Department of Geriatrics, the First Affiliated Hospital of Nanjing Medical University, Nanjing 210029, China

Aim: To elucidate the combined effect of alkylated DNA repair protein alkB homolog 2 (ALKBH2)-targeting gene therapy and cisplatin (cDDP) chemotherapy on the non-small cell lung cancer (NSCLC) H1299 cell line.
Methods: ALKBH2 was down-regulated in H1299 cells by lentivirus-mediated RNA interference (RNAi). Changes in ALKBH2 expression were determined using real-time RT-PCR and Western blotting. Cell viability was evaluated using MTT assay. DNA synthesis in proliferating cells was determined using BrdU incorporation assay. Cell apoptosis was determined using flow cytometry.
Results: Lentivirus-mediated ALKBH2 silencing alone did not induce apoptosis or attenuate the growth potential of H1299 cells within five days post-infection. Combined treatment modalities with lentivirus-mediated ALKBH2 down-regulation and cDDP (333 μmol/L) were significantly more potent in inhibiting cell growth and inducing apoptosis than mono-chemotherapy.
Conclusion: Combined treatment modalities of ALKBH2 knockdown and cDDP chemotherapy have the potential to improve the efficacy in the treatment of NSCLC.

Keywords: lentivirus; RNA interference; alkB homolog 2; cisplatin; non-small cell lung cancer

Acta Pharmacologica Sinica (2011) 32: 393–398; doi: 10.1038/aps.2010.216; published online 31 Jan 2011

Introduction

Lung cancer is currently the leading cause of cancer-related mortality in both men and women (31% and 26%, respectively) worldwide[1]. Four of five lung cancers are classified as non-small cell lung cancers (NSCLC), and the majority of these patients have advanced disease (stage III/IV) when diagnosed, with poor prognosis[2]. The lung cancer cure rates have not improved for 40 years, and further substantial increase in cure rates is not to be expected with the current treatment modalities. In an effort to improve survival, new therapeutic approaches focusing on the molecular mechanisms that mediate tumor cell growth or survival have gained much attention.

Combination therapy that includes a platinum-based compound has been the primary treatment for cancer patients diagnosed with advanced NSCLC[3]. Cisplatin, *cis*-platinum, or *cis*-diamminedichloroplatinum (II) (cDDP), which is classified as an alkylating agent, is a platinum-based chemotherapy drug commonly used to treat various types of cancers[4]. As the first member of the platinum complexes that now also includes carboplatin and oxaliplatin, cDDP reacts *in vivo*, binding to and inducing DNA cross-linking, which ultimately triggers apoptosis. However, acquired resistance confines the application of cDDP in chemotherapeutics. Drug resistance is shown to be a cumulative process that eventually can overcome tumor regression, leading to treatment failure[5]. The lung tumor initially responds to cDDP by sensing DNA damage, which results in cell cycle arrest and apoptosis, leading to a significant reduction in tumor burden. Prolonged cDDP treatment, however, promotes the emergence and clonal expansion of drug-resistant tumor cells with enhanced repair capacity. These cDDP-resistant tumors are cross-resistant to platinum analogs, exhibit advanced histopathology, and display abundant genomic alterations[6].

The AlkB family of dioxygenases, which directly reverse DNA base damage by oxidative demethylation, belong to the superfamily of 2-oxoglutarate- and iron (II)-dependent oxygenases[7]. *E coli* AlkB is a direct dealkylation DNA repair protein that repairs single-stranded DNA (ssDNA) lesions or damaged bases in RNA using a unique oxidative dealkylation mechanism[8, 9]. There are nine different potential human homologues of AlkB, denoted ALKBH1-ALKBH9[10, 11]. Two of these, ALKBH2 and ALKBH3, have similar repair activities to *E coli* AlkB[12–14]. ALKBH2 is a housekeeping enzyme and has the primary role of guarding mammalian genomes against 1-meA damage by repairing this lesion in double-stranded DNA (dsDNA). The *in vivo* function of ALKBH3 is still

---

* To whom correspondence should be addressed.
E-mail jianqingwu@yeah.net
Received 2010-06-10 Accepted 2010-12-02

unclear, although it exhibits a distinct preference for repairing ssDNA and RNA[13].

Because ALKBH2 is a direct dealkylation DNA repair protein, we hypothesized that down-regulation of ALKBH2 expression should be a promising approach to enhancing the efficacy of alkylating agents such as cisplatin, which are widely used in cancer therapy and exert anticancer effects by creating cytotoxic DNA lesions in tumor cells. In this study, we inhibited ALKBH2 expression by lentivirus-mediated RNA interference to elucidate the combined effect of ALKBH2-targeting gene therapy and cDDP chemotherapy on NSCLC cell line H1299. Here we establish the impact of lentivirus-mediated transfer of small interfering RNAs targeting ALKBH2 on human H1299 cells and demonstrate the additive efficacy of ALKBH2 knockdown combined with cDDP chemotherapy in causing tumor cell death.

Materials and methods

Cell culture

The NSCLC cell line H1299 was purchased from ATCC (Manassas, VA, USA). It was maintained in Dulbecco's modified Eagle's medium (DMEM) containing 10% fetal bovine serum (FBS) and cultured in a humidified atmosphere of 95% air and 5% CO_2 at 37 ºC.

Reagents and dosage

cDDP and paclitaxel (PTX) were purchased from Sigma Chemical Co (St Louis, MO, USA). cDDP and PTX treatment was administered to cells at the concentration of 333 µmol/L and 100 nmol/L, respectively. MTT was purchased from Shanghai Dingguo Biotechnology Co, Ltd (Shanghai, China). Annexin V-FITC Apoptosis Detection Kit was purchased from Abcam (Cambridge, MA, USA).

Construction of lentiviral vector and cell infection

A 19 nt ALKBH2-targeting sequence of oligonucleotides was designed by Oligoengine Inc (Seattle, WA, USA) and selected as the template: 5′-CCTTCAACTTTGTGCTCAT-3′. The negative construct (NC), a scrambled sequence with no homology to any human gene, was 5′-AATGTACTGCGCGTGGAGA-3′. The oligonucleotides were cloned into pGCSIL-GFP (GeneChem, Shanghai, China) to generate the lentiviral vectors. Recombinant lentiviral vectors and packaging vectors were then transfected into 293T cells. Supernatants containing lentiviruses expressing ALKBH2 short hairpin RNA (shRNA) or negative control shRNA were harvested 72 h after transfection. Then, the lentiviruses were purified using ultracentrifugation, and the titer of lentiviruses was determined. H1299 cells were infected with the lentivirus constructs at multiplicity of infection (MOI)=10, and mock-infected H1299 cells were used as negative controls.

RNA extraction and quantitative real-time RT-PCR

Total RNA was extracted from cells with Trizol reagent (Invitrogen, Carlsbad, CA, USA) according to the manufacturer's instructions. Gene expression was detected by quantitative real-time RT-PCR (qRT-PCR) using the standard SYBR Green RT-PCR kit (Takara, Otsu, Japan) according to the manufacturer's instructions. Briefly, the cDNA was synthesized using the RevertAid First-Strand cDNA Synthesis kit (MBI Fermentas, Vilnius, Lithuania) according to the manufacturer's protocol. Specific primer pairs and the amplified products are shown in Table 1. The relative levels of gene mRNA transcripts were normalized to the control *β-actin*. Relative gene expression was quantified using GraphPad Prism 4.0 software (GraphPad Software, San Diego, CA, USA).

Table 1. The specific primer pairs and the amplified products in quantitative real-time RT-PCR.

Gene	Primer pairs	Product
ALKBH2	Sense: 5'-GACTGGACAGACCTTCAAC-3';	
	Antisense: 5'-AGGAGACAGAGGCAATGG-3'	122 bp
Bcl-2	Sense: 5'-GTGTGGAGAGCGTCAACC-3';	
	Antisense: 5'-CTTCAGAGACAGCCAGGAG-3'	182 bp
Bax	Sense: 5'-ATGCGTCCACCAAGAAGC-3';	
	Antisense: 5'-ACG GCG GCA ATCATCCTC-3'	91 bp
bFGF	Sense: 5'-ATCAAAGGAGTGTGTGCTAACC-3';	
	Antisense: 5'-ACTGCCCAGTTCGTTTCAGTG-3'	178 bp
PDGFA	Sense: 5'-CGGAGGAAGAGAAGCATCG-3';	
	Antisense: 5'-GGCTGGCACTTGACACTG-3'	179 bp
PDGFB	Sense: 5'-GCACCAACGCCAACTTCC-3';	
	Antisense: 5'-GCTTCTTCCGCACAATCTCG-3'	150 bp
β-actin	Sense: 5'-GGCGGCACCACCATGTACCCT-3';	
	Antisense: 5'-AGGGGCCGGACTCGTCATACT-3'	202 bp

Western blot analysis

The cells were lysed in lysis buffer (0.1% SDS, 1% NP-40, 50 mmol/L HEPES, pH 7.4, 2 mmol/L EDTA, 100 mmol/L NaCl, 5 mmol/L sodium orthovanadate, and 1% protease inhibitor mixture set I; Calbiochem, San Diego, CA, USA) on ice for 30 min, and the cell lysates were cleared by centrifugation at 12 000 round per minute for 15 min. Proteins were separated in 10% SDS-PAGE and electroblotted onto polyvinylidene difluoride membrane, blocked for 1.5 h at room temperature in 5% BSA, and probed with anti-ALKBH2 (Cell Signaling Technology, Beverly, MA, USA), and anti-GAPDH (Sigma, St Louis, MO, USA) antibody. Following incubation with the appropriate peroxidase-conjugated secondary antibodies, chemiluminescent detection was performed with the ECL kit (Pierce Chemical Co, Rockford, IL, USA).

MTT assay

Cell viability was evaluated by MTT assay with some modifications as reported previously[15]. The test cells in exponential growth were plated at a final concentration of 2×10^3 cells/well in 96-well culture plates for different culture times. Ten microlitres of 10 mg/mL MTT was then added. After an additional 4 h of incubation, the reaction was terminated by removal of the supernatant and the addition of 150 μL DMSO for 30 min. Optical density (OD) of each well was measured at 570 nm using an ELISA reader (ELx808, Bio-Tek Instruments, Winooski, VT, USA).

BrdU incorporation assay

DNA synthesis in proliferating cells was determined using a BrdU incorporation assay[15]. After incubation with BrdU (10 μmol/L) (BD Pharmingen, San Diego, CA, USA) for 24 h, the cells were fixed and labeled with peroxidase-conjugated anti-BrdU antibody. Peroxidase substrate (tetramethylbenzidine) was then added and incubated for 30 min; then, the absorbance values were measured at 490 nm using an ELISA reader (ELx808, Bio-Tek Instruments, Winooski, VT, USA). Background BrdU immunofluorescence was determined in cells not exposed to BrdU but stained with the BrdU antibody.

Detection of apoptosis by flow cytometry

Cells were simultaneously stained with fluorescein isothiocyanate (FITC) labeled annexin-V and propidium iodide (PI) to discriminate intact cells (annexin$^-$/PI$^-$) from apoptotic cells (annexin$^+$/PI$^-$) and necrotic cells (annexin$^+$/PI$^+$). A total of 1.0×10^6 cells were washed twice with ice-cold PBS and incubated for 30 min in binding buffer (1 μg/mL PI and 1 μg/mL FITC labeled annexin-V). FACS analysis for annexin-V and PI staining was performed by an Epics Altra flow cytometer (Beckmann Coulter, Krefeld, Germany). All experiments were performed in triplicate.

Statistical analysis

Data were expressed as means±SD. Statistical analysis was performed using SPSS software (Release 11.0, SPSS Inc, Chicago, IL, USA). The difference between two groups was analyzed by Student's *t*-test. A value of $P<0.05$ was considered statistically significant.

Results

ALKBH2 expression after treatment with lentivirus-mediated RNAi

To determine the effect of RNAi on the expression of ALKBH2 in H1299 cells, we generated lentiviral vectors that expressed the ALKBH2 specific-RNAi or the negative control-RNAi. Three days after lentivirus infection, H1299 cells were visualized using a fluorescence microscope. The bright-field and fluorescent images showed that most cells had green fluorescent signals (Figure 1A). After the cells were infected with ALKBH2 specific-RNAi or control-RNAi, the mRNA and protein levels of ALKBH2 were analyzed. The level of ALKBH2 mRNA in cells expressing ALKBH2 specific-RNAi significantly decreased by approximately 70% ($P<0.05$) compared to the control cells (Figure 1B). In accordance with the decreased mRNA expression, ALKBH2 protein was also down-regulated in cells expressing the ALKBH2-specific RNAi (Figure 1C). Thus, ALKBH2-specific RNAi down-regulated ALKBH2 expression efficiently.

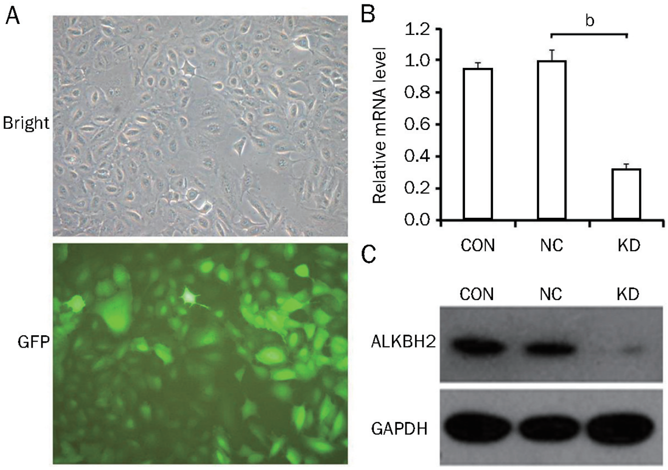

Figure 1. Down-regulation of ALKBH2 expression using lentivirus-mediated RNAi. (A) Expression of lentivirus-mediated RNAi in H1299 cells. Three days after infection with lentivirus, H1299 cells were visualized using a fluorescence microscope. The phase contrast (Bright) and fluorescence (GFP) photographs were taken with the same exposure times at a magnification. (B) The relative levels of *ALKBH2* mRNA transcripts were analyzed by qRT-PCR. Data shown are the mean results±SD repeated three times with triplicate samples per treatment ($n=3$, $^bP<0.05$). (C) Silencing effects of ALKBH2 protein was measured using Western blot. CON: parent cells; NC: cells infected with negative control RNAi; KD: cells infected with ALKBH2 specific RNAi.

Effects of concurrent treatments of H1299 cells with lentiviruses expressing ALKBH2-specific RNAi and cDDP

First, the MTT assay was used to investigate the potential effects of RNAi-mediated ALKBH2 down-regulation on the growth of H1299 cells. Following a 5-d incubation period, the growth of cells expressing ALKBH2-specific-RNAi was almost indistinguishable from that of the control cells (Figure 2A). We concluded that the down-regulation of ALKBH2 expression alone had no obvious impact on the growth or viability of H1299 cells. We then investigated the combined effects of ALKBH2 inhibition and cDDP treatment on H1299 cells. Forty-eight hours after infection with lentiviruses expressing ALKBH2-specific-RNAi or control-RNAi, the infected and non-infected cells were subsequently treated with cDDP (333 μmol/L) for 24 h[16]. The MTT assay showed that the inhibition ratio in the cells infected with ALKBH2-RNAi lentivirus (KD) was increased about 1.8-fold and 2-fold compared to the mock-infected (NC) and non-infected (CON) cells ($P<0.05$), respectively. These results indicate that cDDP is cytotoxic to H1299 cells and that this combination treatment resulted in lower cell viability than treatment with cDDP alone (Figure 2B). To compare the effects of ALKBH2 inhibition on cytotoxicity by a chemotherapeutic agent that does not act by inducing DNA damage, we measured the cytotoxicity of PTX on H1299 cells by MTT assay. Following 24 h of PTX (100 nmol/L) treatment, the inhibition ratio was not increased significantly in ALKBH2-RNAi lentivirus infected cells ($P<0.05$) compared with that in mock-infected and non-infected cells (Figure 2C). To further investigate the combined effects of ALKBH2 inhibition and

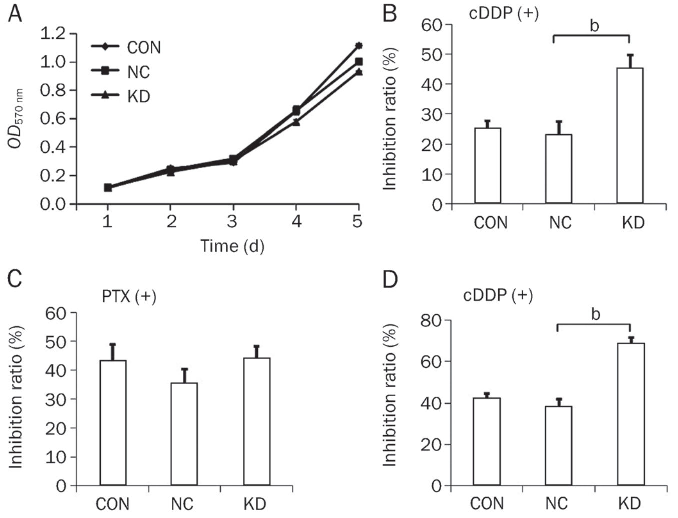

Figure 2. Effect of down-regulated ALKBH2 on H1299 cell growth. (A) Proliferation of parent H1299 cells (CON), cells infected with ALKBH2-specific RNAi (KD), and cells infected with negative control RNAi (NC). Their growth dynamics were determined daily using MTT. (B) Cytotoxicity of combined cDDP-based chemotherapy with lentivirus-mediated RNAi treatment. Uninfected cells (CON), ALKBH2 RNAi infected cells or control RNAi infected cells were treated with cDDP, and the inhibition ratio was measured by MTT. Data shown are the mean results±SD of a representative experiment performed in triplicate (n=3, $^{b}P<0.05$). (C) Cytotoxicity of combined PTX-based chemotherapy with lentivirus-mediated RNAi treatment. (D) The DNA synthesis rate in H1299 cells treated with cDDP and ALKBH2-specific RNAi was analyzed using the BrdU incorporation assay.

cDDP treatment on the DNA synthesis rate in H1299 cells, BrdU incorporation assay was performed. As shown in Figure 2D, the inhibition ratio of ALKBH2 RNAi lentivirus infected cells was enhanced significantly by treatment with cDDP ($P<0.05$) compared to mock-infected and non-infected cells. These results indicate that concurrent treatment of H1299 cells with cDDP and RNAi targeted to ALKBH2 resulted in a lower proliferation rate compared to that of cells treated with cDDP alone.

Enhancement of cDDP-induced apoptosis in H1299 cells by ALKBH2 RNAi

The therapeutic efficacy of anti-cancer agents depends strongly on their ability to trigger apoptosis in target tumor cells[17]. To determine the effect of ALKBH2 knockdown on cDDP-induced apoptosis in H1299 cells, apoptosis was evaluated in uninfected cells, cells expressing ALKBH2 specific-RNAi, or negative control RNAi-expressing cells by flow cytometry analysis following cDDP treatment. As shown in Figure 3, without cDDP treatment the number of apoptotic and necrotic cells in the control, negative control and knockdown groups was almost indistinguishable. However, compared to the control cells, the addition of cDDP significantly increased apoptosis in cells infected with ALKBH2 specific-RNAi ($P<0.01$), suggesting that combining ALKBH2 inhibition with cDDP can enhance the induction of apoptosis.

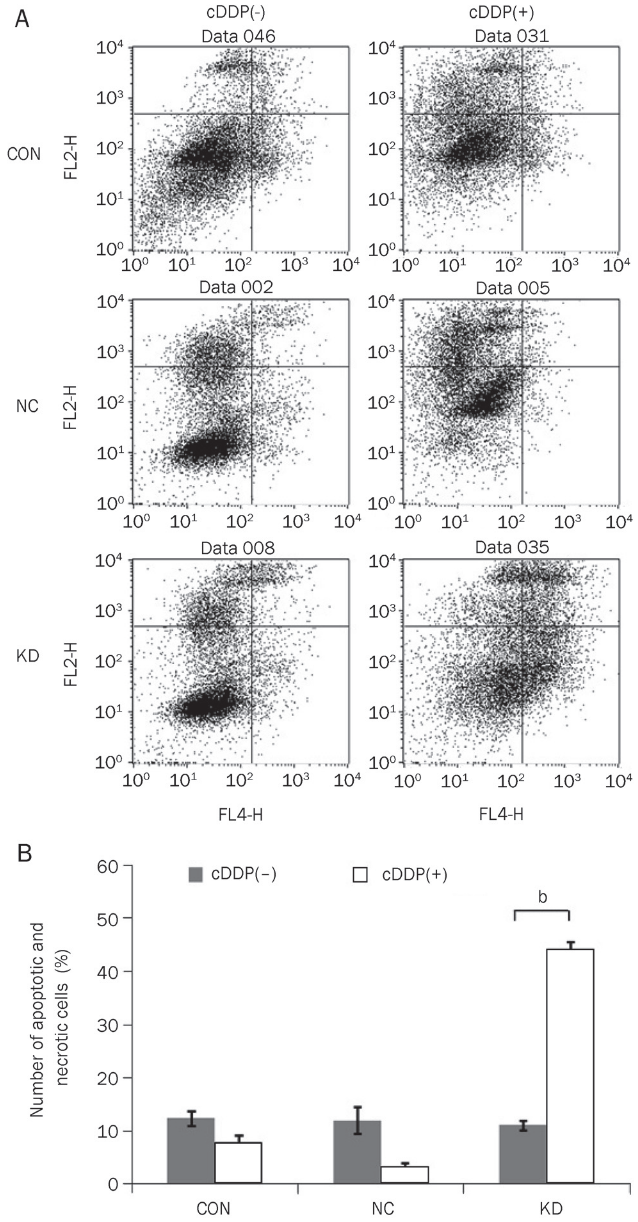

Figure 3. Enhancement of cDDP-induced apoptosis in H1299 cells using ALKBH2 RNAi. (A) H1299 cells were transfected with lentivirus expressing ALKBH2-specific RNAi (KD) or negative control-RNAi (NC), with the parent H1299 cells used as a control (CON). (B) The data presented are the average number of apoptotic and necrotic cells (±SD) in three independent experiments. The infection with ALKBH2 RNAi (KD) enhanced the level of cDDP-induced apoptosis and necrosis compared to the negative control RNAi (NC) or the parent H1299 cells (CON) (n=3, $^{b}P<0.05$).

Influence of ALKBH2 down-regulation on the expression of relevant genes during cDDP-induced apoptosis

Next, we investigated potential pathways involved in the enhancement of cDDP-induced apoptosis by ALKBH2 down-regulation. As shown in Figure 4A and 4B, after the addition

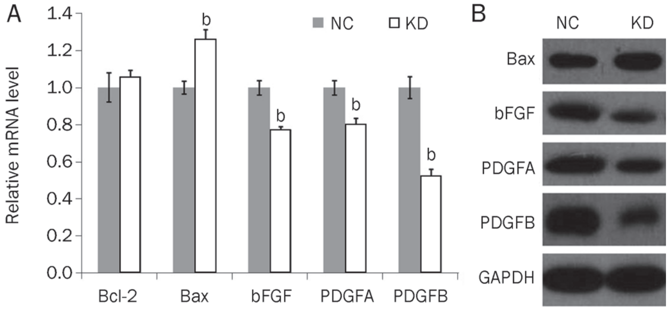

Figure 4. The effect of down-stream gene expression on the cDDP-induced apoptosis by ALKBH2 down-regulation. (A) Bax, rather than Bcl-2 gene transcripts, was up-regulated, and bFGF, PDGFA and PDGFB genes transcripts were down-regulated in the ALKBH2 specific-RNAi infected cells using qRT-PCR. Data shown are the mean results±SD of a representative experiment performed in triplicate (*n*=3, $^{b}P<0.05$). (B) Alteration of Bax, bFGF, PDGFA, and PDGFB protein expression in H1299 cells following ALKBH2 inhibition and cDDP treatment.

of cDDP, the mRNA and protein level of Bax, a member of the Bcl-2 family (Bcl-2, Bcl-XL, and Bax), was found to be up-regulated in H1299 cells infected with ALKBH2 specific-RNAi lentivirus compared to cells infected with negative control-RNAi lentivirus ($P<0.05$). bFGF, a member of the fibroblast growth factor (FGF) family, and the platelet-derived growth factors (PDGF) PDGFA and PDGFB, were found to be down-regulated in the cells infected with ALKBH2 specific-RNAi lentivirus compared to the cells infected with negative control-RNAi lentivirus ($P<0.05$). These results suggest that FGF and PDGF receptor tyrosine kinases signaling pathways and Bcl-2-related apoptosis pathways may be involved in the enhancement of cDDP-induced apoptosis by ALKBH2 down-regulation.

Discussion

NSCLC is the leading cause of cancer-related deaths worldwide. Unfortunately, traditional chemotherapy and radiotherapy remain inadequate for attaining disease control because of their limited efficacy, significant toxicity, development of resistance, and high relapse rates; thus, new therapeutic approaches are urgently required[18]. Combining traditional therapies with modern bioengineered therapeutics has become a new and innovative approach to the treatment of NSCLC. More recently, signal transduction pathways as well as oncogenes and tumor-suppressor genes that are known to be aberrant in lung cancer have been targeted with novel agents[19]. However, the eventual development of acquired resistance also hampers the clinical outcome of these agents during NSCLC treatment[20]. Therefore, further studies targeting multiple treatment modalities and/or the inhibition of multiple signaling pathways are required to develop a novel therapeutic agent to enhance anticancer efficacy and/or prevent treatment resistance. Intensive cancer therapy strategies have thus far focused on sensitizing cancer cells to anticancer drug-mediated cell apoptosis to overcome drug resistance, and this strategy has resulted in more effective cancer therapeutics[21]. cDDP is an effective anticancer drug used to treat many types of cancer. cDDP-based combination chemotherapy is currently considered one of the most effective treatments for advanced NSCLC. The mechanism of cDDP-based anticancer activity is generally accepted to be dependent on its ability to form adducts with DNA (inter- and intra-strand DNA cross-links) and to cause DNA strand breaks in the nucleus. These changes in the DNA interfere with normal transcription and/or DNA replication, leading to either repair of the DNA damage and cell survival or apoptosis[22]. Some early observations have shown that cells deficient in DNA repair pathways are hypersensitive to cDDP. The AlkB family of oxygenases represents a novel class of DNA base-repair enzymes that use an oxidative dealkylation mechanism. In this study, our data show that lentivirus-mediated ALKBH2 gene silencing has no effect on basal H1299 cell growth. However, the combination of ALKBH2 RNAi lentivirus infection and cDDP-based chemotherapy is significantly more potent than cDDP monotherapy, as measured by growth inhibition and the induction of apoptosis in H1299 cells. Therefore, we hypothesized that silencing the ALKBH2 gene in cDDP-resistant patients may safely enhance the efficacy of cDDP in the treatment of lung cancer. However, the main mechanisms for ALKBH2 inhibition-mediated sensitivity to cDDP need further investigation. Our results indicate that down-regulation of ALKBH2 in cDDP-treated H1299 cells alters the expression of basic fibroblast growth factor (*bFGF*), platelet-derived growth factor (*PDGFA, PDGFB*) and Bcl-2. bFGF, an angiogenic cytokine produced by tumor cells, affects vessel formation, tumor growth, invasion and metastasis, and down-regulated bFGF may inhibit tumor growth[23]. Cell-surface receptor tyrosine kinases play pivotal roles in different diseases, ranging from cancer to vascular disorders, so disruption of PDGF signaling pathways could inhibit tumor stromogenesis[24]. Bcl-2 family proteins regulate the propagation of apoptotic signals and cell survival and are divided into two subclasses: antiapoptotic members including Bal-2, Mcl-1, Bcl-XL, and Bcl2A1 and proapoptotic members including Bax and Bak[25]. Down-regulation of ALKBH2 in the cDDP-treated H1299 cells led to increased Bax expression and decreased *bFGF*, *PDGFA,* and *PDGFB* expression. Therefore, the regulation of these genes may be the mechanism underlying the enhanced anti-tumor effect of cDDP in combination with ALKBH2 inhibition in NSCLC therapy.

In conclusion, we demonstrate that lentivirus-mediated ALKBH2 knockdown enhances the sensitivity of human H1299 cells to cDDP-based chemotherapy. As a result of this additive efficacy of ALKBH2 gene inhibition and chemotherapy on cell death and cell proliferation in NSCLC cells, this combined treatment modality has the potential to improve the anticancer efficacy of cDDP.

Acknowledgements

This work was supported by a grant from the National Natural Science Foundation of China (No 30971320).

Author contribution

Shuang-shuang WU and Jian-qing WU designed the research; Shuang-shuang WU, Wei XU, Xue-li WANG, Yan WANG, and Shi-feng LIU performed the research; Shuang-shuang WU, Wei XU, Shan LIU, Bo CHEN, and Jian-qing WU analyzed the data and wrote the paper.

References

1 Jemal A, Siegel R, Ward E, Murray T, Xu J, Thun MJ. Cancer statistics, 2007. CA Cancer J Clin 2007; 57: 43–66.
2 Pfister DG, Johnson DH, Azzoli CG, Sause W, Smith TJ, Baker S Jr, *et al*. American Society of Clinical Oncology treatment of unresectable non-small cell lung cancer guideline: update 2003. J Clin Oncol 2004; 22: 330–53.
3 Ramalingam S, Belani C. Systemic chemotherapy for advanced non-small cell lung cancer: recent advances and future directions. Oncologist 2008; 13: 5–13.
4 Oliver TG, Mercer KL, Sayles LC, Burke JR, Mendus D, Lovejoy KS, *et al*. Chronic cisplatin treatment promotes enhanced damage repair and tumor progression in a mouse model of lung cancer. Genes Dev 2010; 24: 837–52.
5 Marcu L, Bezak E, Olver I, van Doorn T. Tumour resistance to cisplatin: a modelling approach. Phys Med Biol 2005; 50: 93–102.
6 Stordal B, Davey M. Understanding cisplatin resistance using cellular models. IUBMB Life 2007; 59: 696–9.
7 Aravind L, Koonin EV. The DNA-repair protein AlkB, EGL-9, and leprecan define new families of 2-oxoglutarate- and iron-dependent dioxygenases. Genome Biol 2001; 2: RESEARCH0007.
8 Sedgwick B. Repairing DNA-methylation damage. Nat Rev Mol Cell Biol 2004; 5: 148–57.
9 Mishina Y, He C. Oxidative dealkylation DNA repair mediated by the monomuclear non-heme iron AlkB proteins. J Inorg Biochem 2006; 100: 670–8.
10 Kurowski MA, Bhagwat AS, Papaj G, Bujnicki JM. Phylogenomic identification of five new human homologs of the DNA repair enzyme AlkB. BMC Genomics 2003; 4: 48.
11 Yang CG, Yi C, Duguid EM, Sullivan CT, Jian X, Rice PA, *et al*. Crystal structures of DNA/RNA repair enzymes AlkB and ABH2 bound to dsDNA. Nature 2008; 452: 961–5.
12 Duncan T, Trewick SC, Koivisto P, Bates PA, Lindahl T, Sedgwick B. Reversal of DNA alkylation damage by two human dioxygenases. Proc Natl Acad Sci USA 2002; 99: 16660–5.
13 Aas PA, Otterlei M, Falnes PO, Vågbø CB, Skorpen F, Akbari M, *et al*. Human and bacterial oxidative demethylases repair alkylation damage in both RNA and DNA. Nature 2003; 421: 859–63.
14 Lee DH, Jin SG, Cai S, Chen Y, Pfeifer GP, O'Connor TR. Repair of methylation damage in DNA and RNA by mammalian AlkB homologues. J Biol Chem 2005; 280: 39448–59.
15 Xu Y, Wang Z, Wang J, Li J, Wang H, Yue W. Lentivirus-mediated knockdown of cyclin Y (CCNY) inhibits glioma cell proliferation. Oncol Res 2010; 18: 359–64.
16 Blandino G, Levine AJ, Oren M. Mutant p53 gain of function: differential effects of different p53 mutants on resistance of cultured cells to chemotherapy. Oncogene 1999; 18: 477–85.
17 Fisher DE. Apoptosis in cancer therapy: crossing the threshold. Cell 1994; 78: 539–42.
18 Pomeroy M, Moriarty M. Clinical significance of cellular resistance in tumours to cytotoxic chemotherapy and radiotherapy. Cytotechnology 1993; 12: 385–91.
19 Murdoch D, Sager J. Will targeted therapy hold its promise? An evidence-based review. Curr Opin Oncol 2008; 20: 104–11.
20 Yang CT, Li JM, Weng HH, Li YC, Chen HC, Chen MF. Adenovirus-mediated transfer of siRNA against survivin enhances the radiosensitivity of human non-small cell lung cancer cells. Cancer Gene Therapy 2010; 17: 120–30.
21 Oh S, Kim Y, Kim J, Kwon D, Lee E. Elevated pressure, a novel cancer therapeutic tool for sensitizing cisplatin-mediated apoptosis in A549. Biochem Biophys Res Commun 2010; 399: 91–7.
22 Siddik ZH. Cisplatin: mode of cytotoxic action and molecular basis of resistance. Oncogene 2003; 22: 7265–79.
23 Bremnesa RM, Campsc C, Sirerac R. Angiogenesis in non-small cell lung cancer: The prognostic impact of neoangiogenesis and the cytokines VEGF and bFGF in tumours and blood. Lung Cancer 2006; 51: 143–58.
24 Andrae J, Gallini R, Betsholtz C. Role of platelet-derived growth factors in physiology and medicine. Gene Dev 2008; 22: 1276–312.
25 Vogler M, Dinsdale D, Dyer MJ, Cohen GM. Bcl-2 inhibitors: small molecules with a big impact on cancer therapy. Cell Death Differ 2009; 16: 360–7.

Acta Pharmacologica Sinica (2011) 32: 399–407
© 2011 CPS and SIMM All rights reserved 1671-4083/11 $32.00
www.nature.com/aps

Original Article

Substrate-dependent modulation of the catalytic activity of CYP3A by erlotinib

Pei-pei DONG[1, 2], Zhong-ze FANG[1, 2], Yan-yan ZHANG[1], Guang-bo GE[1], Yu-xi MAO[1, 2], Liang-liang ZHU[1, 2], Yan-qing QU[3], Wei LI[1, 2], Li-ming WANG[3], Chang-xiao LIU[4], Ling YANG[1, *]

[1]Laboratory of Pharmaceutical Resource Discovery, Dalian Institute of Chemical Physics, Chinese Academy of Sciences, Dalian 116023, China; [2]Graduate University of Chinese Academy of Sciences, Beijing 100049, China; [3]the Second Affiliated Hospital of Dalian Medical University, Dalian 116027, China; [4]Tianjin Key Laboratory of Pharmacokinetics and Clinical Pharmacology, Tianjin Institute of Pharmaceutical Research, Tianjin 300193, China

---

Aim: To ascertain the effects of erlotinib on CYP3A, to investigate the amplitude and kinetics of erlotinib-mediated inhibition of seven major CYP isoforms in human liver microsomes (HLMs) for evaluating the magnitude of erlotinib in drug-drug interaction *in vivo*.
Methods: The activities of 7 major CYP isoforms (CYP1A2, CYP2A6, CYP3A, CYP2C9, CYP2D6, CYP2C8, and CYP2E1) were assessed in HLMs using HPLC or UFLC analysis. A two-step incubation method was used to examine the time-dependent inhibition of erlotinib on CYP3A.
Results: The activity of CYP2C8 was inhibited with an IC_{50} value of 6.17±2.0 μmol/L. Erlotinib stimulated the midazolam 1′-hydroxy reaction, but inhibited the formation of 6β-hydroxytestosterone and oxidized nifedipine. Inhibition of CYP3A by erlotinib was substrate-dependent: the IC_{50} values for inhibiting testosterone 6β-hydroxylation and nifedipine metabolism were 31.3±8.0 and 20.5±5.3 μmol/L, respectively. Erlotinib also exhibited the time-dependent inhibition on CYP3A, regardless of the probe substrate used: the value of K_I and k_{inact} were 6.3 μmol/L and 0.035 min^{-1} for midazolam; 9.0 μmol/L and 0.045 min^{-1} for testosterone; and 10.1 μmol/L and 0.058 min^{-1} for nifedipine.
Conclusion: The inhibition of CYP3A by erlotinib was substrate-dependent, while its time-dependent inhibition on CYP3A was substrate-independent. The time-dependent inhibition of CYP3A may be a possible cause of drug-drug interaction, suggesting that attention should be paid to the evaluation of erlotinib's safety, especially in the context of combination therapy.

Keywords: erlotinib; CYP isoform; human liver microsomes; substrate-dependent inhibition (or modulation); drug interaction

Acta Pharmacologica Sinica (2011) 32: 399–407; doi: 10.1038/aps.2010.218

Introduction

Erlotinib (Tarceva; Genentech Inc, San Francisco, CA, USA) is an orally available, reversible human epidermal growth factor receptor (EGFR) tyrosine kinase inhibitor[1, 2]. It received approval from the US Food and Drug Administration in November 2004 for the second-line treatment of locally advanced or metastatic non-small cell lung cancer after the failure of at least 1 previous chemotherapeutic regimen[3, 4]. Erlotinib was also approved by the United States for the treatment of locally advanced, unresectable or metastatic pancreatic cancer in combination with gemcitabine[5]. In addition, clinical trials in a number of other solid tumors are also underway[6–8].

Erlotinib is considered better tolerated and less toxic than cytotoxic drugs, with the most common adverse reactions in patients being rash and diarrhea[9]. However, erlotinib is frequently involved in clinical drug-drug interactions (DDIs). With 45 interactions reported before 2007, the DDI frequency of erlotinib was just second to that of ifosfamide and paclitaxel among all antineoplastic drugs[10]. Co-administration of erlotinib has been reported to enhance carboplatin exposure[11] and increase the serum concentration of phenytoin[12]. A case of rhabdomyolysis was reported due to the interaction of erlotinib with simvastatin[13]. International Normalized Ratio (INR) elevations and bleeding events associated with erotinib-warfarin co-administration have been reported[4]. Because the drugs involved usually had narrow therapeutic indices, DDIs might impair the clinical safety of erlotinib.

One of the major reasons for clinical DDIs has been recognized to be inhibition or induction of drug metabolism enzymes. Erlotinib is extensively metabolized, predominantly by CYP3A4/5 and to a lesser extent by CYP1A2 and the

---

[*] To whom correspondence should be addressed.
E-mail yling@dicp.ac.cn

Received 2010-06-04 Accepted 2010-12-02

extrahepatic isoform CYP1A1[14]. As for the influence of erlotinib on the catalytic activity of CYP3A, conflicting data have been published concerning its clinical consequences. Li *et al* found that erlotinib stimulated CYP3A-mediated midazolam metabolism in liver and intestinal microsomes[15]. Nevertheless, in a cell-based CYP3A activity assay, erlotinib was shown to decrease the formation of 1′-hydroxymidazolam, showing the potency to inhibit CYP3A activity[16]. As for the phase II enzymes, erlotinib was shown to exhibit inhibition activity on human UDP-glucuronosyltransferase (UGT) 1A1[17]. The effects of erlotinib on other phase I CYP isoforms are still unknown. Thus, the current data were insufficient to explain the widespread DDI cases. Ascertaining the effect of erlotinib on major CYP isoforms will benefit the clinical safety evaluation of erlotinib in combination with other drugs.

The aim of this study was to ascertain the effect of erlotinib on CYP3A activity and to investigate the amplitude and kinetics of erlotinib-mediated inhibition of seven major CYP isoforms in HLMs. An *in vivo* magnitude of interaction will be extrapolated from the *in vitro* inhibition kinetic data to help explain the clinical DDIs associated with erlotinib.

Materials and methods

Chemicals and reagents

Erlotinib (OSI-774, >99%) was purchased from Nanjing Ange Pharmaceutical Co, Ltd (Nanjing, China). *D*-glucose-6-phosphate, glucose-6-phosphate dehydrogenase, NADP$^+$, corticosterone, phenacetin, acetaminophen, 7-hydroxycoumarin, 4′-hydroxydiclofenac, sulfaphenazole, 8-methoxypsoralen, clomethiazole, montelukast, nifedipine, oxidized nifedipine, midazolam, 1′-OH-midazolam, troleandomycin (TAO), 6-hydroxychlorzoxazone, 7-hydroxycoumarin, paclitaxel, 6β-hydroxytestosterone and furafylline were purchased from Sigma-Aldrich (St Louis, MO, USA). Testosterone was from Acros Organics (Morris Plains, NJ, USA). Coumarin, diclofenac, dextromethorphan and ketoconazole were from ICN Biomedicals (Aurora, OH, USA). Human liver microsomes (HLMs) were prepared according to the method described by Guengerich (1989) and other previous reports[18, 19]. Protein concentrations were determined using bovine serum albumin as a standard[20]. Millipore water (Millipore, Bedford, MA, USA) and HPLC grade methanol and acetonitrile (Tedia, Fairfield, OH, USA) were used throughout; other reagents were of the highest grade commercially available.

Probe substrate assays for major CYP isoforms

Probe reactions for CYP3A, CYP1A2, CYP2C8, CYP2A6, CYP2C9, CYP2D6, and CYP2E1 were testosterone 6β-hydroxylation, phenacetin *O*-demethylation, paclitaxel 6α-hydroxylation, coumarin 7-hydroxylation, diclofenac 4′-hydroxylation, dextromethorphan *O*-demethylation and chlorzoxazone 6-hydroxylation activities separately. Midazolam 1′-hydroxylation and nifedipine oxidation reactions were also performed to examine the effect of erlotinib on CYP3A activity. The basic incubation system contained 100 mmol/L potassium phosphate buffer (pH 7.4), a NADPH-generating system (1 mmol/L NADP$^+$, 10 mmol/L glucose-6-phosphate, 1 unit/mL of glucose-6-phosphate dehydrogenase and 4 mmol/L $MgCl_2$) and the appropriate concentrations of HLMs, the appropriate probe substrate and erlotinib (or a positive control inhibitor) in a final volume of 200 μL. After a 3-min preincubation at 37 °C, the reaction was initiated by adding the NADPH-generating system and terminated by adding 100 μL acetonitrile (10% trichloroacetic acid for CYP2A6) with internal standard. The mixture was centrifuged at 20 000×*g* for 10 min, and an aliquot of supernatant was then transferred to a 0.3-mL auto-injector vial for HPLC or UFLC analysis. The incubation conditions, including substrate and protein concentrations and incubation times, have been reported[21, 22]. The HPLC system (SHIMADZU, Kyoto, Japan) consisted of a SCL-10A system controller, two LC-10AT pumps, a SIL-10A autoinjector, and a SPD-10AVP UV detector or a RF-10AXL fluorescence detector. HPLC separation was achieved using a C18 column (150 mm×4.6 mm ID, 5 μm, Shimadzu) at a flow rate of 1 mL/min. A Shimadzu Prominence UFLC^{TM} system with a Shim-pack XR-ODS (75.0 mm×2.0 mm ID, 2.2 μm, Shimadzu) analytical column was used. The eluent flow rate was 0.3 mL/min and the column temperature was maintained at 40 °C. Analysis conditions for the P450 isoforms are shown in Table 1. All analytical methods were shown to be precise and accurate. The intra- and inter-day precisions were less than 15%, with accuracy in the range of 86.7%–112.5%[19, 21–23].

Enzyme inhibition experiments

Marker assays for each CYP isoform were performed in the presence of 100 μmol/L erlotinib to evaluate its inhibitory effect toward the seven major human CYP isoforms. The concentrations of positive control inhibitors used are as follows[21, 24, 25]: 1 μmol/L ketoconazole for CYP3A, 10 μmol/L furafylline for CYP1A2, 10 μmol/L sulfaphenazole for CYP2C9, 5 μmol/L montelukast for CYP2C8, 2.5 μmol/L 8-methoxypsoralen for CYP2A6, 10 μmol/L quinidine for CYP2D6 and 50 μmol/L clomethiazole for CYP2E1. For CYP isoforms that were strongly inhibited, the concentrations at which the enzymes were 50% inhibited (IC_{50} values) were determined using various concentrations of erlotinib for CYP3A and for CYP2C8. Inhibition constant (K_i) values were determined by incubating various probe substrates (5–50 μmol/L paclitaxel, 30–100 μmol/L testosterone or 5–50 μmol/L nifedipine) in the presence or absence of erlotinib. K_i values were calculated by nonlinear regression using the equations for competitive inhibition (eq 1), noncompetitive inhibition (eq 2), or mixed inhibition (eq 3)[17].

$$v=(V_{\max}S)/(K_m\ (1+I/K_i)+S) \tag{1}$$

$$v=(V_{\max}S)/(K_m+S)(1+I/K_i) \tag{2}$$

$$v=(V_{\max}S)/(K_m+S)(1+I/\alpha K_i) \tag{3}$$

Activation of midazolam metabolism by erlotinib

Midazolam was incubated in pooled HLMs (0.1 mg/mL) for 10 min in the presence or absence of erlotinib. To investigate

Table 1. Analysis conditions for the relevant P450 isoforms.

CYPs	Internal standard concentration (μmol/L)	Mobile phase gradient	Detection
1A2	7-Hydroxycoumarin (30 μmol/L)	Methanol (A): Phosphate buffer (pH=3.0, 50 mmol/L) (B)=34:66	HPLC, UV 245 nm
2A6	–	Acetonitrile (A): Acetic acid (0.1%, *v/v*) (B)=35:65	HPLC, Fluo E_x/E_m: 340 nm/456 nm
2C9	Coumarin (60 μmol/L)	Acetonitrile (A): Phosphate buffer (pH=7.4, 100 mmol/L) (B)=32:68, 0–9 min, 68%B–32%B	HPLC, UV 280 nm
2D6	–	Acetonitrile (A): Phosphate buffer (pH=3.0, 50 mmol/L) (B)=25:75	HPLC, Fluo E_x/E_m: 235 nm/310 nm
2E1	Phenacetin (300 μmol/L)	Acetonitrile (A): Acetic acid (0.5%, *v/v*) (B)=22:78, 1–10 min, 78%B–40%B	HPLC, UV 287 nm
3A4 (Testosterone)	Corticosterone (20 μmol/L)	Methanol (A): Water (B)=52:48, 0–15 min, 48%B–30%B; 15–22 min, 30%B–20%B	HPLC, UV 254 nm
3A4 (Nifedipine)	–	Methanol (A): Water (B)=50:50, 0–20 min, 50%B–45%B	HPLC, UV 250 nm
3A4 (Midazolam)		Methanol (A): Acetic acid (0.5%, *v/v*) (B)=40:60, 0–10 min, 60%B–20%B	UFLC, UV 254 nm
2C8		Methanol (A): Water (B)=0–2 min, 88%B–44% B; 2–4 min, 44%B–38%B; 4–9.5 min, 38%B–32%B	UFLC, UV 230 nm

the concentration dependence of midazolam metabolism activation phenomena, various concentrations of erlotinib (1–20 μmol/L) were incubated with midazolam at different concentrations (2–20 μmol/L). 1'-hydroxymidazolam was measured using a validated method based on UFLC as described in Table 1. To further explore the potential mechanism of activation phenomena, kinetic data were fit to a two-site model[26],

$$v=\frac{V_{\max}\times[S]}{K_m\frac{(1+\frac{[B]}{K_B})}{(1+\frac{\beta[B]}{\alpha K_B})}+[S]\frac{(1+\frac{[B]}{\alpha K_B})}{(1+\frac{\beta[B]}{\alpha K_B})}} \tag{4}$$

where S is the substrate, B is the effector, $V_{\max}$ and K_m are the kinetic constants for substrate metabolism, K_B is the binding constant for the effector, α is the change in K_m resulting from the effector binding, and β is the change in $V_{\max}$ from the effector binding. For activation, $\alpha<1$ and/or $\beta>1$.

Single point inactivation experiments

Single point inactivation experiments were used as previously reported to determine NADPH-dependent and preincubation-dependent inhibition by erlotinib[27]. Briefly, erlotinib was incubated with pooled HLMs (1 mg/mL) in the absence and presence of the NADPH-generating system for 30 min at 37 °C. For CYP3A and CYP2C8, the concentration of erlotinib utilized was ten times the concentration that gave 25% inhibition under conditions of reversible inhibition. For other CYP isoforms, 50 μmol/L of erlotinib was used. Moreover, midazolam was also used as a probe substrate to perform single point inactivation experiments for CYP3A, and 50 μmol/L of erlotinib was used. After incubation, an aliquot (20 μL) was transferred to another incubation tube (final volume 200 μL) containing an NADPH-generating system and probe substrates whose concentrations were proximal to K_m values. Further incubations were performed to measure residual activity.

Inactivation constant (K_I and k_{inact}) assays

To determine the K_I and k_{inact} values for the inactivation of CYP3A, five concentrations of erlotinib (0, 5, 10, 20 and 50 μmol/L) were incubated for 0 to 30 min with pooled HLMs (1 mg/mL) at 37 °C. After preincubation, an aliquot (20 μL) was transferred to another incubation tube (final volume 200 μL) containing an NADPH-generating system and different probe substrates for CYP3A to measure residual activity. Substrate concentrations of four times the K_m were selected to minimize the reversible inhibition caused by erlotinib. The concentrations used for different probe substrates were as follows: 400 μmol/L testosterone, 20 μmol/L midazolam and 60 μmol/L nifedipine. To determine the k_{obs} (observed inactivation rate) values, the decrease in natural logarithm of the activity over time was plotted for each erlotinib concentration, and the k_{obs} values were described as the negative slopes of the lines. Inactivation kinetic parameters were calculated using nonlinear regression of the data according to equation (5):

$$k_{obs}=\frac{k_{inact}\times[I]}{K_I+[I]} \tag{5}$$

$$K_{I,u}=K_I\times f_{u,m} \tag{6}$$

$$f_{u,m}=\frac{1}{(C_{mic}\times 10^{0.56\text{LogP}-1.41})+1} \tag{7}$$

where [I] is the initial inhibitor concentration, k_{inact} is the maximal inactivation rate constant and K_I is the inhibitor concentration required for half the maximal rate of inactivation. The unbound K_I ($K_{I,u}$) was calculated according to equation (6), where $f_{u,m}$ is the free fraction of erlotinib in the microsomes. $f_{u,m}$ is predicted according to equation (7) as previously reported[28]. The terms are defined as follows: C_{mic} is the microsomal protein concentration used in the preincubation, and logP is the log of the octanol-water (pH 7.4) partition (P) coefficient of the erlotinib. A concentration of 1 mg/mL was used for C_{mic} in this experiment, and LogP is approximately

2.7, according to the literature[4]. Thus, $f_{\mathrm{u,\,m}}$ is calculated to be 44.2%.

Quantitative prediction of the DDI potential of erlotinib ($\mathrm{AUC_i}$/AUC)

The equations (8) and (9) were utilized to predict the interaction potential of erlotinib caused by reversible inhibition and TDI of CYP3A. Equation (10) was used to predict the interaction potential by reversible inhibition of CYP2C8. All equations were adapted as reported[27, 29].

$$\frac{\mathrm{AUC_i}}{\mathrm{AUC}}=\frac{1}{1-f_{\mathrm{m(CYP3A)}}+\dfrac{f_{\mathrm{m(CYP3A)}}}{1+\dfrac{[\mathrm{I}]_{in\ vivo}}{K_{\mathrm{i}}}}} \tag{8}$$

$$\frac{\mathrm{AUC_i}}{\mathrm{AUC}}=\frac{1}{\dfrac{f_{\mathrm{m(CYP3A)}}}{1+\dfrac{k_{\mathrm{inact}}\times[\mathrm{I}]_{in\ vivo}}{K_{\mathrm{I,\,u}}\times k_{\mathrm{deg(CYP3A)}}}}+(1-f_{\mathrm{m(CYP3A)}})} \tag{9}$$

$$\frac{\mathrm{AUC_i}}{\mathrm{AUC}}=\frac{1}{1-f_{\mathrm{m(CYP2C8)}}+\dfrac{f_{\mathrm{m(CYP2C8)}}}{1+\dfrac{[\mathrm{I}]_{in\ vivo}}{K_{\mathrm{i}}}}} \tag{10}$$

The terms are defined as follows: $\mathrm{AUC_i}$/AUC is the predicted ratio of *in vivo* exposure of the interacting drug with co-administration of erlotinib *versus* that in the control situation, $f_{\mathrm{m(CYP3A)}}/f_{\mathrm{m(CYP2C8)}}$ is the portion of total clearance of the interacting drug to which CYP3A/CYP2C8 contributes, $k_{\mathrm{deg(CYP3A)}}$ is the first-order rate constant of *in vivo* degradation of CYP3A, k_{inact} is the maximum inactivation rate constant, $K_{\mathrm{I,\,u}}$ is the unbound K_{I}, K_{i} is the reversible inhibition constant, and $[\mathrm{I}]_{in\ vivo}$ is the *in vivo* concentration of erlotinib at the enzyme active site. The general assumption is that only unbound drug is available for interaction with the enzyme active site. However, at present, there is no consensus on the *in vivo* precipitant concentration that should be used. According to a recent publication, the reversible inhibition portion performed the best when the unbound portal vein concentration was used for $[\mathrm{I}]_{in\ vivo}$, while for irreversible inactivation and induction the unbound systemic concentration was the best. Thus, in this research, the unbound portal vein concentration (0.16, 0.18, and 0.31 μmol/L) was used for the reversible inhibition portion (for 50, 100, and 150 mg/d doses, respectively), while the unbound systemic concentration (0.07, 0.19, and 0.13 μmol/L) was adopted to avoid over-prediction of irreversible inactivation[30]. The values for $[\mathrm{I}]_{in\ vivo}$ were derived from references[17, 31]. A $k_{\mathrm{deg(CYP3A)}}$ of 0.000321 $\mathrm{min^{-1}}$ was adopted, in accordance with Obach *et al*[27]. The values of $f_{\mathrm{m(CYP3A)}}$ and $f_{\mathrm{m(CYP2C8)}}$ were arbitrarily set to be 0.1–1 to predict the DDI risk for all possible coadministered drugs[17].

Results

Inhibition of major CYP isoforms by erlotinib

Erlotinib with the concentration of 100 μmol/L inhibited the activities of CYP1A2, CYP2C9, CYP2A6, CYP2D6, CYP2C8, and CYP2E1 by 30.0%, 49.0%, 9%, 37%, 76%, and -7%, respectively. For CYP3A, 100 μmol/L erlotinib inhibited 69.3% and 71.6%, respectively, of the enzyme's testosterone 6β-hydroxylation and nifedipine oxidation activities. However, erlotinib stimulated the midazolam 1′-hydroxy activity by 171%. All positive control inhibitors strongly inhibited the corresponding probe reactions, with less than 20% of control activity remaining upon inhibition. Further kinetic analysis was conducted for CYP3A (testosterone 6β-hydroxylation, nifedipine oxidation) and CYP2C8 (paclitaxel 6α-hydroxylation), whose activities were inhibited by more than 50%. As shown in Figure 1, erlotinib inhibited testosterone 6β-hydroxylation in a concentration-dependent manner with an $\mathrm{IC_{50}}$ of 31.3±8.0 μmol/L. Lineweaver-Burk and Dixon plots showed that the inhibition of CYP3A by erlotinib was well fitted to a competitive model of inhibition. The K_{i} value was calculated to be 14.1±4.3 μmol/L using a nonlinear regression equation (eq 1). Erlotinib also inhibited the metabolism of nifedipine in a competitive manner with an $\mathrm{IC_{50}}$ of 20.5±5.3 μmol/L. A K_{i} value of 4.3±0.9 μmol/L was obtained by nonlinear fitting. The results demonstrated that erlotinib inhibited paclitaxel 6α-hydroxylation in a concentration-dependent manner, with an $\mathrm{IC_{50}}$ of 6.17±2.0 μmol/L. Lineweaver-Burk and Dixon plots suggested that erlotinib also competitively inhibited CYP2C8. The K_{i} value was calculated to be 5.8±1.9 μmol/L using a nonlinear regression equation (eq 1).

Activation of midazolam metabolism

As shown in Figure 2, using different concentrations of midazolam (2–20 μmol/L), erlotinib stimulated the formation of 1′-OH-midazolam. At a constant concentration of midazolam, the formation of 1′-OH-midazolam increased with increasing amounts of erlotinib (1–20 μmol/L). The two-site model fitting results are listed in Table 2. The data fit this model (Table 2) well with an α=0.50 and a β=1.80, indicating a decrease in K_{m} and an increase in V_{max}, respectively[32]. These results showed the existence of activation.

Time- and NADPH-dependent inhibitions

When erlotinib was pre-incubated with HLMs for 30 min in the presence of NADPH, the percentage of inhibition on CYP3A by erlotinib increased significantly compared with that without NADPH (using testosterone and nifedipine as

Table 2. Kinetic parameter estimates derived from two-site model for midazolam metabolism in the presence of erlotinib.

Substrate	Effector	V_{max}	K_{m}	K_{B}	α	β	$\mathrm{R^2}$
Midazolam	Erlotinib	0.34 (0.03)	2.63 (0.93)	7.96 (5.9)	0.50 (0.33)	1.80 (0.27)	0.93

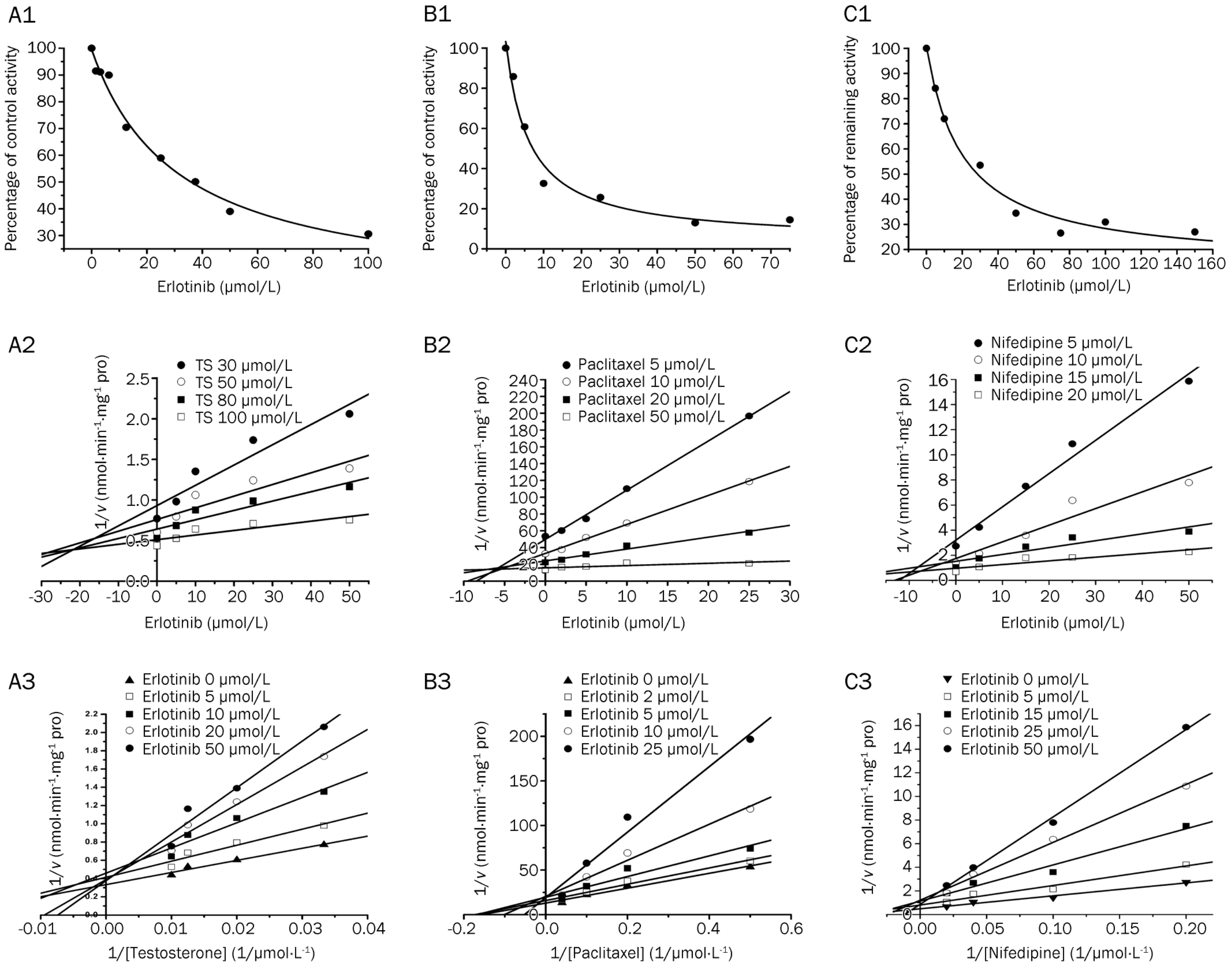

Figure 1. Reversible inhibition of CYP3A and CYP2C8 by erlotinib. A1: Inhibition by erlotinib of testosterone 6β-hydroxylation activity. A2: Dixon plot of the inhibitory effect of erlotinib on testosterone 6β-hydroxylation (TS) activity. A3: Lineweaver-Burk plot of the inhibitory effect of erlotinib on testosterone 6β-hydroxylation activity. B1: Inhibition by erlotinib of paclitaxel 6α-hydroxylation activity. B2: Dixon plot of the inhibitory effect of erlotinib on paclitaxel 6α-hydroxylation activity. B3: Lineweaver-Burk plot of the inhibitory effect of erlotinib on paclitaxel 6α-hydroxylation activity. C1: Inhibition by erlotinib of nifedipine oxidation activity. C2: Dixon plot of the inhibitory effect of erlotinib on nifedipine oxidation activity. C3: Lineweaver-Burk plot of the inhibitory effect of erlotinib on nifedipine oxidation activity.

probe substrates). When midazolam was used as a probe substrate, interesting results were obtained (Figure 3). When NADPH was not present during the preincubation process, erlotinib stimulated the metabolism of midazolam, but when NADPH was added to the preincubation, erlotinib showed an inhibitory effect on the activity of CYP3A. Inactivation kinetic parameters were obtained using different probe substrates. As calculated from the observed inactivation plots (Figure 4), inactivation parameters (K_I and k_{inact}, respectively) for CYP3A were calculated to be 6.3 μmol/L and 0.035 min^{-1}, 9.0 μmol/L and 0.045 min^{-1}, 10.1 μmol/L and 0.058 min^{-1} for the probe substrates midazolam, testosterone and nifedipine, respectively. The inhibition of other isoforms by erlotinib was not time and NADPH dependent (data not shown).

In vitro-in vivo extrapolation of DDI magnitudes

For reversible inhibition of CYP2C8, adopting a K_i of 5.8 μmol/L and unbound portal vein concentrations of 0.16, 0.18, and 0.31 μmol/L for 50, 100, and 150 mg/d doses, respectively, the AUC$_i$/AUCs were predicted to be 1.0027–1.0276, 1.0030–1.0310 and 1.0051–1.0534 for an f_m value between 0.1 and 1. For reversible inhibition of CYP3A (with the probe substrate testosterone), using a K_i of 14.1 μmol/L and the same unbound portal vein concentrations as for CYP2C8, the AUC$_i$/AUCs were predicted to be 1.0011–1.0113, 1.0013–1.0128, and 1.0022–1.0220 for an f_m value between 0.1 and 1, for 50, 100, and 150 mg/d doses, respectively. For the probe substrate nifedipine, using a K_i of 4.3 μmol/L and the same unbound portal vein concentration, the corresponding results of AUC$_i$/

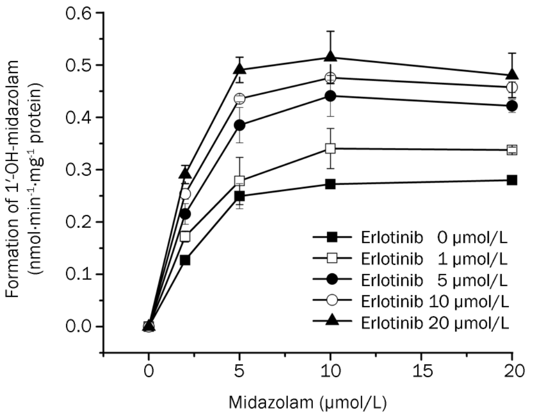

Figure 2. Activation of midazolam 1′-hydroxylation by 1–20 μmol/L erlotinib.

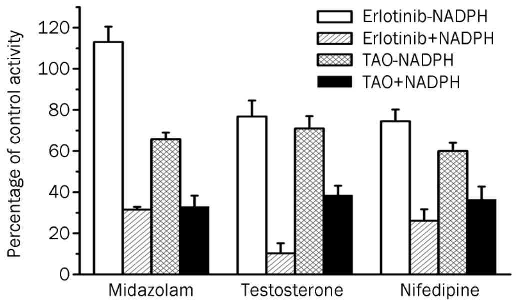

Figure 3. Single point inactivation of CYP3A by erlotinib measured using midazolam, testosterone and nifedipine as probe substrates in HLM. The concentrations for erlotinib were 50 μmol/L, 75 μmol/L and 75 μmol/L when using midazolam, testosterone and nifedipine as probe substrates, respectively. The concentration of the positive control inhibitor TAO was 250 μmol/L. Each data point represents the mean±SD of duplicate incubations.

AUCs were 1.0036–1.0372, 1.0040–1.0419, and 1.0068–1.0721 for an f_m value between 0.1 and 1, for 50, 100, and 150 mg/d doses, respectively. For irreversible inactivation of CYP3A (using different probe substrates), unbound systemic concentrations of 0.07, 0.13, and 0.19 μmol/L were adopted to avoid over-prediction for three oral doses[17]. With a $K_{I,u}$ and a k_{inact} of erlotinib for probe substrates midazolam, testosterone and

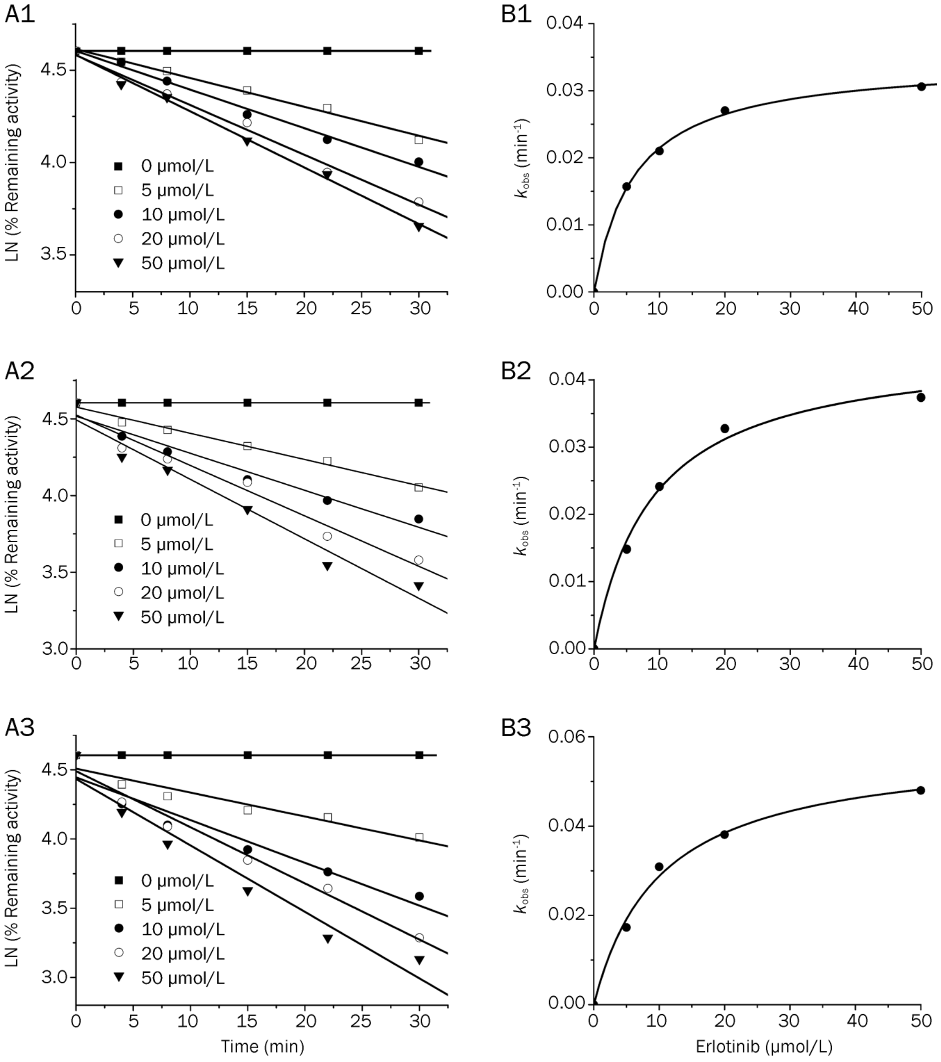

Figure 4. Time- and concentration-dependent inactivation of CYP3A by erlotinib. (A) At the indicated time points, the remaining CYP3A activity was measured by a midazolam 1′-hydroxylation (A1), testosterone 6β-hydroxylation (A2) or nifedipine oxidation (A3) assay. Each point represents the mean of triplicate incubations. The observed inactivation rate constants, k_{obs}, were calculated from the slopes of the regression lines in A. (B) The hyperbolic plot of k_{obs} *versus* erlotinib concentration was used to calculate kinetic constants.

nifedipine being 2.8 μmol/L and 0.035 min^{-1}, 4.0 μmol/L and 0.045 min^{-1} and 4.5 μmol/L and 0.058 min^{-1}, respectively, the AUC was calculated to increase to 107.9%–372.6%, 109.1%–606.2%, and 109.7%–839.9% for midazolam; 107.7%−345.3%, 108.9%–555.6%, and 109.5%–765.9% for testosterone; 108.0%–381.1%, 109.2%–622.0%, and 109.7%–862.9% for nifedipine.

Discussion

Human CYP3A is one of the most important CYP isoforms involved in drug clearance and metabolized more than 50% of the drugs on the market[33]. Inhibition or stimulation of the catalytic activity of this enzyme could play a key role in clinical DDIs. In previous studies, conflicting data were obtained about the effects of erlotinib on metabolism of the substrate midazolam mediated by CYP3A[34]. Thus, rigorously ascertaining erlotinib's effect on CYP3A will provide important information that may aid in the prevention of clinical DDIs. In this study, our experimental results showed that DDI patterns via modulation of CYP3A by erlotinib are substrate dependent. Erlotinib stimulated the formation of 1′-hydroxymidazolam in HLMs. However, it inhibited the reactions of testosterone 6β-hydroxylation and nifedipine oxidation. Erlotinib's time-dependent inhibition of CYP3A was not substrate dependent.

The patterns of interaction between drug compounds and CYP3A were previously shown to be substrate dependent[35]. For example, the flavonoid α-naphthoflavone, although well known to activate CYP3A4[36], may also inhibit the enzyme[37], depending on the CYP3A4 substrate. In a recent report, substrate-dependent phenomena were found for ginsenosides' effects on CYP3A[38]. Until now, the mechanism of substrate-dependent modulation of CYP3A activity remained unclear. The relatively large active site cavity and the conformational flexibility of CYP3A were considered the major causes of these phenomena[39, 40]. CYP3A can bind multiple ligands simultaneously, resulting in changes in the affinity of the substrate-binding site for different substrates[26]. This multiple ligand-binding property may contribute to the complex substrate-dependent effects, but whether conformational changes occurred simultaneously was unknown. In the case of erlotinib, further investigation was needed to explore the molecular and structural basis of these substrate-dependent effects.

The substrate-dependent effects of erlotinib on CYP3A point to the need for greater attention to the safety of combined medications. In the case of heteroactivation, the clearance of the interacting drug would increase. Alternatively, if erlotinib inhibited the metabolism of the interacting drug, the AUC of the latter drug would increase. In either case, a different DDI might occur and possibly cause harm to the patient. When substrate-dependent effects may be present, it is prudent to employ a testing strategy using several probe substrates to evaluate the DDI potential[41, 42]. Moreover, CYP3A4 and CYP3A5 are the most abundant members of the CYP3A subfamily. A recent study has shown significant differences between the heteroactivation potential of CYP3A4 and CYP3A5 for CYP3A-mediated carbamazepine 10,11-epoxidation[43]. Inhibitors of CYP3A usually have different potencies for inhibition of CYP3A4 and CYP3A5 in terms of both reversible and irreversible inhibition[44, 45]. Thus, the different expression levels of CYP3A4 and CYP3A5 may contribute to interindividual variability in erlotinib interactions.

The time-dependent inhibition of CYP3A was found to be substrate independent. After preincubation, erlotinib showed enhanced inhibition activity for the midazolam 1′-hydroxylation, testosterone 6β-hydroxylation and nifedipine oxidation reactions (Figure 3). The TDI parameters (K_I and k_{inact}) were 6.3 μmol/L and 0.035 min^{-1}, 9.0 μmol/L and 0.045 min^{-1} and 10.1 μmol/L and 0.058 min^{-1}, respectively, for the midazolam 1′-hydroxylation, testosterone 6β-hydroxylation and nifedipine oxidation reactions. When midazolam was used as the probe substrate, the following similar inactivation kinetic parameters were reported by Li *et al*[46]: k_{inact}=0.09 min^{-1} and K_I=22 μmol/L. The discrepancy in parameters may be due to the differences between labs. It should be noted that tyrosine kinase inhibitors such as dasatinib have been reported to inhibit CYPs via generation of reactive intermediates[47, 48]. Recently, the bioactivation of erlotinib was also reported; in that study, reactive epoxide and quinone-imine electrophiles were detected, providing a possible mechanism for the time dependent inhibition of CYP3A[46].

Based on the results shown above, the conflicting data about the effect of erlotinib on CYP3A can be explained as follows. First, without preincubation the action of erlotinib on CYP3A was substrate dependent (Figure 3). Erlotinib stimulated the formation of 1′-hydroxymidazolam[15]. Second, the time-dependent inhibition of CYP3A was actually substrate independent (Figure 3). In the cell-based CYP3A activity assessment method by Harmsen *et al*, the cells were cultured in medium containing erlotinib for two consecutive days before measurement of the formation of 1′-hydroxymidazolam[16]. During the 2-d culture period, time dependent inhibition of CYP3A could occur, thus decreasing the formation of 1′-hydroxy midazolam.

Using the kinetic information we obtained regarding the reversible and time-dependent inhibition of CYP enzymes, the *in vivo* DDI magnitude of erlotinib was extrapolated. For the reversible inhibition of CYP3A and 2C8, even using a dose of 150 mg/d and an f_m of 1, the increase in the AUC was predicted to be no more than 10%. On the contrary, the AUC was predicted to increase significantly even with the lower oral dose and the smaller f_m when adopting the TDI prediction equation. The DDI potential of erlotinib on phase II UDP-Glucuronosyltransferases has been evaluated previously[17]. The maximum increase in AUC was estimated to be less than 50% for drugs predominantly cleared by UGT1A1, even at a dose of 150 mg/d. Therefore, time-dependent inhibition of CYP3A might be one of the most important factors leading to clinical DDIs.

Conclusion

In conclusion, our results demonstrate that the action of erlotinib on CYP3A was substrate dependent. It stimulated the metabolism of midazolam and inhibited the formation of

6β-hydroxy testosterone and oxidized nifedipine. In contrast, the time-dependent inhibition of erlotinib on CYP3A was substrate-independent. Moreover, the time-dependent inhibition of CYP3A was a possible reason for clinical DDIs related to erlotinib. Cancer patients often receive multiple concurrent medications and should be carefully monitored for possible DDIs. A better understanding of the modulatory effects of erlotinib on the major CYP isoforms could inform clinical safety evaluations of drug combinations.

Acknowledgements

This work was supported by the National Natural Science Foundation of China (No 30630075, 30772608, 30973590, and 81072698), the National Key Technology R&D Program in the 11th Five-year Plan of China (No 2008ZX10002-019) and the National Science & Technology Pillar Program of China (No 2009BADB9B02).

Author contribution

Ling YANG and Pei-pei DONG designed research; Pei-pei DONG, Yu-xi MAO, Liang-liang ZHU, Yan-qing QU, and Wei LI performed research; Ling YANG, Chang-xiao LIU, and Li-ming WANG contributed new analytical tools and reagents; Pei-pei DONG, Zhong-ze FANG, Yan-yan ZHANG, and Guang-bo GE analyzed data; and Pei-pei DONG wrote the paper.

References

1 Ciardiello F, Tortora G. A novel approach in the treatment of cancer: Targeting the epidermal growth factor receptor. Clin Cancer Res 2001; 7: 2958–70.
2 Smith J. Erlotinib: Small-molecule targeted therapy in the treatment of non-small-cell lung cancer. Clin Ther 2005; 27: 1513–34.
3 Shepherd FA, Pereira JR, Ciuleanu T, Tan EH, Hirsh V, Thongprasert S, *et al*. Erlotinib in previously treated non-small-cell lung cancer. N Engl J Med 2005; 353: 123–32.
4 Cohen MH, Johnson JR, Chen YF, Sridhara R, Pazdur R. FDA drug approval summary: Erlotinib (Tarceva (R)) tablets. Oncologist 2005; 10: 461–6.
5 Moore MJ, Goldstein D, Hamm J, Figer A, Hecht JR, Gallinger S, *et al*. Erlotinib plus gemcitabine compared with gemcitabine alone in patients with advanced pancreatic cancer: a phase III trial of the National Cancer Institute of Canada clinical trials group. J Clin Oncol 2007; 25: 1960–6.
6 Vasey PA, Gore M, Wilson R, Rustin G, Gabra H, Guastalla JP, *et al*. A phase Ib trial of docetaxel, carboplatin and erlotinib in ovarian, fallopian tube and primary peritoneal cancers. Br J Cancer 2008; 98: 1774–80.
7 Lin CC, Calvo E, Papadopoulos KP, Patnaik A, Sarantopoulos J, Mita AC, *et al*. Phase I study of cetuximab, erlotinib, and bevacizumab in patients with advanced solid tumors. Cancer Chemother Pharmacol 2009; 63: 1065–71.
8 Thomas F, Rochaix P, White-Koning M, Hennebelle I, Sarini J, Benlyazid A, *et al*. Population pharmacokinetics of erlotinib and its pharmacokinetic/pharmacodynamic relationships in head and neck squamous cell carcinoma. Eur J Cancer 2009; 45: 2316–23.
9 Gridelli C, Rossi A, Malone P, Colantuoni G, Del Gaizo F, Ferrara C, *et al*. Erlotinib in non-small-cell lung cancer. Expert Opin Pharmacother 2007; 8: 2579–92.
10 Schwiertz V, Bertin C, Henry A, Charpiat B. Number and nature of drug interactions concerning antineoplastic drugs. Bull Cancer 2007; 94: 477–82.
11 Patnaik A, Wood D, Tolcher AW, Hamilton M, Kreisberg JI, Hammond LA, *et al*. Phase 1, pharmacokinetic, and biological study of erlotinib in combination with paclitaxel and carboplatin in patients with advanced solid tumors. Clin Cancer Res 2006; 12: 7406–13.
12 Grenader T, Gipps M, Shavit L, Gabizon A. Significant drug interaction: Phenytoin toxicity due to erlotinib. Lung Cancer 2007; 57: 404–6.
13 Veeraputhiran M, Sundermeyer M. Rhabdomyolysis resulting from pharmacologic interaction between erlotinib and simvastatin. Clin Lung Cancer 2008; 9: 232–34.
14 Ling J, Johnson KA, Miao Z, Rakhit A, Pantze MP, Hamilton M, *et al*. Metabolism and excretion of erlotinib, a small molecule inhibitor of epidermal growth factor receptor tyrosine kinase, in healthy male volunteers. Drug Metab Dispos 2006; 34: 420–6.
15 Li J, Zhao M, He P, Hidalgo M, Baker SD. Differential metabolism of gefitinib and erlotinib by human cytochrome P450 enzymes. Clin Cancer Res 2007; 13: 3731–7.
16 Harmsen S, Meijerman I, Beijnen JH, Schellens JHM. Nuclear receptor mediated induction of cytochrome P450 3A4 by anticancer drugs: a key role for the pregnane X receptor. Cancer Chemother Pharmacol 2009; 64: 35–43.
17 Liu Y, Ramirez J, House L, Ratain MJ. Comparison of the drug-drug interactions potential of erlotinib and gefitinib via inhibition of UDP-glucuronosyltransferases. Drug Metab Dispos 2010; 38: 32–9.
18 Zhang YY, Liu Y, Zhang JW, Ge GB, Liu HX, Wang LM, *et al*. C-7 configuration as one of determinants in taxanes metabolism by human cytochrome P450 enzymes. Xenobiotica 2009; 39: 903–14.
19 Liang SC, Ge GB, Liu HX, Zhang YY, Wang LM, Zhang JW, *et al*. Identification and characterization of human udp-glucuronosyltransferases responsible for the *in vitro* glucuronidation of daphnetin. Drug Metab Dispos 2010; 38: 973–80.
20 Lowry OH, Rosebrough NJ, Farr AL, Randall RJ. Protein measurement with the folin phenol reagent. J Biol Chem 1951; 193: 265–75.
21 Liu Y, Ma H, Zhang JW, Deng MC, Yang L. Influence of ginsenoside Rh-1 and F-1 on human cytochrome P450 enzymes. Planta Med 2006; 72: 126–31.
22 Zhang JW, Liu Y, Li W, Hao DC, Yang L. Inhibitory effect of medroxyprogesterone acetate on human liver cytochrome P450 enzymes. Eur J Clin Pharmacol 2006; 62: 497–502.
23 Dong PP, Ge GB, Zhang YY, Ai CZ, Li GH, Zhu LL, *et al*. Quantitative structure-retention relationship studies for taxanes including epimers and isomeric metabolites in ultra fast liquid chromatography. J Chromatogr A 2009; 1216: 7055–62.
24 Liu YT, Hao K, Liu XQ, Wang GJ. Metabolism and metabolic inhibition of gambogic acid in rat liver microsomes. Acta Pharmacol Sin 2006; 27: 1253–58.
25 Fang ZZ, Zhang YY, Ge GB, Huo H, Liang SC, Yang L. Time-dependent inhibition (TDI) of CYP3A4 and CYP2C9 by noscapine potentially explains clinical noscapine-warfarin interaction. Br J Clin Pharmacol 2010; 69: 193–9.
26 Korzekwa KR, Krishnamachary N, Shou M, Ogai A, Parise RA, Rettie AE, *et al*. Evaluation of atypical cytochrome P450 kinetics with two-substrate models: Evidence that multiple substrates can simultaneously bind to cytochrome P450 active sites. Biochemistry 1998; 37: 4137–47.
27 Obach RS, Walsky RL, Venkatakrishnan K. Mechanism-based inactivation of human cytochrome P450 enzymes and the prediction of drug-drug interactions. Drug Metab Dispos 2007; 35: 246–55.

28 Austin RP, Barton P, Cockroft SL, Wenlock MC, Riley RJ. The influence of nonspecific microsomal binding on apparent intrinsic clearance, and its prediction from physicochemical properties. Drug Metab Dispos 2002; 30: 1497–503.

29 Brown HS, Ito K, Galetin A, Houston JB. Prediction of *in vivo* drug-drug interactions from *in vitro* data: impact of incorporating parallel pathways of drug elimination and inhibitor absorption rate constant. Br J Clin Pharmacol 2005; 60: 508–18.

30 Fahmi OA, Hurst S, Plowchalk D, Cook J, Guo F, Youdim K, *et al*. Comparison of different algorithms for predicting clinical drug-drug interactions, based on the use of cyp3a4 *in vitro* data: predictions of compounds as precipitants of interaction. Drug Metab Dispos 2009; 37: 1658–66.

31 Yamamoto N, Horiike A, Fujisaka Y, Murakami H, Shimoyama T, Yamada Y, *et al*. Phase I dose-finding and pharmacokinetic study of the oral epidermal growth factor receptor tyrosine kinase inhibitor Ro50-8231 (erlotinib) in Japanese patients with solid tumors. Cancer Chemother Pharmacol 2008; 61: 489–96.

32 Hutzler JM, Kolwankar D, Hummel MA, Tracy TS. Activation of CYP2C9-mediated metabolism by a series of dapsone analogs: Kinetics and structural requirements. Drug Metab Dispos 2002; 30: 1194–200.

33 Rendic S. Summary of information on human CYP enzymes: Human P450 metabolism data. Drug Metab Rev 2002; 34: 83–448.

34 van Erp NP, Gelderblom H, Guchelaar HJ. Clinical pharmacokinetics of tyrosine kinase inhibitors. Cancer Treat Rev 2009; 35: 692–706.

35 Wang RW, Newton DJ, Liu N, Atkins WM, Lu AYH. Human cytochrome P-450 3A4: *In vitro* drug-drug interaction patterns are substrate-dependent. Drug Metab Dispos 2000; 28: 360–6.

36 Schwab GE, Raucy JL, Johnson EF. Modulation of rabbit and human hepatic cytochrome-p-450-catalyzed steroid hydroxylations by alpha-naphthoflavone. Mol Pharmacol 1988; 33: 493–9.

37 Yun CH, Wood M, Wood AJJ, Guengerich FP. Identification of the pharmacogenetic determinants of alfentanil metabolism-cytochrome p-450-3a4 — an explanation of the variable elimination clearance. Anesthesiology 1992; 77: 467–74.

38 Hao M, Zhao YQ, Chen PZ, Huang H, Liu H, Jiang HL, *et al*. Structure-activity relationship and substrate-dependent phenomena in effects of ginsenosides on activities of drug-metabolizing p450 enzymes. PLoS One 2008; 3: e2697.

39 Williams PA, Cosme J, Vinkovic DM, Ward A, Angove HC, Day PJ, *et al*. Crystal structures of human cytochrome P450 3A4 bound to metyrapone and progesterone. Science 2004; 305: 683–6.

40 Tracy TS. Atypical enzyme kinetics: Their effect on *in vitro-in vivo* pharmacokinetic predictions and drug interactions. Curr Drug Metab 2003; 4: 341-6.

41 Nomeir AA, Ruegg C, Shoemaker M, Favreau LV, Palamanda JR, Silber P, *et al*. Inhibition of CYP3A4 in a rapid microtiter plate assay using recombinant enzyme and in human liver microsomes using conventional substrates. Drug Metab Dispos 2001; 29: 748–53.

42 Grimm SW, Einolf HJ, Hall SD, He K, Lim HK, Ling KHJ, *et al*. The conduct of *in vitro* studies to address time-dependent inhibition of drug-metabolizing enzymes: a perspective of the pharmaceutical research and manufacturers of america. Drug Metab Dispos 2009; 37: 1355–70.

43 Henshall J, Galetin A, Harrison A, Houston JB. Comparative analysis of CYP3A heteroactivation by steroid hormones and flavonoids in different *in vitro* systems and potential *in vivo* implications. Drug Metab Dispos 2008; 36: 1332–40.

44 Gibbs MA, Thummel KE, Shen DD, Kunze KL. Inhibition of cytochrome P-450 3A (CYP3A) in human intestinal and liver microsomes: Comparison of K–I values and impact of CYP3A5 expression. Drug Metab Dispos 1999; 27: 180–7.

45 McConn DJ, Lin YS, Allen K, Kunze KL, Thummel KE. Differences in the inhibition of cytochromes P450 3A4 and 3A5 by metabolite-inhibitor complex-forming drugs. Drug Metab Dispos 2004; 32: 1083–91.

46 Li XH, Kamenecka TM, Cameron MD. Cytochrome P450-mediated bioactivation of the epidermal growth factor receptor inhibitor erlotinib to a reactive electrophile. Drug Metab Dispos 2010; 38: 1238–45.

47 Li X, Kamenecka TM, Cameron MD. Bioactivation of the epidermal growth factor receptor inhibitor gefitinib: implications for pulmonary and hepatic toxicities. Chem Res Toxicol 2009; 22: 1736–42.

48 Li XH, He YJ, Ruiz CH, Koenig M, Cameron MD. Characterization of dasatinib and its structural analogs as cyp3a4 mechanism-based inactivators and the proposed bioactivation pathways. Drug Metab Dispos 2009; 37: 1242–50.

npg Acta Pharmacologica Sinica (2011) 32: 408–414
© 2011 CPS and SIMM All rights reserved 1671-4083/11 $32.00
www.nature.com/aps

Original Article

Pharmacodynamic and pharmacokinetic study of pegylated liposomal doxorubicin combination (CCOP) chemotherapy in patients with peripheral T-cell lymphomas

Yun FAN[1], Neng-ming LIN[2, *], Lü-hong LUO[1], Luo FANG[2], Zhi-yu HUANG[1], Hai-feng YU[1], Feng-qin WU[1]

[1]*Department of Chemotherapy Center, Zhejiang Cancer Hospital, Hangzhou 310022, China*; [2]*Laboratory of Clinical Pharmacy, Zhejiang Cancer Hospital, Hangzhou 310022, China*

Aim: To investigate the pharmacodynamic and pharmacokinetic parameters of pegylated liposomal doxorubicin (PLD) combined with cyclophosphamide, vincristine, and prednisolone in patients with peripheral T-cell lymphomas (PTCL).
Methods: Seven chemonaive patients and four patients with relapsed peripheral T-cell lymphomas were treated with a CCOP regimen consisting of an intravenous administration of cyclophosphamide (750 mg/m^2), vincristine (1.4 mg/m^2), and PLD (30 mg/m^2) on d 1, as well as an oral administration of prednisolone (60 mg/m^2) on d 1–5. This regimen was repeated every 3 weeks for six cycles, and the clinical response and toxicity of the regimen were monitored. In addition, the plasma concentration of PLD at different time points was determined before and after treatment. The pharmacokinetics (PKs) software was used to estimate the pharmacokinetic parameters of PLD.
Results: The 11 PTCL patients received 35 treatment cycles. Three of them achieved complete response (CR), two partial response (PR), four stable disease (SD), and two progressive disease (PD). The overall response rate (ORR) was 45.5%, and the CR rate was 27.3%. In the 7 chemonaive patients, three achieved CR, two PR, one SD, and one PD. The ORR was 71.4%, and CR rate was 42.9%. The median follow-up time was 15 months, but 6 out of 11 patients were dead at the time of data analysis. The 1-year overall survival rate was 45.5%, and the median progression-free survival (PFS) rate was 6.5 [95% confidence interval (95% CI) 3.17–19.02] with a survival rate of 11.5 months (95% CI 6.65–16.36). The main toxicity was myelosuppression. Oral mucositis and hand-foot syndrome seldom occurred. The PLD plasma concentration from nine patients ranged from 1.7036 to 9.2207 mg·L^{-1} after administration of the CCOP regimen (0–168 h). The pharmacokinetic parameters AUC$_{0-\infty}$, CL, $t_{1/2}$, and V_d were 910.76 mg/L·h, 0.043 L·h^{-1}·m^{-2}, 68.40 h, and 3.56 L/m^2, respectively.
Conclusion: The CCOP regimen was effective and well tolerated in patients with peripheral T-cell lymphomas. The results of the pharmacokinetic parameters showed that PLD had long retention time in blood circulation.

Keywords: pegylated liposomal doxorubicin; peripheral T-cell lymphomas; pharmacodynamics; pharmacokinetics; cyclophosphamide; vincristine; prednisolone

---

Acta Pharmacologica Sinica (2011) 32: 408–414; doi: 10.1038/aps.2010.217

Introduction

Peripheral T-cell lymphomas (PTCL) are a group of rare and heterogeneous non-Hodgkin lymphoma (NHL), which have a poor prognosis and low survival rate[1]. The 5-year overall survival (OS) for common subtypes of PTCL, such as PTCL not otherwise specified (NOS) and angioimmunoblastic T-cell lymphoma, is 32% compared with only 14% for adult T-cell leukemia lymphoma[2], and there is no standard treatment regimen at present. High-dose therapy and autologous stem-cell transplants are still controversial[3, 4]. The regimen of cyclophosphamide, doxorubicin, vincristine, and prednisolone (CHOP) remains the most commonly used chemotherapeutic treatment for PTCL. However, CHOP has poor efficacy, a low CR rate (10%–60%) and a median overall survival (OS) of <3 years[5–7]. Moreover, doxorubicin has a low therapeutic index and significant treatment-related toxicities, whereas pegylated liposomal doxorubicin (PLD) has a stable spatial structure and demonstrates reduced binding to plasma proteins. Com-

---

* To whom correspondence should be addressed.
E-mail lnm1013@163.com
Received 2010-08-08 Accepted 2010-12-02

pared to conventional doxorubicin injection, PLD has a longer retention time in blood circulation, lower cardiotoxicity and improved targeted efficiency[8]. Recently, there have been several clinical studies on PLD-based NHL treatment that have shown it to be superior in the treatment of the elderly or patients with primarily cutaneous T-cell lymphomas (CTCL) with aggressive NHL[9–11].

However, there are few relative studies on the pharmacodynamic and pharmacokinetic characteristics of the cyclophosphamide, vincristine, PLD, and prednisolone (CCOP) regimen in PTCL patients. In this study, we aimed to investigate the efficiency and toxicities of a PLD-based CCOP regimen in PTCL patients, and to study the pharmacokinetics of PLD by determining its plasma concentrations at different time points after administration.

Materials and methods

Patient eligibility criteria

Patients were eligible for this study if they had histologically confirmed chemonaive or relapsed PTCL (except external precursor T-cell lymphomas) with at least one measurable lesion. The patients met several other eligibility criteria: (1) no current chemotherapy or radiotherapy treatment; (2) Eastern Cooperative Oncology Group (ECOG) performance status (PS) of 0–2; (3) age between 18 and 75 years; (4) survival prediction ≥3 months; (5) acceptable hematologic parameters [white blood cell (WBC) $\geq 3.5\times10^9$ L^{-1}, absolute neutrophil count (ANC) $\geq 1.5\times10^9$ L^{-1}, hemoglobin (HB) ≥9.0 g/L, and platelets $\geq 100\times10^9$ L^{-1}]; and (6) adequate hepatic and renal functions (liver: bilirubin ≤1.5 times the upper limit of normal (ULN), aspartate aminotransferase/alanine amiotransferase (AST/ALT) ≤1.5 times ULN or ≤5 times ULN if hepatic metastases were present; kidney: serum creatinine ≤1.5 times ULN or creatinine clearance ≥50 mL/min). The following groups were excluded: (1) pregnant or lactating women; (2) patients with other malignant tumors, except for carcinoma of the cervix uteri *in situ* and basal cell carcinoma of the skin; (3) patients with reactivated infection; and (4) patients with serious or untreated cardiac disease. The study was approved by the Ethics Committee of Zhejiang Cancer Hospital and all patients gave written informed consent.

Treatment plan

Patients received an intravenous (iv) infusion of cyclophosphamide (750 mg/m^2) within 10 min, vincristine (1.4 mg/m^2) within 15 min, and pegylated liposomal doxorubicin (30 mg/m^2) within one hour on d 1. Prednisolone (100 mg) was administered orally on d 1 to d 5, and the entire regimen was repeated every 3 weeks for six cycles. Before the treatment a 5-HT$_3$ receptor antagonist was used to prevent vomiting. Granulocyte colony-stimulating factor (G-CSF) was not used in the first course as regular prevention, but it was used in the next course if grade 3/4 granulocytopenia and febrile neutropenia were present. Treatment was delayed if grade 3/4 hematologic toxicities, grade 2/4 mucositis or skin toxicities occurred.

Response analysis

Response to therapy was assessed every two cycles according to the Response Evaluation Criteria in Solid Tumors (RECIST), which included complete responses (CR), partial responses (PR), stable disease (SD), progressive disease (PD), and CR plus PR as overall response rate (ORR). Patients who were evaluated as CR, PR, and SD continued treatment. Patients who were evaluated as CR and PR were reexamined after 4 weeks. The Kaplan-Meier Survival Analysis was performed by SPSS software (version 16.0).

Toxicity analysis

Toxicity was evaluated every cycle according to the National Cancer Institute Common Toxicity Criteria, version 3.0.

Pharmacokinetics study

Reagents and materials

Pegylated liposomal doxorubicin (Caelyx®) was provided by Ben Venue Laboratories Inc (Bedford, USA). Doxorubicin reference (98.8%) was provided by Zhejiang Hisun Pharmaceutical Co Ltd (Taizhou, China). The internal standard daunorubicin reference (98.0%) was obtained from Zhejiang Hisun Pharmaceutical Co Ltd (Taizhou, China). All other chemicals and solvents were of chromatographic or analytical grade and were obtained from several commercial sources. Drug-free heparinized human plasma was obtained from Hangzhou Central Blood Station (Hangzhou, China).

Chromatographic equipment and conditions

The Agilent 1100 high-performance liquid chromatography (HPLC) system was equipped with a G1311A pump, a G1314A programmable diode array detector (DAD) and a G1313A auto-injector. A Hewlett Packard (HP) 1000 computer with in-house developed software was used for on-line data acquisition and subsequent calculations. Separation was carried out using a Zorbax Elipse XDB-C18 (5 μm, 4.6 mm×150 mm, Agilent) column at 25 °C and detected at 254 nm. The mobile phase consisted of acetonitrile and 40 mmol/L ammonium acetate buffer solution. Samples were eluted in gradient mode (Table 1), and the flow rate was 0.8 mL/min. The injection volume was 50 μL. This method resulted in good separations (Figure 1).

Preparation of stock and standard solutions

A reference stock solution of doxorubicin (940.0 mg/L) and an

Table 1. The linear gradient elution of the mobile phase.

Time (min)	Acetonitrile (%)	Buffer (%)
0	10	90
5	10	90
10	15	85
15	20	80
25	40	60
30	40	60

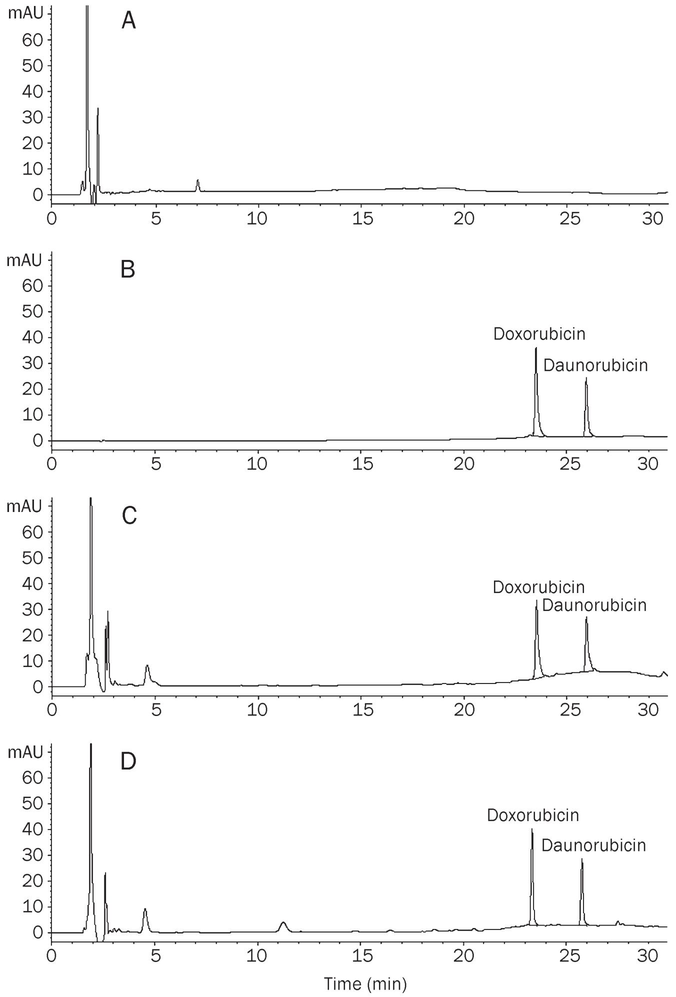

Figure 1. HPLC chromatograms.

internal standard solution of daunorubicin (20.4 mg/L) were prepared in sterile water (pH 6.8) and stored at 4 °C until use.

Assay procedure

The internal standard solution (100 μL) was added to drug-free human plasma (0.5 mL) and vortexed for one minute, followed by the addition of a 20% zinc sulfate methanol solution (0.6 mL). The sample was vortexed for one minute and then centrifuged at 10 000 round per minute for 10 min. The supernatant was filtered using a 0.45 μm filter and then 50 μL was injected into the liquid chromatography (LC) system.

Calibration curve preparation

A series of drug-free human plasma was mixed with different concentrations of doxorubicin; the final concentrations of doxorubicin were 0.18, 0.36, 0.73, 1.46, 2.93, 5.87, 11.75, 23.50, 47.00, and 94.00 mg/L. Five replicates were prepared for each concentration of doxorubicin. The calibration curves were obtained by plotting the peak area ratio (y) of doxorubicin over internal standard versus doxorubicin concentration. The regression equations of doxorubicin at low concentrations (0.18–2.93 mg/L) and high concentrations (2.93–94.00 mg/L) were $y=0.2378x-0.0161$, $r=0.9997$, and $y=0.262x-0.3315$, $r=0.9992$, respectively. The limit of detection (LOD) and the limit of quantification (LOQ) were 0.06 mg/L and 0.1 mg/L, respectively, for doxorubicin. The average recoveries of doxorubicin at various concentrations were 97.8%–110.2%. For intra- and inter-day precision, the corresponding standard deviations of the measurements were both less than 5.74%.

Pharmacokinetic studies and analysis

Blood samples were collected during the first cycle. Approximately 3 mL of whole blood samples were collected from patients' forearm veins into heparinized polypropylene centrifuge tubes before pegylated liposomal doxorubicin was infused as well as at 0.75, 2, 8, 24, 48, 72, 120, and 168 h after infusion. The blood samples were immediately placed on ice. Plasma was obtained by centrifugation of the samples (3000 round per minute for 10 min at 4 °C) and then stored at -20 °C until analysis. The plasma concentration-time data were analyzed by pharmacokinetic software for fitting the pharmacokinetic model and estimating the pharmacokinetic parameters.

Statistical analysis

Pharmacodynamic data were calculated using SPSS software (version 16.0). Pharmacokinetic parameters were obtained by DAS software (Drug and Statistics version 2.1.1, Mathematical Pharmacology Professional Committee of China, Shanghai, China). Data were expressed as the mean±SD. The mean values with 95% confidence interval and *t*-test were used to determine statistical significances in comparing pharmacokinetics between male and female patients (SPSS software, version 16.0). $P<0.05$ was considered statistically significant.

Results

Patient characteristics

Eleven patients with PTCL were enrolled in this study from February 2006 to December 2008. There were seven male and four female patients, and their median age was 36 years (range: 28–65 years). Seven patients were chemonaive, and four had relapsed (Table 2). Eight patients had performance status (PS) 0–1 and three had PS 2; four patients were in stage I–II, seven patients were in stage III–IV, and six patients had B symptoms. The serum lactate dehydrogenase (LDH) of seven patients was elevated. Patients were evaluated using the International Prognostic Index (IPI) score: six patients were given a score of 0–1, three were given a score of 2 and two were given a score of 3. The pathological types were PTCL and NOS (six cases), nasal type of NK/T-cell lymphoma (two relapsed cases after radiotherapy), angioimmunoblastic T-cell lymphoma (one case), anaplastic large cell lymphoma (one case of ALK negative), and γ–δ cell skin lymphoma (one case).

Treatment received

A total of 35 cycles of chemotherapy was administered, with a median number of 3.2 cycles (range: 2–6 cycles). Six patients received 2 treatment cycles, one patient received 3 cycles, two

Table 2. Clinical characteristics of 11 patients with PTCL.

Parameters	Score
Median age (year)	36
Age range (year)	28–65
Male (%)	63.6 (*n*=7)
Female (%)	36.4 (*n*=4)
Body surface area (m^2)	1.67
Body weight (kg)	64.3
Performance status (ECOG)	
0–1 (%)	72.7 (*n*=8)
2 (%)	27.3 (*n*=3)
Stage	
I–II (%)	36.4 (n=4)
III–IV (%)	63.6 (*n*=7)
B symptoms (%)	54.5 (*n*=6)
Elevated serum LDH (%)	63.6 (*n*=7)
IPI scores	
0–1 (%)	54.5 (*n*=6)
2 (%)	27.3 (*n*=3)
3 (%)	18.2 (*n*=2)
Pathological types	
PTCL, NOS (%)	54.5 (*n*=6)
Nasal type of NK/T-cell lymphoma (%)	18.2 (*n*=2)
Angioimmunoblastic T-cell lymphoma (%)	9.1 (*n*=1)
Anaplastic large cell lymphoma (ALK negative) (%)	9.1 (*n*=1)
γ–δ cell skin lymphoma (%)	9.1 (*n*=1)

patients received 4 cycles, and the remaining two patients received 6 cycles. Among the seven patients who received 2 or 3 treatment cycles, one quit the program due to poor compliance. The other six SD or PD patients received second-line chemotherapy. The remaining patients reached CR or PR, and two received high-dose therapy and autologous stem-cell therapy. Two patients received delayed treatment in 3 cycles. One NK/T cell lymphoma patient with B symptoms switched to the second-line regimen, received radiotherapy treatment and was still disease-free after the three months follow-up.

Efficacy and survival

Efficacy and survival were evaluated. Three patients had CR, two had PR, four had SD, and two had PD. The ORR was 45.5% and the CR rate was 27.3%. For the seven chemonaive patients, three had CR, two had PR, one had SD, and one had PD; the ORR was 71.4% and the CR rate was 42.9%. For the four relapsed patients, there was no CR or PR patient, but three patients had SD and one patient had PD. The median follow-up time for the 11 patients was 15 months (ranging from 5 to 36 months); however, six were dead as of the time of data analysis. The one-year overall survival rate was 45.5%, and the median PFS (progression-free survival) and survival time were 6.5 months (95% CI 3.17–19.02) and 11.5 months (95% CI 6.65–16.36), respectively. A Kaplan-Meier curve for survival time was generated (Figure 2).

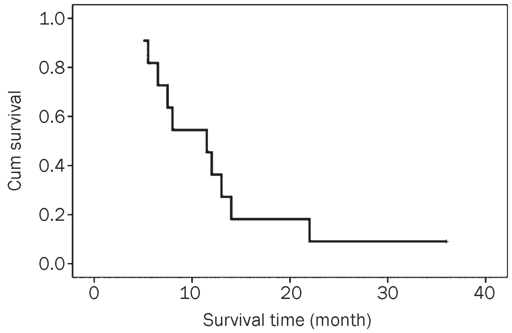

Figure 2. Survival curve for 11 patients with peripheral T-cell lymphomas treated with the CCOP regimen.

Toxicity analysis

The toxicity results of the 11 patients are shown in Table 3. Generally, the toxicities were tolerable. The main toxicities were myelosuppression including anemia (grade 3/4, one case), neutropenia (grade 3/4, three cases) and thrombocytopenia (grade 3/4, one case). The other toxicities were rare, with no treatment-related deaths.

Table 3. Toxicities of 11 patients with PTCL.

Toxicities	Grade 1/2 (%)	Grade 3/4 (%)
Anaemia	5 (45.5)	1 (9.1)
Neutropenia	4 (36.4)	3 (27.3)
Febrile neutropenia	2 (18.2)	0
Thrombocytopenia	3 (27.3)	1 (9.1)
Nausea/Vomiting	4 (36.4)	0
SGOT/SGPT	2 (18.2)	0
Oral mucositis	2 (18.2)	0
Hand-foot syndrome	1 (9.1)	0
Alopecia	2 (18.2)	0
Cardiac toxicity	0	0

SGOT, serum glutamic-oxaloacetic transaminase; SGPT, serum glutamic-pyruvic transaminase.

Plasma concentration analysis

Blood samples from nine patients treated with a CCOP regimen (without dose modification) were analyzed for plasma concentrations. Initially, at 0–8 h, plasma concentrations increased and peaked (8.490–9.221 mg/L), then they slowly decreased to an average level of 1.704 mg/L at 168 h (Figure 3).

Pharmacokinetic analysis

The plasma concentration-time data were processed by DAS software. Pegylated liposomal doxorubicin fits a biphasic kinetic model, and its pharmacokinetic parameters are shown in Table 4. The pharmacokinetic characteristics of pegylated liposomal doxorubicin injection were significantly different

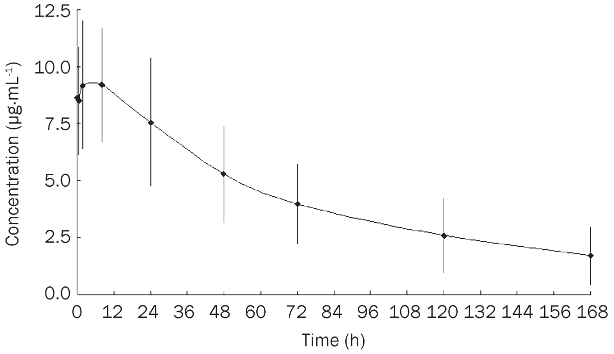

Figure 3. Plot of plasma concentration (mean±SD) *versus* time of doxorubicin in patients with PTCL treated with 30 mg/m^2 of pegylated liposomal doxorubicin in combination with a CCOP regimen (n=9).

Table 4. Pharmacokinetic parameters in patients with PTCL treated with 30 mg/m^2 of pegylated liposomal doxorubicin in combination with CCOP regimen (n=9).

Parameters	Mean	SD	SEM	95 % CI Lower bound	95 % CI Upper bound
$AUC_{(0-\infty)}$ (mg/L·h)	910.76	462.33	154.12	555.38	1266.14
$AUC_{(0-t)}$ (mg/L·h)	715.61	298.39	99.46	486.25	944.97
CL (L·h^{-1}·m^{-2})	0.043	0.025	0.0083	0.0239	0.062
C_{max} (mg/L)	9.93	2.97	0.99	7.64	12.21
$t_{1/2}$ (h)	68.40	28.39	9.46	46.58	90.23
t_{max} (h)	6.78	7.71	2.57	0.85	12.70
V_d (L/m^2)	3.56	1.13	0.38	2.69	4.42

AUC, area under the curve; CL (L·h^{-1}·m^{-2}), clearance; C_{max} (mg/L), maximum concentration; $t_{1/2}$ (h), half life time; t_{max} (h), the peak time; V_d (L/m^2), Volume of distribution; SD, standard deviation; SEM, standard error.

from conventional doxorubicin injection[12] (Table 5), where the $t_{1/2}$ of pegylated liposomal doxorubicin was 68 h, which was 6.58 times longer than conventional doxorubicin injection. Moreover, the area under curve (AUC) of pegylated liposomal doxorubicin increased 260 fold when compared to conventional doxorubicin injection, and the clearance of pegylated liposomal doxorubicin was 0.29% of conventional doxorubicin injection. This result indicates that pegylated liposomal doxorubicin has a longer retention time in plasma circulation than conventional doxorubicin injection, and the lower V_d (1.63%) indicates that it is localized and less distributed in other organs. These results are in agreement with the phase I/II clinical trials conducted by Hong[13, 14]. Gender did not affect the pharmacokinetic parameters of pegylated liposomal doxorubicin, and no significant difference was found in AUC_{0-168}, $AUC_{0-\infty}$, CL, C_{max}, $t_{1/2}$, t_{max}, or V_d (P=0.199−0.684) (Table 6).

Table 6. Comparison of pharmacokinetics between male and female patients administered pegylated liposomal doxorubicin.

Parameters	Male (n=6)	Female (n=3)	P Value^a
$AUC_{(0-\infty)}$ (g/L·h)	0.8±0.5	1.1±0.3	0.316
$AUC_{(0-t)}$ (g/L·h)	0.6±0.3	0.9±0.2	0.234
CL (L·h^{-1}·m^{-2})	0.051±0.027	0.027±0.008	0.199
C_{max} (mg/L)	9.5±2.9	10.8±3.6	0.605
$t_{1/2}$ (h)	61±31	83±16	0.298
t_{max} (h)	4±4	12.±11	0.331
V_d (L/m^2)	3.7±1.2	3.3±1.1	0.684

^{a}Parameters of male *vs* female.

Discussion

The CHOP regimen (cyclophosphamide, doxorubicin, vincristine, and prednisolone) has been used extensively to treat patients with PTCL. However, it has resulted in poor outcomes except for cases of anaplasic large-cell-lymphoma kinase (ALK)-positive lymphoma. Moreover, doxorubicin has a low therapeutic index and can induce several adverse effects, such as myelosuppression, as well as heart and digestive system toxicities, especially heart damage caused by drug accumulation[15, 16]. To avoid doxorubicin toxicities, PLD was used in the current study and evaluated for clinical administration.

PLD is a long-circulating pegylated liposome, which is prone to target cancer cells. Therefore, it can reduce the toxicities associated with doxorubicin, especially the myelosuppression and cardiotoxicity. Owing to its stable spatial structure and encapsulated form, PLD has longer plasma circulation, lower clearance rate, higher blood concentration, and longer $t_{1/2}$ (68 h) when compared with conventional doxorubicin injection. Generally, normal tissues have an integrated capillary wall and most liposomes cannot pass through it, but the permeability of new vessels in tumor tissues is much higher.

Table 5. Comparison of pharmacokinetics between patients administered pegylated liposomal doxorubicin and conventional doxorubicin injection.

Drug form	Tumor type	Dose (mg/m^2)	n	Parameters C_{max} (mg/L)	$AUC_{(0-\infty)}$ (mg/L·h)	CL (L·h^{-1}·m^{-2})	CL (L/h)^a	V_d (L/m^2)	V_d (L)^b	$t_{1/2}$ (h)
PLD	PTCL	30	9	9.93	910.76	0.043	0.073^a	3.56	5.946^b	68.40
Conventional doxorubicin (CD)[7]	Misc solid	50	4	5.90	3.50	–	25.30	–	365.00	10.40
	Rate (PLD/CD)			1.68	260	–	0.0029	–	0.0163	0.0029

^{a}CL (L/h)=CL (L·h^{-1}·m^{-2})×body surface area (m^2); ^{b}V_d (L)=CL (L/m^2)×body surface area (m^2).

Additionally, liposomal doxorubicin releases more slowly and can directly act on the tumor tissues, which makes doxorubicin better at targeted delivery. Compared to the conventional doxorubicin injection, PLD has improved pharmacodynamics and pharmacokinetics.

Several studies have reported that PLD has good remission and survival rates when used to treat basal T-cell lymphoma of the skin[15, 16], which suggests that it is essential to investigate specific treatments for different subtypes of the PTCL. In this study, the ORR of the 11 patients was 45.5% and the CR rate was 27.3%; the 1-year overall survival rate was 45.5%, and the median PFS and survival time were 6.5 months (95% CI 3.17–19.02) and 11.5 months (95% CI 8.07–21.24), respectively. For the seven chemonaive patients, the ORR was 71.4% and the CR was 42.9%. The results were consistent with results previously described in detail using the CHOP regimen[15–19].

The grade 3/4 toxicities were myelosuppression including anemia (one case, 9.1%), neutropenia (three cases, 27.3%), and thrombocytopenia (one case, 9.1%), which were higher than other CHOP regimen reports[19, 20]. However, there was no cardiac toxicity case in this study. Dose-dependent cardiac toxicity is a main side effect of doxorubicin, especially in elderly patients where there is a high rate of pre-existing cardiac disease[21]. However, cardiac toxicity is common even in younger patients[22]. It has also been reported that PLD has low concentrations in the heart, kidney, stomach, and small intestine, which reduces the incidence of adverse effects in these organs normally induced by free doxorubicin[23]. Therefore, the CCOP regimen has a better therapeutic index than the CHOP regimen with equivalent or superior efficacy and lower toxicity. Of the four relapsed patients, three experienced a short paracmasis. Thus, other new regimens are still needed to treat these types of patients. The results of the pharmacokinetic parameters (Table 5) indicate that PLD had a long circulation time in the plasma, enhancing accumulation in tumor tissues, and demonstrating a superior therapeutic activity over free doxorubicin. There were no significant differences in pharmacokinetic parameters of PLD due to the patients' gender (Table 6).

Although the data from this study of the pharmacokinetics and toxicity profile of the CCOP regimen are very favorable and encouraging, further investigations with more patients and randomized controlled studies in comparison to the CHOP regimen are warranted before new PTCL treatment guidelines can be proposed.

Acknowledgements

This work was sponsored by the Zhejiang Provincial Program for the Cultivation of High-level Innovative Health Talents as well as the Medical Science Research Foundation of Zhejiang Province, China (No 2006B010). We would like to thank Ben Venue Laboratories Inc and Zhejiang Hisun Pharmaceutical Co Ltd for providing pegylated liposomal doxorubicin and the standard references of doxorubicin and daunorubicin.

Author contribution

Yun FAN and Neng-ming LIN designed the research; Yun FAN, Lü-hong LUO, Luo FANG, Zhi-yu HUANG, Hai-feng YU, and Feng-qin WU performed the research; and Yun FAN and Neng-ming LIN analyzed the data and wrote the paper.

References

1 Savage KJ, Chhanabhai M, Gascoyne RD, Connors JM. Characterization of peripheral T-cell lymphomas in a single North American institution by the WHO classification. Ann Oncol 2004; 15: 1467–75.

2 Vose J, Armitage J, Weisenburger D; International T-Cell Lymphoma Project. International peripheral T-cell and natural killer/T-cell lymphoma study: pathology findings and clinical outcomes. J Clin Oncol 2008; 26: 4124–30.

3 Nickelsen M, Ziepert M, Zeynalova S, Glass B, Metzner B, Leithaeuser M, *et al*. High-dose CHOP plus etoposide (MegaCHOEP) in T-cell lymphoma: a comparative analysis of patients treated within trials of the German High-Grade Non-Hodgkin Lymphoma Study Group (DSHNHL). Ann Oncol 2009; 20: 1977–84.

4 Reimer P, Rüdiger T, Geissinger E, Weissinger F, Nerl C, Schmitz N, *et al*. Autologous stem-cell transplantation as first-line therapy in peripheral T-cell lymphomas: results of a prospective multicenter study.J Clin Oncol 2009; 27: 106–13.

5 Morabito F, Gallamini A, Stelitano C, Callea V, Guglielmi C, Neri S, *et al*. Clinical relevance of immunophenotype in a retrospective comparative study of 297 peripheral T-cell lymphomas unspecified, and 496 diffuse large B-cell lymphomas: experience of the Intergruppo Italiano Linfomi. Cancer 2004; 101: 1601-8.

6 Rüdiger T, Weisenburger DD, Anderson JR, Armitage JO, Diebold J, MacLennan KA, *et al*. Peripheral T-cell lymphoma (excluding anaplastic large-cell lymphoma): results from the Non-Hodgkin's Lymphoma Classification Project. Ann Oncol 2002; 13: 140-9.

7 Gabizon A, Catane R, Uziely B, Kaufman B, Safra T, Cohen R, *et al*. Prolinged circulation time and enhanced accumulation in malignant exudates of doxorubicin encapsulated in polyethylene-glycol coated liposomes. Cancer Res 1994; 54: 987–92.

8 Gabizon A, Shmeeda H, Barenholz SR. Pharmacokinetics of pegylated liposomal doxorubicin: review of animal and human studies. Clin Pharmacokinet 2003; 42: 419–36.

9 Quereux G, Marques S, Nguyen JM, Bedane C, D'incan M, Dereure O, *et al*. Prospective multicenter study of pegylated liposomal doxorubicin treatment in patients with advanced or refractory mycosis fungoides or Sézary syndrome. Arch Dermatol 2008; 144: 727–33.

10 Pulini S, Rupoli S, Goteri G, Pimpinelli N, Alterini R, Tassetti A, *et al*. Pegylated liposomal doxorubicin in the treatment of primary cutaneous T-cell lymphomas. Haematologica 2007; 92: 686–9.

11 Visani G, Guiducci B, D'Adamo F, Mele A, Nicolini G, Leopardi G, *et al*. Cyclophosphamide, pegylated liposomal doxorubicin, vincristine and prednisone (CDOP) plus rituximab is effective and well tolerated in poor performance status elderly patients with non-Hodgkin's lymphoma. Leuk Lymphoma 2005; 46: 477-9.

12 Crawford J. Clinical uses of pegylated pharmaceuticals in oncology. Cancer Treat Rev 2002; 28: 7–11.

13 Hong RL, Tseng YL. Phase I and pharmacokinetic study of a stable, polyethylene-glycolated liposomal doxorubicin in patients with solid tumors. Cancer 2001; 91: 1826–33.

14 Hong RL, Tseng YL. A phase II and pharmacokinetic study of pegylated liposomal doxorubicin in patients with advanced hepatocellular carcinoma. Cancer Chemother Pharmacol 2003; 51: 433–8.

15 Pan ZH, Huang HQ, Cai QQ, Bo Q, Wang BF, Liao H. Clinical analysis of prognosis for 96 patients with peripheral T-cell lymphoma. Chin J Clin Oncol 2007; 34: 702–5.

16 Savage KJ. Prognosis and primary therapy in peripheral T-cell lymphomas. Hematology Am Soc Hematol Educ Program 2008: 280–8.

17 Giri SN, Al-Bayati MA, Du X, Schelegle E, Mohr FC, Margolin SB. Amelioration of doxorubicin-induced cardiac and renal toxicity by pirfenidone in rats. Cancer Chemother Pharmacol 2004; 53: 141–50.

18 Schmitz N, Trümper L, Ziepert M, Nickelsen M, Ho AD, Metzner B, *et al*. Treatment and prognosis of mature T-cell and NK-cell lymphoma: an analysis of patients with T-cell lymphoma treated in studies of the German High-Grade Non-Hodgkin's Lymphoma Study Group (DSHNHL). Blood 2010; 116; 3418–25.

19 Gallamini A, Zaja F, Patti C, Billio A, Specchia MR, Tucci A, *et al*. Alemtuzumab (Campath-1H) and CHOP chemotherapy as first-line treatment of peripheral T-cell lymphoma: results of a GITIL (Gruppo Italiano Terapie Innovative nei Linfomi) prospective multicenter trial. Blood 2007; 110: 2316–23.

20 Vose J, Armitage J, Weisenburger D. International peripheral T-cell and natural killer/T-cell lymphoma study: pathology findings and clinical outcomes. J Clin Oncol 2008; 26: 4124–30.

21 Havlik RJ, Yancik R, Long S, Ries L, Edwards B. The National Institute on Aging and the National Cancer Institute SEER collaborative study on co-morbidity and early diagnosis of cancer in the elderly. Cancer 1994; 74: 2101–6.

22 van der Pal HJ, van Dalen EC, Hauptmann M, Kok WE, Caron HN, van den Bos C, *et al*. Cardiac function in 5-year survivors of childhood cancer: a long-term follow-up study. Arch Intern Med 2010; 170: 1247–55.

23 Lu WL, Qi XR, Zhang Q, Li RY, Wang GL, Zhang RJ, *et al*. A pegylated liposomal platform: pharmacokinetics, pharmacodynamics, and toxicity in mice using doxorubicin as a model drug. J Pharmacol Sci 2004; 95: 381–9.